

Photon-Related Elliptic Azimuthal Asymmetry and Photon-Hadron Correlations with an Isolation

Cut in Au+Au Collisions at $\sqrt{s_{NN}} = 200$ GeV at RHIC-PHENIX

A dissertation presented to

the faculty of

the College of Arts and Sciences of Ohio University

In partial fulfillment

of the requirements for the degree

Doctor of Philosophy

Tyler Danley

December 2018

© 2018 Tyler Danley. All Rights Reserved.

This dissertation titled

Photon-Related Elliptic Azimuthal Asymmetry and Photon-Hadron Correlations with an Isolation

Cut in Au+Au Collisions at $\sqrt{s_{NN}} = 200$ GeV at RHIC-PHENIX

by

TYLER DANLEY

has been approved for

the Department of Physics and Astronomy

and the College of Arts and Sciences by

Justin Frantz

Associate Professor of Physics and Astronomy

Joseph Shields

Interim Dean, College of Arts and Sciences

ABSTRACT

DANLEY, TYLER, Ph.D., December 2018, Physics and Astronomy

Photon-Related Elliptic Azimuthal Asymmetry and Photon-Hadron Correlations with an Isolation

Cut in Au+Au Collisions at $\sqrt{s_{NN}} = 200$ GeV at RHIC-PHENIX (281 pp.)

Director of Dissertation: Justin Frantz

A form of matter made up of deconfined quarks and gluons, called a quark-gluon plasma (QGP), can be formed by colliding nuclei at ultra-relativistic energies. Partons created from the initial nucleon scattering lose energy and fragment to produce jets of hadrons (h) as they traverse the QGP. Direct photons also originate from the initial hard scattering and can be correlated with jet particles to study the jet's energy loss. This energy loss also causes an azimuthal asymmetry, the strongest component of which is called v_2 .

In this dissertation, we have developed a method of obtaining direct photons that uses an isolation cut. We have derived single and two-particle second order event plane correlation functions including the isolation cut. These equations are used to extract v_2 of isolated photons and π^0 's in Au+Au collisions at center-of-mass energy 200 GeV at RHIC-PHENIX. Generally, we find that the isolated photon v_2 is consistent with the direct photon v_2 and less than the inclusive photon v_2 . The v_2 of isolated π^0 are less than that of inclusive π^0 which could be relevant for constraining the inclusion of jet fragmentation shower-dependent effects in energy loss models.

Using the two-particle angular correlations method, we compare away-side yields of isolated photon-hadron pairs in Au+Au collisions to those in $p + p$ collisions through I_{AA} ($= Y_{Au+Au} / Y_{p+p}$). This elucidates how the QGP changes the jets that come out of the collision. We find that at low hadron fractional momentum, z_T ($= p_T^h / p_T^\gamma$), the I_{AA} is enhanced, the jet particle production is increased compared to $p+p$, and at high z_T , the I_{AA} is suppressed. We present the first quantification of such enhancement as a function of centrality at RHIC. Comparison to theory shows that the data is consistent with the interpretation that the suppression is due to the high z_T particles' lost energy and the enhancement is from the lost energy enhancing the production of low z_T particles.

ACKNOWLEDGMENTS

First, I must thank Dr. Justin Frantz for his patience and guidance through this project. I would also like to thank my committee members, Dr. Madappa Prakash, Dr. Paul King, and Dr. Daniel Hembree for taking time out of their schedules at the busiest time of the year to play a role on my dissertation committee. This would could not have happened without my wife, Theresa Danley. And finally, I would like to thank all my friends and family for their infallible support.

TABLE OF CONTENTS

	Page
Abstract	3
Acknowledgments	5
List of Tables	10
List of Figures	11
 1 Introduction	27
1.1 The Standard Model	27
1.1.1 Gauge Bosons	27
1.1.2 Quarks	28
1.1.3 Leptons	29
1.1.4 Quantum Chromodynamics	30
1.2 The Big Bang	32
1.3 Heavy-Ion Collisions - Little Bangs	34
1.3.1 Event Evolution	34
1.3.2 Event Characterization	36
1.3.2.1 Centrality	36
1.3.2.2 Coordinate Systems	37
1.3.2.3 Reaction Planes and Flow Harmonics	38
1.4 QGP Signatures	41
1.4.1 Harmonic Flow	42
1.4.2 Single Particle Suppression	43
1.4.3 Jet Suppression	44
1.5 Photon-Hadron Correlations	46
1.5.1 Introduction to Correlations	47
1.6 Previous Photon-Hadron Correlation Measurements from PHENIX	49
1.6.1 I_{AA}	51
1.7 QCD and Jet Energy Loss Theory	53
1.8 Purpose of This Dissertation	55
 2 Experimental Details	57
2.1 Relativistic Heavy Ion Collider	57
2.2 Pioneering High Energy Nuclear Interaction Experiment	58
2.2.1 Central Magnet	60
2.2.2 Beam Beam Counter	61
2.2.3 Electromagnetic Calorimeter	62
2.2.4 Drift Chamber	63
2.2.5 Pad Chamber	64

3	Data Selection	66
3.1	Introduction	66
3.2	Event Selection - Centrality	66
3.3	Event Selection - Trigger	68
3.4	Particle Selection - Photons	68
3.4.1	Hot/Dead tower maps	69
3.4.2	Isolation Cut Method	71
3.5	Particle Selection - π^0 's	72
3.5.1	π^0 Trigger Efficiency	73
3.6	Particle Selection - Decay Photons	74
3.7	Particle Selection - Hadrons	75
3.7.1	Hadron Efficiency	75
4	Derivation of Isolated Particle Azimuthal Asymmetry and Simulation Verification	79
4.1	Introduction	79
4.2	Summary of my previous work	79
4.2.1	Finding v_{2E}	82
4.3	Derivation of Reaction Plane Efficiency Trigger Distribution With Event Plane Resolution	85
4.4	Confirmation of Reaction Plane Efficiency Trigger Distribution With Event Plane Resolution	91
4.4.1	Smearing	91
4.5	Special Cases	95
4.5.1	$ v_{2T} = v_{2E} $	96
4.5.2	$ v_{2E} > v_{2T} $	98
4.5.3	$v_{2E} = 0$	100
4.5.4	Fit Parameters for Combinations of v_{2E} and χ	102
4.6	Conclusion	109
5	Analysis Details - Isolated Particle v_2	110
5.1	Introduction	110
5.2	Acceptance Correction	110
5.2.1	Resolution Correction	111
5.3	Analysis Procedure	112
5.3.1	Inclusive Photons and π^0	112
5.3.2	Isolated Photons and π^0	114
5.3.3	Flow Systematic Errors	120
6	Results and Discussion - Isolated Particle v_2	125
6.1	Introduction	125
6.1.1	Inclusive Photon and $\pi^0 v_2$	125
6.1.1.1	Discussion	128
6.1.2	Isolated Photon and $\pi^0 v_2$	128
6.1.2.1	$v_{2T} + v_{2E}$	128

6.1.2.2	v_{2T}	131
6.1.2.3	Discussion of $v_{2T} + v_{2E}$ and v_{2T}	134
7	Analysis Details: Gamma-Hadron Correlations	136
7.1	Introduction	136
7.2	Analysis Procedure	136
7.3	Hadron v_2	136
7.4	Background Procedure - Mean Seeds Mean Partners	137
7.4.1	Mean Seeds Mean Partners with Isolated Particles	140
7.5	Decay Photons	142
7.5.1	Decay Probabilities - Sharkfins	143
7.5.1.1	Isolation Modifications to Decay Probabilities	144
7.5.1.2	Cutoff Correction to the Sharkfin Procedure	146
7.5.2	π^0 Combinatoric Background Effects in Decay Yield Estimation	147
7.5.3	Non- π^0 Hadron Decay Effects in Decay Yield Estimation	150
7.5.4	HIJING Study of Decay Photon Yield Method with Isolation Cut	152
7.6	R_γ	153
7.7	Systematic Errors	155
7.7.1	Decay Photon Systematics - Method	156
7.7.2	Decay Photon Systematics - S/B	156
7.7.3	Decay Photon Systematics - π^0 Cutoff	158
7.7.4	Decay Photon Systematics - η Contribution	158
7.7.5	Non-Decay Method Systematics	159
7.7.6	Systematics Summary	161
8	Results - Isolated Gamma-Hadron Correlations	165
8.1	Introduction	165
8.2	Correlation Functions	165
8.3	Jet Functions	166
8.4	Away-side Yields	167
8.5	I_{AA}	168
8.6	Isolation Method Cross-checks	176
8.6.1	Modification of the Elliptic Flow and the MSMP ξ	176
8.6.2	Modification of the Correlation and Jet Functions	179
8.6.3	Modification of the I_{AA}	181
8.6.4	Systematic Error with the Modified b	189
8.7	Results Summary and Combined Run 10 + Run11 Au+Au Results	191
8.8	Comparisons to Previous PHENIX Results	200
9	Discussion - Isolated Gamma-Hadron Correlations	201
9.1	Comparisons to Theoretical Calculations	201
9.2	$I_{AA}(p_{Th})$ versus $I_{AA}(z_T)$	203
9.3	Comparisons to Other Experiments	207
9.3.1	PYTHIA study of $R_{D(z)}$ shape	210

10 Summary and Future Work	213
10.1 Isolated Particle v_2	214
10.2 Isolated $\gamma - h$ Correlations	215
10.3 Future Work and Outlook	218
References	220
Appendix A: Correlation and Jet Functions	225
Appendix B: Systematic errors on the Away-side Yields	257
Appendix C: Licenses for Figures	263

LIST OF TABLES

Table	Page
1.1 The fundamental forces with their theories and mediators. The only mediators with mass are the mediators for the weak force. The ranges of the strong and weak forces are very small while the electromagnetic and gravitational forces have infinite range [1].	28
1.2 The quarks with their masses and charges [1].	29
1.3 The leptons with their masses, charges and lifetimes. Tau is the most massive and fastest decaying lepton. The neutrino masses are approximately zero [1].	30
2.1 Selected PHENIX event characterization and central arm detectors with their acceptance and purpose. Adapted from [2].	60
3.1 Isolation cut parameters for all centralities of Au+Au collisions [3].	72
3.2 Table of parameters for the Run 10 and central Run 11 efficiency functions that are shown in Figure 3.8. The functions have the form of Equation 3.7. These parameters come from References [3–5] for Run 10 and Reference [6] for Run 11.	76
3.3 Table of the Run 10 occupancy corrections, ϵ_{Occ} , for each centrality.	77
4.1 Input and fit parameters from the fits of Equations 4.3, 4.5, and 4.29 to Figures 4.9, 4.10, and 4.11, respectively. For the case $v_{2T} = 0.21$, $v_{2E} = -0.21$ and $\chi = 1.0$	98
4.2 Input and fit parameters from the fits of Equations 4.3, 4.5, and 4.29 to Figures 4.12, 4.13, and 4.14, respectively. For the case $v_{2T} = 0.11$, $v_{2E} = -0.21$, and $\chi = 1.6$	100
4.3 Input and fit parameters from the fits of Equations 4.3, 4.5, and 4.29 to Figures 4.15, 4.16, and 4.17, respectively. For the case $v_{2T} = 0.15$, $v_{2E} = 0$, and $\chi = 0.8$	102
7.1 R_γ , ρ , and R'_γ values for each trigger p_T for each centrality.	155

LIST OF FIGURES

Figure	Page
1.1 QCD phase diagram showing the phase transition from hadron gas to quark gluon plasma [7]. Courtesy Brookhaven National Laboratory.	32
1.2 The history of the universe. Time starts with the big bang on the left, the universe expands to where we are today 13.8 billion years later [8].	33
1.3 A simulation of a heavy-ion collision with time flowing from left to right. The leftmost panel shows the Lorentz contracted gold nuclei. In the middle left panel the ions collide. The red spheres in the next panel are the deconfined quarks and gluons. The rightmost panel shows the expanding quark gluon plasma [9]. Courtesy Brookhaven National Laboratory. See Figure C.1 and C.2 for more details.	35
1.4 A relativistic heavy-ion collision. The collision occurs on the left and forms a QGP. The QGP expands and cools to form hadrons. The particles that are read out in the detectors are formed during kinetic freeze-out [10].	36
1.5 Centrality examples with the impact parameter labeled for central collisions (Left) and peripheral collisions (Right). The beamline is out of the page.	37
1.6 A typical collision with purely elliptic flow. The participants form the almond shape (orange ellipsoid) while the spectators continue to travel along the beamline (blue spheres). The green grid is the reaction plane with the red arrow showing the impact parameter. The blue arrows show the direction of the pressure that is largest in the plane and smallest outside the plane[11].	39
1.7 The probability distribution of the reaction plane, Equation 1.9, for a few values of χ [12].	41
1.8 Elliptic flow coefficient v_2 as a function of p_T in (a) and KE_T in (b) for various particles detected by PHENIX and STAR at RHIC. The meson and baryon v_2 are not consistent with one another at high p_T [13]. This figure has been used with permission. See Figure C.3 and C.4 for more details.	42
1.9 Elliptic flow coefficient v_2 as a function of p_T in (a) and KE_T in (b) for various collision systems scaled by the number of valence quarks. The mesons and baryon collision systems are no longer inconsistent at high p_T , indicating that the quarks are causing the anisotropy, not the hadrons [13]. This figure has been used with permission. See Figures C.3 and C.4 for more details.	43
1.10 Compilation of PHENIX measured R_{AA} as a function of p_T in central Au+Au collisions for direct photons (red open squares), π^0 (blue solid circles), η (red solid circles), ϕ (green solid squares), protons (purple open diamonds), 0-20% central J/ψ (burgundy downward solid triangles), 0-20% central ω (black open crosses), heavy flavor e^\pm (black open circles), and K^\pm (blue downward triangles) [14].	44
1.11 $h - h$ correlations made with partner hadrons with $p_T > 2\text{GeV}/c$ relative to a trigger hadron with $p_{T\text{trig}} > 4 \text{ GeV}/c$ high p_T trigger for 3 collision systems, $d + Au$ (red points), $p+p$ (black points), and $Au+Au$ (blue stars), measured by the STAR experiment. One can see that only the away-side Au+Au jets are suppressed [15]. This figure has been used with permission. See Figure C.5 for more details.	45

1.12	Leading order direct γ production mechanisms, Compton scattering ($qg \rightarrow q\gamma$) in (a) and annihilation ($q\bar{q} \rightarrow g\gamma$) in (b) [3].	46
1.13	A typical correlation function. The gold region is the background, the red region is the jet function. The background level is b_0 , while the shape is determined by Equation 1.13 [16]. This figure has been used with permission. See Figure C.6 for more details.	48
1.14	(a) Inclusive photon-hadron (green diamonds), decay photon-hadron (purple squares), and direct photon-hadron (black points) jet functions for $5 < p_T^\gamma < 7$ and $3 < p_T^h < 5$ GeV/c in $p+p$ (top) and Au+Au (bottom) collisions [17]. (b) Direct photon-hadron jet functions in $p+p$ (blue squares) and Au+Au (black circles) collisions for $5 < p_T^\gamma < 9$ and different ξ regions[18]. These figures have been used with permission. See Figures C.7 and C.8 for more details.	50
1.15	(a) $ \Delta\phi - \pi < \pi/5$ away-side yield as a function of p_T^h for four different p_T^γ bins for Au+Au (red squares) and $p+p$ (blue points) collisions [17]. (b) (top) Per trigger yield for $5 < p_T^\gamma < 9$ GeV/c and $0.5 < p_T^h < 7$ GeV/c as a function of $\xi = \ln(1/z_T)$ where $z_T = p_T^h/p_T^\gamma$ for central Au+Au (black circles) and $p+p$ (blue squares) collisions. (bottom) Full $\Delta\phi > \pi/2$ away-side I_{AA} (black circles) versus ξ with BW-MLLA (red dashed line) and YaJEM (blue dashed line) calculations [18]. These figures have been used with permission. See Figures C.7 and C.8 for more details.	51
1.16	(a) I_{AA} as a function of ξ for 0-40% central Au+Au collisions and $5 < p_T^\gamma < 9$ GeV/c and $0.5 < p_T^h < 7$ GeV/c for $\Delta\phi > \pi/2$ away-side (black), $\Delta\phi > \pi/3$ away-side (red), and $\Delta\phi > \pi/6$ away-side (blue) [18]. (b) The ratio of the $\Delta\phi > \pi/2$ I_{AA} to $\Delta\phi > \pi/2$ I_{AA} . This figure has been used with permission. See Figure C.8 for more details.	52
1.17	I_{AA} of $\gamma_{dir} - h$ pairs with $5 < p_T^\gamma < 15$ GeV/c and $3 < p_T^h < 5$ GeV/c (blue points), the red points are $h - h$ pairs with $5 < p_T^h < 10$ GeV/c and $3 < p_T^h < 4$ GeV/c (red squares) as a function of N_{part} for the $\pi/5$ away-side region. The shaded gray region is the R_{AA} of π^0 's with $p_T > 5$ GeV/c [17]. This figure has been used with permission. See Figure C.7 for more details.	53
2.1	An aerial view of RHIC with the experiments and accelerators labeled [19]. Courtesy Brookhaven National Laboratory. See Figure C.1 and C.2 for more details.	57
2.2	Configuration of PHENIX for Run 10 as seen along (Top) and perpendicular to the beamline (Bottom) [20]. This figure has been used with permission. See Figure C.9 for more details.	59
2.3	PHENIX magnetic field orientation viewed perependicular to the beamline [21]. This figure has been used with permission. See Figures C.10 and C.11 for more details.	61
2.4	(Left) A single radiator attached to a PMT. (Right) A BBC module consisting of 64 radiators attached to PMTs [22].	62
2.5	(Left) A module of PbSc showing the four towers made up of layers of lead and scintillator. (Right) A module of PbGl showing the 24 towers [23]. This figure has been used with permission. See Figures C.12 and C.13 for more details.	63
2.6	(Left) Side view of the DCH with each wire plane labeled. (Right) Top view showing the U, X, and V wire orientations in the DC [24]. This figure has been used with permission. See Figures C.14 and C.15 for more details.	64
2.7	Pad chamber geometry described in text [25].	65

3.1	Illustration of how N_{ch} is related to quantities calculated with the Glauber model [26]. This figure has been used with permission. See Figure C.16 for more details.	67
3.2	BBC total charge distribution (blue) (x -axis) with a negative binomial distribution fit (red) that is used to find the trigger efficiency [27].	68
3.3	(a) A map of the excluded towers with hits with $p_T \leq 5$ GeV/c. (b) A map of the excluded towers with hits with $p_T > 5$ GeV/c. (c) A map of all additional towers found after the maps in (a) and (b) have been applied. In all three figures, each bin is a tower in the detector, the x axis is the tower position along the beamline ($zpos$) and the y axis is the tower height ($ ypos$).	70
3.4	Photon hits for all energies after hot/dead maps have been applied. Each plot is an EMCAL sector, each bin is an individual tower. The color corresponds to the number of hits in each tower for the entire Run 11 MinBias data set.	70
3.5	Definition of the isolation cut method that is used to find isolated photons. The black arrows are particles inside the cone [3].	72
3.6	π^0 trigger efficiency correction ($1/\pi^0$ trigger efficiency) as a function of p_T for the four centralities, 0-20% (black points), 20-40% (red points), 40-60% (green points), and 60-92 % (blue points).	74
3.7	An example π^0 decay probability function as a function of $\pi^0 p_T$	75
3.8	Single hadron efficiency for Run 10 (black line) and central Run 11 (red line) as a function of p_T that have the form of Equation 3.7 with the parameters defined in Table 3.2.	77
3.9	Single particle charged track efficiencies used in Run 11 for each centrality, the y -axis has arbitrary units.	78
4.1	The steps we follow to obtain v_{2E} . Left of the green line is the isolated particles' histograms while on the right is that of all of the particles. The ϕ plots ((a) and (c)) are convoluted with the ϕ_{RP} plots ((b) and (d)) to get the acceptance correction ((f) and (h)). We then divide the raw $\Delta\phi = \phi - \Psi_{RP}$ plots ((e) and (g)) by the acceptance correction to get the corrected $\Delta\phi$ distributions ((i) and (j)). We extract the v_{2E} by fitting the final plot formed by dividing the isolated $\Delta\phi$ (i) by all the $\Delta\phi$ (j) to Equation 4.2 (red line). This figure is for illustrative purposes only, for this reason we have left the plots and axis labels small.	83
4.2	Example of agreement of the parameters in Equation 4.3 to the Monte Carlo simulation input parameters. Specifically, fit parameters of Equation 4.3 as a function of input v_{2T} with a fixed $v_{2E} = -0.05$. The vertical magenta line is the absolute value of v_{2E} . The fit values are the open circles, the squares are the true input values, and the triangles near $y = 1$ are the ratio of the fit value to the true value.	84
4.3	Example of agreement of the parameters in Equation 4.5 to the Monte Carlo simulation input parameters. Specifically, fit parameters of Equation 4.5 as a function of input v_{2T} with a fixed $v_{2E} = -0.05$. The vertical magenta line is the absolute value of v_{2E} . The fit values are the open circles, the squares are the true input values, and the triangles near $y = 1$ are the ratio of the fit value to the truth value.	85
4.4	(Upper panel) \mathcal{S} and \mathcal{C} terms of Equation 4.27 are shown as a function of χ and the sum (lower panel) for $0 \leq \chi \leq 4$	90

4.5	The probability distribution of the reaction plane, Equation 1.9, for a few values of χ [12].	92
4.6	Reaction (a) and event (b) plane angles. Reaction planes are generated uniformly from $-\frac{\pi}{2} \leq \Psi_{RP} \leq \frac{\pi}{2}$ and smeared according to Equation 1.9. The $\Delta\Psi = \Psi_{RP} - \Psi_{EP}$ distribution is shown in (c).	93
4.7	$\Delta\phi = \phi_T - \Psi_{EP}$ distribution, generated using event planes from Figure 4.6b with $v_{2T} = 0.12$ and $v_{2E} = 0.05$, and fit to Equation 4.29 (red line).	94
4.8	Example of agreement of the parameters in Equation 4.29 to the Monte Carlo simulation input parameters. Specifically, fit parameters of Equation 4.29 as a function of input v_{2T} with a fixed $v_{2E} = -0.05$ and $\chi = 0.8$. The vertical magenta line is the absolute value of v_{2E} . The fit values are the open circles, the squares are the true input values, and the triangles near $y = 1$ are the ratio of the fit value to the true value.	95
4.9	$\Delta\phi = \phi_T - \Psi_{RP}$ distribution for $ v_{2T} = 0.21$ and $v_{2E} = -0.21$. The red line is a fit to Equation 4.3, the fit parameters are summarized in Table 4.1.	96
4.10	$\Delta\phi = \phi_T - \phi_A$ distribution for $ v_{2T} = 0.21$ and $v_{2E} = -0.21$. The red line is a fit to Equation 4.5, the fit parameters are summarized in Table 4.1.	97
4.11	$\Delta\phi = \phi_T - \Psi_{EP}$ distribution for $ v_{2T} = 0.21$, $v_{2E} = -0.21$ and $\chi = 1.0$. The red line is a fit to Equation 4.29, the fit parameters are summarized in Table 4.1.	97
4.12	$\Delta\phi = \phi_T - \Psi_{RP}$ distribution for $v_{2T} = 0.11$ and $v_{2E} = 0.21$. The red line is a fit to Equation 4.3, the fit parameters are summarized in Table 4.2.	98
4.13	$\Delta\phi = \phi_T - \phi_A$ distribution for $v_{2T} = 0.11$ and $v_{2E} = -0.21$. The red line is a fit to Equation 4.5, the fit parameters are summarized in Table 4.2.	99
4.14	$\Delta\phi = \phi_T - \Psi_{EP}$ distribution for $v_{2T} = 0.11$ and $v_{2E} = -0.21$ with $\chi = 1.6$. The red line is a fit to Equation 4.29, the fit parameters are summarized in Table 4.2.	99
4.15	$\Delta\phi = \phi_T - \Psi_{RP}$ distribution for $v_{2T} = 0.15$ and $v_{2E} = 0$. The red line is a fit to Equation 4.3, the fit parameters are summarized in Table 4.3.	100
4.16	$\Delta\phi = \phi_T - \phi_A$ distribution for $v_{2T} = 0.15$ and $v_{2E} = 0$. The red line is a fit to Equation 4.5, the fit parameters are summarized in Table 4.3.	101
4.17	$\Delta\phi = \phi_T - \Psi_{EP}$ distribution for $v_{2T} = 0.15$ and $v_{2E} = 0$ with $\chi = 0.8$. The red line is a fit to Equation 4.29, the fit parameters are summarized in Table 4.3.	101
4.18	Example of agreement of the parameters in Equation 4.3 to the Monte Carlo simulation input parameters. Specifically, fit parameters of Equation 4.3 as a function of input v_{2T} with a fixed $v_{2E} = 0$. The vertical magenta line is the absolute value of v_{2E} . The fit values are the open circles, the squares are the true input values, and the triangles near $y = 1$ are the ratio of the fit value to the truth value.	103
4.19	Example of agreement of the parameters in Equation 4.5 to the Monte Carlo simulation input parameters. Specifically, fit parameters of Equation 4.5 as a function of input v_{2T} with a fixed $v_{2E} = 0$. The vertical magenta line is the absolute value of v_{2E} . The fit values are the open circles, the squares are the true input values, and the triangles near $y = 1$ are the ratio of the fit value to the truth value. Note that $v_{2TA} = v_{2A}(v_{2T} + v_{2E})$	104

4.20 Example of agreement of the parameters in Equation 4.29 to the Monte Carlo simulation input parameters. Specifically, fit parameters of Equation 4.29 as a function of input v_{2T} with a fixed $v_{2E} = 0$. Each panel is a different value of χ , starting from the top and going down the $\chi = 20, 1.6, 1, 0.8, 0.4$. The vertical magenta line is the absolute value of v_{2E} . The fit values are the open circles, the squares are the true input values, and the triangles near $y = 1$ are the ratio of the fit value to the truth value.	105
4.21 Example of agreement of the parameters in Equation 4.3 to the Monte Carlo simulation input parameters. Specifically, fit parameters of Equation 4.3 as a function of input v_{2T} with a fixed $v_{2E} = -0.15$. The vertical magenta line is the absolute value of v_{2E} . The fit values are the open circles, the squares are the true input values, and the triangles near $y = 1$ are the ratio of the fit value to the true value.	106
4.22 Example of agreement of the parameters in Equation 4.5 to the Monte Carlo simulation input parameters. Specifically, fit parameters of Equation 4.5 as a function of input v_{2T} with a fixed $v_{2E} = -0.15$. The vertical magenta line is the absolute value of v_{2E} . The fit values are the open circles, the squares are the true input values, and the triangles near $y = 1$ are the ratio of the fit value to the true value. Note that $v_{2TA} = v_{2A}(v_{2T} + v_{2E})$	107
4.23 Example of agreement of the parameters in Equation 4.29 to the Monte Carlo simulation input parameters. Specifically, fit parameters of Equation 4.29 as a function of input v_{2T} with a fixed $v_{2E} = -0.15$. Each panel is a different value of χ , starting from the top and going down the $\chi = 20, 1.6, 1, 0.8, 0.4$. The vertical magenta line is the absolute value of v_{2E} . The fit values are the open circles, the squares are the true input values, and the triangles near $y = 1$ are the ratio of the fit value to the true value.	108
5.1 (a) Trigger angle versus reaction plane angle. (b) Trigger angle versus $\Delta\phi = \phi_T - \Psi_{2EP}$. (c) Acceptance function for the accepted trigger azimuthal angles and event plane angles. (d) Acceptance corrected trigger-event plane correlation.	111
5.2 BBC event plane resolution as a function of centrality for Run 10 (blue triangles) and Run 11 (magenta triangles) compared to the previously published BBC event plane resolution taken from Reference [28] (red circles).	112
5.3 Run 11 Au+Au 0 - 20% central event inclusive photon $\Delta\phi = \phi_T - \Psi_{2EP}$ distributions. Each plot is a trigger photon p_T bin. The blue line is a fit to Equation 5.4 and the extracted v_2 are plotted versus p_T in Figure 5.4.	113
5.4 Run 11 Au+Au 0 - 20% central event inclusive photon v_2 as a function of p_T . The $\Delta\phi = \phi_T - \Psi_{2EP}$ distributions are shown in Figure 5.3.	114
5.5 Run 11 Au+Au 0 - 20% central events $\Delta\phi$ distributions for photon triggers. The solid green line is a fit to Equation 4.29.	115
5.6 Run 11 Au+Au 0 - 20% central events fit parameters, defined by Equation 4.30, extracted from the green lines on Figure 5.5.	116
5.7 Method used to obtain v_{2E} . The $\Delta\phi$ distributions for isolated cones (left) and all cones (right) and the ratio of isolated to all (bottom). The red line on the bottom plot is a fit to Equation 5.5.	117
5.8 Run 11 Au+Au 0 - 20% central events $\Delta\phi$ distributions for isolated cones. The solid red line is a fit to Equation 5.5.	118
5.9 Run 11 Au+Au 0 - 20% central events v_{2E} as a function of p_T . These were obtained by fitting 5.5 to each plot in Figure 5.8.	119

5.10 Isolated photon v_{2T} as a function of p_T for three event planes, BBNS (red points), BBCN (green points), and BBCNS (black points) measured with 20 - 40% photons in the Run 11 data set. The blue points are direct photon v_2 measured in the Run 7 Au+Au PHENIX data set [29].	120
5.11 Inclusive photon v_2 in Au+Au collisions as a function of p_T for different EmCal shower shape cuts (top row). Ratio of each cut v_2 to the average v_2 . This figure is taken from Reference [30].	122
5.12 Inclusive photon v_2 in Au+Au collisions as a function of p_T using different event planes (top row). Ratio of each event plane v_2 to the average v_2 . This figure is taken from Reference [30].	123
5.13 Inclusive photon v_2 in Au+Au collisions as a function of p_T using two different methods (top row). Ratio of each method v_2 to the average v_2 . This figure is taken from Reference [30].	124
6.1 Inclusive photon v_2 as a function of p_T for (a) 0 - 20%, (b) 20 - 40%, (c) 40 - 60%, and (d) 60 - 92% events for both Run 10 (brown points) and Run 11 (green points) measured by the BBC. The boxes are systematic error bars. The green points are the inclusive photon v_2 as a function of p_T as measured by the BBC that are taken from Reference [29].	126
6.2 Extracted v_2 of inclusive π^0 as a function of p_T for (a) 0 - 20%, (b) 20 - 40%, (c) 40 - 60%, and (d) 60 - 92% events for both Run 10 (brown points) and Run 11 (green points) measured by the BBC. The boxes are systematic error bars. The green points are the v_2 of inclusive π^0 as a function of p_T as measured by the BBC that are taken from Reference [29].	127
6.3 Isolated photon $v_{2T} + v_{2E}$ as a function of p_T for (a) 0 - 20%, (b) 20 - 40%, (c) 40 - 60%, and (d) 60 - 92% events for both Run 10 (blue points) and Run 11 (magenta points) measured by the BBC. The boxes are systematic error bars. The red points are the inclusive photon v_2 and the green points direct photon v_2 as a function of p_T as measured by the BBC that are taken from Reference [29].	129
6.4 Extracted $v_{2T} + v_{2E}$ of isolated π^0 as a function of p_T for (a) 0 - 20%, (b) 20 - 40%, (c) 40 - 60%, and (d) 60 - 92% events for both Run 10 (blue points) and Run 11 (magenta points) measured by the BBC. The boxes are systematic error bars. The green points are the v_2 of inclusive π^0 as a function of p_T as measured by the BBC that are taken from Reference [29].	130
6.5 Isolated photon v_{2T} as a function of p_T for (a) 0 - 20%, (b) 20 - 40%, (c) 40 - 60%, and (d) 60 - 92% events for both Run 10 (blue points) and Run 11 (magenta points) measured by the BBC. The boxes are systematic error bars. The red points are the inclusive photon v_2 and the green points direct photon v_2 as a function of p_T as measured by the BBC that are taken from Reference [29].	132
6.6 Extracted v_{2T} of isolated π^0 as a function of p_T for (a) 0 - 20%, (b) 20 - 40%, (c) 40 - 60%, and (d) 60 - 92% events for both Run 10 (blue points) and Run 11 (magenta points) measured by the BBC. The boxes are systematic error bars. The green points are the v_2 of inclusive π^0 as a function of p_T as measured by the BBC that are taken from Reference [29].	133

6.7 Isolated direct + decay photon v_2 ($v_{2T} + v_{2E}$) as a function of p_T for 0 - 20% (left) and 20 - 40% (right) central events in Au+Au collisions. The boxes are systematic error bars. The red points are the direct photon v_2 and the brown points are inclusive photon v_2 for 0 - 20% and 20 - 40% central events that are taken from Reference [29, 31]. This figure has been used with permission. See Appendix C for more details.	135
7.1 Hadron v_2 as function of p_T for the four centrality bins, 0-20% (black points), 20-40% (red points), 40-60% (green points), and 60-92% (blue points). The blue points have a constant offset for clarity. These are the same points used in References [3, 5, 32].	137
7.2 Trigger photon yield as a function of N_{part} (top left) and N_{coll} (top right) and Partner hadron yield as a function of N_{part} (bottom left) and N_{coll} (bottom right). These are for triggers with $7 \leq p_T \leq 9$ GeV/c and partners with $3 \leq p_T \leq 5$ GeV/c. The red and blue lines are fits to Equation 7.1 and Equation 7.2.	138
7.3 Glauber model-calculated probability distributions for 5% centrality bins in Au+Au collisions as a function of N_{part} (a) and N_{coll} (b).	139
7.4 MSMP ξ as a function of centrality for inclusive photons in Run 10 Au+Au MinBias collisions. Each color is a trigger p_T bin and each row is a partner p_T bin, both have been artificially offset for clarity. The open points are points used in previous analyses [3, 5].	140
7.5 Trigger photon yield as a function of N_{part} (top left) and N_{coll} (top right) and partner hadron yield as a function of N_{part} (bottom left) and N_{coll} (bottom right). These are for triggers with $7 \leq p_T \leq 9$ GeV/c and partners with $3 \leq p_T \leq 5$ GeV/c. The red and blue lines are fits to Equation 7.1 and Equation 7.2. The green lines are fits to Equation 7.7.	141
7.6 MSMP ξ as a function of centrality for isolated photons in Run 10 Au+Au MinBias collisions. Each color is a trigger p_T bin and each row is a partner p_T bin, both have been artificially offset for clarity. The open points are points used in previous analyses [3, 5].	142
7.7 An example $\pi^0 - h$ decay probability function, or sharkfin, as a function of p_T of the π^0	143
7.8 Energy distributions within cones of a size used in the analysis around various kinds of particles used in the analysis.	144
7.9 Isolation probability function as a function of π^0 energy for four different decay photon energy ranges: $5 < E_\gamma < 7$ GeV (top left), $7 < E_\gamma < 9$ GeV (top right), $9 < E_\gamma < 12$ GeV (bottom left), and $5 < E_\gamma < 10$ GeV (bottom right) [3, 33].	145
7.10 An example $\pi^0 - h$ decay probability function (sharkfin) as a function of π^0 energy with an isolation cut (red line) and without an isolation cut (green line) [3, 33].	146
7.11 Example of increased S/B level for π^0 combinatorics in the isolated sample. The left panel shows the isolated $\pi^0 m_{\gamma\gamma}$ peak with the ratio if the integral of the red line to the black line (the S/B) shown. The right panel shows the $m_{\gamma\gamma}$ peak of inclusive π^0 with the ratio if the integral of the red line to the black line (the S/B) shown [32].	148
7.12 Inclusive Y_{bkg} ($\equiv Y_{sideband}$)/ Y_{tot} as a function of $\Delta\phi$ for three p_T bin combinations [34].	149
7.13 $ \Delta\phi - \pi > \pi/2$ away-side Y_{tot} (black points) and Y_{bkg} (red points) in the upper panels and the ratio (Y_{tot}/Y_{bkg}) in the lower panels, both are plotted as a function of trigger p_T . The left side is for $1 < p_T^{hadron} < 2$ in 0 - 20% central events and the right side is for $3 < p_T^{hadron} < 5$ in 40-60% central events.	150

- 7.14 Per-trigger yield for $5 < p_T^\gamma < 7$ GeV/c and $2 < p_T^{hadron} < 3$ GeV/c for $\pi^0 - h$ (red circles), $\gamma_{decay \ from \ \pi^0} - h$ (magenta crosses), $\eta - h$ (green triangles), $\gamma_{decay \ from \ \eta} - h$ (magenta crosses) in $p+p$ collisions [17]. This figure has been used with permission. See Figure C.7 for more details. 151
- 7.15 The %-error of the derived from the true HIJING $\gamma_{dec} - h$ pair correlation functions, background, and jet functions, as a function of z_T , in all centrality bins with the isolation cut applied. The yellow band indicates 2% ranges. The red points are $7 < p_{T,dec} < 9$ and the green points are $9 < p_{T,dec} < 12$ 153
- 7.16 Isolated π^0 invariant mass ($m_{\gamma,\eta}$) peak for 0 - 20% events for each trigger bin used in this analysis. The red line is a Gaussian-plus-line fit to the data, the green line is the Gaussian from the fit, and the black line is the line from the fit. The S/B ratios are found by integrating the green line in 2σ of the peak (the region between the vertical magenta lines) and dividing it by the integral of the line in the same region. The signal-to-background ratio (S/B) is shown in each panel. 158
- 7.17 Summary of the HIJING study carried out in References [3, 33]. The left side shows the jet functions for the 20-40% central events for $7 < p_T^\gamma < 9$ GeV/c and $2 < p_T^{hadron} < 3$ GeV/c (top) and $7 < p_T^\gamma < 9$ GeV/c and $5 < p_T^{hadron} < 7$ GeV/c (bottom) for both the derived direct photons (blue points) and the true direct photons (red). The right side shows the ratio of derived $\pi/2$ away-side direct photon-hadron yield to the true $\pi/2$ away-side direct photon-hadron yield for $7 < p_T^\gamma < 9$ GeV/c (red) and $9 < p_T^\gamma < 12$ GeV/c (green) triggers. The yellow band shows the 20% deviation. 160
- 7.18 Error contributions of the direct photon $\pi/2$ away-side yield broken down by source for Run 10 (red) and Run 11 (black) central events. Each source is a different bin from left to right, v_2 , normalization (MSMP), decay photons, R_γ , total systematic error, and total statistical error. Each plot is a different p_T bin combination. Trigger p_T increases to the right while partner p_T increases going down. 162
- 7.19 Systematic error contributions of the direct photon $\pi/2$ away-side yield broken down by source for Run 10 (red) and Run 11 (black) central events. Each source is a different bin from left to right, v_2 , normalization (MSMP), decay photons, R_γ , and total systematic error. Each plot is a different p_T bin combination. Trigger p_T increases to the right while partner p_T increases going down. This is the same as Figure 7.18 but without the statistical error for each p_T bin combination. 163
- 7.20 Systematic error contributions of the direct photon $\pi/5$ away-side yield broken down by source for Run 10 (red) and Run 11 (black) central events. Each source is a different bin from left to right, v_2 , normalization (MSMP), decay photons, R_γ , and total systematic error. Each plot is a different p_T bin combination. Trigger p_T increases to the right while partner p_T increases going down. 164
- 8.1 Run 11 Au+Au $\gamma_{iso} - h$ correlation functions for the 20-40% central events. Each plot is a different p_T bin combination. Trigger p_T increases from left to right while partner p_T increases from top to bottom. The black line represents the background level, the red lines around it is the error on the black line. 166
- 8.2 Run 11 Au+Au $\gamma_{iso} - h$ (black points), $\gamma_{dec} - h$ (red points), and $\gamma_{dir} - h$ (blue points) jet functions for 0 - 20% central events. Each plot is a different p_T bin combination. Trigger p_T increases from left to right while partner p_T increases from top to bottom. 167

8.3 Run 10 Au+Au $\gamma_{dir} - h \pi/3$ away-side yield as a function of z_T for the four centrality bins used in this analysis, 0 - 20% (orange points), 20 - 40% (green points), 40 - 60% (blue points), and 60 - 92% (magenta points). The $p+p$ points are shown in red. Each trigger p_T bin has a different marker style. The colored lines are just there to guide the eye.	168
8.4 Run 10 Au+Au I_{AA} as a function of z_T for the $\pi/3$ integrated away-side for each centrality bin. Each trigger p_T bin is a different color and the four p_{Tassoc} bins: 1-2, 2-3, 3-5, and 5-10 GeV/c increase from left to right. The gray horizontal lines are fits to the data to average it. The yellow bands around them are the error on the fits.	169
8.5 Run 10 Au+Au I_{AA} as a function of z_T for the $\pi/2$ (a) and the $\pi/5$ (b) integrated away-side for each centrality bin. Each trigger p_T bin is a different color and the four p_{Tassoc} bins: 1-2, 2-3, 3-5, and 5-10 GeV/c that increase from left to right. The gray horizontal lines are fits to the data to average it. The yellow bands around them are the error on the fits.	170
8.6 Run 11 Au+Au I_{AA} as a function of z_T for the $\pi/3$ integrated away-side for each centrality bin. Each trigger p_T bin is a different color and the four p_{Tassoc} bins: 1-2, 2-3, 3-5, and 5-10 GeV/c that increase from left to right. The gray horizontal lines are fits to the data to average it. The yellow bands around them are the error on the fits.	171
8.7 Run 11 Au+Au I_{AA} as a function of z_T for the $\pi/2$ (a) and the $\pi/5$ (b) integrated away-side for each centrality bin. Each trigger p_T bin is a different color and the four p_{Tassoc} bins: 1-2, 2-3, 3-5, and 5-10 GeV/c that increase from left to right. The gray horizontal lines are fits to the data to average it. The yellow bands around them are the error on the fits.	172
8.8 Associated particle p_T as a function of z_T . For each associated p_T , the lowest trigger p_T is the right most bin, and increases from left to right. The vertical lines show boundaries of the two averaging ranges.	173
8.9 Run 10 I_{AA} as a function of N_{part} for each integration region $\pi/2$ (a), $\pi/3$ (b), and $\pi/5$ (c). The red points in the top panels is the high z_T average and the blue points in the low z_T average. The bottom panels shows the centrality dependence of ratio of high to low z_T fit values which more accurately reflects the true centrality dependence of the low z_T enhancement in the per-jet fragmentation function since per-photon I_{AA} always folds in the overall suppression of the away-side jets.	174
8.10 Run 11 I_{AA} as a function of N_{part} for each integration region $\pi/2$ (a), $\pi/3$ (b), and $\pi/5$ (c). The red points in the top panels is the high z_T average and the blue points in the low z_T average. The bottom panels shows the centrality dependence of ratio of high to low z_T fit values which more accurately reflects the true centrality dependence of the low z_T enhancement in the per-jet fragmentation function since per-photon I_{AA} always folds in the overall suppression of the away-side jets.	175
8.11 Elliptic flow coefficients ($v_{2T} + v_{2E}$) used to subtract background shape from isolated gamma-hadron correlation functions as a function of p_T for the centrality bins used in this analysis. The black points are with the modified b cones and the blue points are the original Run 10 points shown in Figure 6.3.	177

8.12 MSMP ξ as a function of centrality for isolated photons found with the modified b in Run 10 Au+Au collisions. Each color is a trigger p_T bin and each row is a partner p_T bin, both have been artificially offset for clarity. The open points are the solid points in Figure 7.6.	179
8.13 Run 10 Au+Au $\gamma_{iso} - h$ correlation functions for 0 - 20% central events with the modified b cone parameter. Each plot is a different p_T bin combination. Trigger p_T increases to the right while partner p_T increases going down. The black line represents the background level, the red lines around it is the error on the black line.	180
8.14 Run 10 Au+Au $\gamma_{iso} - h$ (black), $\gamma_{dec} - h$ (red), and $\gamma_{dir} - h$ (blue) jet functions for 0 - 20% central events with the modified b cone parameter. Each plot is a different p_T bin combination. Trigger p_T increases to the right while partner p_T increases going down.	181
8.15 Run 10 away-side yields as a function of z_T for modified b cones for each integration region $\pi/2$ (a), $\pi/3$ (b), and $\pi/5$ (c) and each centrality bin: 0 - 20% (orange), 20 - 40% (green), 40 - 60% (blue), and 60 - 92% (magenta). The red points are the $p+p$ baseline. The colored lines are just there to guide the eye.	182
8.16 Run 10 I_{AA} as a function of z_T for modified b cones for each integration region $\pi/2$ (a), $\pi/3$ (b), and $\pi/5$ (c) for each centrality bin. Each trigger p_T bin is a different color. The gray horizontal lines are fits to the data to average it. The yellow bands around them are the error on the fits.	183
8.17 Run 10 I_{AA} as a function of z_T with the original b (solid points) and the modified b (open points) for the $\pi/2$ integration region for each centrality bin: 0-20% (a), 20-40% (b), 20-40% (c), 60-92% (d). The solid points are the same as the points in Figure 8.5, the open points are from Figure 8.16.	185
8.18 Run 10 I_{AA} as a function of z_T with the original b (solid points) and the modified b (open points) for the $\pi/3$ integration region for each centrality bin: 0-20% (a), 20-40% (b), 20-40% (c), 60-92% (d). The solid points are the same as the points in Figure 8.4, the open points are from Figure 8.16.	186
8.19 Run 10 I_{AA} as a function of z_T with the original b (solid points) and the modified b (open points) for the $\pi/5$ integration region for each centrality bin: 0-20% (a), 20-40% (b), 20-40% (c), 60-92% (d). The solid points are the same as the points in Figure 8.5, the open points are from Figure 8.16.	187
8.20 Run 10 I_{AA} as a function of N_{part} for modified b cones for each integration region $\pi/2$ (a), $\pi/3$ (b), and $\pi/5$ (c). The red points in the top panels is the high z_T average and the blue points in the low z_T average. The bottom panels shows the centrality dependence of the <i>ERF</i>	188
8.21 Error contributions of the direct photon $\pi/2$ away-side yield broken down by source for Run 10 with the original b (red) and Run 10 with the modified b (black) for 0 - 20% events. Each source is a different bin from left to right, v_2 , normalization (MSMP), decay photons, R_γ , total systematic error, and total statistical error. Each plot is a different p_T bin combination. Trigger p_T increases to the right while partner p_T increases going down.	189

8.22 Error contributions of the direct photon $\pi/5$ away-side yield broken down by source for Run 10 with the original b (red) and Run 10 with the modified b (black) for 0 - 20% events. Each source is a different bin from left to right, v_2 , normalization (MSMP), decay photons, R_γ , total systematic error, and total statistical error. Each plot is a different p_T bin combination. Trigger p_T increases to the right while partner p_T increases going down.	190
8.23 Ratios of Run 11 over Run 10 integrated per-trigger yields for the $\pi/5$ away-side. Each trigger p_T bin is a different color and the four p_{Tassoc} bins: 1-2, 2-3, 3-5, and 5-10 GeV/c that increase from left to right.	191
8.24 Run 10 and Run 11 combined away-side yields as a function of z_T for each integration region $\pi/2$ (a), $\pi/3$ (b), and $\pi/5$ (c) and each centrality bin: 0 - 20% (orange), 20 - 40% (green), 40 - 60% (blue), and 60 - 92% (magenta). The red points are the $p+p$ baseline.	193
8.25 Combined Run 10 + Run 11 I_{AA} as a function of z_T for the $\pi/2$ away-side integration region. Each trigger p_T bin is a different color and the four p_{Tassoc} bins: 1-2, 2-3, 3-5, and 5-10 GeV/c that increase from left to right. Constant fits to high and low z_T regions are shown with statistical error in purple [31]. This figure has been used with permission. See Appendix C for more details.	195
8.26 Combined Run 10 + Run 11 I_{AA} as a function of z_T for the $\pi/3$ away-side integration region. Each trigger p_T bin is a different color and the four p_{Tassoc} bins: 1-2, 2-3, 3-5, and 5-10 GeV/c that increase from left to right. Constant fits to high and low z regions are shown with statistical error in purple.	196
8.27 Combined Run 10 + Run 11 I_{AA} as a function of z_T for the $\pi/5$ away-side integration region. Each trigger p_T bin is a different color and the four p_{Tassoc} bins: 1-2, 2-3, 3-5, and 5-10 GeV/c that increase from left to right. Constant fits to high and low z regions are shown with statistical error in purple.	197
8.28 Run 10 and Run 11 combined I_{AA} as a function of N_{part} for each integration region $\pi/2$ (a), $\pi/3$ (b), and $\pi/5$ (c). The red points in the top panels is the high z_T average and the blue points in the low z_T average. The bottom panels shows the centrality dependence of ratio of low to high z_T fit values, the energy recovery factor, which more accurately reflects the true centrality dependence of the low z_T enhancement in the per-jet fragmentation function since per-photon I_{AA} always folds in the overall suppression of the away-side jets [31]. These figures has been used with permission. See Appendix C for more details.	199
8.29 Run 10 + 11 Au+Au $\gamma_{dir} - h$ I_{AA} as a function of $\xi = \ln(1/z_T)$ for for each integration region $\pi/2$ (a) and $\pi/3$ (b) from this anaylsis (green points). The black and blue points are Run 7 + 10 + 11 Au+Au 0 - 40 % central events I_{AA} carried out in Reference [32, 35]. Each panel is a trigger p_T bin.	200
9.1 Run 10 + 11 Au+Au direct photon I_{AA} as a function of N_{part} for each integration region $\pi/3$ (a) and $\pi/5$ (b) from this anaylsis [31]. The gray band is the R_{AA} of π^0 for π^0 with $p_T > 5$ GeV/c from Reference [36]. These figures has been used with permission. See Appendix C for more details.	201

9.2 Non-Isolated γ -h results from separate analysis—not part of this dissertation—of other PHENIX collaborators Ge H. and Jacak, B et. al. Run 7 + 10 + 11 Au+Au 0 - 40 % central events I_{AA} as function of $\xi = \ln(1/z_T)$ for three trigger p_T bins: $5 < p_T^\gamma < 7$ GeV/c (top panel), $7 < p_T^\gamma < 9$ GeV/c (middle panel), and $9 < p_T^\gamma < 12$ GeV/c (bottom panel). The lines are two theoretical calculations, CoLBT_Hydro (solid line) and BW-MLLA (dashed line) [35, 37, 38]. This figure has been used with permission. See Figures C.17 and C.18 for more details.	203
9.3 Non-Isolated γ -h results from separate analysis—not part of this dissertation—of other PHENIX collaborators Ge H. and Jacak, B et. al. I_{AA} as a function of associated hadron p_T or three trigger p_T bins: $5 < p_T^\gamma < 7$ GeV/c (top panel), $7 < p_T^\gamma < 9$ GeV/c (middle panel), and $9 < p_T^\gamma < 12$ GeV/c (bottom panel). The black points are 0-40% central events in Au+Au collisions, the same points shown in Figure 9.2, and the magenta points are 0-100% central events in d+Au collisions at $\sqrt{s_{NN}} = 200$ GeV [32].	204
9.4 Combined Run 10 + Run 11 I_{AA} as a function of associated hadron p_T for the $\pi/5$ away-side integration region. Each trigger p_T bin is a different color that has been offset for clarity.	206
9.5 Combined Run 10 + Run 11 I_{AA} as a function of associated hadron p_T for the $\pi/3$ away-side integration region. Each trigger p_T bin is a different color that has been offset for clarity.	206
9.6 Combined Run 10 + Run 11 I_{AA} as a function of associated hadron p_T for the $\pi/2$ away-side integration region. Each trigger p_T bin is a different color that has been offset for clarity.	207
9.7 I_{AA} as a function of z_T for $\gamma_{dir} - h$ (red points) and $\pi_0 - h$ (blue points) for triggers with $12 < p_T^{trig} < 20$ GeV/c measured with STAR. The lines are theoretical calculations: Qin (red dotted line), $\gamma_{dir} - h$ ZOWW (red solid line), $\pi_0 - h$ ZOWW (blue solid line), and the Renk YaJem model (red dot dashed line) [39]. This figure has been used with permission. See Appendix C for more details.	208
9.8 $R_{D(z)}$ (left) and $R_{D(p_T)}$ (right) (blue points) in Pb+Pb collisions at $\sqrt{s_{NN}} = 2.76$ TeV with the systematic error in yellow [40]. This figure has been used with permission. See Appendix C for more details.	210
9.9 PYTHIA jet yield as a function of z_T for $R = 0.3$ jets with $p_T > 8$ GeV/c. The black points are the normal jets and the red points are the high z_T weighted jets.	211
9.10 True PYTHIA $R_{D(z)}$ (a) and I_{AA} for trigger particles with $p_T > 10$ GeV/c as a function of hadron p_T (b). The I_{AA} shows no high p_T enhancement.	212
10.1 (Left) I_{AA} of $\gamma_{dir} - h$ pairs with $5 < p_T^\gamma < 15$ GeV/c and $3 < p_T^h < 5$ GeV/c (blue points), the red points are $h - h$ pairs with $5 < p_T^h < 10$ GeV/c and $3 < p_T^h < 4$ GeV/c (red squares) as a function of N_{part} for the $\pi/5$ away-side region. The shaded gray region is the R_{AA} of π^0 's with $p_T > 5$ GeV/c [17]. (Right) Run 10 + 11 Au+Au $\gamma_{dir} - h$ I_{AA} as a function of N_{part} for the $\pi/5$ away-side region from this analysis. The gray band is the R_{AA} of π^0 for π^0 with $p_T > 5$ GeV/c from Reference [36].	216
10.2 Average I_{AA} as a function of N_{part} for each away-side integration region $\pi/2$ (left), $\pi/3$ (middle), and $\pi/5$ (right). The red points in the top panels is the high z_T average and the blue points are the low z_T average. The bottom panels show the centrality dependence of ratio of high to low z_T average I_{AA} , the energy recovery factor.	217

10.3 Current sPHENIX design with the major subsystems labeled: inner and outer hadron calorimeters (HCal), intermediate silicon tracker (INTT), Monolithic-Active-Pixel-Sensor-based VerTeX Detector (MVTX), the solenoid magnet, electromagnetic calorimeter (EMCal), and the time projection chamber (TPC) [41].	219
A.1 Run 10 Au+Au $\gamma_{iso} - h$ correlation functions for 0-20% events. Each plot is a different p_T bin combination. Trigger p_T increases to the right while partner p_T increases going down. The black line represents the background level, the red lines around it is the error on the black line.	225
A.2 Run 11 Au+Au $\gamma_{iso} - h$ correlation functions for the centrality labeled in the figure. Each plot is a different p_T bin combination. Trigger p_T increases to the right while partner p_T increases going down. The black line represents the background level, the red lines around it is the error on the black line.	226
A.3 Run 10 Au+Au $\gamma_{iso} - h$ correlation functions for the centrality labeled in the figure. Each plot is a different p_T bin combination. Trigger p_T increases to the right while partner p_T increases going down. The black line represents the background level, the red lines around it is the error on the black line.	227
A.4 Run 11 Au+Au $\gamma_{iso} - h$ correlation functions for the centrality labeled in the figure. Each plot is a different p_T bin combination. Trigger p_T increases to the right while partner p_T increases going down. The black line represents the background level, the red lines around it is the error on the black line.	228
A.5 Run 10 Au+Au $\gamma_{iso} - h$ correlation functions for 0-20% events. Each plot is a different p_T bin combination. Trigger p_T increases to the right while partner p_T increases going down. The black line represents the background level, the red lines around it is the error on the black line.	229
A.6 Run 11 Au+Au $\gamma_{iso} - h$ correlation functions for the centrality labeled in the figure. Each plot is a different p_T bin combination. Trigger p_T increases to the right while partner p_T increases going down. The black line represents the background level, the red lines around it is the error on the black line.	230
A.7 Run 10 Au+Au $\gamma_{iso} - h$ correlation functions for the centrality labeled in the figure. Each plot is a different p_T bin combination. Trigger p_T increases to the right while partner p_T increases going down. The black line represents the background level, the red lines around it is the error on the black line.	231
A.8 Run 11 Au+Au $\gamma_{iso} - h$ correlation functions for the centrality labeled in the figure. Each plot is a different p_T bin combination. Trigger p_T increases to the right while partner p_T increases going down. The black line represents the background level, the red lines around it is the error on the black line.	232
A.9 Run 10 Au+Au $\pi^0 - h$ correlation functions for 0-20% events. Each plot is a different p_T bin combination. Trigger p_T increases to the right while partner p_T increases going down. The black line represents the background level, the red lines around it is the error on the black line.	233
A.10 Run 11 Au+Au $\pi^0 - h$ correlation functions for the centrality labeled in the figure. Each plot is a different p_T bin combination. Trigger p_T increases to the right while partner p_T increases going down. The black line represents the background level, the red lines around it is the error on the black line.	234

A.11 Run 10 Au+Au $\pi^0 - h$ correlation functions for the centrality labeled in the figure. Each plot is a different p_T bin combination. Trigger p_T increases to the right while partner p_T increases going down. The black line represents the background level, the red lines around it is the error on the black line.	235
A.12 Run 11 Au+Au $\pi^0 - h$ correlation functions for the centrality labeled in the figure. Each plot is a different p_T bin combination. Trigger p_T increases to the right while partner p_T increases going down. The black line represents the background level, the red lines around it is the error on the black line.	236
A.13 Run 10 Au+Au $\pi^0 - h$ correlation functions for 0-20% events. Each plot is a different p_T bin combination. Trigger p_T increases to the right while partner p_T increases going down. The black line represents the background level, the red lines around it is the error on the black line.	237
A.14 Run 11 Au+Au $\pi^0 - h$ correlation functions for the centrality labeled in the figure. Each plot is a different p_T bin combination. Trigger p_T increases to the right while partner p_T increases going down. The black line represents the background level, the red lines around it is the error on the black line.	238
A.15 Run 10 Au+Au $\pi^0 - h$ correlation functions for the centrality labeled in the figure. Each plot is a different p_T bin combination. Trigger p_T increases to the right while partner p_T increases going down. The black line represents the background level, the red lines around it is the error on the black line.	239
A.16 Run 11 Au+Au $\pi^0 - h$ correlation functions for the centrality labeled in the figure. Each plot is a different p_T bin combination. Trigger p_T increases to the right while partner p_T increases going down. The black line represents the background level, the red lines around it is the error on the black line.	240
A.17 Run 10 Au+Au $\gamma_{dec} - h$ correlation functions for 0-20% events. Each plot is a different p_T bin combination. Trigger p_T increases to the right while partner p_T increases going down. The black line represents the background level, the red lines around it is the error on the black line.	241
A.18 Run 11 Au+Au $\gamma_{dec} - h$ correlation functions for the centrality labeled in the figure. Each plot is a different p_T bin combination. Trigger p_T increases to the right while partner p_T increases going down. The black line represents the background level, the red lines around it is the error on the black line.	242
A.19 Run 10 Au+Au $\gamma_{dec} - h$ correlation functions for the centrality labeled in the figure. Each plot is a different p_T bin combination. Trigger p_T increases to the right while partner p_T increases going down. The black line represents the background level, the red lines around it is the error on the black line.	243
A.20 Run 11 Au+Au $\gamma_{dec} - h$ correlation functions for the centrality labeled in the figure. Each plot is a different p_T bin combination. Trigger p_T increases to the right while partner p_T increases going down. The black line represents the background level, the red lines around it is the error on the black line.	244
A.21 Run 10 Au+Au $\gamma_{dec} - h$ correlation functions for 0-20% events. Each plot is a different p_T bin combination. Trigger p_T increases to the right while partner p_T increases going down. The black line represents the background level, the red lines around it is the error on the black line.	245

A.22 Run 11 Au+Au $\gamma_{dec} - h$ correlation functions for the centrality labeled in the figure. Each plot is a different p_T bin combination. Trigger p_T increases to the right while partner p_T increases going down. The black line represents the background level, the red lines around it is the error on the black line.	246
A.23 Run 10 Au+Au $\gamma_{dec} - h$ correlation functions for the centrality labeled in the figure. Each plot is a different p_T bin combination. Trigger p_T increases to the right while partner p_T increases going down. The black line represents the background level, the red lines around it is the error on the black line.	247
A.24 Run 11 Au+Au $\gamma_{dec} - h$ correlation functions for the centrality labeled in the figure. Each plot is a different p_T bin combination. Trigger p_T increases to the right while partner p_T increases going down. The black line represents the background level, the red lines around it is the error on the black line.	248
B.1 Systematic error contributions of the direct photon $\pi/2$ away-side yield broken down by source for Run 10 (red) and Run 11 (black) 20-40% events. Each source is a different bin from left to right, v_2 , normalization (MSMP), decay photons, R_γ , and total systematic error. Each plot is a different p_T bin combination. Trigger p_T increases to the right while partner p_T increases going down.	257
B.2 Systematic error contributions of the direct photon $\pi/5$ away-side yield broken down by source for Run 10 (red) and Run 11 (black) 20-40% events. Each source is a different bin from left to right, v_2 , normalization (MSMP), decay photons, R_γ , and total systematic error. Each plot is a different p_T bin combination. Trigger p_T increases to the right while partner p_T increases going down.	258
B.3 Systematic error contributions of the direct photon $\pi/2$ away-side yield broken down by source for Run 10 (red) and Run 11 (black) 40-60% events. Each source is a different bin from left to right, v_2 , normalization (MSMP), decay photons, R_γ , and total systematic error. Each plot is a different p_T bin combination. Trigger p_T increases to the right while partner p_T increases going down.	259
B.4 Systematic error contributions of the direct photon $\pi/5$ away-side yield broken down by source for Run 10 (red) and Run 11 (black) 40-60% events. Each source is a different bin from left to right, v_2 , normalization (MSMP), decay photons, R_γ , and total systematic error. Each plot is a different p_T bin combination. Trigger p_T increases to the right while partner p_T increases going down.	260
B.5 Systematic error contributions of the direct photon $\pi/2$ away-side yield broken down by source for Run 10 (red) and Run 11 (black) 60-92% events. Each source is a different bin from left to right, v_2 , normalization (MSMP), decay photons, R_γ , and total systematic error. Each plot is a different p_T bin combination. Trigger p_T increases to the right while partner p_T increases going down.	261
B.6 Systematic error contributions of the direct photon $\pi/5$ away-side yield broken down by source for Run 10 (red) and Run 11 (black) 60-92% events. Each source is a different bin from left to right, v_2 , normalization (MSMP), decay photons, R_γ , and total systematic error. Each plot is a different p_T bin combination. Trigger p_T increases to the right while partner p_T increases going down.	262
C.1 Page 1 of 2 of the permissions license is for Figures 1.1, 1.3, and 2.1.	264

C.2	Page 2 of 2 of the permissions license is for Figures 1.1, 1.3, and 2.1.	265
C.3	Page 1 of 1 of the permissions license is for Figures 1.8 and 1.9.	266
C.4	Page 1 of 2 of the permissions license is for Figure 1.11.	267
C.5	Page 2 of 2 of the permissions license is for Figure 1.11.	268
C.6	Page 1 of 1 of the permissions license is for Figure 1.13.	269
C.7	Page 1 of 1 of the permissions license is for Figures 1.14a, 1.15a, 1.17 and 7.14.	270
C.8	Page 1 of 1 of the permissions license is for Figures 1.14b, 1.15b, and 1.16.	271
C.9	Page 1 of 1 of the permissions license is for Figure 2.2.	272
C.10	Page 1 of 2 of the permissions license is for Figure 2.3.	273
C.11	Page 2 of 2 of the permissions license is for Figure 2.3.	274
C.12	Page 1 of 2 of the permissions license is for Figure 2.5.	275
C.13	Page 2 of 2 of the permissions license is for Figure 2.5.	276
C.14	Page 1 of 2 of the permissions license is for Figure 2.6.	277
C.15	Page 2 of 2 of the permissions license is for Figure 2.6.	278
C.16	Page 1 of 1 of the permissions license is for Figure 3.1.	279
C.17	Page 1 of 2 of the permissions license is for Figure 9.2.	280
C.18	Page 2 of 2 of the permissions license is for Figure 9.2.	281

1 INTRODUCTION

1.1 The Standard Model

The standard model of particle physics is a theory that encompasses elementary particles and the forces that act on them. Particles are divided into three classes: gauge bosons, quarks, and leptons. There are four fundamental forces: gravity, strong, weak, and electromagnetic. The latter three are included in the standard model [42].

1.1.1 Gauge Bosons

Gauge bosons are the force carriers in the standard model. The four forces act on different elementary particles on different length scales. The strong and weak force act at extremely short distances (less than 1 fm) while the electromagnetic and gravity are infinite in range. The strong force forms hadrons by holding quarks together through the exchange of gluons and is described by quantum chromodynamics (QCD). The weak force is responsible for radioactive decay and fusion, is mediated by W and Z bosons, and can be described using quantum flavor dynamics (QFD). Photons carry the electromagnetic force between charged particles. The electromagnetic force is described by quantum electrodynamics (QED). The electro-weak theory merges QFD with QED and predicts that the strength of their respective forces become similar above an energy of approximately 250 GeV. Gravity is theorized to be mediated by the graviton, a massless boson yet to be observed. A summary of the fundamental forces and gauge bosons is shown in Table 1.1.

Table 1.1: The fundamental forces with their theories and mediators. The only mediators with mass are the mediators for the weak force. The ranges of the strong and weak forces are very small while the electromagnetic and gravitational forces have infinite range [1].

Interaction	Theory	Mediator	Mass (GeV/c ²)	Range (m)
Strong	Quantum Chromodynamics	gluon	0	10^{-15}
Weak	Quantum Flavordynamics	W^\pm, Z^0	80.4, 91.2	10^{-18}
Electromagnetic	Quantum Elecrodynamics	photon	0	∞
Gravity	General Relativity	graviton	0	∞

Another notable boson, the Higgs boson, was predicted by the standard model after the prediction of the Higgs mechanism and discovered in July 2012 by the CMS and ATLAS collaborations at the Large Hadron Collider (LHC) [43, 44]. It has no charge, spin or color and is very unstable. Particles interact with the Higgs field which causes them to acquire mass.

1.1.2 Quarks

There are six types of quarks: up, down, charm, strange, top, and bottom. The theory of QCD requires three color charges, resulting in 18 types of quarks. Mostly, quarks combine in two ways: three quark systems, called baryons (e.g. proton, neutron, Λ) or quark antiquark systems, called mesons (e.g. π^+ , π^0 , K^-). Baryons and mesons are collectively named hadrons because they are composed of quarks. The charge of an individual quark is less than the charge of an electron, e^- , and is always divisible by three because they combine to form integer charges. A quark summary is shown in Table 1.2.

Table 1.2: The quarks with their masses and charges [1].

Quark	Charge (e)	Mass (MeV/c 2)
up	+2/3	1.7 - 3.1
down	-1/3	4.1 - 5.7
charm	+2/3	1290
strange	-1/3	100
top	+2/3	172900
bottom	-1/3	4190

1.1.3 Leptons

The last main class of particles is leptons. There are six leptons: electron, muon, tau, electron neutrino, muon neutrino, and tau neutrino. The electron, muon, and tau have charge $-e$ while all neutrinos are neutral. Taus are the most massive leptons, followed by muons, and then electrons, while neutrinos are the least massive. All neutrinos have a small nonzero mass; because of this, the mass hierarchy is difficult to determine. Table 1.3 shows a summary of leptons.

Table 1.3: The leptons with their masses, charges and lifetimes. Tau is the most massive and fastest decaying lepton. The neutrino masses are approximately zero [1].

Lepton	Charge (e)	Mass (MeV/c 2)	Lifetime (s)
electron	-1	0.511	∞
electron neutrino	0	≈ 0	∞
muon	-1	105.7	2.2×10^{-6}
muon neutrino	0	≈ 0	∞
tau	-1	1777	2.91×10^{-13}
tau neutrino	0	≈ 0	∞

Each quark and lepton have a corresponding antiparticle with the opposite quantum numbers, such as charge and spin. Antiquarks can combine with quarks and other antiquarks to form a myriad of mesons and baryons. The fundamental forces act in the same manner for both particles and antiparticles.

1.1.4 Quantum Chromodynamics

Quantum chromodynamics (QCD) is the theory of the strong force that works through the exchange of color-charged-mediators called gluons. The color charges are commonly called red, green, or blue. There are also anti charges, anti-red, anti-green, and anti-blue. Quarks and gluons do not physically have color; the use of color is to signify three different charges. Mesons contain a colored quark and an anti-colored antiquark, the color must be the same so that the meson is color neutral. In baryons, the three colors may combine to become neutral. For example, the Δ baryon, a uuu system, contains one quark of each color in order for it to be colorless. This must be true in order for quarks to be fermions, because they are required to obey the Pauli exclusion principle.

The strong force causes the quarks to be confined in the hadrons, a phenomena called quark confinement. If the distance separating the quarks gets larger, the force gets stronger. If enough energy and density is given to the quarks they are squeezed together and the strong force between them goes to zero, this is called asymptotic freedom. When this occurs, the quarks become deconfined from the nuclei and form a state of matter called a quark-gluon plasma (QGP). The work presented in this dissertation studies QCD through the interaction of the quarks and gluons in hadrons with the QGP. The basics of some theoretical models used to model the QGP are discussed in Section 1.7.

Figure 1.1 shows the QCD phase diagram, temperature versus net baryon density (i.e. density of protons, neutrons). Normal nuclear matter lies at temperature approximately zero and baryon chemical potential approximately 900 MeV. Notice that the current RHIC experiments have a low baryon density and high temperature. The first order phase transition line marks the transition from hadron gas to the QGP. This line is hypothesized to end at a critical point at a temperature of about 170 MeV.

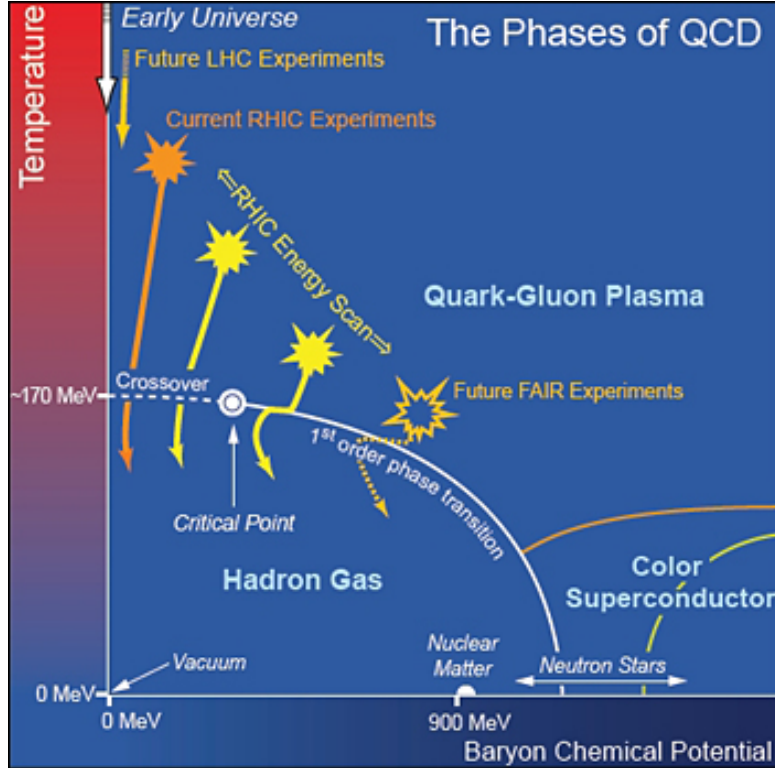


Figure 1.1: QCD phase diagram showing the phase transition from hadron gas to quark gluon plasma [7]. Courtesy Brookhaven National Laboratory.

1.2 The Big Bang

The universe existed in a quark-gluon plasma phase for a few millionths of a second immediately after the big bang [45]. It was in this phase due to an extremely high energy density that created a high temperature. At one second, it had expanded and cooled enough for a phase transition to occur and hadrons to form. This is shown on the extreme left of Figure 1.2. This figure shows the history of the universe. Time begins at the Big Bang on the left and flows to the right. After inflation, nucleons form and nuclei follow. About 3×10^5 years after the Big Bang, the nucleons capture the free streaming electrons to form atoms. This sets the energy scale of the cosmic microwave background. This is as far back in time that telescopes can see. About a billion years after the Big Bang, galaxies and other large scale structure form. Today, we are about 13.8 billion years after the Big Bang. The LHC and the relativistic heavy ion collider (RHIC) are able

to probe the state of matter similar to the universe immediately after the Big Bang. Understanding how QGP interacts could help determine how the universe behaved right after the Big Bang and why it behaves the way it does today. However, this is not the main motivation for studying the QGP.

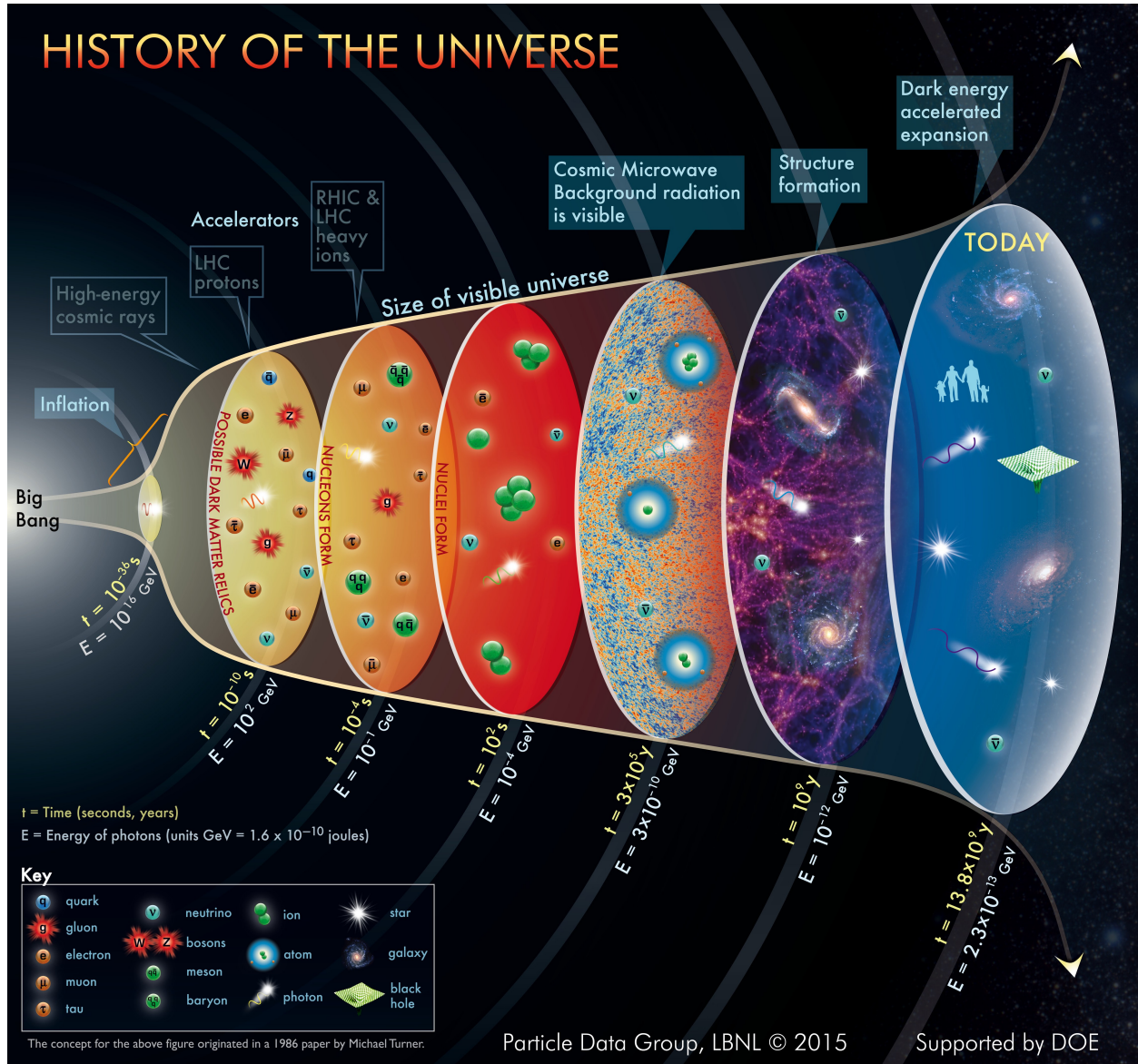


Figure 1.2: The history of the universe. Time starts with the big bang on the left, the universe expands to where we are today 13.8 billion years later [8].

1.3 Heavy-Ion Collisions - Little Bangs

It is impossible to squeeze baryons to increase their density, without also increasing their temperature, so that they undergo the phase transition to form a QGP on Earth. The only way to form a QGP on Earth is to increase the baryon's temperature by colliding it with another baryon at nearly the speed of light. Only two facilities can do this, the LHC in Geneva, Switzerland [45] and RHIC in Upton, New York [9].

1.3.1 Event Evolution

RHIC forms QGP by colliding heavy ions at 99.999% the speed of light (c). At that velocity, the energy per nucleon pair of the reaction center-of-mass frame ($\sqrt{s_{NN}}$) is 200 GeV. A typical heavy ion, a gold nucleus has a diameter of about 15 fm, but when accelerated to 99.999% c , it is Lorentz contracted along the direction of travel to a 0.13-fm-thick disk. This contraction causes the ions to only overlap during the collision for 4.38×10^{-25} s (0.13 fm/c). Not all collisions have complete overlap of the nuclei. A large overlap produces a large number of participants, the particles that form the QGP, while small overlap has a large number of spectators, the particles that travel unimpeded down the beamline. Outgoing particles with high transverse-to-the-beamline momentum (>5 GeV/c) are called jets. They get their momentum from hard scattering processes of the parent nuclei's quarks or gluons. After the collision, the QGP expands and cools which causes it to transition back to hadrons. This phase transition is called hadronization. At this point in the event, the quark flavors inside the hadrons are fluctuating due to inelastic scattering of the hadrons. After further expansion and cooling, chemical freeze out occurs, ceasing inelastic scattering; this causes the flavors of the quarks to stop changing. Thermal freeze out occurs after more expansion when the outgoing hadrons and leptons are no longer interacting. They can decay if it is energetically favorable. Once all of this occurs, the outgoing particles' momenta and type are identified by detectors. This entire process is called an event. Figure 1.3 shows a simulation of a single event. The original description of this evolution was described by Bjorken in Refrence [46].

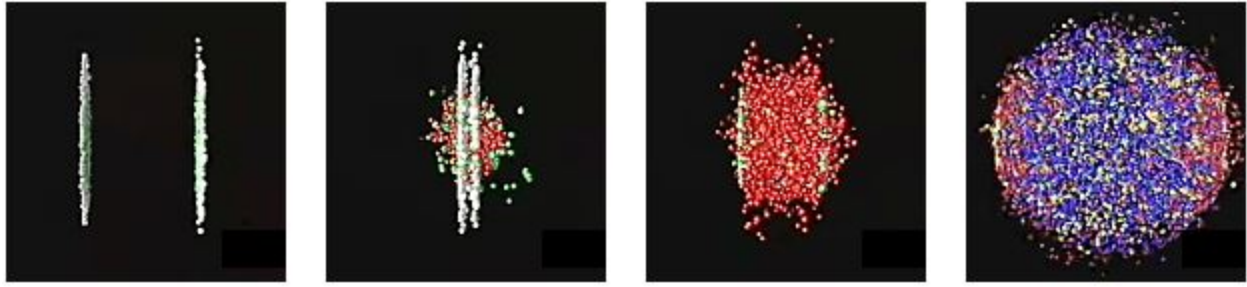


Figure 1.3: A simulation of a heavy-ion collision with time flowing from left to right. The leftmost panel shows the Lorentz contracted gold nuclei. In the middle left panel the ions collide. The red spheres in the next panel are the deconfined quarks and gluons. The rightmost panel shows the expanding quark gluon plasma [9]. Courtesy Brookhaven National Laboratory. See Figure C.1 and C.2 for more details.

Each event is analogous to the universe expanding after the Big Bang. This 'little bang' is shown in Figure 1.4. It starts with the nucleons colliding on the left, then the QGP forms, expands and cools undergoing hadronization and kinetic freeze-out to form the particles that are read out by the detectors. This kinetic freeze out is analogous to the freeze out of the cosmic microwave background, which is as far back in time that we can see. We can see some photons that are created before and during the hadronization phase, these are the yellow, red, and green waves. The time axis is shown at the bottom of the figure, it should be noted that $1 \text{ fm}/c = 3 \times 10^{-24} \text{ seconds}$ so this entire process occurs on very short timescales.

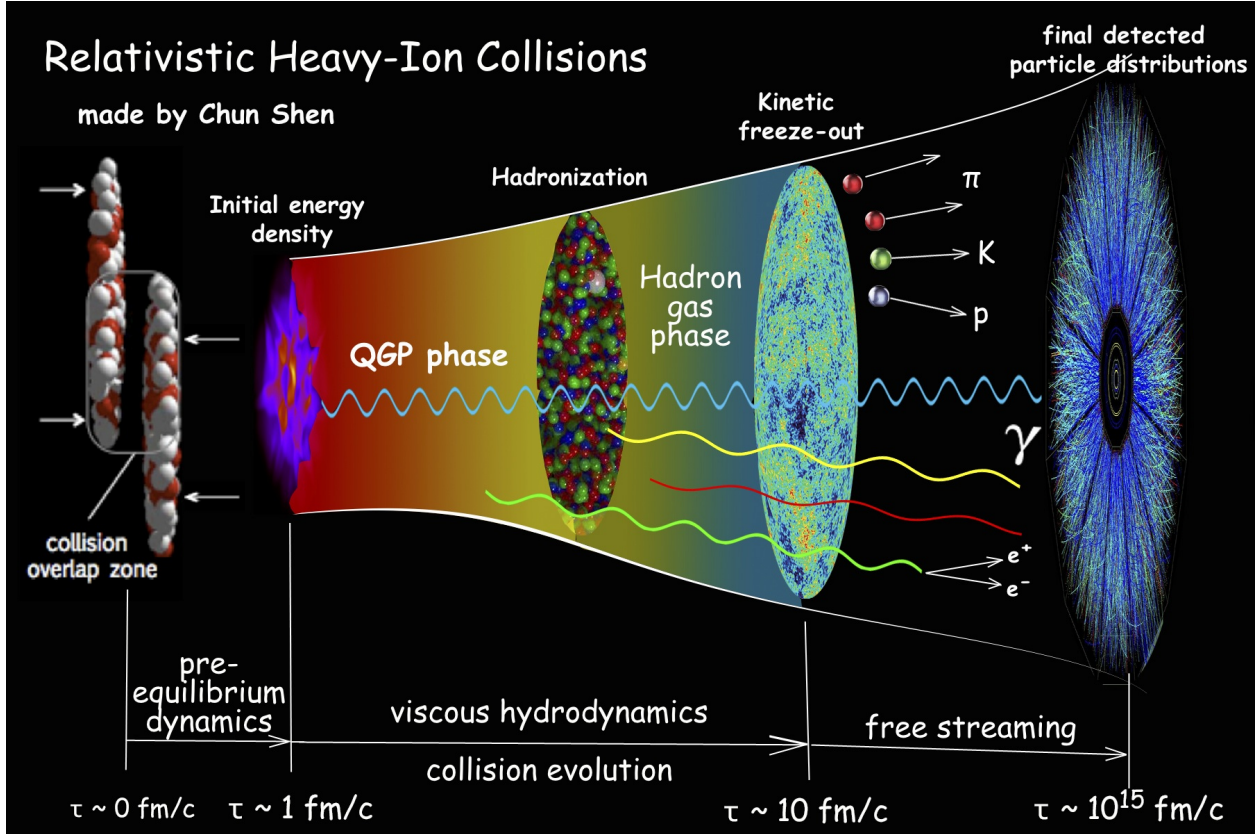


Figure 1.4: A relativistic heavy-ion collision. The collision occurs on the left and forms a QGP. The QGP expands and cools to form hadrons. The particles that are read out in the detectors are formed during kinetic freeze-out [10].

1.3.2 Event Characterization

Each event is characterized by its centrality and reaction plane angle. This subsection introduces centrality, the experimental measure of the impact parameter and the reaction plane, the plane in which the impact parameter lies.

1.3.2.1 Centrality

Since each event is unique, there is a set of variables used to classify them. The most descriptive of these is the distance separating the center of the colliding nuclei, or impact parameter, b . For small b , the overlap between the nuclei is large and the number of participants is large. For

large b , the overlap is small and there are a small number of participants. Unfortunately, impact parameters cannot be measured directly. Instead, a variable called centrality is used. Centrality is measured in percentage. This percentage is the percentage of collisions with larger multiplicity. Multiplicity is the number of particles created in the collision in a carefully selected region of the outgoing particle phase space. Events with large multiplicity are named central, while small multiplicity events are called peripheral. This is shown in Figure 1.5. The blue and red circles are the colliding nuclei and the purple region is the overlap region. The beamline is out of the page. The left panel is a central event, it has a small impact parameter, and the right panel is a peripheral event, it has a large impact parameter.

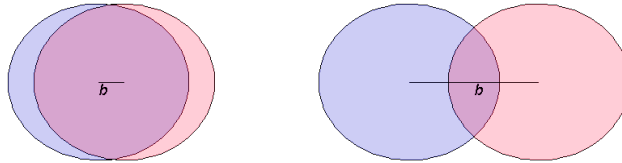


Figure 1.5: Centrality examples with the impact parameter labeled for central collisions (Left) and peripheral collisions (Right). The beamline is out of the page.

1.3.2.2 Coordinate Systems

In order to discuss the reaction plane angle a few coordinate systems commonly used in heavy-ion collisions must be introduced. Coordinate systems are placed with the origin at the nominal collision point in order to map out where the outgoing particles travel. In some instances, a Cartesian coordinate system with the $+z$ axis along one of the beam lines and the $+y$ axis perpendicularly upward is used. A spherical system can also be used with θ defined as the angle above the beam line with $\theta = 0$ along the Cartesian $+z$ axis and ϕ defined as the angle around the beam line, with $\phi = 0$ along the $+x$ axis.

There are two useful unit-less variables, rapidity (y) and pseudorapidity (η), that describe forward and backward angles with respect to the nominal collision point and beam line. Rapidity

is commonly used because it is boost invariant while θ is not. Rapidity is defined as

$$y = \frac{1}{2} \ln \frac{1 + \beta \cos \theta}{1 - \beta \cos \theta} = \frac{1}{2} \ln \frac{1 + \beta_z}{1 - \beta_z}, \quad (1.1)$$

where $\beta = v/c$, v is the particle's velocity and c is the speed of light. It conveys a particle's velocity along the beam line, its velocity in the $+z$ direction, $\beta_z = v_z/c$. The problem with rapidity is that it requires knowing the information equivalent to the particle's velocity (e.g E , p_z). A better quantity, pseudorapidity, only relies on the particle's angle. It is defined as

$$\eta = \frac{1}{2} \ln \frac{1 + \cos \theta}{1 - \cos \theta}. \quad (1.2)$$

Notice that as a particle's velocity approaches the speed of light, β goes to one and rapidity and pseudorapidity are equal except at 0° and 180° .

1.3.2.3 Reaction Planes and Flow Harmonics

The plane defined by the impact parameter and the beam line is called the reaction plane. The angle of this plane, Ψ_{RP} , is the azimuthal angle with respect to the beamline is measured by determining the azimuthal asymmetry of the outgoing particles. The asymmetry is described by

$$\frac{d(N)}{d(\phi - \Psi_{RP})} = \frac{\langle wN \rangle}{2\pi} \left(1 + 2 \sum_{n=1}^{\infty} v_n \cos(n(\phi - \Psi_{RP})) \right), \quad (1.3)$$

a Fourier expansion where N is the number of detected particles, w a weight associated with those particles, typically the particle's energy, n is the harmonic of the reaction plane angle, that is further explained below, ϕ is the azimuthal angle of the outgoing particle, and the Fourier coefficient,

$$v_n = \langle \cos(n(\phi - \Psi_{RP})) \rangle, \quad (1.4)$$

is called the flow coefficient [47]. The angle brackets indicate an average over particles in all events. The flow coefficient is the magnitude of the azimuthal anisotropy. The coefficient v_1 ($n = 1$) is often called directed flow, v_2 ($n = 2$) is called elliptic flow, and v_3 ($n = 3$) is called triangular flow. Figure 1.6 shows the event plane (green grid) with the colliding nuclei (blue spheres) and almond shaped QGP (orange ellipsoid). The large blue arrows on the nuclei show their direction

along the beamline. The small blue arrows on the orange QGP are momentum vectors. One can see that there is a large momentum in plane (longer arrows) and it gets smaller farther from plane (short arrows). This event is purely an elliptic flow event. The higher order flow harmonics are present in all collisions because the colliding nuclei are not perfect liquid drops. They can be considered a collection of discrete spherical nucleons. This makes the participants less of an almond shape.

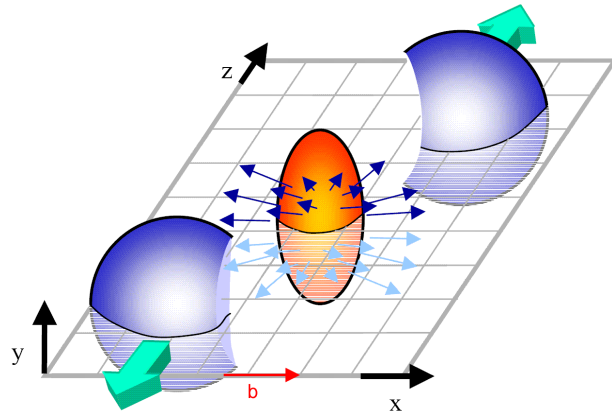


Figure 1.6: A typical collision with purely elliptic flow. The participants form the almond shape (orange ellipsoid) while the spectators continue to travel along the beamline (blue spheres). The green grid is the reaction plane with the red arrow showing the impact parameter. The blue arrows show the direction of the pressure that is largest in the plane and smallest outside the plane[11].

The reaction plane angle cannot be known with full certainty because there are fluctuations in the nucleons that participate in the collision. If each nucleus is considered a collection of billiard balls, when they collide, one cannot know with full certainty the plane in which the collision took place. This uncertainty causes a new variable to be used instead of the reaction plane; it is called the event plane angle (Ψ_{EP}) and is used to signify the reaction plane without full certainty. Each

harmonic of the particle's azimuthal distribution has its own event plane, and is described by

$$\Psi_{nEP} = \frac{1}{n} \arctan \frac{Y_n}{X_n} = \frac{1}{n} \arctan \frac{\sum_{i=1}^N w_i \sin(n\phi_i)}{\sum_{i=1}^N w_i \cos(n\phi_i)}, \quad (1.5)$$

where the sum over i is a sum over particles in the collision, w_i is a weight associated with the particle (typically the particle's energy is used as this weight), and ϕ_i is the azimuthal angle of that particle. The flow vectors X_n and Y_n are along the x and y axis, respectively. From Equation 1.5, the limits of the event and reaction plane angle are

$$-\frac{\pi}{n} \leq \Psi_n \leq \frac{\pi}{n}. \quad (1.6)$$

For the sake of clarity, in the rest of this dissertation, the subscript n is dropped as we are only focused on the $n = 2$ term. Also, we make the distinction between the event plane and reaction plane, that is, Ψ_{EP} is the second order event plane that is measured in the detector Ψ_{2EP} and Ψ_{RP} is the second order true reaction plane Ψ_{2RP} .

To correct the measured event plane to the true reaction plane, the measured v_2 must be divided by the event plane resolution correction factor. Explicitly, this is

$$v_2 = \frac{v_2^{raw}}{\langle \cos(2\delta\Psi) \rangle}, \quad (1.7)$$

where v_2^{raw} is the raw measured elliptic flow coefficient, $\delta\Psi = \Psi_{RP} - \Psi_{EP}$, where Ψ_{EP} is the measured second order event plane, Ψ_{RP} is the second order reaction plane. The denominator is called the resolution factor. Using the definition in Equation 1.4, this equation can be written another way,

$$\langle \cos(2\Psi_{EP}) \rangle = \langle \cos(2\Psi_{RP}) \rangle \langle \cos(2\delta\Psi) \rangle. \quad (1.8)$$

The probability distribution of $\delta\Psi$, according to References [12, 48], is given by

$$\frac{dN}{d(2\delta\Psi)} = \frac{1}{\pi} e^{-\frac{\chi^2}{2}} \left[1 + z \sqrt{\pi} e^z (1 + \text{erf}(z)) \right], \quad (1.9)$$

where $z = \frac{1}{\sqrt{2}}\chi \cos(2\delta\Psi)$, χ is a constant parameter, and erf is the standard error function. This function for a few values of χ is shown in Figure 1.7. The parameter χ does not have any physical

significance, it is just an amplitude factor for the probability distribution. It can be shown that the distributions (Equation 1.9) in Figure 1.7 are normalized to one in the range $-\frac{\pi}{2} \leq \delta\Psi \leq \frac{\pi}{2}$.

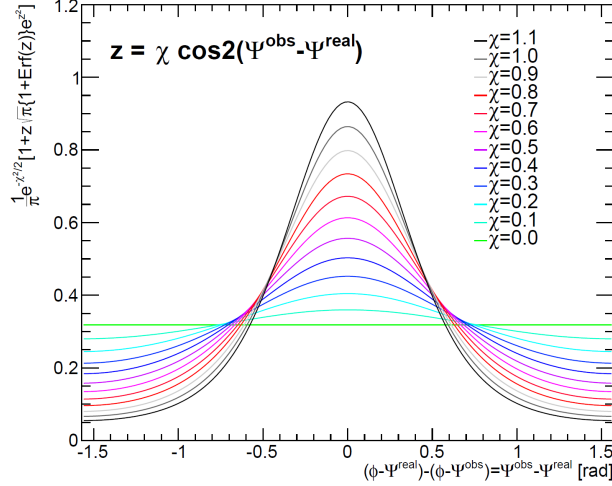


Figure 1.7: The probability distribution of the reaction plane, Equation 1.9, for a few values of χ [12].

The resolution of the event plane depends on χ according to

$$\langle \cos(2\delta\Psi) \rangle = \frac{\sqrt{\pi}}{2\sqrt{2}} \chi e^{-\frac{\chi^2}{4}} \left[I_0\left(\frac{\chi^2}{4}\right) + I_1\left(\frac{\chi^2}{4}\right) \right], \quad (1.10)$$

where I_0 (I_1) are modified Bessel functions of the first kind [12, 48]. We will use these equations in Chapter 4 to verify some equations in a toy Monte Carlo simulation. The resolution correction used to correct the data is discussed further in Section 5.2.1.

1.4 QGP Signatures

Three landmark signatures that verified the QGP was formed in heavy-ion collisions at RHIC are harmonic flow, single particle suppression, R_{AA} , and jet suppression, I_{AA} . All three of these factors are large areas of study in heavy-ion physics and a short explanation is given here. Typically, quantities measured in heavy-ion collisions are compared to the same quantities in $p+p$ collisions because a QGP likely does not form in $p+p$ collisions. So to see how the QGP modifies

the quantity, the ratio of the measured quantity in Au+Au collision is divided by the same quantity in $p + p$ collisions. Two such quantities, R_{AA} and I_{AA} , are described later in this section.

1.4.1 Harmonic Flow

The second order flow coefficient, v_2 has been measured at RHIC. These coefficients are often plotted versus transverse momentum (p_T) or transverse kinetic energy (KE_T) of the measured particle. Figure 1.8 shows v_2 as a function of p_T in (a) and KE_T in (b) for different particles measured by PHENIX and STAR. It is shown that at high p_T and KE_T the particles fall into two groups, the baryons and the mesons. If the v_2 values are scaled by the number of valence quarks (n_q), 3 for baryons and 2 for mesons, v_2/n_q shows no separation when plotted as a function of p_T and KE_T shown Figure 1.9. This is evidence that it is not the hadrons that cause the anisotropy, but the quarks.

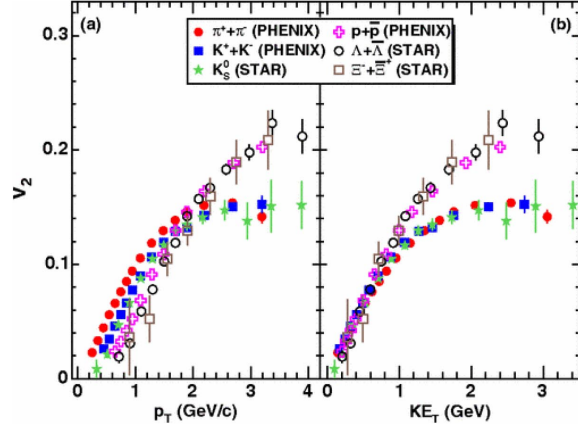


Figure 1.8: Elliptic flow coefficient v_2 as a function of p_T in (a) and KE_T in (b) for various particles detected by PHENIX and STAR at RHIC. The meson and baryon v_2 are not consistent with one another at high p_T [13]. This figure has been used with permission. See Figure C.3 and C.4 for more details.

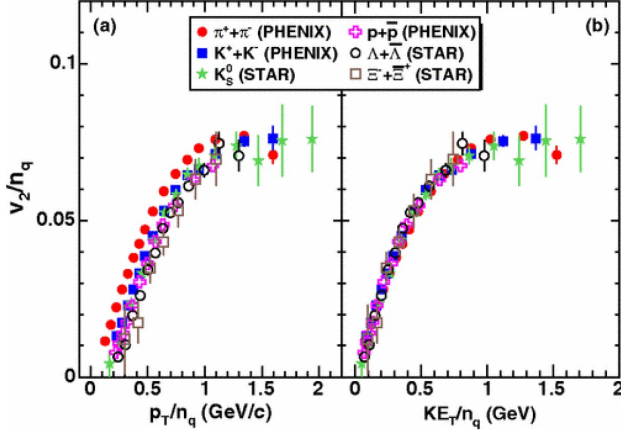


Figure 1.9: Elliptic flow coefficient v_2 as a function of p_T in (a) and KE_T in (b) for various collision systems scaled by the number of valence quarks. The mesons and baryon collision systems are no longer inconsistent at high p_T , indicating that the quarks are causing the anisotropy, not the hadrons [13]. This figure has been used with permission. See Figures C.3 and C.4 for more details.

1.4.2 Single Particle Suppression

Naively, one expects the number of particles produced in heavy-ion collisions to be a multiplicative factor times the number of particles produced in $p+p$ collisions. This is because heavy-ion collisions could be thought of as just a collection of $p+p$ collisions occurring at one time. This expectation turns out to be false because the QGP created in heavy-ion collisions suppresses the particle production. This is shown in Figure 1.10, it shows the nuclear modification factor, R_{AA} , versus p_T for different particles in central Au+Au collisions measured by PHENIX. For Au+Au collisions,

$$R_{AA} = \frac{1}{N_{coll}} \frac{d^2N^{AA}/dydp_T}{\langle T_{AA} \rangle d^2\sigma_{pp}/dydp_T}, \quad (1.11)$$

where N_{coll} is the effective number of nucleon-nucleon collisions for an equivalent $p+p$ collision, $d^2N^{AA}/dydp_T$ is the invariant yield of the Au+Au collision, $d^2\sigma_{pp}/dydp_T$ is the $p+p$ cross section, and $\langle T_{AA} \rangle$ is a scale factor, called the nuclear thickness function, that is determined using a Glauber Monte Carlo calculation. As shown in Figure 1.10, direct photons are not suppressed because they

do not interact through the strong force because they are colorless while most of the mesons are highly suppressed.

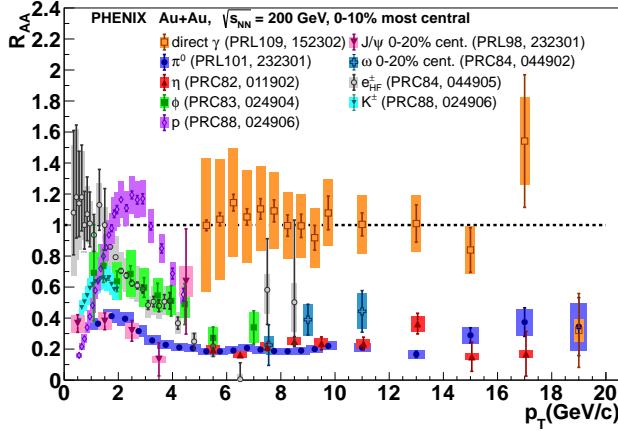


Figure 1.10: Compilation of PHENIX measured R_{AA} as a function of p_T in central Au+Au collisions for direct photons (red open squares), π^0 (blue solid circles), η (red solid circles), ϕ (green solid squares), protons (purple open diamonds), 0-20% central J/ψ (burgundy downward solid triangles), 0-20% central ω (black open crosses), heavy flavor e^\pm (black open circles), and K^\pm (blue downward triangles) [14].

1.4.3 Jet Suppression

A jet is a high momentum spray of collimated particles that are emitted from a collision. A typical momentum scale for a jet is particles with $p_T > 5$ GeV/c. Determining what particles composed a jet is a nontrivial task. There are two general methods which determine if a particle makes up a jet, a direct method and an indirect method. The direct method consists of a jet reconstruction algorithm that tags individual particles then determines whether or not they are in a jet according to the predefined algorithm. This method is highly effective in $p+p$ collisions but it has difficulties in heavy-ion collisions because there are a copious amount of underlying high p_T particles that increase the algorithm's probability of finding false jets.

An alternative technique for heavy-ion collisions is the indirect method. In this method, the two particle correlation is measured. Two-particle correlations consist of the correlation between two particles as a function of their azimuthal difference, as shown in Figure 1.11. Specifically, this figure shows a $h - h$ jet function, the azimuthal difference between hadrons pairs that has been background subtracted. Jet functions will be discussed in detail later in Section 1.5.1. The peak at $\Delta\phi = 0$ is called the near-side peak; it is caused by particles that have no azimuthal angle difference therefore they are particles from the same jet. The peak at $\Delta\phi = \pi$ is called the away-side peak; it is caused by particles that have maximum azimuthal angle difference. They are particles from opposing jets. These jets originate from the hard scattering processes that take place at the beginning of the collision. Figure 1.11 shows high p_T charged hadron-hadron ($h - h$) correlations measured by STAR at RHIC for three different collision systems. The Au+Au collisions have no away-side peak. This indicates that the jet that has to travel through the QGP loses all of its energy before it makes it through the medium. This lack of away-side jet is called jet suppression.

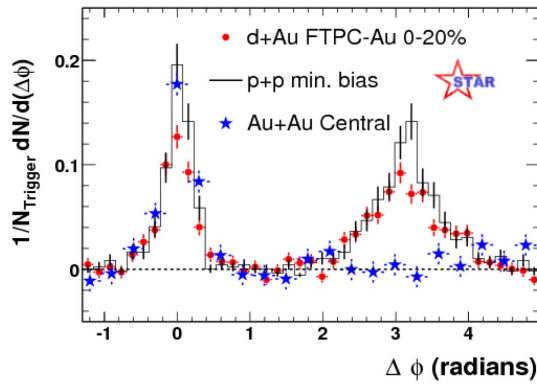


Figure 1.11: $h - h$ correlations made with partner hadrons with $p_T > 2\text{GeV}/c$ relative to a trigger hadron with $p_{T\text{trig}} > 4\text{ GeV}/c$ high p_T trigger for 3 collision systems, $d + Au$ (red points), $p+p$ (black points), and $Au+Au$ (blue stars), measured by the STAR experiment. One can see that only the away-side $Au+Au$ jets are suppressed [15]. This figure has been used with permission. See Figure C.5 for more details.

When making correlation measurements, one should be cautious of the QGP's surface bias. A surface bias occurs if only high p_T trigger particles (the first particle in the correlation) are sampled because doing so cuts out trigger particles that lose energy as they travel through the medium. This process is called surface bias because very high p_T particles originate from the surface of the QGP.

1.5 Photon-Hadron Correlations

Instead of measuring $h - h$ correlations, direct photon-hadron (γ_{dir} -h) correlations are often preferred. There are several reasons for this, one is because there is no way to get the unmodified hadron jet momentum; it must be approximated through a jet reconstruction algorithm. Another is because of surface bias discussed in the previous section. Also, because both jets may be modified by the QGP, it is hard to get their true energy. Direct photons are photons that are created through hard scattering processes such as annihilation ($q\bar{q} \rightarrow g\gamma$) and Compton scattering ($qg \rightarrow q\gamma$) as shown in Figure 1.12. Direct photons are colorless entities and therefore not affected by the QGP. Because of this, many of the problems with $h - h$ correlations are solved. Conservation of momentum implies that the energy of the photon is the same as the energy of the hadron jet. As the photons emitted are colorless and do not interact inside the QGP they suffer no surface bias.

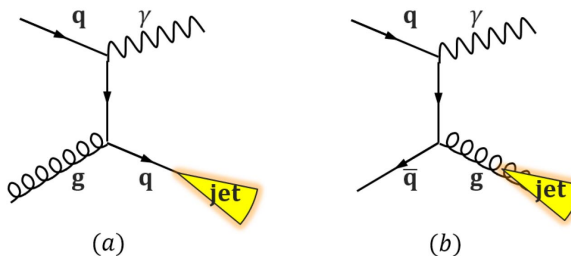


Figure 1.12: Leading order direct γ production mechanisms, Compton scattering ($qg \rightarrow q\gamma$) in (a) and annihilation ($q\bar{q} \rightarrow g\gamma$) in (b) [3].

However, there is a problem with using γ_{dir} -h correlations. Many different types of photons are created in each event and deciphering which ones are direct is difficult to do. Inclusive photons are all of the photons in the event but they can be further classified into two categories, decay and

non-decay. Most decay photons are created by the decay of π^0 mesons, others come from decays of underlying event hadrons. Direct photons are generally isolated because they are created from the initial hard scattering of the nuclei and do not form jets. Determining which photons are isolated is straight-forward. A cone is fit around the photon, the energy of the particles inside the cone is measured and if the energy is less than a certain threshold, the photon is isolated. This process is called the isolation cut method and is described in more detail in Section 3.4.2.

1.5.1 Introduction to Correlations

To obtain the jet function in Figure 1.11 one must first measure the correlation function. The correlation function is measured by filling a histogram with $\Delta\phi_{AB} = \phi_A - \phi_B$, where ϕ_A is the azimuthal angle of particle A and ϕ_B is the azimuthal angle of particle B . This dissertation uses isolated photons and π^0 's for particle A and hadrons for particle B . Once the correlation function is found, the background must be subtracted from it. The magnitude of the background can be found using different methods and will be discussed in a later section. The background shape comes from the two particle's flow contributions. Explicitly this is,

$$C(\Delta\phi_{AB}) = J(\Delta\phi_{AB}) + b_0 \frac{dN_{comb}^{AB}}{d\Delta\phi_{AB}}, \quad (1.12)$$

where $\Delta\phi_{AB} = \phi_A - \phi_B$, $C(\Delta\phi_{AB})$ is the measured correlation function, $J(\Delta\phi_{AB})$ is the jet function, b_0 is the background level, and $\frac{dN_{comb}^{AB}}{d\Delta\phi_{AB}}$ is defined by Equation 1.13 and is described in the next paragraph. A generic correlation function with b_0 labeled is shown in Figure 1.13. The gold region is the background while the red region is the jet distribution we are interested in measuring.

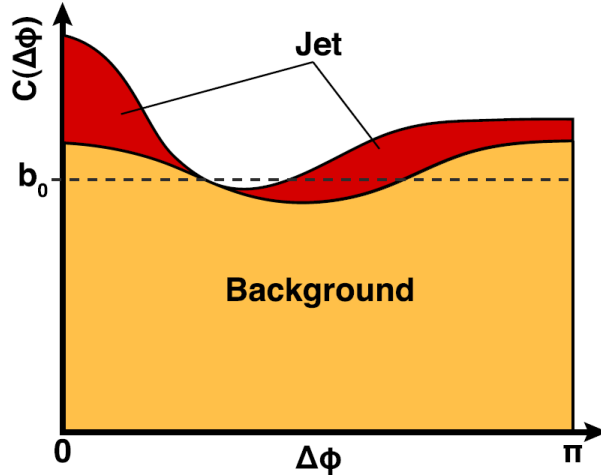


Figure 1.13: A typical correlation function. The gold region is the background, the red region is the jet function. The background level is b_0 , while the shape is determined by Equation 1.13 [16]. This figure has been used with permission. See Figure C.6 for more details.

The underlying event particles exhibit anisotropic flow as described by Equation 1.3. The magnitude of the elliptic flow coefficient may be different for the different types of particle pairs in the correlation function. To account for this, the background is described by multiplying Equation 1.3 for particle A with Equation 1.3 for particle B , that is,

$$\frac{dN_{comb}^{AB}}{d\Delta\phi_{AB}} \propto 1 + 2v_2^A v_2^B \cos(2\Delta\phi_{AB}) + 3v_3^A v_3^B \cos(3\Delta\phi_{AB}) + \dots, \quad (1.13)$$

where v_2^A and v_2^B are the event averaged v_2 of particle A and B . This equation can be truncated after the $n = 2$ term because the higher order terms can be considered perturbations to the elliptic shape. Equation 1.13 is often called the combinatoric background distribution.

There are two common methods to find the background level, absolute normalization (ABS) and zero yield at minimum (ZYAM). ABS is a calculation method where the background level is determined by dividing the average number of mixed AB pairs by the trigger. The essence of ZYAM is the fact that somewhere in the correlation function, typically close to $\Delta\phi = \pi/2$, the correlation function should be zero. This method relies on fitting the function by a suitable

function, finding the minimum of that function, then subtracting the y-value of that minimum from the data.

Equation 1.12 can be solved for the jet function. It is typical to divide through by the number of A particles to remove any efficiency of detecting particle A . There are also factors of detector efficiency for particle B and detector acceptance. This leads Equation 1.12 to be

$$\frac{1}{N_A} \frac{dN^{AB}}{d\Delta\phi_{AB}} = \frac{1}{N_A} \frac{dN_{real}^{AB}}{d\Delta\phi_{AB}} \frac{\epsilon_B}{Acc(\Delta\phi)} - b_0(1 + 2v_2^A v_2^B \cos(2\Delta\phi_{AB})), \quad (1.14)$$

where N_A is the number of A particles, $1/N_A dN^{AB}/d\Delta\phi_{AB}$ is the jet function, $dN_{real}^{AB}/d\Delta\phi_{AB}$ is the correlation function, ϵ_B is the efficiency of detecting B particles, $Acc(\Delta\phi)$ is the $\Delta\phi$ acceptance function, and the last term is the combinatoric background contribution. For this dissertation, A particles are isolated photons or π^0 's and B particles are hadrons.

1.6 Previous Photon-Hadron Correlation Measurements from PHENIX

This section is devoted to summarizing previously published PHENIX photon-hadron correlations results, mainly References [17] and [18]. Both of these publications laid the groundwork for the work in this dissertation therefore it is important for the reader to understand these results.

Figures 1.14a and 1.14b show jet functions measured in $p+p$ and Au+Au collisions. Figure 1.14a shows inclusive photon-hadron (green diamonds), decay photon-hadron (purple squares), and direct photon-hadron (black points) jet functions for $5 < p_T^\gamma < 7$ and $3 < p_T^h < 5$ GeV/c in $p+p$ (top) and 0-40% central Au+Au (bottom) collisions [17]. Notice that the away-side of the jet function is suppressed in Au+Au but not in $p + p$. Figure 1.14b shows direct photon-hadron jet functions in $p+p$ (blue squares) and 0-20% central Au+Au (black circles) collisions for $5 < p_T^\gamma < 9$ and different momentum fraction regions [18]. The momentum fraction $\xi = \ln(1/z_T)$ where $z_T = p_T^h/p_T^\gamma$ was used to focus on the low z_T region. It was expected that the jet fragmentation function would scale with z_T .

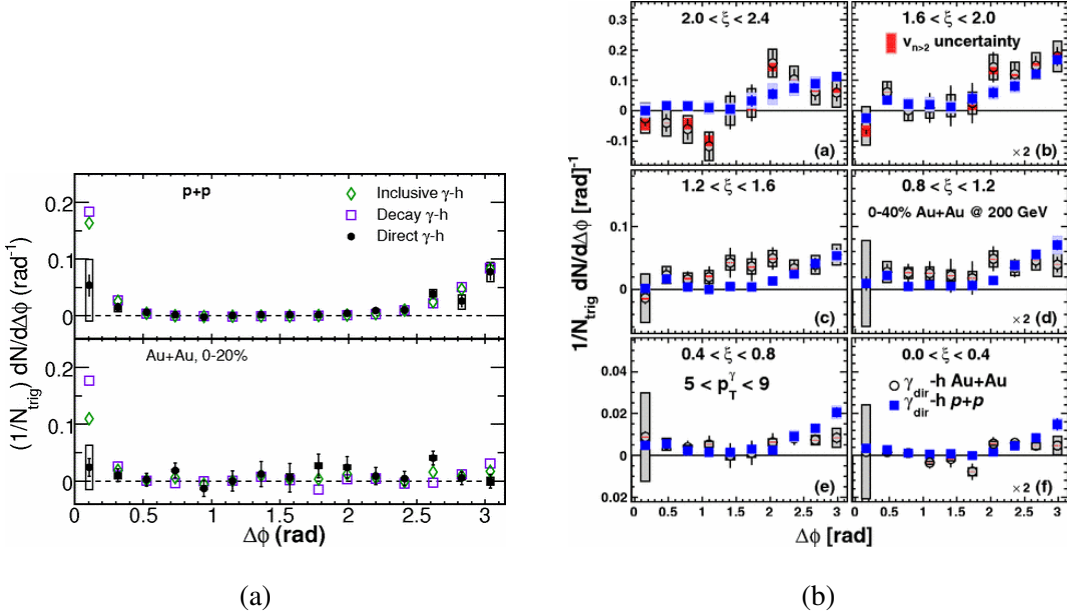


Figure 1.14: (a) Inclusive photon-hadron (green diamonds), decay photon-hadron (purple squares), and direct photon-hadron (black points) jet functions for $5 < p_T^\gamma < 7$ and $3 < p_T^h < 5$ GeV/c in $p+p$ (top) and Au+Au (bottom) collisions [17]. (b) Direct photon-hadron jet functions in $p+p$ (blue squares) and Au+Au (black circles) collisions for $5 < p_T^\gamma < 9$ and different ξ regions[18]. These figures have been used with permission. See Figures C.7 and C.8 for more details.

These jet functions can be integrated over their away-sides to find an away-side yield, which is often called the per-trigger yield as the jet functions are normalized per trigger particle. Figure 1.15a shows the $|\Delta\phi - \pi| < \pi/5$ away-side yield as a function of p_T^h for four different p_T^γ bins for Au+Au (red squares) and $p+p$ (blue points) collisions [17]. The top panel of Figure 1.15b shows the $|\Delta\phi - \pi| < \pi/5$ away-side yield as a function of z_T and ξ for $5 < p_T^\gamma < 9$ GeV/c and $0.5 < p_T^h < 7$ GeV/c for 0-40% central Au+Au (black points) and $p+p$ (blue points) collisions.

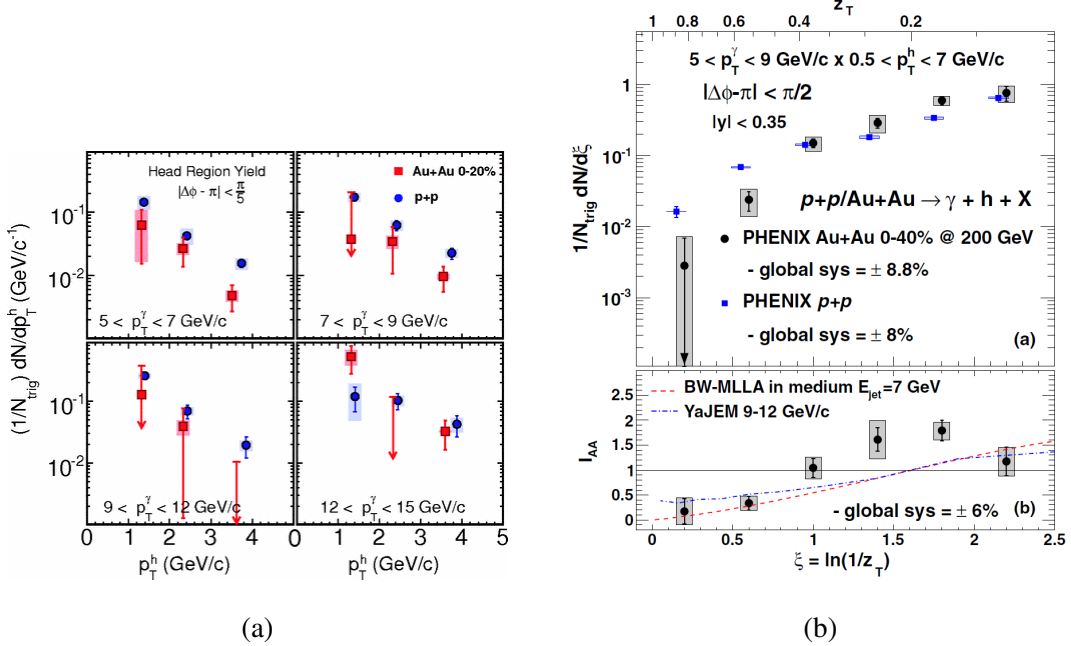


Figure 1.15: (a) $|\Delta\phi - \pi| < \pi/5$ away-side yield as a function of p_T^h for four different p_T^γ bins for Au+Au (red squares) and $p+p$ (blue points) collisions [17]. (b) (top) Per trigger yield for $5 < p_T^\gamma < 9 \text{ GeV}/c$ and $0.5 < p_T^h < 7 \text{ GeV}/c$ as a function of $\xi = \ln(1/z_T)$ where $z_T = p_T^h/p_T^\gamma$ for central Au+Au (black circles) and $p+p$ (blue squares) collisions. (bottom) Full $\Delta\phi > \pi/2$ away-side I_{AA} (black circles) versus ξ with BW-MLLA (red dashed line) and YaJEM (blue dashed line) calculations [18]. These figures have been used with permission. See Figures C.7 and C.8 for more details.

1.6.1 I_{AA}

The quantity that measures the modification of the jet fragmentation with and without the QGP present is called I_{AA} . It is defined as

$$I_{AA} = \frac{Y^{Au+Au}(p_T^\gamma, p_T^h)}{Y^{p+p}(p_T^\gamma, p_T^h)}, \quad (1.15)$$

where Y is the away-side yield of the jet function in some $\Delta\phi$ region in Au+Au or $p+p$ collisions. The bottom panel of Figure 1.15b shows the ratio of the black point to the blue points in the top panel, the I_{AA} versus ξ . One can see that there is a suppression at high z_T and an enhancement at

low z_T . The red and blue curves are two different model calculations. From this figure, we can conclude that there is a suppression of high z_T partons in Au+Au collisions when compared to $p+p$ because the QGP medium causes these particles to lose energy. There is also an enhancement at low z_T that is caused by the QGP medium responding to the high z_T partons losing energy and creating more low z_T partons.

The pattern of suppression and enhancement is also observed in other away-side regions. This is shown in Figure 1.16. The black points are the same black points in the lower panel of Figure 1.15b. The blue points are the $|\Delta\phi - \pi| < \pi/3$ away-side and the red points are the $|\Delta\phi - \pi| < \pi/6$ away-side. The enhancement and suppression pattern has the highest amplitude for the large away-side regions and it decreases as the away-side angle gets smaller. The lower panel of Figure 1.16 compares the smallest away-side region to the largest to show that the low z_T enhancement is mostly at large angles, that is, when $|\Delta\phi - \pi| > \pi/6$.

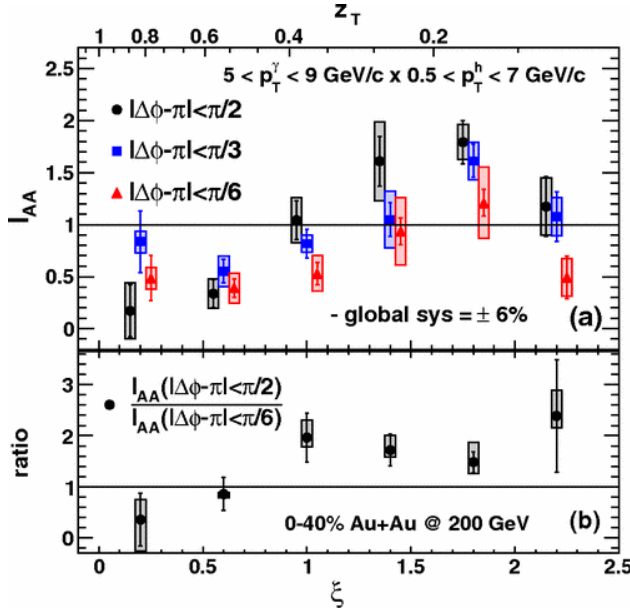


Figure 1.16: (a) I_{AA} as a function of ξ for 0-40% central Au+Au collisions and $5 < p_T^\gamma < 9$ GeV/c and $0.5 < p_T^h < 7$ GeV/c for $\Delta\phi > \pi/2$ away-side (black), $\Delta\phi > \pi/3$ away-side (red), and $\Delta\phi > \pi/6$ away-side (blue) [18]. (b) The ratio of the $\Delta\phi > \pi/2$ I_{AA} to $\Delta\phi > \pi/2$ I_{AA} . This figure has been used with permission. See Figure C.8 for more details.

The I_{AA} can be plotted as a function of centrality so the centrality dependence of the jet modification can be seen. This is shown in Figure 1.17. The x -axis is N_{part} which is a proxy of centrality, the most central collisions are at high N_{part} and peripheral events are at low N_{part} . The blue points are the I_{AA} of $\gamma_{dir} - h$ pairs with $5 < p_T^\gamma < 15$ GeV/c and $3 < p_T^h < 5$ GeV/c, the red points are $h - h$ pairs with $5 < p_T^h < 10$ GeV/c and $3 < p_T^h < 4$ GeV/c. The shaded blue region is the R_{AA} of π^0 's with $p_T > 5$ GeV/c. The points show that there is suppression in all centrality bins for both types of correlations. Also, the I_{AA} is consistent with the R_{AA} of π^0 , which means that the geometry of the suppression in the medium is the same as the geometry of the π^0 's emitted from the QGP.

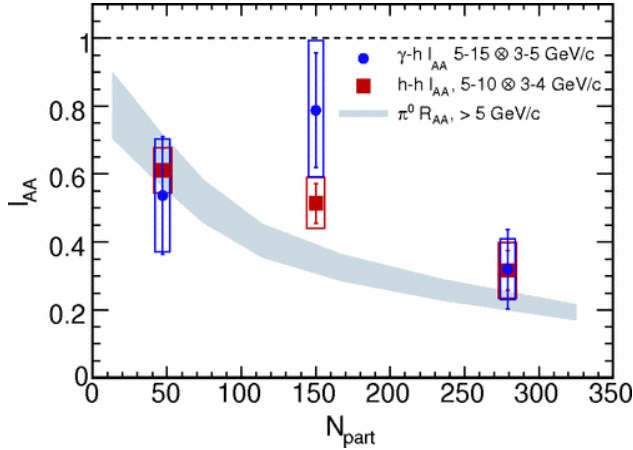


Figure 1.17: I_{AA} of $\gamma_{dir} - h$ pairs with $5 < p_T^\gamma < 15$ GeV/c and $3 < p_T^h < 5$ GeV/c (blue points), the red points are $h - h$ pairs with $5 < p_T^h < 10$ GeV/c and $3 < p_T^h < 4$ GeV/c (red squares) as a function of N_{part} for the $\pi/5$ away-side region. The shaded gray region is the R_{AA} of π^0 's with $p_T > 5$ GeV/c [17]. This figure has been used with permission. See Figure C.7 for more details.

1.7 QCD and Jet Energy Loss Theory

For virtually any application, such as for anything related to nuclear or particle physics, the theory of QCD can only be easily used to calculate high energy situations, in which case the theory is called perturbative QCD or pQCD. Unfortunately the quarks and gluons in the QGP are mostly

at lower energy scales. In this non-perturbative regime, QCD can be solved using a method called lattice QCD. This method solves QCD at a grid of points called a lattice. This method can describe some aspects of the QGP but requires too much computing power to be feasible for most QGP physics. For soft observables, such as v_2 at low p_T , models use hydrodynamics to describe the QGP. To describe jet energy loss in the QGP, mostly perturbative energy loss models are used, as jets are, by definition, high energy. However, these models generally combine two ideas, parton energy loss in the QGP that is perturbative, and redistribution of this lost energy to other the partons in the QGP that is non-perturbative. The method of modeling these two ingredients varies between the models, a few of which are described below. This is the most important motivation for the specific results in this dissertation, to sort out the redistribution mechanisms as described below. Some finer details of even the perturbative part of the models are still being developed, for example whether the energy loss depends on the fragmentation function of the hadrons.

The CoLBT_Hydro model is a linearized Boltzman transport model for parton propagation with a hydrodynamic model of the QGP evolution [37]. It tracks the thermal partons and their interactions in the QGP and includes jets that excite the QGP. A similar model, BW-MLLA, is the Borghini and Wiedemann modified leading logarithmic approximation model [38]. This model uses increased parton splitting probability to model the energy loss and includes jets that excite the QGP. This model is compared to PHENIX results in the lower panel of Figure 1.15b. The Qin model includes a hydrodynamic evolution with energy loss in the medium and includes fragmentation photons as well as photons from partons in the medium [49]. The ZOWW model is similar to Qin but does not include the fragmentation photons or the photons from the partons in the medium [50]. These two models do not include the redistribution of the energy lost by the high z_T particles to the low z_T particles. The Renk YaJem model uses gluon radiation for the energy loss and includes the energy redistribution to the medium [51]. This model is also compared to PHENIX results in the lower panel of Figure 1.15b.

By comparing results to theory the field of heavy-ion collisions is trying to understand the details of how the energy loss works. This dissertation provides new two-particle correlations data

that can confirm the mechanism that redistributes the lost energy. Each theory has different energy loss mechanisms that interacts with the jets, understanding these will tell us how the QGP behaves. This dissertation also provides new data for the v_2 of isolated π^0 's that may constrain how energy loss depends on fragmentation. We are also attempting to understand the true plasma constituents. As an example, if the plasma is truly made up of free quarks and gluons, why do they interact so strongly? To answer this question, we need to understand what models have the proper ingredients so they can be trusted over a wide range of jet energies/phase space. Calibrating these models helps to move our understanding of the QGP forward.

1.8 Purpose of This Dissertation

The purpose of this dissertation is to measure isolated photon-hadron correlations and v_2 of isolated photons and π^0 's. This is accomplished by employing an isolation cut on the trigger photons to increase the direct photon signal-to-background ratio. The use of the isolation cut biases the trigger photons elliptic flow measurement. We have developed a method to account for this bias and present measurements of isolated photon and $\pi^0 v_2$ as a function of p_T .

The first and second chapters of this dissertation are largely adapted from my master's thesis, Reference [52]. Chapter 2 discusses where the data analyzed in this work was taken, the PHENIX experiment at RHIC. Chapter 3 explains the data and analysis cuts on the events and particles used in this analysis. Chapter 4 outlines the groundwork for the functions used to find the isolated photon and v_2 of π^0 that was developed in Reference [52] and work that has occurred since that was published to include the event plane resolution and a verification using a Monte Carlo simulation. Chapter 5 explains the analysis procedure used in the data to extract the v_2 . Chapter 7 explains the nuances of the gamma-hadron correlations and all the inputs that are required. The results are shown in Chapter 6, for the isolated photon v_2 measurements, and Chapter 8, for the correlations results. Chapter 9 discusses the correlation results and relates them to theory and similar results from other experiments. And finally, the summary and future work is in Chapter 10. As described

in the previous section, this data will directly improve our understanding of the details of the mechanisms of energy loss in the QGP and their theoretical descriptions.

2 EXPERIMENTAL DETAILS

2.1 Relativistic Heavy Ion Collider

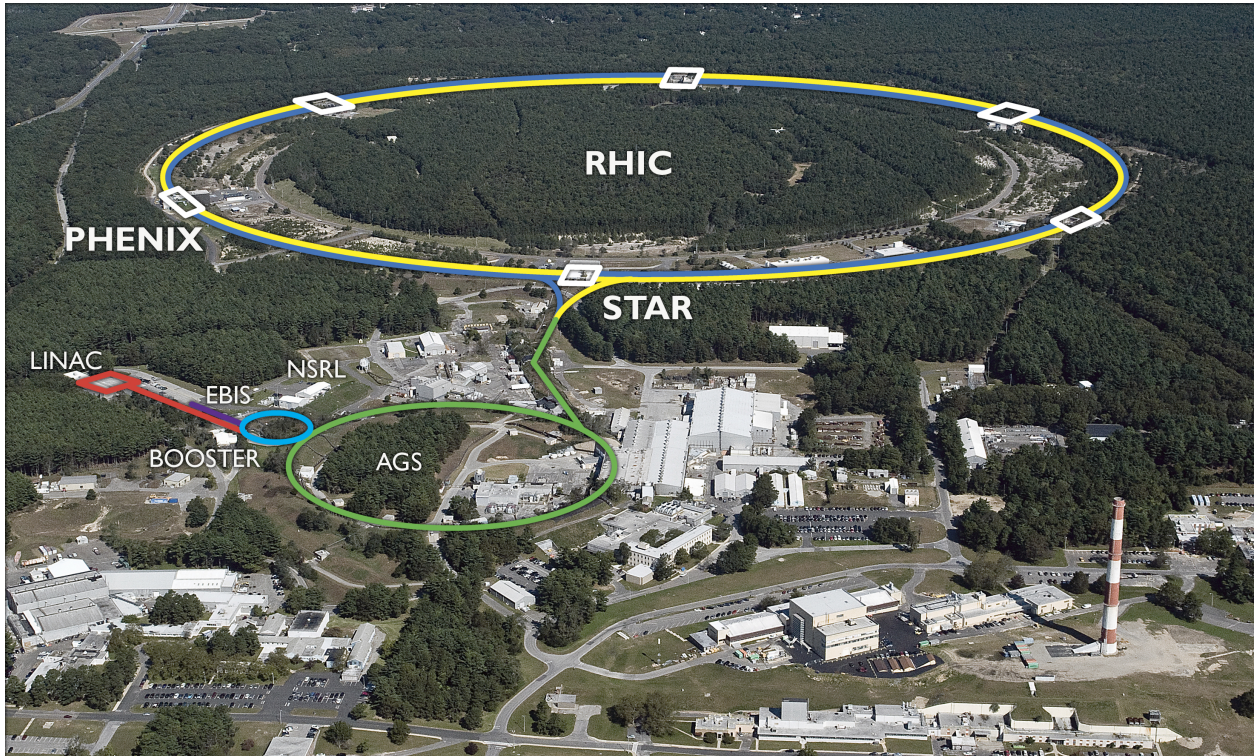


Figure 2.1: An aerial view of RHIC with the experiments and accelerators labeled [19]. Courtesy Brookhaven National Laboratory. See Figure C.1 and C.2 for more details.

The Relativistic Heavy Ion Collider (RHIC) is located at Brookhaven National Laboratory in Upton, New York [53]. It consists of accelerators that bring ions from rest to nearly the speed of light and two concentric 3.8 kilometer storage rings that preserve the ions until they are collided in the experimental areas. There are four experimental areas at RHIC: BRAHMS, PHOBOS, STAR, and PHENIX. RHIC is capable of colliding a myriad of particle types at center-of-mass pair energies below 510 GeV. An aerial view of RHIC is shown in Figure 2.1. For more information on how RHIC operates, see reference [53]. The experiment used to collect the data set used in this thesis, PHENIX, is described in the next section. PHENIX, BRAHMS, and PHOBOS have been

decommissioned. PHENIX has been dismantled to make room for the next generation detector that is being developed and will be placed in the PHENIX experimental hall. RHIC is still in operation and is delivering collisions to STAR.

2.2 Pioneering High Energy Nuclear Interaction Experiment

The Pioneering High Energy Nuclear Interaction eXperiment (PHENIX) was an array of detectors used to identify particles and their momentum emitted from the collision of ions [54]. The experiment was overseen by a collaboration of about 500 physicists from around the world. PHENIX had its first data taking Run (Run 1) in 2000. PHENIX, shown in Figure 2.2, did not have full azimuthal coverage. This is because of the large magnets that are above and below the two central arms. The azimuthal acceptance was $-0.57 \geq \phi \geq 0.97$ radians and $2.14 \geq \phi \geq 3.72$ radians. The central arm of the detector had a small η acceptance, $|\eta| < 0.35$. The major detectors used in this analysis reside in the central arm. The detectors vital to the analysis in this thesis are described in the following sections and are listed in Table 2.1.

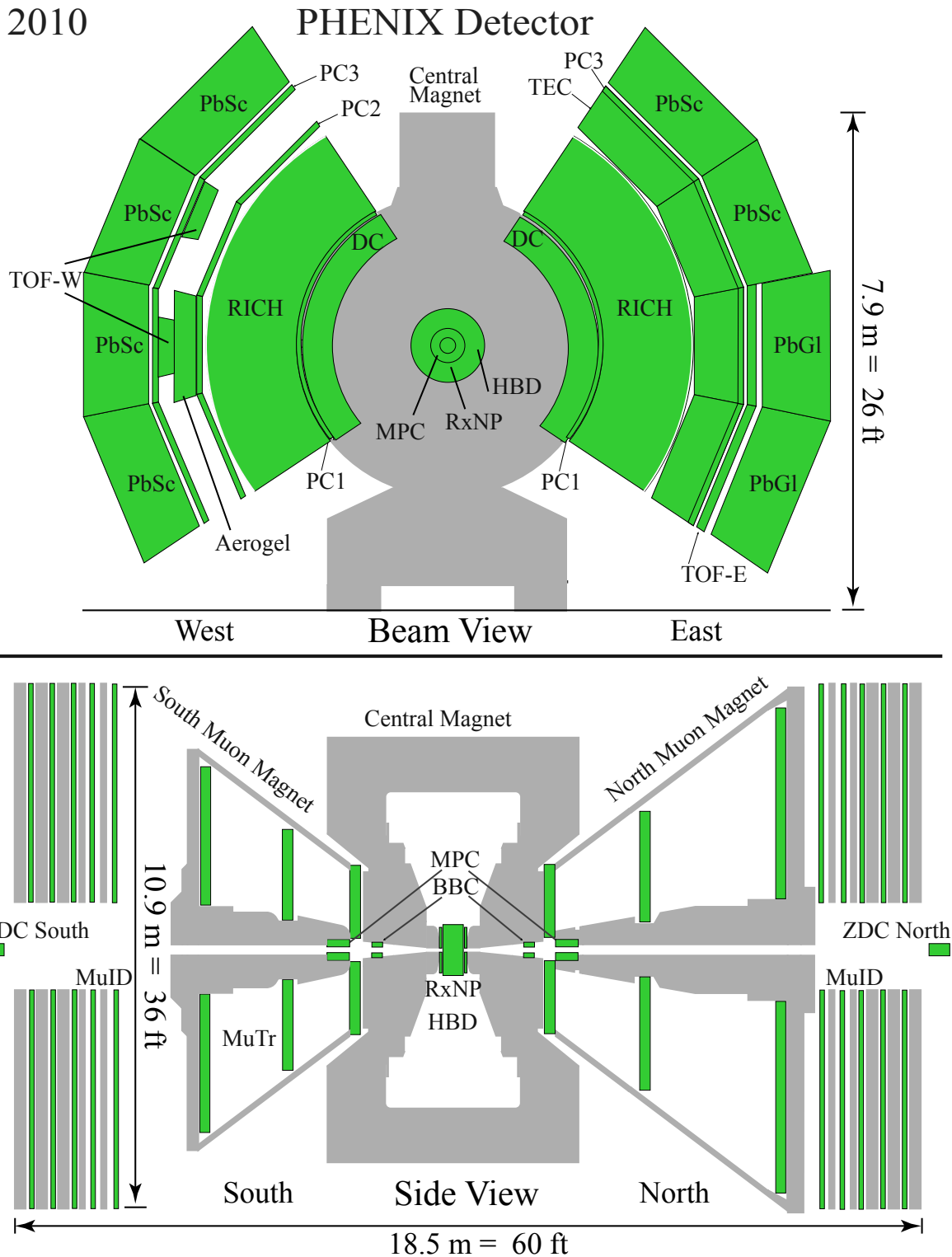


Figure 2.2: Configuration of PHENIX for Run 10 as seen along (Top) and perpendicular to the beamline (Bottom) [20]. This figure has been used with permission. See Figure C.9 for more details.

Table 2.1: Selected PHENIX event characterization and central arm detectors with their acceptance and purpose. Adapted from [2].

Detector Subsystem	ϕ	η	Purpose
Central Magnet	2π	$ \eta < 0.35$	Bends charged particles so they can be identified and their momentum measured
BBC	2π	$3.0 < \eta < 9$	Initiates timing, determines collision vertex, centrality
EMCal			
PbSc	$\frac{\pi}{2} + \frac{\pi}{4}$	$ \eta < 0.35$	High timing resolution, Photon identification through showers
PbGl	$\frac{\pi}{4}$	$ \eta < 0.35$	High energy resolution and granularity
DC	$\frac{\pi}{2} \times 2$	$ \eta < 0.35$	Measures charged particles position and momentum
PC	$\frac{\pi}{2} \times 2$	$ \eta < 0.35$	Measures charged particles position and momentum

2.2.1 Central Magnet

PHENIX had a large central magnet used to bend the path of charged particles as they move away from the interaction point. Figure 2.3 shows the orientation of the magnetic fields in PHENIX. The central arm magnet steel (shown in green) is the region in $|z| < 2\text{m}$. The regions with $|z| > 2\text{m}$ are the muon arm magnets and are not used in this analysis. The red boxes show the locations of the magnetic field coils which energize the magnet. They were run separately to achieve different field strengths. The central magnet has an axial magnetic field as indicated by the

black lines connecting the green regions. The field integral at 90 degrees to the beamline was 0.8 Tm [54].

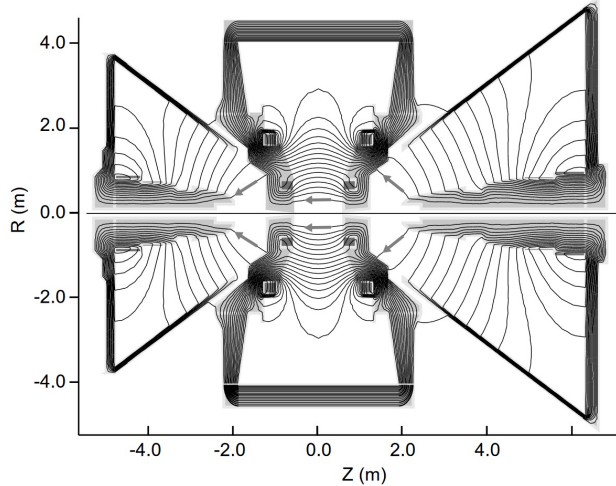


Figure 2.3: PHENIX magnetic field orientation viewed perependicular to the beamline [21]. This figure has been used with permission. See Figures C.10 and C.11 for more details.

2.2.2 Beam Beam Counter

The Beam Beam Counter (BBC) was made up of north and south modules, each module had full azimuthal coverage and pseudorapidity in the range $3 < |\eta| < 3.9$. Each module consisted of 64 three-centimeter-long quartz Cherenkov radiators attached to photomultiplier tubes (PMTs). The detector served five basic purposes:

- determined the collision vertex by

$$z_{vertex} = \frac{(T_S - T_N)c}{2}, \quad (2.1)$$

where T_S and T_N are the times at which the south and north modules detected hits, and c is the speed of light,

- set time zero for the time of flight measurements,
- determined the event plane angle,

- determined collision centrality, and
- served as the minimum bias trigger.

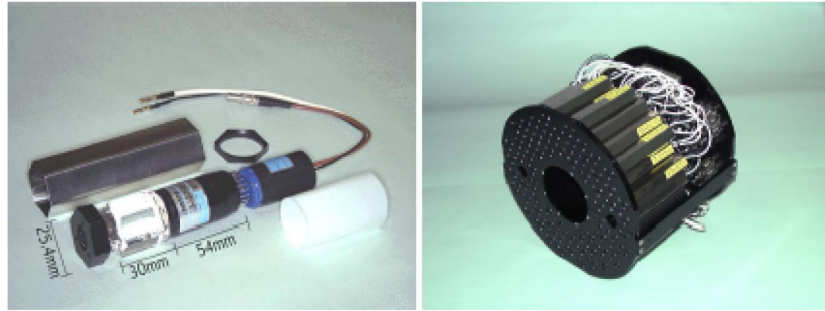


Figure 2.4: (Left) A single radiator attached to a PMT. (Right) A BBC module consisting of 64 radiators attached to PMTs [22].

2.2.3 Electromagnetic Calorimeter

The Electromagnetic Calorimeter (EMCal) was a system of lead scintillator (PbSc) and lead glass (PbGl) detectors with acceptance $|\eta| < 0.375$ and $\phi = 90^\circ \times 2$. Using two different types of detectors allowed for a better understanding of systematic uncertainties, and therefore increase the confidence in our results. There were 6 sectors of PbSc, four in the west arm and two at the top of the east arm. Each sector was made up of 18 supermodules, each supermodule was made up 36 modules, each module was made of four towers, and each tower was made of alternating layers of lead and scintillator that were connected to PMTs via fiber optics. There were 2 sectors of PbGl, each made of 192 supermodules, each supermodule was made of 24 modules, and each module consisted of a lead glass crystal attached to a PMT. A diagram of a module of both detector types can be seen in Figure 2.5. The PbGl had better energy resolution and granularity than the PbSc.

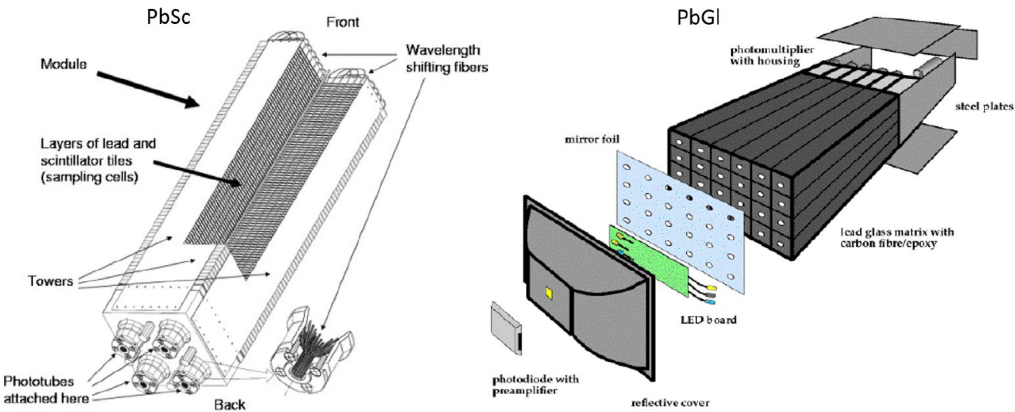


Figure 2.5: (Left) A module of PbSc showing the four towers made up of layers of lead and scintillator. (Right) A module of PbGl showing the 24 towers [23]. This figure has been used with permission. See Figures C.12 and C.13 for more details.

2.2.4 Drift Chamber

The drift chamber (DCH) was used to identify charged hadrons and measure their momenta. There was a DCH for each arm located 2.02 m to 2.48 m radially from the interaction point. Each DCH contained six planes (X1, U1, V1, X2, U2, V2) of 80 wires each. The region between the wires was filled with a mix of argon, ethane, and ethanol gas. The charged hadron ionizes the gas, the released electrons drift to the wires to be readout. The X1 wire planes were parallel to the beamline and used to determine the track's azimuthal angle. The U and V planes determined the z of the charged track. The orientation of the wire planes is shown in Figure 2.6, the side view (left) and along the beamline (right). The middle insert shows the individual wire configuration in a single plane. Each anode wire was surrounded by a potential wire that created a strong electric field. The gate and back wires limited electron drift.

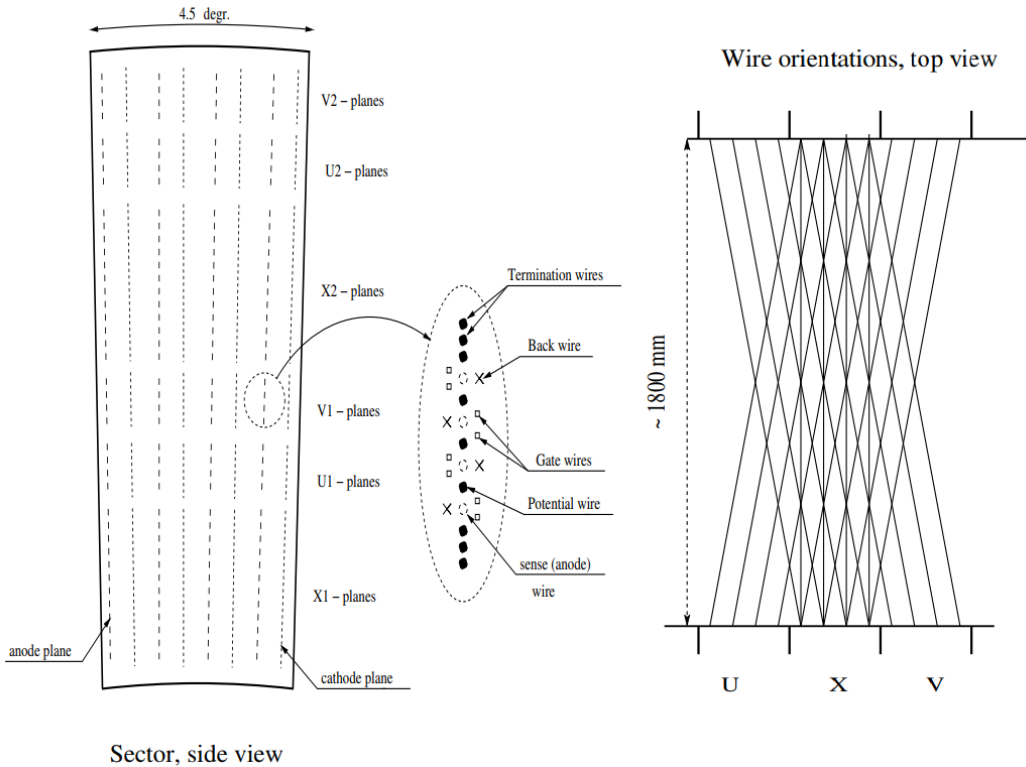


Figure 2.6: (Left) Side view of the DCH with each wire plane labeled. (Right) Top view showing the U, X, and V wire orientations in the DC [24]. This figure has been used with permission. See Figures C.14 and C.15 for more details.

2.2.5 Pad Chamber

The pad chambers measure the position and momenta of charged particle. There were 3 pad chamber (PC) detectors in PHENIX, PC1 and PC3 in the east arm while the west arm contained PC1, PC2, and PC3 (see Figure 2.2). Each PC was a multiwire proportional counter, that is, they consisted of a plane of finely spaced wires (anodes) between copper planes (cathodes). One of the cathode planes had cells, each of which contained three layers that are chained together to make a total of nine pixels. A hit must have had signals from at least three pixels. This geometry is shown in Figure 2.7. Panel a (left) of this figure shows three anode wires with a single cell labeled, panel b (left center) shows the three cathode planes with the same overlapped cell labeled. Panel c (right center) shows each pixel on each plane and how they overlap and their relation to the horizontal

anode wires. Panel d (right) shows the nine chained pixels that are split between the anode wires. PC1 was mainly used in track reconstruction while PC2 and PC3 were used to verify track samples. PC2 was not used in this analysis.

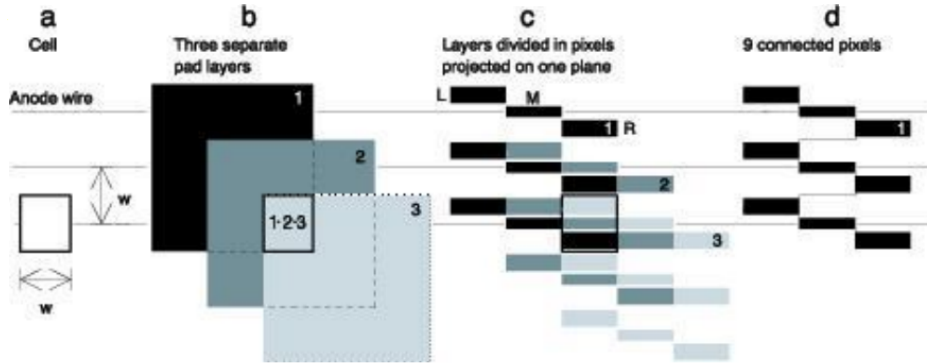


Figure 2.7: Pad chamber geometry described in text [25].

3 DATA SELECTION

3.1 Introduction

The data used in this analysis is RHIC-Run 10 Au+Au and RHIC-Run 11 Au+Au at $\sqrt{s_{NN}} = 200$ GeV. Run 10 contains 7.7 billion events and Run 11 contains 4.9 billion events. These data were taken in 2010 and 2011. This chapter outlines the event selection by detailing the trigger and centrality selection. It also defines the requirements on the photons, π^0 's, and hadrons used in this analysis.

3.2 Event Selection - Centrality

As introduced in Chapter 1, centrality is a measure of the overlap of the colliding nucleons. This quantity cannot be measured directly. Instead, Glauber model Monte Carlo calculations are used to match the data to find the centrality bins. The Glauber model describes the colliding nuclei by describing the interactions of the nucleons. This is done with a Monte Carlo by using a nucleon density distribution and an impact parameter. The nucleons then collide independently and interact according to the inelastic nucleon-nucleon cross section. Figure 3.1 shows how the total charged particle multiplicity, N_{ch} , is related to Glauber model calculated quantities impact parameter, b , and number of participants, N_{part} . The blue line is the N_{ch} distribution, the upper x -axes are $\langle b \rangle$ and $\langle N_{part} \rangle$ and the lower x -axes are fraction of total cross-section and N_{ch} . Centrality percentile is also labeled. The yellow circles are the colliding nucleons and the red regions are the overlap regions. For peripheral events, the overlap, N_{ch} , and N_{part} are small, while centrality percentile and b are large. These are glancing collisions. For central events, the head on collisions, the overlap, N_{ch} , and N_{part} are large, while centrality percentile and b are small. The centrality percentile is found by dividing the N_{ch} distribution such that each percent bin contains the same number of events.

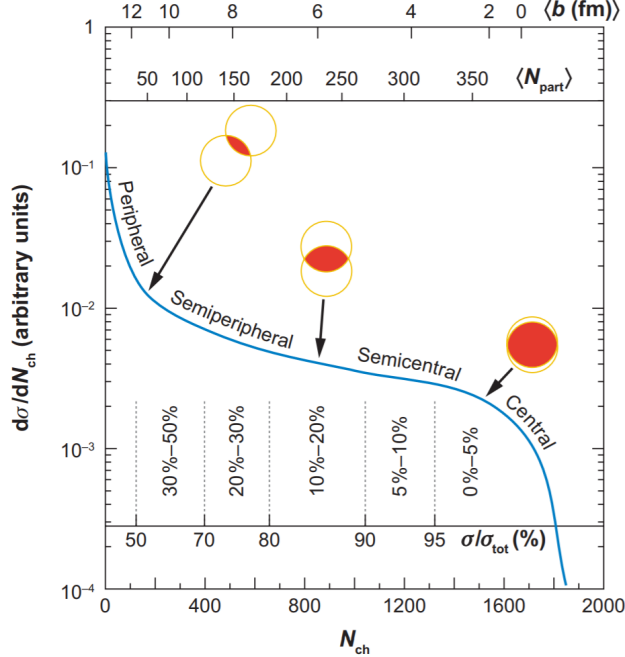


Figure 3.1: Illustration of how N_{ch} is related to quantities calculated with the Glauber model [26].

This figure has been used with permission. See Figure C.16 for more details.

Centrality in PHENIX is determined by plotting the total charge in both BBC modules as shown by the blue line in Figure 3.2. This distribution is then divided into percentile centrality bins such that each bin contains that same number of events. This analysis uses four centrality bins: 0 - 20%, 20 - 40%, 40 - 60%, and 60 - 92% central.

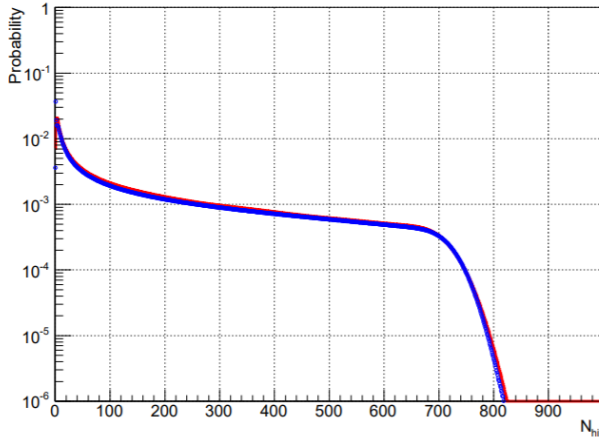


Figure 3.2: BBC total charge distribution (blue) (x -axis) with a negative binomial distribution fit (red) that is used to find the trigger efficiency [27].

3.3 Event Selection - Trigger

The trigger used in this analysis is the minimum bias (MinBias) trigger. This trigger is configured such that it has the minimum bias of any other possible trigger. The requirements for the MinBias trigger is $|z_{vertex}| < 30$ cm and some number of hits in the a BBC module. The exact number of hits depends on the collision species and energy. The trigger is $\approx 100\%$ efficient for centrality below 93.5% and 0% efficient above. This limit is found by fitting the Glauber Model calculated N_{part} distribution with a negative binomial distribution, the red line in Figure 3.2.

3.4 Particle Selection - Photons

There are three types of photons that we are interested in: isolated/direct, decay, and inclusive. Inclusive photons are simply all of the photons in an event. Decay photons are those associated with decaying mesons, the majority of which come from the decay π^0 mesons. Direct photons were discussed in the introduction. Currently, we use trigger photons with $3 \leq p_T \leq 15$ GeV/c. We must ensure that we are not using bad towers in the EMCal. For instance, a tower may be dead or it may be mistakenly detecting energy that is not there. To account for this, we use a hot/dead tower map.

3.4.1 Hot/Dead tower maps

To determine the hot and dead towers, we record the number of hits in each tower for each sector over the entire data set. If a tower has a total number of hits above (below) 5σ of the mean for that sector, the tower is considered hot (dead). This procedure is done twice, once for hits with $p_T \leq 5$ GeV/c and again for hits with $p_T > 5$ GeV/c. We also remove towers immediately surrounding the hot or dead one in order to eliminate any bleed over from the electromagnetic shower. The towers along the edge of the sectors are also removed in order to account for showers that may have been lost outside of the detector. Once these hot/dead towers are determined (Figure 3.3a and Figure 3.3b), they are applied to the EMCal, and the code is run again with these towers excluded. By excluding the towers in Figure 3.3a and Figure 3.3b, the mean and width of the tower hit distribution is different so additional towers that were missed the first time through the data can be found. This “extra” map is shown in Figure 3.3c. The photon hits for all energies after these three maps have been applied are shown in Figure 3.4.

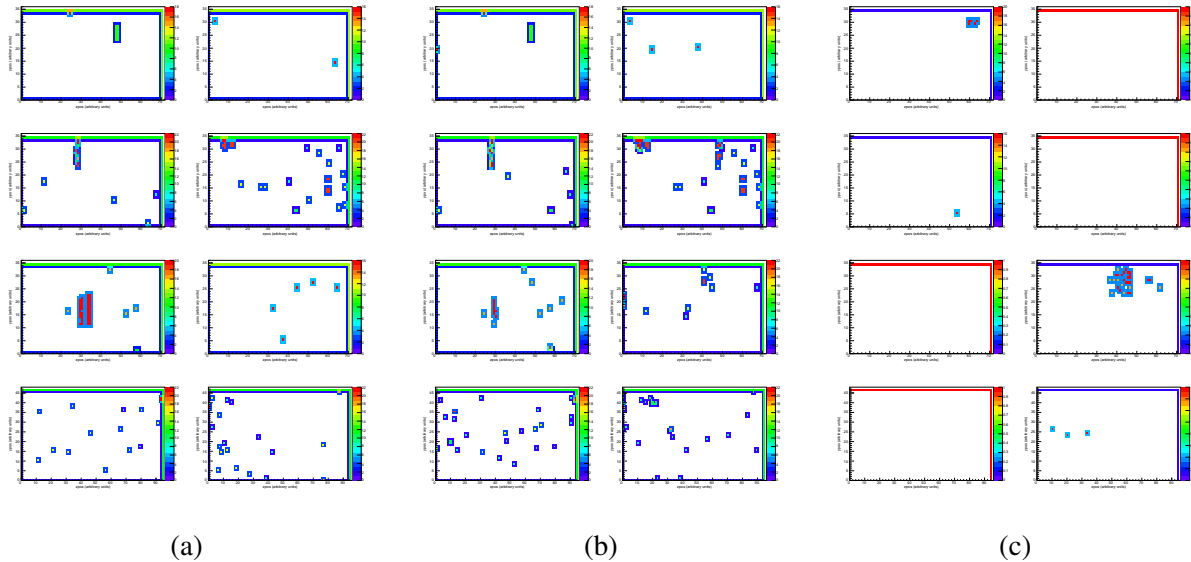


Figure 3.3: (a) A map of the excluded towers with hits with $p_T \leq 5$ GeV/c. (b) A map of the excluded towers with hits with $p_T > 5$ GeV/c. (c) A map of all additional towers found after the maps in (a) and (b) have been applied. In all three figures, each bin is a tower in the detector, the x axis is the tower position along the beamline ($zpos$) and the y axis is the tower height ($ypos$).

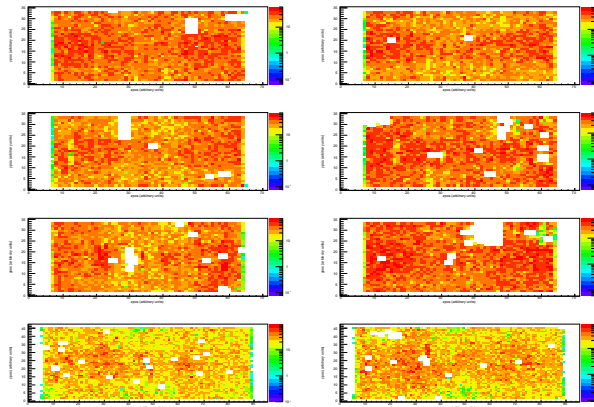


Figure 3.4: Photon hits for all energies after hot/dead maps have been applied. Each plot is an EMCAL sector, each bin is an individual tower. The color corresponds to the number of hits in each tower for the entire Run 11 MinBias data set.

We use two methods to obtain direct photons, an isolation cut and a statistical method. The statistical method is based on the probability that the photon in question came from a decay. This is because the number of decay photons is subtracted from the number of total photons to find the number of direct photons. The per trigger yield of the direct photons can be written as

$$Y^{dir} = \frac{R_\gamma Y^{inc} - Y^{dec}}{R_\gamma - 1}, \quad (3.1)$$

where $Y = \frac{1}{N^\gamma} \frac{dN^{\gamma-h}}{d\Delta\phi}$ and $R_\gamma = \frac{N^{inc}}{N_{dec}}$ [3]. This equation is derived and described in more detail in Section 7.6. The statistical subtraction method is a doubly-indirect method, it relies on measuring the inclusive photons yield as well as obtaining an accurate probability for determining decay photons. A direct method of obtaining direct photons, via the isolation cut, is described in the next section.

3.4.2 Isolation Cut Method

Isolated photons originate from the initial hard scattering of the nucleons that make up the beam. It is important to remember that photons are color neutral so they are not modified by the quark-gluon plasma. Determining which photons originated from a decay or were from the initial scattering is a nontrivial task. An isolation cut is used to remove these decay photons from the outgoing particle distribution. Each photon in each event has a cone around it with a radius according to

$$R_{cone} = \sqrt{(\Delta\phi)^2 + (\Delta\eta)^2}, \quad (3.2)$$

where ϕ is the angle around the beampipe and η is the pseudorapidity, the angle along the beampipe. The energy inside the cone is then measured, if it is smaller than the threshold energy (E_{TH}), the photon is classified as isolated. If the energy is greater, the photon is not isolated and probably originated from a decay. This process is depicted in Figure 3.5. The threshold energy is determined using

$$E_{TH} = aE_\gamma + b, \quad (3.3)$$

where a and b , not impact parameter, are parameters defined in Table 3.1 and E_γ is the central photon's total energy. The parameters a , b , and R_{cone} vary with centrality due to the magnitude of

the underlying event. These parameters were found via an optimization procedure in Reference [3].

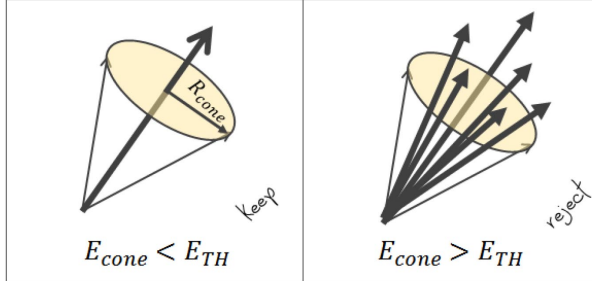


Figure 3.5: Definition of the isolation cut method that is used to find isolated photons. The black arrows are particles inside the cone [3].

Table 3.1: Isolation cut parameters for all centralities of Au+Au collisions [3].

Centrality (%)	R_{cone}	a	b (GeV)
0 - 20	0.1	0.1	2.0
20 - 40	0.2	0.1	4.0
40 - 60	0.2	0.1	2.0
60 - 92	0.3	0.1	1.0

Once the isolated photons are found, we subtract the decay photon contribution from the isolated photon sample using Equation 3.1 with a modified R_γ . This is described in more detail in Chapter 7.

3.5 Particle Selection - π^0 's

We use π^0 's with $4 \leq p_T \leq 17$ GeV/c. We use momentum less than the trigger photon to account for the finite detector resolution, the upper limit is because the π^0 signal starts to fade

because the photon showers in the EMCAL merge and become indistinguishable. The mass of the π^0 is 0.134 GeV [1]. We calculate the invariant mass of the two photons using

$$m_{\gamma_1\gamma_2} = \sqrt{2E_{\gamma_1}E_{\gamma_2}(1 - \cos(\phi_{\gamma_1\gamma_2}))}, \quad (3.4)$$

where E_{γ_1} (E_{γ_2}) is the energy of photon 1 (2) and $\phi_{\gamma_1\gamma_2}$ is the opening angle between the two. The π^0 's pass this invariant mass cut if they are in the range of $0.12 \leq m_{\gamma_1\gamma_2} \leq 0.16$ GeV. The opening angle is limited by requiring the photons to be detected in the same PHENIX arm. A few example invariant mass distributions are shown later in Figure 7.11. The 0-40% central event photons and those that make up π^0 's with $p_T \leq 5.25$ GeV/c also undergo an energy asymmetry cut. This cut is defined by

$$a = \left| \frac{E_{\gamma_1} - E_{\gamma_2}}{E_{\gamma_1} + E_{\gamma_2}} \right|. \quad (3.5)$$

If the value of a is less than $0.15 + 0.85(E_{\pi^0} - 4)^2 / 1.25^2$, where $E_{\pi^0} = E_{\gamma_1} + E_{\gamma_2}$, then the two photons are said to be from a π^0 . This asymmetry cut reduces the number of low- p_T and high- p_T pairs. This is necessary because there is a copious amount of low- p_T photons that satisfy the invariant mass condition with a high- p_T photon.

3.5.1 π^0 Trigger Efficiency

The π^0 trigger efficiency correction ($1/\pi^0$ trigger efficiency) we use for Run 11 is shown in Figure 3.6. The y-axis scale is in arbitrary units, just the shape of the curves matter. The efficiency for Run 10 (11) was determined by scaling the raw π^0 spectrum from the Run 10 (11) MinBias data to the published π^0 spectrum in Reference [36]. These corrections can be dependent on calibration that can vary on a run-by-run or even run number-by-run number bases, but the effects have been determined to be negligible.

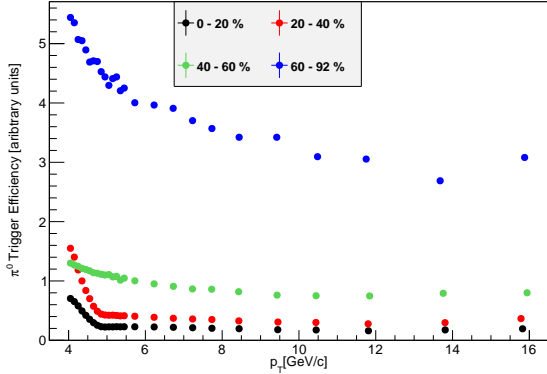


Figure 3.6: π^0 trigger efficiency correction ($1/\pi^0$ trigger efficiency) as a function of p_T for the four centralities, 0-20% (black points), 20-40% (red points), 40-60% (green points), and 60-92 % (blue points).

3.6 Particle Selection - Decay Photons

Most decay photons come from the decay of π^0 . We use the decay probability distribution of the π^0 to decay to two photons. This probability distribution is often called a sharkfin. Sharkfins are π^0 decay probability functions that depend on p_T and the EmCal z coordinate of the π^0 . An example is shown in Figure 3.7. We use the same sharkfins as References [3, 5, 32, 33]. The sharkfins we use are described in more detail in Section 7.5.1. Additional details for calculating sharkfins can be found in References [3, 17, 34].

As described in Reference [3], the isolation cut implies the need for alterations to the standard sharkfins. The shape and efficacy of the new modified sharkfin, along with the efficacy of the entire method to estimate the isolated π^0 decay contribution is summarized in Section 7.5.4.

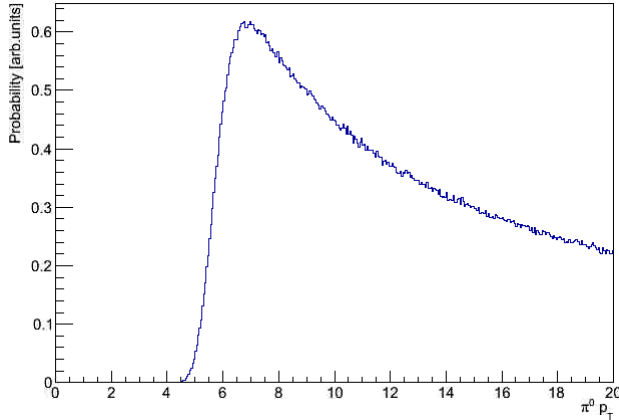


Figure 3.7: An example π^0 decay probability function as a function of $\pi^0 p_T$.

3.7 Particle Selection - Hadrons

Hadrons are selected via their tracks in the DC, PC1, and PC3. We are use hadrons with $1 \leq p_T \leq 10$ GeV/c. Hadrons are reconstructed by reconstructing their charged tracks. We choose tracks that have hits in PC1 and can be matched to specific wires in the drift chamber. We also have a cut on the sigmalized distance between their track position in the DCH/PC1 and PC3 in order to cut out high momentum false tracks. This is carried out by determining the mean and width of the distribution of the distances between tracks in the DCH/PC1 and PC3 in the ϕ and z directions. For each track, this is defined as

$$\sigma_\phi = \frac{d\phi - \langle d\phi \rangle}{\sigma_{d\phi}}, \quad \sigma_z = \frac{dz - \langle dz \rangle}{\sigma_{dz}}, \quad (3.6)$$

where $d\phi$ (dz) is the distance in ϕ (z) of the tracks actual position and its projected position in the PC3 or EMCAL. The angular brackets denote average over all tracks and $\sigma_{d\phi, dz}$ is the standard deviation of the average. We accept tracks with $\sqrt{\sigma_\phi^2 + \sigma_z^2} < 2$ in the PC3. For Run 11, there is an additional cut of $\sqrt{\sigma_\phi^2 + \sigma_z^2} < 2$ in the EMCAL to cut tracks that create signals in the EmCal.

3.7.1 Hadron Efficiency

Hadron efficiency is a term in the per trigger yield (Equation 1.14). The hadron efficiency has two components, the single particle efficiency, ϵ_{SP} , and the occupancy correction, ϵ_{Occ} . The single

particle efficiency is the efficiency for detecting single hadrons in the tracking system and includes the limited PHENIX acceptance. The occupancy correction accounts for the large number of tracks created in a heavy-ion collision and the inherent errors that occur during track reconstruction. Each of these components are multiplied by one another and the ϵ_B term in Equation 1.14, $\epsilon_B = 2/\epsilon_{SP}\epsilon_{Occ}$, to correct the PHENIX π azimuthal acceptance to the full 2π azimuth.

The single-particle efficiency is shown in Figure 3.8 for Run 10 (black line) and Run 11 (red line). They were found by simulating the PHENIX tracking system and reconstructing the charged tracks. These efficiencies have the form

$$\epsilon_{SP} = A + Be^{Cp_T}, \quad (3.7)$$

where the parameters A , B , and C are defined in Table 3.2. The dip near $p_T = 5$ GeV/c is caused by the ring imaging cherenkov (RICH) detector veto cut. For $p_T < 5$ GeV/c the RICH veto cut is applied to remove electron tracks. For $p_T > 5$ GeV/c, the veto cut is not applied. The dip in the curve that begins at $p_T < 4.7$ GeV/c is caused by the pions firing the RICH detector.

Table 3.2: Table of parameters for the Run 10 and central Run 11 efficiency functions that are shown in Figure 3.8. The functions have the form of Equation 3.7. These parameters come from References [3–5] for Run 10 and Reference [6] for Run 11.

	Run 10			Run 11		
	A	B	C	A	B	C
$p_T < 3$ GeV	0.496	-0.337	-1.50	0.4007	-0.4413	-1.167
$3 < p_T < 5$ GeV	0.500	-2.13×10^{-13}	5.36	0.3973	-7.951×10^{-5}	1.172
$p_T > 5$ GeV	0.496	-0.337	-1.50	0.4007	-0.4413	-1.167

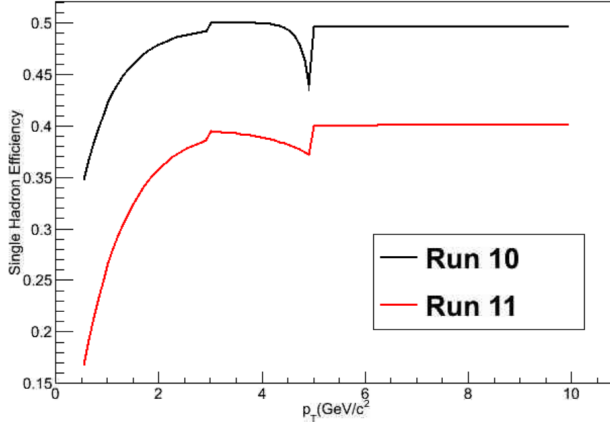


Figure 3.8: Single hadron efficiency for Run 10 (black line) and central Run 11 (red line) as a function of p_T that have the form of Equation 3.7 with the parameters defined in Table 3.2.

We use the same occupancy correction as in the previous Run 7 Au+Au and Run 10 Au+Au analyses in References [3–5] for Run 10. These are summarized in Table 3.3. This correction was studied extensively in Reference [4] by simulating the tracking system and embedding a simulated track in real Au+Au collision data and seeing how efficiently the track is reconstructed.

Table 3.3: Table of the Run 10 occupancy corrections, ϵ_{Occ} , for each centrality.

Centrality (%)	$p_T < 5 \text{ GeV}/c$		$p_T > 5 \text{ GeV}/c$
	$p_T < 5 \text{ GeV}/c$	$p_T > 5 \text{ GeV}/c$	
0 - 20	0.680	$0.761 + 1.640e^{(-4.734p_T)}$	
20 - 40	0.835		0.913
40 - 60	0.925		0.978
60 - 92	0.975		0.992

For Run 11, our initial studies indicated that the centrality dependence of the efficiency is likely different, possibly due to the introduction of the silicon vertex tracker (VTX) or fluctuating DC performance throughout Run 11. Instead of the constant with centrality single particle

efficiency in Run 10, we used a hybrid method for determining the single particle efficiency in Run 11 by partially employing simulation and a bootstrap method of non-triggered charge spectra ratios. In this method, the simulation result was used to set the overall normalization of the efficiency such that the Run 10 and Run 11 hadron yields and correlation functions match. Then the centrality dependence of the ratio of the Run 11 to Run 10 spectra ratio is used to determine the occupancy/centrality dependence; this is what is called the bootstrap method. This leads to a good overall matching between Run 10 and Run 11 across all of the charge spectra (by construction), correlation functions, and per-trigger jet yields. The resulting efficiencies used for Run 11 are shown in 3.9. The yellow points are the same as the red line in Figure 3.8.

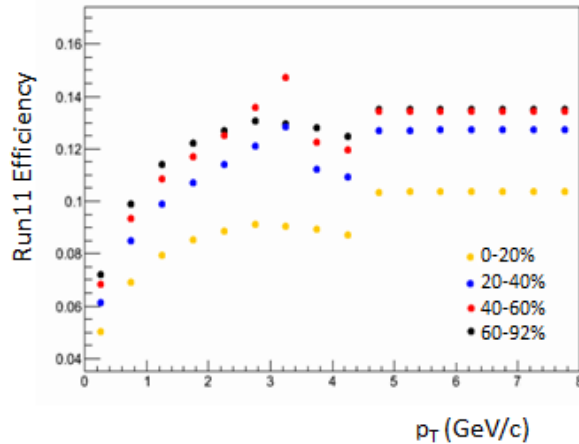


Figure 3.9: Single particle charged track efficiencies used in Run 11 for each centrality, the y-axis has arbitrary units.

4 DERIVATION OF ISOLATED PARTICLE AZIMUTHAL ASYMMETRY AND SIMULATION VERIFICATION

4.1 Introduction

The first goal of this dissertation is the measurement of v_2 that are needed as input to subtract the background from the γ_{dir} -h correlation function. Particles emitted during hadronization have the azimuthal distribution given by Equation 1.3. Most of the higher order terms in this equation can be ignored as noted earlier. In fact, for the work presented here, we truncate that equation at $n = 2$, that is,

$$\frac{d(N)}{d(\phi - \Psi_{RP})} \propto 1 + 2v_2 \cos(2(\phi - \Psi_{RP_2})), \quad (4.1)$$

where $v_2 = \langle \cos(2(\phi - \Psi_{RP_2})) \rangle$. This chapter is devoted to a discussion of my previous work done in Reference [52] with explanation of the simulation verification that has taken place since that work was completed. We have also extended the results presented there to include the reaction plane resolution. These results have also been verified using a simulation.

4.2 Summary of my previous work

In Reference [52], we showed that when the isolation cut method described in Section 3.4.2 is used, there is a reaction plane dependent isolation cut efficiency. This efficiency is caused by the choice of the isolation cut parameters a and b as constant anywhere in a given event so the isolation cut preferentially accepts particles emitted “out-of-plane” with respect to the event plane as isolated since the underlying event modulates to a lower extent there. The converse is also true, the method finds less isolated particles oriented “in-plane” relative to the event plane. This creates a bias when trying to measure the elliptic flow of the isolated particles. We call this bias the isolation cut efficiency and we assume it has the form

$$\epsilon = \epsilon_0(1 + 2v_{2E} \cos(2\Delta\phi)), \quad (4.2)$$

where ϵ_0 is an overall scale factor, v_{2E} is the isolation cut efficiency v_2 that is typically less than zero, $\Delta\phi = \phi_T - \Psi_{RP}$, where ϕ_T is the trigger particle’s azimuthal angle, and Ψ_{RP} is the second order

event plane angle. When this efficiency is included in a particle's azimuthal anisotropy distribution we get

$$\frac{dN_{TE}}{d\Delta\phi} = \mathcal{A}(1 + 2\mathcal{B}\cos(2\Delta\phi) + 4\mathcal{C}\cos^2(2\Delta\phi)), \quad (4.3)$$

where \mathcal{A} is an overall normalization factor, and

$$\begin{aligned} \mathcal{B} &= v_{2T} + v_{2E}, \\ \mathcal{C} &= v_{2T}v_{2E}, \end{aligned} \quad (4.4)$$

where v_{2T} is the v_2 of the trigger particle and v_{2E} is the v_2 of the isolation cut efficiency. Equation 4.3 takes the form because it is the isolation cut efficiency distribution (Equation 4.2) multiplied by the trigger particle's azimuthal distribution (Equation 4.1). Equation 4.3 also shows that when the trigger $\Delta\phi$ distribution is fit to $1 + 2v_2 \cos(2\Delta\phi)$, the v_2 that is measured not just v_{2T} but $v_{2T} + v_{2E}$. There is also a cosine squared term that may have a small effect on the fit. But for specific cases, for example, when $|v_{2T}| \approx |v_{2E}|$, the cosine squared term is dominant. This distribution was then verified using a Monte Carlo simulation.

In Reference [52], we also showed that when two particles are subject to this efficiency, a trigger particle and an associated particle are correlated through

$$\frac{dN_{TA}}{d\Delta\phi} = \mathcal{F}(\mathcal{G} + 2\mathcal{H}\cos(2\Delta\phi_{TA})), \quad (4.5)$$

where \mathcal{F} is an overall normalization factor and $\Delta\phi_{TA} = \phi_T - \phi_A$. The other parameters are defined as

$$\begin{aligned} \mathcal{G} &= 1 + 2v_{2T}v_{2E}, \\ \mathcal{H} &= v_{2A}(v_{2T} + v_{2E}), \end{aligned} \quad (4.6)$$

where v_{2T} is the v_2 of the trigger particle, v_{2A} is the v_2 of the associated particle, and v_{2E} is the v_2 of the isolation cut efficiency. This shows that the combinatoric background distribution for isolated photon-hadron correlations is not the simple form in Equation 1.13. It has a more complicated structure that depends strongly on v_{2E} .

The Monte Carlo we used to verify the above equations in Reference [52] generates random $\Delta\phi$ and reaction plane angles, Ψ_{RP} . The $\Delta\phi$ angles were distributed according to

$$1 + 2v_2 \cos(2(\Delta\phi)), \quad (4.7)$$

where v_2 is an input coefficient that can be between $-0.5 \leq v_2 \leq 0.5$. The event plane angles were generated uniformly according to Ψ_2 in Equation 1.6. The $\Delta\phi$ was accepted if $\phi_T = \Delta\phi + \Psi_{RP}$ was in the PHENIX azimuthal acceptance and it passed a Monte Carlo test. The Monte Carlo test consisted of generating a random number, Υ according to

$$\Upsilon = \frac{1 + 2v_{2E} \cos(2(\Delta\phi))}{1 + 2v_{2E}}, \quad (4.8)$$

where v_{2E} is an input efficiency value. The denominator was chosen to force $0 \leq \Upsilon \leq 1$. If Υ is greater than a uniform random number between zero and unity, then the $\Delta\phi$ passes the Monte Carlo test and is accepted. When this is done a large number of times, it generates a particle distribution. These distributions are then fit to Equations 4.3 and 4.5 to extract the various v_2 parameters. These parameters agreed with the input parameters within the fit error so the equations were considered verified. This Monte Carlo simulation verifies the equations but does not include an isolation cut.

Since Reference [52] was published, the simulation was improved to mock up the isolation cut in one dimension. This is acceptable because flow only depends on the azimuthal angle of the particle. In this more sophisticated simulation, we generate values of the reaction plane angle the same way it is done in the simple simulation; the associated particle ϕ values are sampled according to the reaction plane angle and the $1 + 2v_{2A} \cos 2\Delta\phi$ distribution. The trigger $\Delta\phi$ is subject to a different test this time. Once it is determined to be in the PHENIX acceptance, a random number is generated according to a Poisson distribution with the mean

$$P_{mean} = 10 \times \left(1 + 2v_{2U} \cos(2(\phi_T - \phi_{RP})) \right) \\ \times \frac{\int_{\phi_T-0.2}^{\phi_T+0.2} \left(1 + 2v_{2T} \cos(2(\phi_T - \phi_{RP})) \right) d(\phi_T - \phi_{RP})}{0.4}. \quad (4.9)$$

Poissonian numbers were used because they emulate the isolation cone energy distributions observed in the data. This exact form for the mean was chosen for a few reasons: the integral

provides for a one dimensional isolation cut with a width of 0.4, the efficiency is given by the term before the integral, v_{2U} is an input value that is similar to the underlying event v_2 , and the factor of 10 ensures the distribution is similar to the energy distribution of the isolation cones in the data.

If the Poissonian generated number is less than a cutoff value, the trigger is accepted. The cut off value is determined such that the number of accepted triggers is 70% of the total generated triggers, this is

$$N_{\text{Poisson}} \leq N_{\text{cut}} = \frac{\text{accepted triggers}}{\text{all triggers}} \approx 0.7. \quad (4.10)$$

We use the number of particles as a proxy for energy in this simulation because the more particles in a region, the higher the energy in that region. The value of 70% was chosen to resemble the average efficiency of the isolation cones in the data. This simulation is used later in this Chapter to verify other derivations.

4.2.1 Finding v_{2E}

As we include a realistic ϕ acceptance in the Monte Carlo, we employ the following method to measure v_{2E} in the simulation that is then mimicked in the data. The process is recorded in Figure 4.1. This figure is for illustrative purposes only, one should not read the axis labels literally. We record ϕ , Ψ_{RP} , $\Delta\phi = \phi - \Psi_{RP}$ for the isolated particles (Figure 4.1a,b,e) as well as of all of the particles (Figure 4.1c,d,g). Then we find the acceptance function for both cases by convoluting the ϕ and Ψ_{RP} distributions; the result is shown in Figure 4.1f (for isolated) and h (for all). We divide the raw $\Delta\phi$ distributions by their respective acceptance functions to correct them and obtain Figure 4.1i (for isolated) and j (for all). We then divide the isolated-particle-corrected $\Delta\phi$ distribution by the $\Delta\phi$ distribution all the particles and get Figure 4.1k. We fit the result in this figure to Equation 4.2 in order to extract v_{2E} .

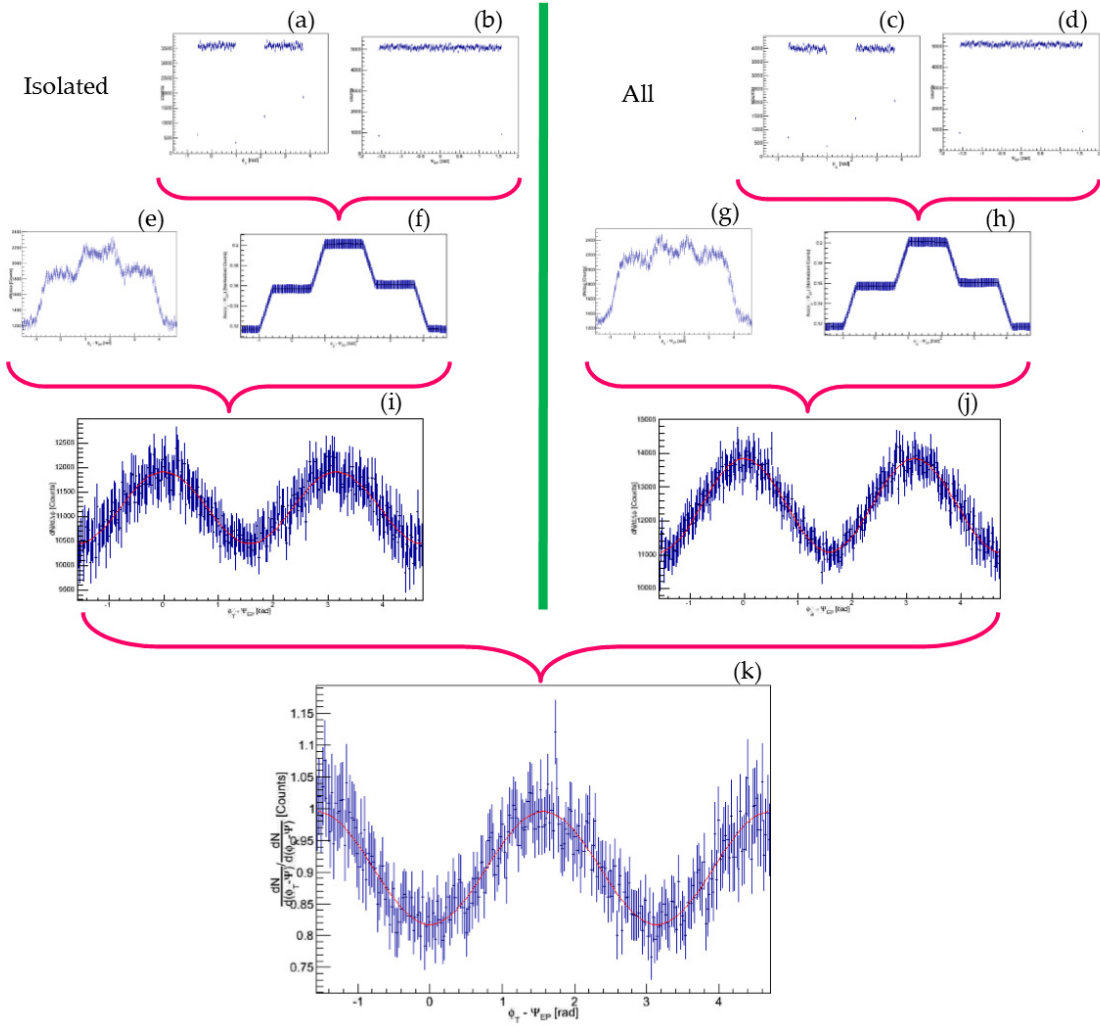


Figure 4.1: The steps we follow to obtain v_{2E} . Left of the green line is the isolated particles' histograms while on the right is that of all of the particles. The ϕ plots ((a) and (c)) are convoluted with the ϕ_{RP} plots ((b) and (d)) to get the acceptance correction ((f) and (h)). We then divide the raw $\Delta\phi = \phi - \Psi_{RP}$ plots ((e) and (g)) by the acceptance correction to get the corrected $\Delta\phi$ distributions ((i) and (j)). We extract the v_{2E} by fitting the final plot formed by dividing the isolated $\Delta\phi$ (i) by all the $\Delta\phi$ (j) to Equation 4.2 (red line). This figure is for illustrative purposes only, for this reason we have left the plots and axis labels small.

The simulation was done for many input v_{2T} and v_{2E} values. The fit parameters were then plotted as a function of input v_{2T} . This is shown in Figure 4.2. This figure shows the fit parameters

of Equation 4.3 as a function of input v_{2T} with a fixed $v_{2E} = -0.05$. The fit values are the open circles, the squares are the true input values, and the triangles are the ratio of the fit value to the true value. It is difficult to see the fit values because the input value markers have been drawn over them. All of the ratios are very close to unity. Error bars are drawn on the fit and ratio values; most are smaller than the marker size. This verifies that Equation 4.3 works, even for extreme v_{2T} .

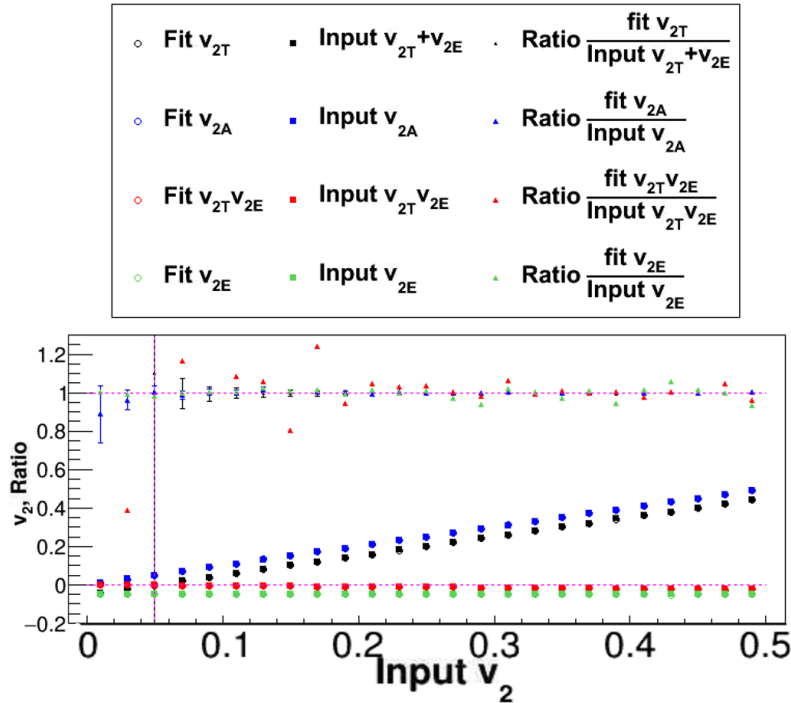


Figure 4.2: Example of agreement of the parameters in Equation 4.3 to the Monte Carlo simulation input parameters. Specifically, fit parameters of Equation 4.3 as a function of input v_{2T} with a fixed $v_{2E} = -0.05$. The vertical magenta line is the absolute value of v_{2E} . The fit values are the open circles, the squares are the true input values, and the triangles near $y = 1$ are the ratio of the fit value to the true value.

Equation 4.5 is further verified by varying input v_{2T} and looking at the fit parameters. This is shown in Figure 4.3 for fixed $v_{2E} = -0.05$. The open circles are the fit values, the squares are the

input true values and the triangles are the ratio of the two. One can see that the ratios are close to unity for most v_{2T} . For v_{2T} less than 0.1 the ratios blow up because the input v_{2T} is small.

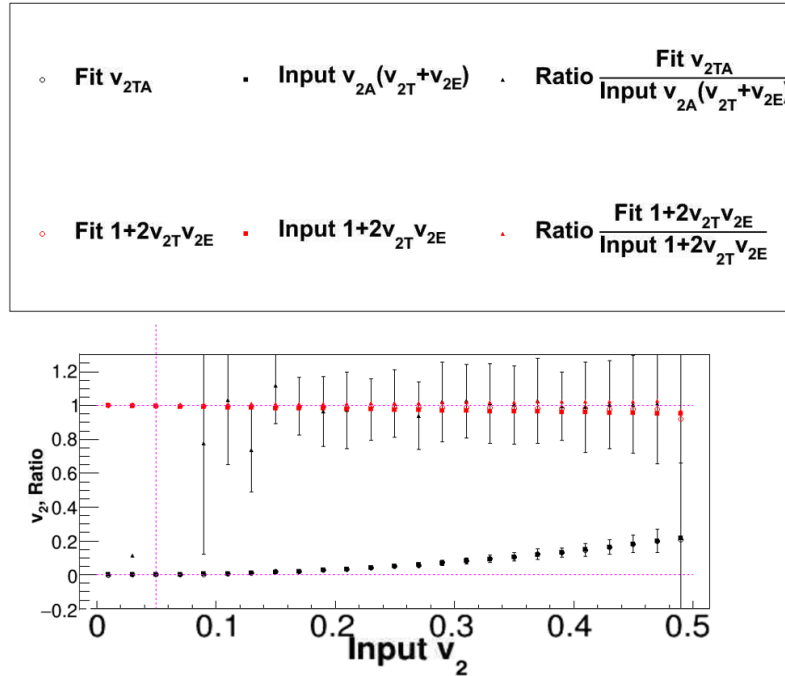


Figure 4.3: Example of agreement of the parameters in Equation 4.5 to the Monte Carlo simulation input parameters. Specifically, fit parameters of Equation 4.5 as a function of input v_{2T} with a fixed $v_{2E} = -0.05$. The vertical magenta line is the absolute value of v_{2E} . The fit values are the open circles, the squares are the true input values, and the triangles near $y = 1$ are the ratio of the fit value to the truth value.

This exercise confirms that the correct amplitudes to use for the γ_{dir} -h correlation background shape (Equation 1.13) is not just $v_{2A}v_{2T}$, but $v_{2A}(v_{2T} + v_{2E})$.

4.3 Derivation of Reaction Plane Efficiency Trigger Distribution With Event Plane Resolution

The above results are correct for perfect reaction planes but experiments do not measure perfect reaction planes, they measure event planes with some resolution. Next, we re-derive the

above equations for event planes with finite resolution. If one assumes smearing on both the trigger distribution and the reaction plane efficiency, one starts with

$$\frac{dN_{ST}}{d\Delta\phi} = 1 + 2v_{2T} \cos(2(\Delta\phi - \Delta\Psi)), \quad (4.11)$$

and

$$\frac{dN_{SE}}{d\Delta\phi} = 1 + 2v_{2E} \cos(2(\Delta\phi - \Delta\Psi)), \quad (4.12)$$

where $\Delta\phi = \phi_T - \Psi_{EP}$, $\Delta\Psi = \Psi_{RP} - \Psi_{EP}$, and the subscripts ST and SE signify smeared trigger and smeared efficiency, respectively. As stated in Chapter 1, the probability distribution of $\delta\Psi$ is given by

$$\frac{dN}{d(2\delta\Psi)} = \frac{1}{\pi} e^{-\frac{\chi^2}{2}} \left[1 + z \sqrt{\pi} e^{z^2} (1 + \text{erf}(z)) \right], \quad (4.13)$$

where $z = \frac{1}{\sqrt{2}}\chi \cos(2\delta\Psi)$, χ is a constant parameter, and erf is the standard error function. This equation is discussed in more detail in the next section.

The correlation function is

$$\frac{dN_{STSE}}{d\Delta\phi} = \int_0^{2\pi} d\Delta\phi \int_{-\frac{\pi}{2}}^{\frac{\pi}{2}} d\delta\Psi \frac{dN_{ST}}{d\Delta\phi} \frac{dN_{SE}}{d\Delta\phi} \frac{dN}{d2\delta\Psi} \text{Acc}(\Delta\phi) \text{Acc}(\delta\Psi) \delta(\Delta\phi - (\Delta\phi - \delta\Psi)) \quad (4.14)$$

where $\text{Acc}(\Delta\phi)$ and $\text{Acc}(\delta\Psi)$ are the acceptance functions of $\Delta\phi$ and $\delta\Psi$, and

$$\begin{aligned} \frac{dN_{ST}}{d\Delta\phi} \frac{dN_{SE}}{d\Delta\phi} &= \left(1 + 2v_{2T} \cos(2(\Delta\phi - \Delta\Psi)) \right) \left(1 + 2v_{2E} \cos(2(\Delta\phi - \Delta\Psi)) \right), \\ &= 1 + 2v_{2T} \cos(2(\Delta\phi - \Delta\Psi)) + 2v_{2E} \cos(2(\Delta\phi - \Delta\Psi)) \\ &\quad + 4v_{2T}v_{2E} \cos^2(2(\Delta\phi - \Delta\Psi)). \end{aligned} \quad (4.15)$$

Using the identity,

$$\cos(a - b) = \cos(a)\cos(b) + \sin(a)\sin(b), \quad (4.16)$$

Equation 4.15 becomes

$$\begin{aligned} \frac{dN_{ST}}{d\Delta\phi} \frac{dN_{SE}}{d\Delta\phi} &= 1 + 2v_{2T} \left(\cos(2\Delta\phi) \cos(2\delta\Psi) + \sin(2\Delta\phi) \sin(2\delta\Psi) \right) \\ &\quad + 2v_{2E} \left(\cos(2\Delta\phi) \cos(2\delta\Psi) + \sin(2\Delta\phi) \sin(2\delta\Psi) \right) \\ &\quad + 4v_{2T}v_{2E} \left(\cos^2(2\Delta\phi) \cos^2(2\delta\Psi) + \sin^2(2\Delta\phi) \sin^2(2\delta\Psi) \right. \\ &\quad \left. + 2 \cos(2\Delta\phi) \cos(2\delta\Psi) \sin(2\Delta\phi) \sin(2\delta\Psi) \right). \end{aligned} \quad (4.17)$$

Inserting this in Equation 4.14 and the following

$$\int_{-\frac{\pi}{2}}^{\frac{\pi}{2}} \frac{dN}{d(2\delta\Psi)} \cos(2\delta\Psi) d\delta\Psi = \langle \cos(2\delta\Psi) \rangle, \quad (4.18)$$

and

$$\int_{-\frac{\pi}{2}}^{\frac{\pi}{2}} \frac{dN}{d(2\delta\Psi)} \sin(2\delta\Psi) d\delta\Psi = 0 \quad (4.19)$$

simplifies Equation 4.14 to

$$\begin{aligned} \frac{dN_{STSE}}{d\Delta\phi} &= 1 + 2(v_{2T} + v_{2E}) \cos(2\Delta\phi) \langle \cos(2\delta\Psi) \rangle \\ &+ 4v_{2T}v_{2E} \left(\cos^2(2\Delta\phi) \int_{-\frac{\pi}{2}}^{\frac{\pi}{2}} \frac{dN}{d2\delta\Psi} \cos^2(2\delta\Psi) d\delta\Psi \right. \\ &\quad \left. + \sin^2(2\Delta\phi) \int_{-\frac{\pi}{2}}^{\frac{\pi}{2}} \frac{dN}{d2\delta\Psi} \sin^2(2\delta\Psi) d\delta\Psi \right). \end{aligned} \quad (4.20)$$

Solving the last integral, the $\sin^2(2\delta\Psi)$ integral, and inserting Equation 1.9 the integral becomes

$$\begin{aligned} &\int_{-\frac{\pi}{2}}^{\frac{\pi}{2}} \frac{dN}{d(2\delta\Psi)} \sin^2(2\delta\Psi) d\delta\Psi \\ &= \int_{-\frac{\pi}{2}}^{\frac{\pi}{2}} \frac{1}{\pi} e^{-\frac{\chi^2}{2}} \left[1 + \frac{1}{\sqrt{2}} \chi \cos(2\delta\Psi) \sqrt{\pi} e^{(\frac{1}{\sqrt{2}} \chi \cos(2\delta\Psi))^2} \left(1 + \operatorname{erf}\left(\frac{1}{\sqrt{2}} \chi \cos(2\delta\Psi)\right) \right) \right] \sin^2(2\delta\Psi) d\delta\Psi. \end{aligned} \quad (4.21)$$

Now, define the variables, $x = 2\delta\Psi$ with the limits $-\pi \leq x \leq \pi$ and $dx = 2 d\delta\Psi$; the integral then becomes

$$\begin{aligned}
& \int_{-\frac{\pi}{2}}^{\frac{\pi}{2}} \frac{dN}{d(2\delta\Psi)} \sin^2(2\delta\Psi) d\delta\Psi \\
&= \int_{-\pi}^{\pi} \frac{1}{2\pi} e^{-\frac{x^2}{2}} \left[1 + \frac{1}{\sqrt{2}} \chi \cos(x) \sqrt{\pi} e^{(\frac{1}{\sqrt{2}} \chi \cos(x))^2} \left(1 + \operatorname{erf}\left(\frac{1}{\sqrt{2}} \chi \cos(x)\right) \right) \right] \sin^2(x) dx, \\
&= \frac{1}{2\pi} e^{-\frac{x^2}{2}} \left[\int_{-\pi}^{\pi} \sin^2(x) dx \right. \\
&\quad \left. + \sqrt{\frac{\pi}{2}} \chi \int_{-\pi}^{\pi} \sin^2(x) \cos(x) e^{(\frac{1}{\sqrt{2}} \chi \cos(x))^2} dx \right. \\
&\quad \left. + \sqrt{\frac{\pi}{2}} \chi \int_{-\pi}^{\pi} \sin^2(x) \cos(x) e^{(\frac{1}{\sqrt{2}} \chi \cos(x))^2} \operatorname{erf}\left(\frac{1}{\sqrt{2}} \chi \cos(x)\right) dx \right].
\end{aligned} \tag{4.22}$$

The first integral, $\int \sin^2(x) dx$, equals π . The second integral vanishes because the integrand is even and periodic in 2π . This simplification makes the total $\sin^2(2\delta\Psi)$ integral in Equation 4.20

$$\int_{-\frac{\pi}{2}}^{\frac{\pi}{2}} \frac{dN}{d(2\delta\Psi)} \sin^2(2\delta\Psi) d\delta\Psi = \frac{1}{2\pi} e^{-\frac{x^2}{2}} \left[\pi + \sqrt{\frac{\pi}{2}} \chi \int_{-\pi}^{\pi} \sin^2(x) \cos(x) e^{(\frac{1}{\sqrt{2}} \chi \cos(x))^2} \operatorname{erf}\left(\frac{1}{\sqrt{2}} \chi \cos(x)\right) dx \right] = \mathcal{S}.
\tag{4.23}$$

We will use the variable \mathcal{S} for substitution later in the derivation.

Solving the second to the last integral, the $\cos^2(2\delta\Psi)$ integral of Equation 4.20, and inserting Equation 1.9 the integral becomes

$$\begin{aligned}
& \int_{-\frac{\pi}{2}}^{\frac{\pi}{2}} \frac{dN}{d(2\delta\Psi)} \cos^2(2\delta\Psi) d\delta\Psi \\
&= \int_{-\frac{\pi}{2}}^{\frac{\pi}{2}} \frac{1}{\pi} e^{-\frac{x^2}{2}} \left[1 + \frac{1}{\sqrt{2}} \chi \cos(2\delta\Psi) \sqrt{\pi} e^{(\frac{1}{\sqrt{2}} \chi \cos(2\delta\Psi))^2} \left(1 + \operatorname{erf}\left(\frac{1}{\sqrt{2}} \chi \cos(2\delta\Psi)\right) \right) \right] \cos^2(2\delta\Psi) d\delta\Psi.
\end{aligned} \tag{4.24}$$

Using $x = 2\delta\Psi$ with the limits $-\pi \leq x \leq \pi$, the integral becomes

$$\begin{aligned}
& \int_{-\frac{\pi}{2}}^{\frac{\pi}{2}} \frac{dN}{d(2\delta\Psi)} \cos^2(2\delta\Psi) d(\delta\Psi) \\
&= \int_{-\pi}^{\pi} \frac{1}{2\pi} e^{-\frac{x^2}{2}} \left[1 + \frac{1}{\sqrt{2}} \chi \cos(x) \sqrt{\pi} e^{(\frac{1}{\sqrt{2}} \chi \cos(x))^2} \left(1 + \operatorname{erf}\left(\frac{1}{\sqrt{2}} \chi \cos(x)\right) \right) \right] \cos^2(x) dx, \\
&= \frac{1}{2\pi} e^{-\frac{x^2}{2}} \left[\int_{-\pi}^{\pi} \cos^2(x) dx \right. \\
&\quad \left. + \sqrt{\frac{\pi}{2}} \chi \int_{-\pi}^{\pi} \cos^3(x) e^{(\frac{1}{\sqrt{2}} \chi \cos(x))^2} dx \right. \\
&\quad \left. + \sqrt{\frac{\pi}{2}} \chi \int_{-\pi}^{\pi} \cos^3(x) e^{(\frac{1}{\sqrt{2}} \chi \cos(x))^2} \operatorname{erf}\left(\frac{1}{\sqrt{2}} \chi \cos(x)\right) dx \right].
\end{aligned} \tag{4.25}$$

The first integral, $\int \cos^2(x) dx$, equals π . The second integral vanishes because the integrand is even and periodic in 2π . This simplification makes the total $\cos^2(2\delta\Psi)$ integral in Equation 4.20

$$\int_{-\frac{\pi}{2}}^{\frac{\pi}{2}} \frac{dN}{d(2\delta\Psi)} \cos^2(2\delta\Psi) d\delta\Psi = \frac{1}{2\pi} e^{-\frac{x^2}{2}} \left[\pi + \sqrt{\frac{\pi}{2}} \chi \int_{-\pi}^{\pi} \cos^3(x) e^{(\frac{1}{\sqrt{2}} \chi \cos(x))^2} \operatorname{erf}\left(\frac{1}{\sqrt{2}} \chi \cos(x)\right) dx \right] = \mathcal{C}. \tag{4.26}$$

We will use the variable \mathcal{C} for substitution later in the derivation.

Combining Equation 4.23 and Equation 4.26 together with Equation 4.20, we arrive at

$$\begin{aligned}
\frac{dN_{STSE}}{d\Delta\phi} &= 1 + 2(v_{2T} + v_{2E}) \cos(2\Delta\phi) \langle \cos(2\delta\Psi) \rangle \\
&\quad + \frac{2}{\pi} v_{2T} v_{2E} e^{-\frac{x^2}{2}} \left(\cos^2(2\Delta\phi) \left(\pi + \sqrt{\frac{\pi}{2}} \chi \int_{-\pi}^{\pi} \cos^3(x) e^{(\frac{1}{\sqrt{2}} \chi \cos(x))^2} \operatorname{erf}\left(\frac{1}{\sqrt{2}} \chi \cos(x)\right) dx \right) \right. \\
&\quad \left. + \sin^2(2\Delta\phi) \left(\pi + \sqrt{\frac{\pi}{2}} \chi \int_{-\pi}^{\pi} \sin^2(x) \cos(x) e^{(\frac{1}{\sqrt{2}} \chi \cos(x))^2} \operatorname{erf}\left(\frac{1}{\sqrt{2}} \chi \cos(x)\right) dx \right) \right) \\
&= 1 + 2(v_{2T} + v_{2E}) \cos(2\Delta\phi) \langle \cos(2\delta\Psi) \rangle + 4v_{2T} v_{2E} (\mathcal{C} \cos^2(2\Delta\phi) + \mathcal{S} \sin^2(2\Delta\phi)),
\end{aligned} \tag{4.27}$$

where for the last equality we have substituted \mathcal{S} and \mathcal{C} for Equations 4.23 and 4.26.

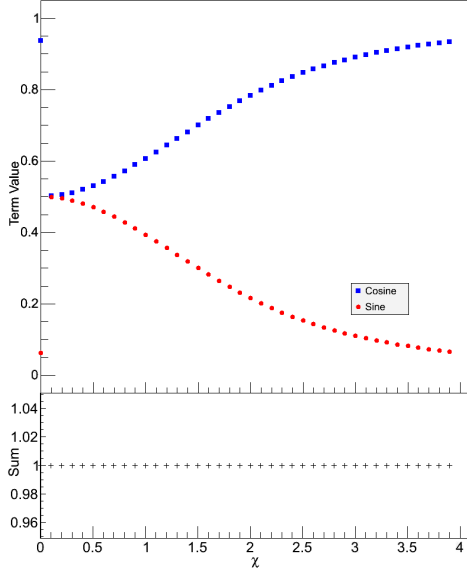


Figure 4.4: (Upper panel) \mathcal{S} and \mathcal{C} terms of Equation 4.27 are shown as a function of χ and the sum (lower panel) for $0 \leq \chi \leq 4$.

The \mathcal{S} (Equations 4.23) and \mathcal{C} (Equation 4.26) terms of Equation 4.27 are shown as a function of χ in Figure 4.4. Note that as χ gets larger, the cosine term (labeled Cosine (blue points)) increases while the sine term (labeled Sine (red points)) decreases. The lower panel of Figure 4.4 shows that $\mathcal{C} + \mathcal{S} = 1$. This allows Equation 4.27 to be further rewritten by substitution of $1 - \mathcal{S}$ for \mathcal{C} , that is,

$$\begin{aligned}
\frac{dN_{STSE}}{d\Delta\phi} &= 1 + 2(v_{2T} + v_{2E}) \cos(2\Delta\phi) \langle \cos(2\delta\Psi) \rangle + 4v_{2T}v_{2E} \left((1 - \mathcal{S}) \cos^2(2\Delta\phi) + \mathcal{S} \sin^2(2\Delta\phi) \right), \\
&= 1 + 2(v_{2T} + v_{2E}) \cos(2\Delta\phi) \langle \cos(2\delta\Psi) \rangle + 4v_{2T}v_{2E} \left(\cos^2(2\Delta\phi) - \mathcal{S} \cos^2(2\Delta\phi) + \mathcal{S} \sin^2(2\Delta\phi) \right), \\
&= 1 + 2(v_{2T} + v_{2E}) \cos(2\Delta\phi) \langle \cos(2\delta\Psi) \rangle + 4v_{2T}v_{2E} \left(\cos^2(2\Delta\phi) + \mathcal{S}(\sin^2(2\Delta\phi) - \cos^2(2\Delta\phi)) \right), \\
&= 1 + 2(v_{2T} + v_{2E}) \cos(2\Delta\phi) \langle \cos(2\delta\Psi) \rangle + 4v_{2T}v_{2E} \cos^2(2\Delta\phi) - 4v_{2T}v_{2E}\mathcal{S} \cos(4\Delta\phi).
\end{aligned} \tag{4.28}$$

For the last equality, we have used the trigonometric identity, $\sin^2(2\Delta\phi) - \cos^2(2\Delta\phi) = -\cos(4\Delta\phi)$. This final form of this equation can be used as the fit function to the smeared trigger distribution

in our simulation. That is, we fit using

$$\frac{dN_{STSE}}{d\Delta\phi} = \mathcal{I} \left(1 + 2\mathcal{J} \cos(2\Delta\phi) + \mathcal{K} \cos^2(2\Delta\phi) - 4\mathcal{L} \cos(4\Delta\phi) \right), \quad (4.29)$$

where \mathcal{I} is a normalization factor and the other parameters are

$$\begin{aligned} \mathcal{J} &= (v_{2T} + v_{2E}) \langle \cos(2\delta\Psi) \rangle, \\ \mathcal{K} &= v_{2T} v_{2E}, \text{ and} \\ \mathcal{L} &= \frac{1}{2\pi} v_{2T} v_{2E} e^{-\frac{\chi^2}{2}} \left[\pi + \sqrt{\frac{\pi}{2}} \chi \int_{-\pi}^{\pi} \sin^2(x) \cos(x) e^{(\frac{1}{\sqrt{2}}\chi \cos(x))^2} \operatorname{erf}\left(\frac{1}{\sqrt{2}}\chi \cos(x)\right) dx \right]. \end{aligned} \quad (4.30)$$

The parameters \mathcal{K} and \mathcal{L} depend on the product $v_{2T} v_{2E}$; each of these values is smaller than one so the product is even smaller. These terms should not be dominant unless $|v_{2T}| = |v_{2E}|$. Equation 4.29 can now be verified in a simulation (see Section 4.4) and used in the Au+Au data (see Chapter 5 and 6).

4.4 Confirmation of Reaction Plane Efficiency Trigger Distribution With Event Plane Resolution

This section is devoted to testing Equation 4.29 using the simulation explained earlier in this Chapter. To make event planes in the simulation, we must smear the thrown reaction plane angles in order to mimic detector response.

4.4.1 Smearing

The probability distribution of the reaction plane angle with resolution smearing is given by Equation 1.9, written again here for convenience:

$$\frac{dN}{d(2\delta\Psi)} = \frac{1}{\pi} e^{-\frac{\chi^2}{2}} \left[1 + z \sqrt{\pi} e^{z^2} (1 + \operatorname{erf}(z)) \right], \quad (4.31)$$

where $z = \frac{1}{\sqrt{2}}\chi \cos(2\delta\Psi)$, χ is a constant parameter, $\delta\Psi = \Psi_{RP} - \Psi_{EP}$, where Ψ_{EP} is the measured second order event plane, Ψ_{RP} is the second order reaction plane, and erf is the standard error function [12, 48]. This function for a few values of χ is shown in Figure 1.7 and is normalized

such that

$$\int_{-\frac{\pi}{2}}^{\frac{\pi}{2}} d\delta\Psi \frac{dN}{d\delta\Psi} = 1. \quad (4.32)$$

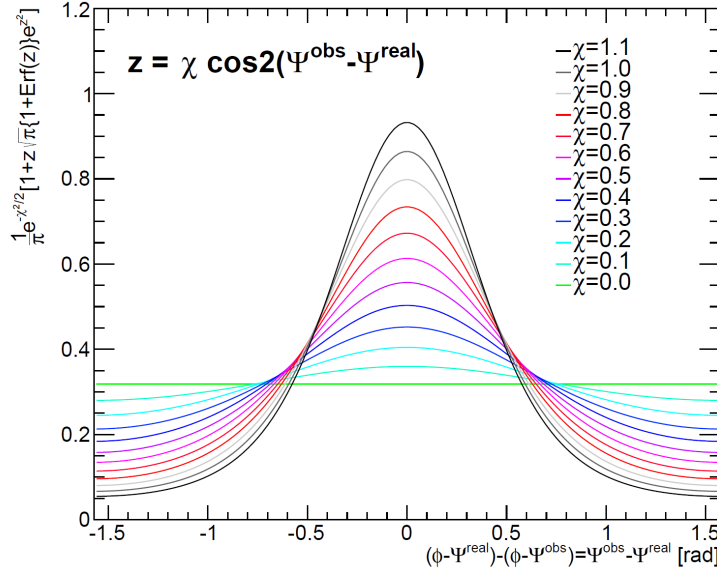


Figure 4.5: The probability distribution of the reaction plane, Equation 1.9, for a few values of χ [12].

We smear uniformly distributed reaction planes (Figure 4.6a) according to Equation 1.9 to make event planes (Figure 4.6b). This is carried out by adding the reaction plane angle to a random number taken from the probability distribution (Equation 1.9). If this angle is less than $-\frac{\pi}{2}$ then $\frac{\pi}{2}$ is added to it, if it is greater than $\frac{\pi}{2}$ then $\frac{\pi}{2}$ is subtracted from it to ensure that $-\frac{\pi}{2} \leq \Psi_{EP} \leq \frac{\pi}{2}$. The resolution of these planes can be calculated two ways, using Equation 1.10 or by just calculating the average directly (left side of Equation 1.8). We have verified that both methods gives the same value.

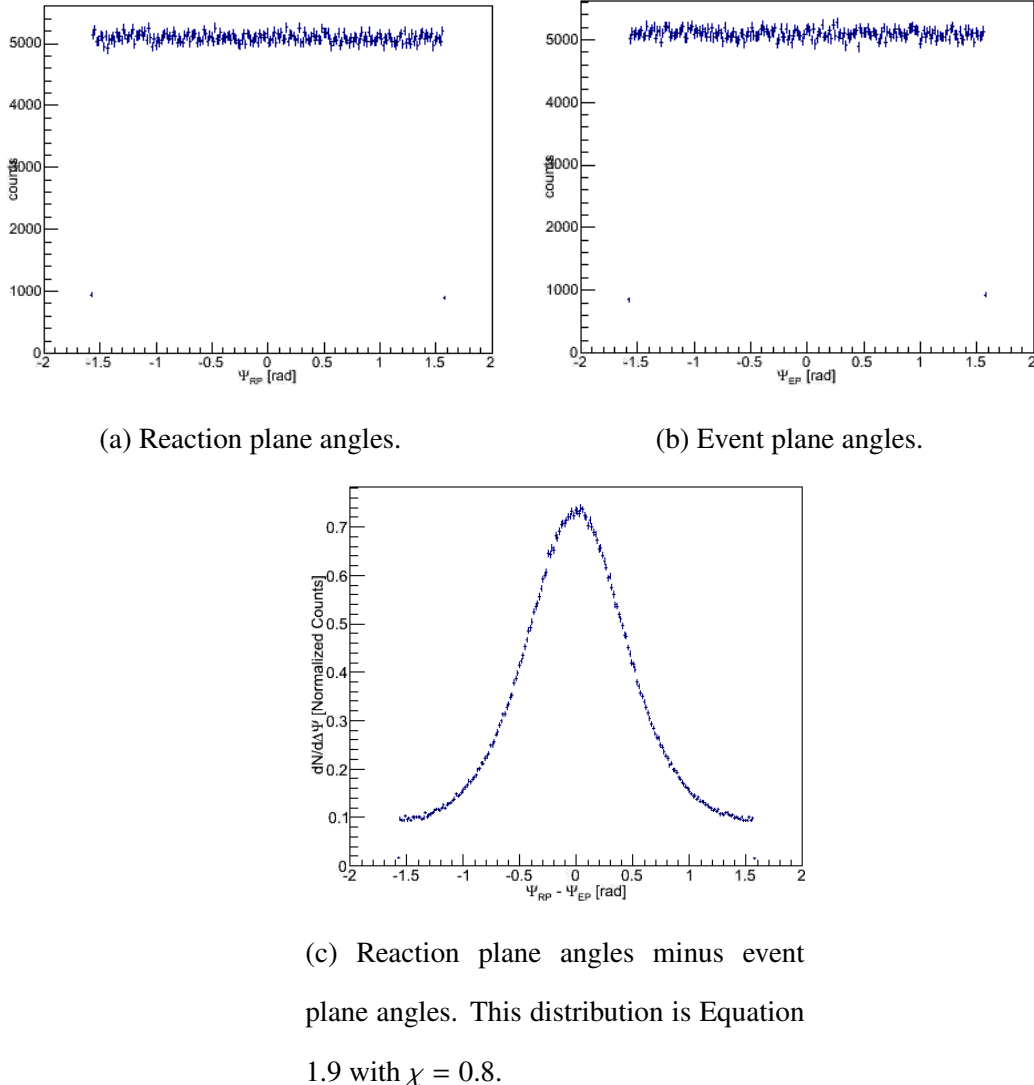


Figure 4.6: Reaction (a) and event (b) plane angles. Reaction planes are generated uniformly from $-\frac{\pi}{2} \leq \Psi_{RP} \leq \frac{\pi}{2}$ and smeared according to Equation 1.9. The $\Delta\Psi = \Psi_{RP} - \Psi_{EP}$ distribution is shown in (c).

These event planes are then used to generate a $\Delta\phi = \phi_T - \Psi_{EP}$ distribution as shown in Figure 4.7. The trigger angles undergo the same Monte Carlo algorithm described earlier in this Chapter. It is this $\Delta\phi$ distribution that is fit with Equation 4.29 (the red line in Figure 4.7). The fit parameters are extracted and they match their expected values.

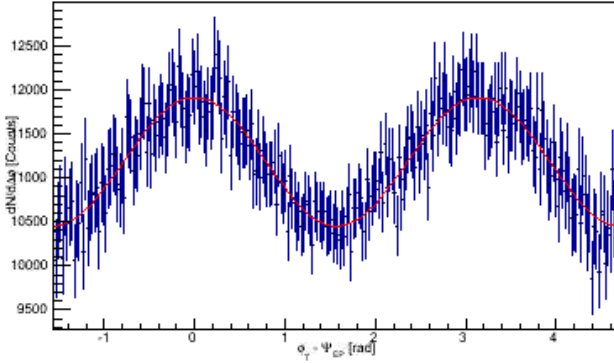


Figure 4.7: $\Delta\phi = \phi_T - \Psi_{EP}$ distribution, generated using event planes from Figure 4.6b with $v_{2T} = 0.12$ and $v_{2E} = 0.05$, and fit to Equation 4.29 (red line).

Figure 4.8 shows these fit parameters as a function of input v_{2T} , for a fixed input v_{2E} . The vertical magenta line is the absolute value of v_{2E} . Here, the resolution is a fixed value, determined by choosing $\chi = 0.8$ in Equations 1.10 and 1.9. Each color is a different parameter, the open circles are the fit values that are output from the simulation, the squares are the values that are input to the simulation by choosing v_{2T} and v_{2E} and the triangles are the ratio of the two. The $v_{2T}v_{2E}$ and \mathcal{L} points fluctuate and have error bars drawn on them because they crowd the plot, but the error bars show that the points are consistent with unity. Section 4.5 contains more tests on Equation 4.5 and Equation 4.29.

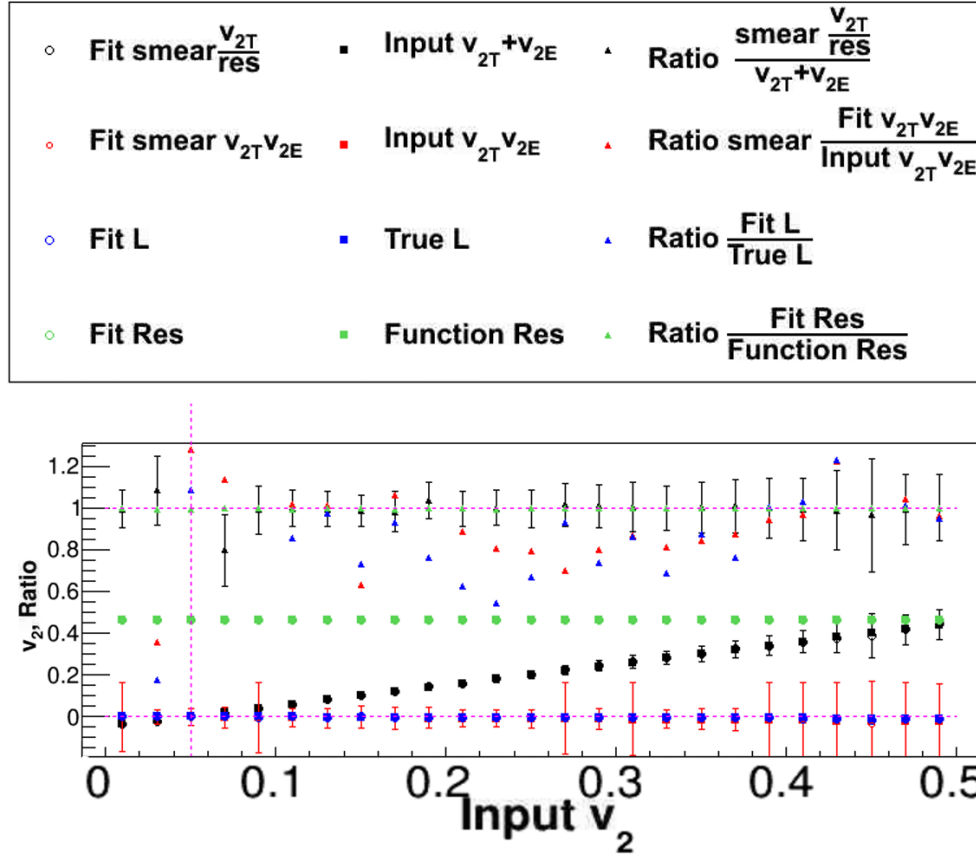


Figure 4.8: Example of agreement of the parameters in Equation 4.29 to the Monte Carlo simulation input parameters. Specifically, fit parameters of Equation 4.29 as a function of input v_{2T} with a fixed $v_{2E} = -0.05$ and $\chi = 0.8$. The vertical magenta line is the absolute value of v_{2E} . The fit values are the open circles, the squares are the true input values, and the triangles near $y = 1$ are the ratio of the fit value to the true value.

4.5 Special Cases

This section is devoted to fitting the various $\Delta\phi$ distributions under special cases. The first subsection is devoted to what these distributions look like and how the fit parameters behave when the input $v_{2T} = v_{2E}$. The second subsection describes what happens when the input $v_{2E} > v_{2T}$. The third section is for $v_{2E} = 0$. Finally, the last section is devoted to looking at the fit parameters as a function of v_{2T} for different v_{2E} and χ values.

4.5.1 $|v_{2T}| = |v_{2E}|$

When $|v_{2T}| = |v_{2E}|$, the v_2 parameter of the fit equations (Equations 4.3, 4.5, and 4.29) is expected to be 0. To test this case, we choose $|v_{2T}| = 0.21$, $v_{2E} = -0.21$, and $\chi = 1.0$. This value of χ corresponds to $\langle \cos(2\delta\Psi) \rangle = 0.56$. The $\Delta\phi = \phi_T - \Psi_{RP}$ distribution is shown in Figure 4.9, the red line is the fit to Equation 4.3. One can see that there is a large $\cos^2(2\Delta\phi)$ dependence on this fit. The fit parameters are summarized in Table 4.1.

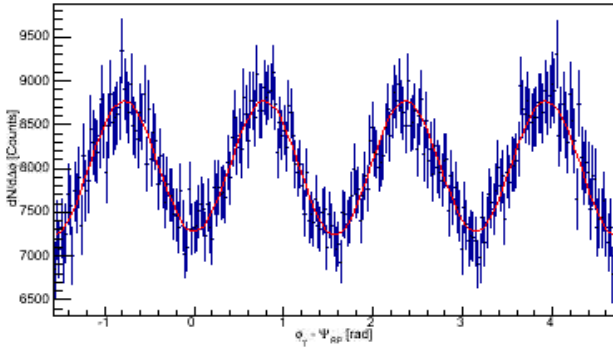


Figure 4.9: $\Delta\phi = \phi_T - \Psi_{RP}$ distribution for $|v_{2T}| = 0.21$ and $v_{2E} = -0.21$. The red line is a fit to Equation 4.3, the fit parameters are summarized in Table 4.1.

The trigger-associated particle distribution with $|v_{2T}| = 0.21$ and $v_{2E} = -0.21$ is shown in Figure 4.10. The associated particles have $v_{2A} = 0.21$. The red line in Figure 4.10 is the fit to Equation 4.5. It can be observed that this distribution is flat, which implies there is an almost negligible dependence on $\cos(2\Delta\phi)$. The fit parameters are summarized in Table 4.1.

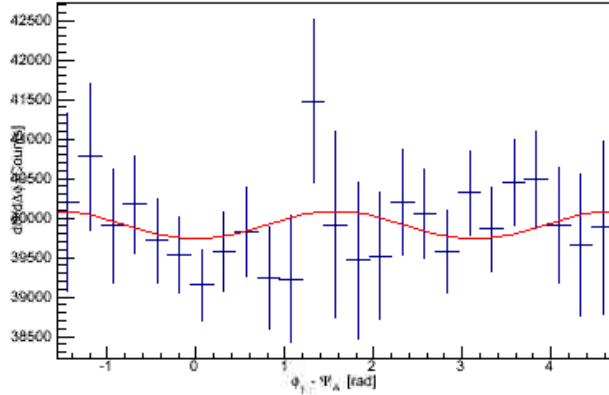


Figure 4.10: $\Delta\phi = \phi_T - \phi_A$ distribution for $|v_{2T}| = 0.21$ and $v_{2E} = -0.21$. The red line is a fit to Equation 4.5, the fit parameters are summarized in Table 4.1.

Figure 4.11 shows the $\Delta\phi = \phi_T - \Psi_{EP}$ distribution with $|v_{2T}| = |v_{2E}| = 0.21$ and $\chi = 1.0$. The red line is the fit to Equation 4.29. There is a large $\cos^2(2\Delta\phi)$ and $\cos(4\Delta\phi)$ dependence on this fit with an almost negligible dependence on $\cos(2\Delta\phi)$. The fit parameters are summarized in Table 4.1.

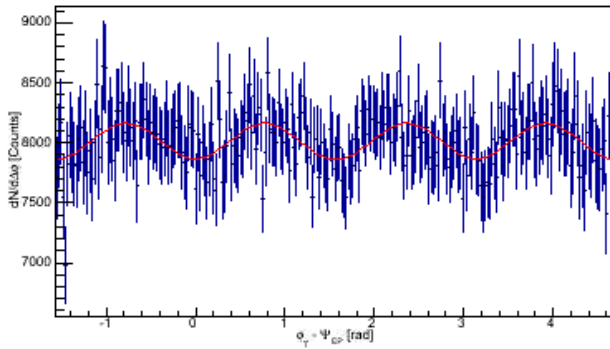


Figure 4.11: $\Delta\phi = \phi_T - \Psi_{EP}$ distribution for $|v_{2T}| = 0.21$, $v_{2E} = -0.21$ and $\chi = 1.0$. The red line is a fit to Equation 4.29, the fit parameters are summarized in Table 4.1.

Table 4.1: Input and fit parameters from the fits of Equations 4.3, 4.5, and 4.29 to Figures 4.9, 4.10, and 4.11, respectively. For the case $v_{2T} = 0.21$, $v_{2E} = -0.21$ and $\chi = 1.0$.

Distribution	Parameter	Fit value	Input value
$\frac{dN_{TE}}{d\Delta\phi}$	$\mathcal{B} = v_{2T} + v_{2E}$	0.0012 (10)	0
	$\mathcal{C} = v_{2T}v_{2E}$	-0.0431 (14)	-0.044
$\frac{dN_{TA}}{d\Delta\phi}$	$\mathcal{G} = 1 + 2v_{2T}v_{2E}$	0.9754 (4722)	0.9118
	$\mathcal{H} = v_{2A}(v_{2T} + v_{2E})$	-0.0021 (26)	0
$\mathcal{J} = (v_{2T} + v_{2E})\langle \cos(2\delta\Psi) \rangle$		0.0006 (28)	0
$\frac{dN_{STSE}}{d\Delta\phi}$	$\mathcal{K} = v_{2T}v_{2E}$	-0.0438 (2200)	-0.044
\mathcal{L} (see Equation 4.30)		-0.0177 (926)	-0.0174

4.5.2 $|v_{2E}| > |v_{2T}|$

To observe what happens to the various $\Delta\phi$ distributions when $|v_{2T}| < |v_{2E}|$ we choose $v_{2T} = 0.11$, $v_{2E} = 0.21$, and $\chi = 1.6$. This value of χ corresponds to $\langle \cos(2\delta\Psi) \rangle = 0.76$. The $\Delta\phi = \phi_T - \Psi_{RP}$ distribution is shown in Figure 4.12, the red line is the fit to Equation 4.3. Instead of the fit having peaks at 0 and π , the distribution now has troughs. The fit parameters are summarized in Table 4.2.

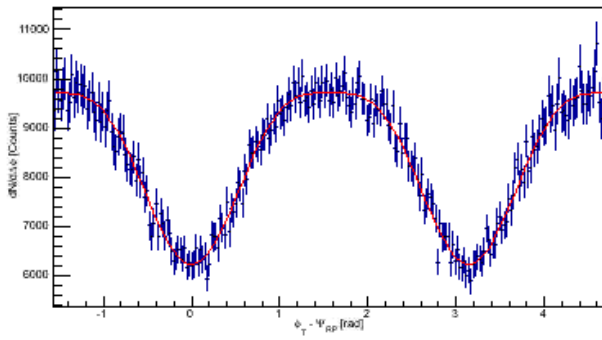


Figure 4.12: $\Delta\phi = \phi_T - \Psi_{RP}$ distribution for $v_{2T} = 0.11$ and $v_{2E} = 0.21$. The red line is a fit to Equation 4.3, the fit parameters are summarized in Table 4.2.

The trigger-associated particle distribution with $v_{2T} = 0.11$ and $v_{2E} = 0.21$ is shown in Figure 4.13. The associated particles have $v_{2A} = 0.11$. The red line in Figure 4.13 is the fit to Equation 4.5. The fit parameters are summarized in Table 4.2.

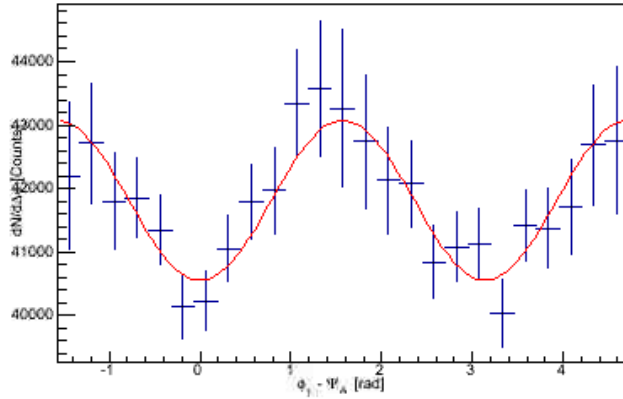


Figure 4.13: $\Delta\phi = \phi_T - \phi_A$ distribution for $v_{2T} = 0.11$ and $v_{2E} = -0.21$. The red line is a fit to Equation 4.5, the fit parameters are summarized in Table 4.2.

Figure 4.14 shows the $\Delta\phi = \phi_T - \Psi_{EP}$ distribution with $v_{2T} = 0.11$ and $v_{2E} = 0.21$ and $\chi = 1.6$. The red line is the fit to Equation 4.29. The fit parameters are summarized in Table 4.2.

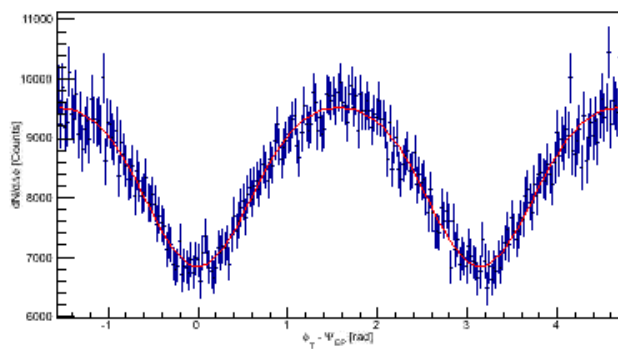


Figure 4.14: $\Delta\phi = \phi_T - \Psi_{EP}$ distribution for $v_{2T} = 0.11$ and $v_{2E} = -0.21$ with $\chi = 1.6$. The red line is a fit to Equation 4.29, the fit parameters are summarized in Table 4.2.

Table 4.2: Input and fit parameters from the fits of Equations 4.3, 4.5, and 4.29 to Figures 4.12, 4.13, and 4.14, respectively. For the case $v_{2T} = 0.11$, $v_{2E} = -0.21$, and $\chi = 1.6$.

Distribution	Parameter	Fit value	Input value
$\frac{dN_{TE}}{d\Delta\phi}$	$\mathcal{B} = v_{2T} + v_{2E}$	-0.0995 (16)	-0.1
	$C = v_{2T}v_{2E}$	-0.0220 (15)	-0.0231
$\frac{dN_{TA}}{d\Delta\phi}$	$\mathcal{G} = 1 + 2v_{2T}v_{2E}$	0.9875 (4920)	0.9538
	$\mathcal{H} = v_{2A}(v_{2T} + v_{2E})$	-0.0148 (43)	-0.011
$\frac{dN_{STSE}}{d\Delta\phi}$	$\mathcal{J} = (v_{2T} + v_{2E})\langle \cos(2\delta\Psi) \rangle$	-0.1000 (133)	-0.1
	$\mathcal{K} = v_{2T}v_{2E}$	-0.0218 (550)	-0.0231
	\mathcal{L} (see Equation 4.30)	-0.0056 (447)	-0.0065

4.5.3 $v_{2E} = 0$

If $v_{2E} = 0$, we should recover the typical correlation functions. To verify this we choose $v_{2T} = 0.15$, $v_{2E} = 0$, and $\chi = 0.8$. This value of χ corresponds to $\langle \cos(2\delta\Psi) \rangle = 0.25$. The $\Delta\phi = \phi_T - \Psi_{RP}$ distribution is shown in Figure 4.15, the red line is the fit to Equation 4.3. This figure exhibits typical flow, the cosine curve is very symmetric. The fit parameters are summarized in Table 4.3.

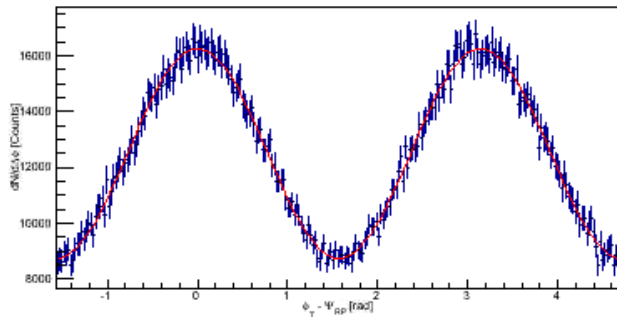


Figure 4.15: $\Delta\phi = \phi_T - \Psi_{RP}$ distribution for $v_{2T} = 0.15$ and $v_{2E} = 0$. The red line is a fit to Equation 4.3, the fit parameters are summarized in Table 4.3.

The trigger-associated particle distribution with $v_{2T} = 0.15$ and $v_{2E} = 0$ is shown in Figure 4.16. The associated particles have $v_{2A} = 0.15$. The red line in Figure 4.16 is the fit to Equation 4.5. The fit parameters are summarized in Table 4.3.

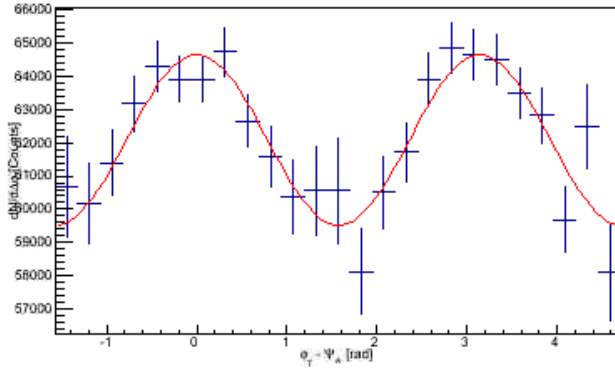


Figure 4.16: $\Delta\phi = \phi_T - \phi_A$ distribution for $v_{2T} = 0.15$ and $v_{2E} = 0$. The red line is a fit to Equation 4.5, the fit parameters are summarized in Table 4.3.

Figure 4.17 shows the $\Delta\phi = \phi_T - \Psi_{EP}$ distribution with $v_{2T} = 0.15$ and $v_{2E} = 0$ and $\chi = 0.8$. The red line is the fit to Equation 4.29. The fit parameters are summarized in Table 4.3.

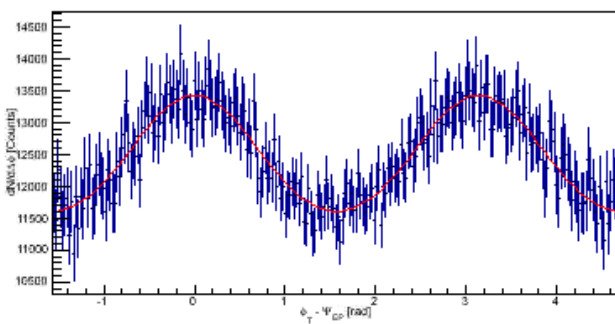


Figure 4.17: $\Delta\phi = \phi_T - \Psi_{EP}$ distribution for $v_{2T} = 0.15$ and $v_{2E} = 0$ with $\chi = 0.8$. The red line is a fit to Equation 4.29, the fit parameters are summarized in Table 4.3.

Table 4.3: Input and fit parameters from the fits of Equations 4.3, 4.5, and 4.29 to Figures 4.15, 4.16, and 4.17, respectively. For the case $v_{2T} = 0.15$, $v_{2E} = 0$, and $\chi = 0.8$.

Distribution	Parameter	Fit value	Input value
$\frac{dN_{TE}}{d\Delta\phi}$	$\mathcal{B} = v_{2T} + v_{2E}$	0.1510 (14)	0.15
	$\mathcal{C} = v_{2T}v_{2E}$	0.0007 (15)	0
$\frac{dN_{TA}}{d\Delta\phi}$	$\mathcal{G} = 1 + 2v_{2T}v_{2E}$	1.0000 (4992)	1
	$\mathcal{H} = v_{2A}(v_{2T} + v_{2E})$	0.0207 (23)	0.0225
	$\mathcal{J} = (v_{2T} + v_{2E})\langle \cos(2\delta\Psi) \rangle$	0.1494 (35)	0.15
$\frac{dN_{TSE}}{d\Delta\phi}$	$\mathcal{K} = v_{2T}v_{2E}$	0.0000 (2353)	0
	\mathcal{L} (see Equation 4.30)	-0.0007 (23)	0

The fit parameters for the three special cases above prove that the new equations work for extreme cases. All of the parameters are consistent with their input values and their error is consistent throughout all three tests.

4.5.4 Fit Parameters for Combinations of v_{2E} and χ

We will now look at the fit parameters over the entire range of v_{2T} , instead of specific cases described above. We examine at the output fit parameters, not the individual $\Delta\phi$ distributions. We trust that the fits are good because of the way they behave in the cases above. For the figures involving the $\Delta\phi = \phi_T - \Psi_{EP}$ fit parameters, each panel corresponds to a different χ value. Starting from the top and going down, they are 20, 1.6, 1.0, 0.8, and 0.4. These χ values correspond to resolutions of 1, 0.76, 0.56, 0.46, and 0.25. We start by choosing $v_{2E} = 0$. The parameters can be seen in Figure 4.18 for the trigger distribution with reaction planes fit to Equation 4.3, Figure 4.19 for the trigger-associated 2-particle fit to Equation 4.5, and Figure 4.20 for the trigger fit with event planes to Equation 4.29.

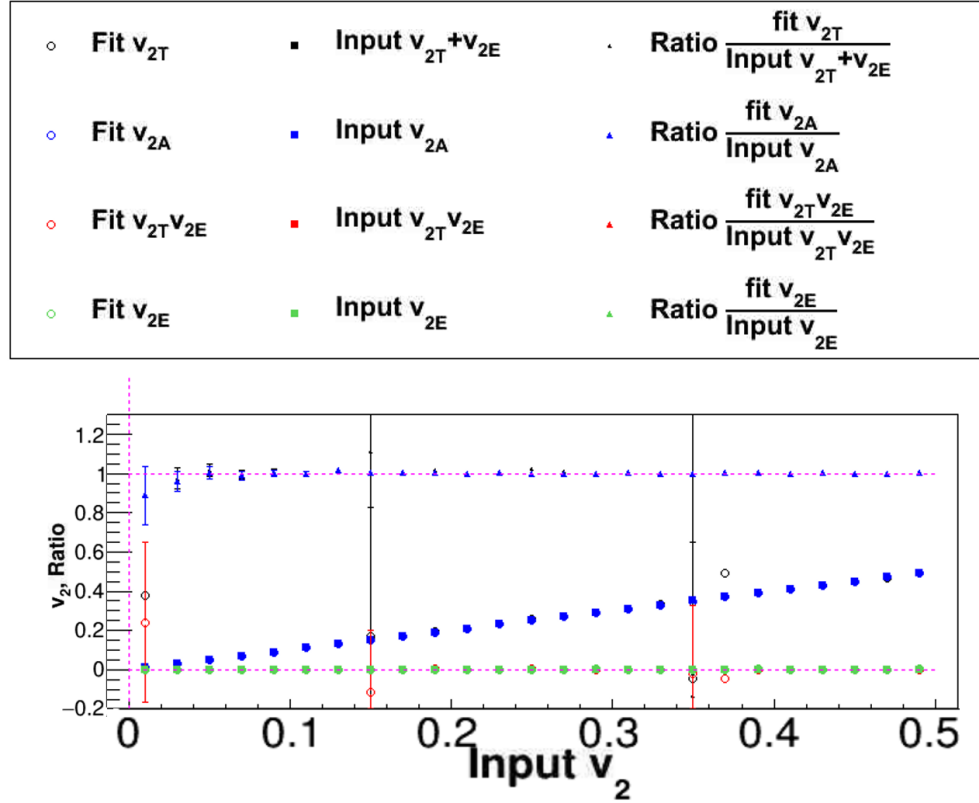


Figure 4.18: Example of agreement of the parameters in Equation 4.3 to the Monte Carlo simulation input parameters. Specifically, fit parameters of Equation 4.3 as a function of input v_{2T} with a fixed $v_{2E} = 0$. The vertical magenta line is the absolute value of v_{2E} . The fit values are the open circles, the squares are the true input values, and the triangles near $y = 1$ are the ratio of the fit value to the truth value.

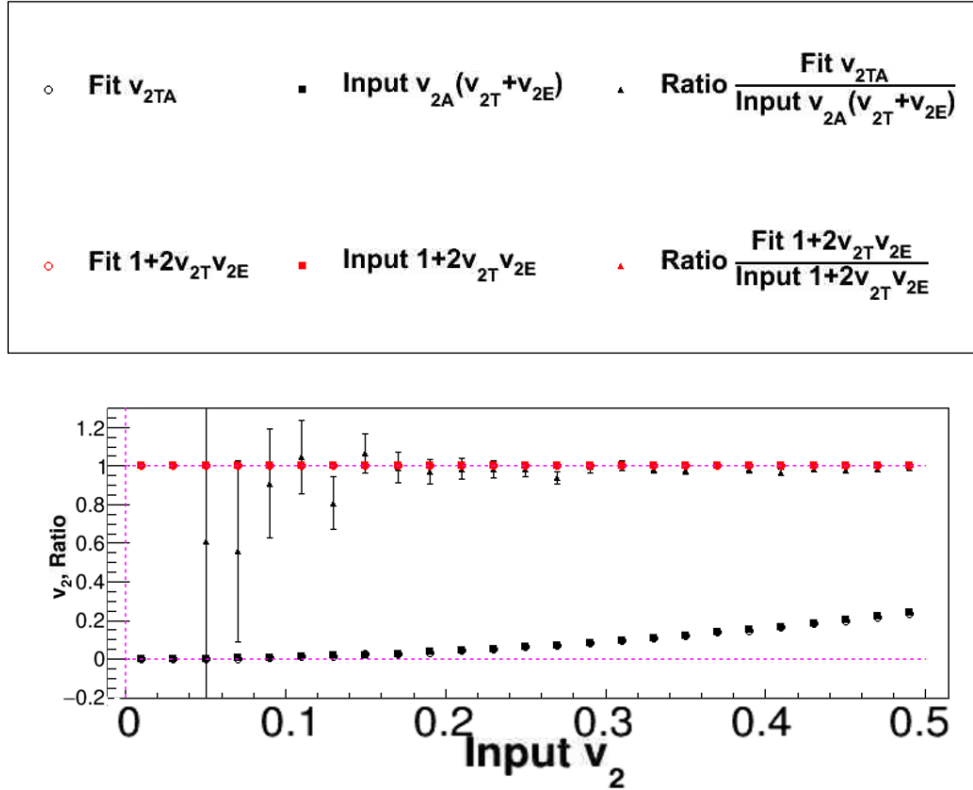


Figure 4.19: Example of agreement of the parameters in Equation 4.5 to the Monte Carlo simulation input parameters. Specifically, fit parameters of Equation 4.5 as a function of input v_{2T} with a fixed $v_{2E} = 0$. The vertical magenta line is the absolute value of v_{2E} . The fit values are the open circles, the squares are the true input values, and the triangles near $y = 1$ are the ratio of the fit value to the truth value. Note that $v_{2\text{TA}} = v_{2A}(v_{2T} + v_{2E})$.

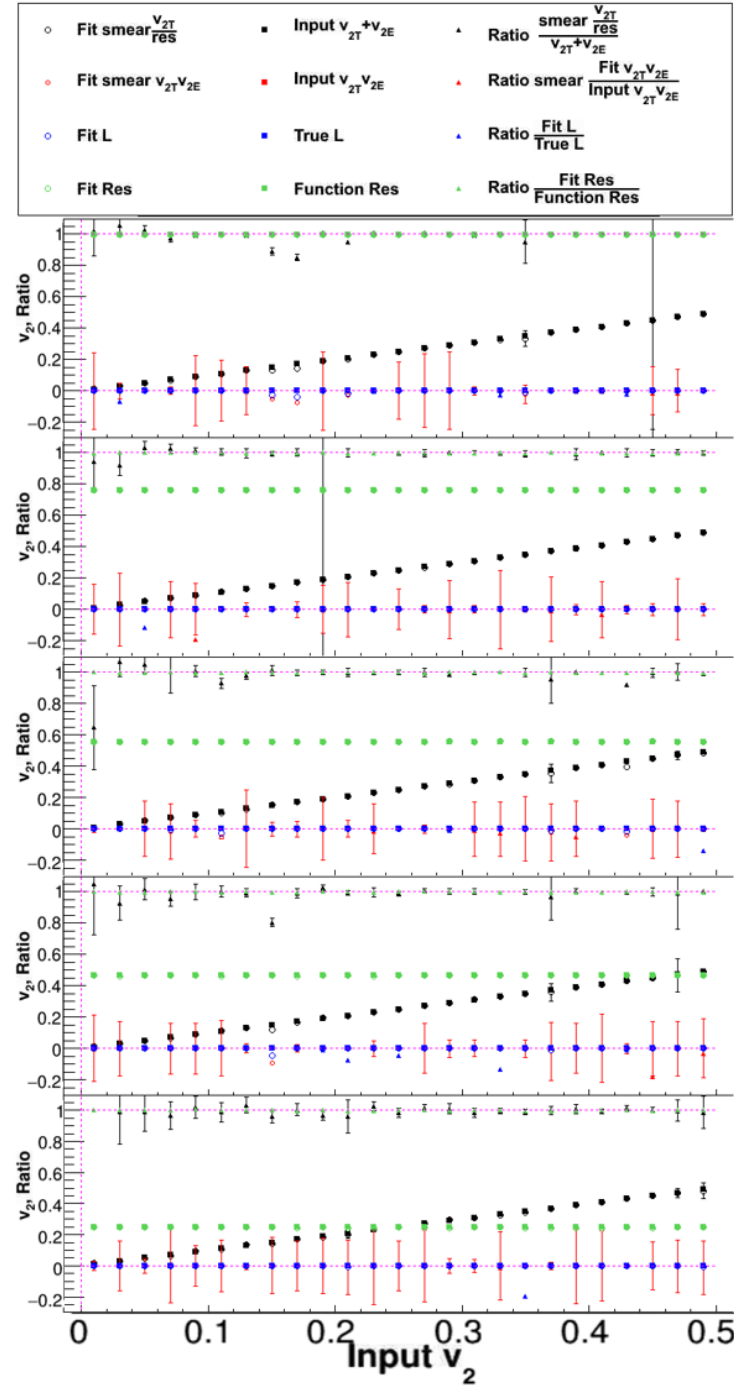


Figure 4.20: Example of agreement of the parameters in Equation 4.29 to the Monte Carlo simulation input parameters. Specifically, fit parameters of Equation 4.29 as a function of input v_{2T} with a fixed $v_{2E} = 0$. Each panel is a different value of χ , starting from the top and going down the $\chi = 20, 1.6, 1, 0.8, 0.4$. The vertical magenta line is the absolute value of v_{2E} . The fit values are the open circles, the squares are the true input values, and the triangles near $y = 1$ are the ratio of the fit value to the truth value.

Note that in Figure 4.18, all the fit values agree with the input values, which makes all of the ratios unity. For Figure 4.19, the $v_{2TA} = v_{2A}(v_{2T} + v_{2E})$ ratio blows up for input v_{2T} less than 0.05 because the true v_{2TA} is small. Above input $v_{2T} = 0.05$, the ratio is consistent with unity. In Figure 4.20, the $v_{2T} + v_{2E}$ fit is consistent with the input values for all input v_{2T} . The $v_{2T}v_{2E}$ and \mathcal{L} fit terms are consistent with 0. These values are not surprising as the input $v_{2E} = 0$. If the input $|v_{2E}|$ is increased to $v_{2E} = -0.15$, the fit parameters are shown in Figures 4.21, 4.22, and 4.23.

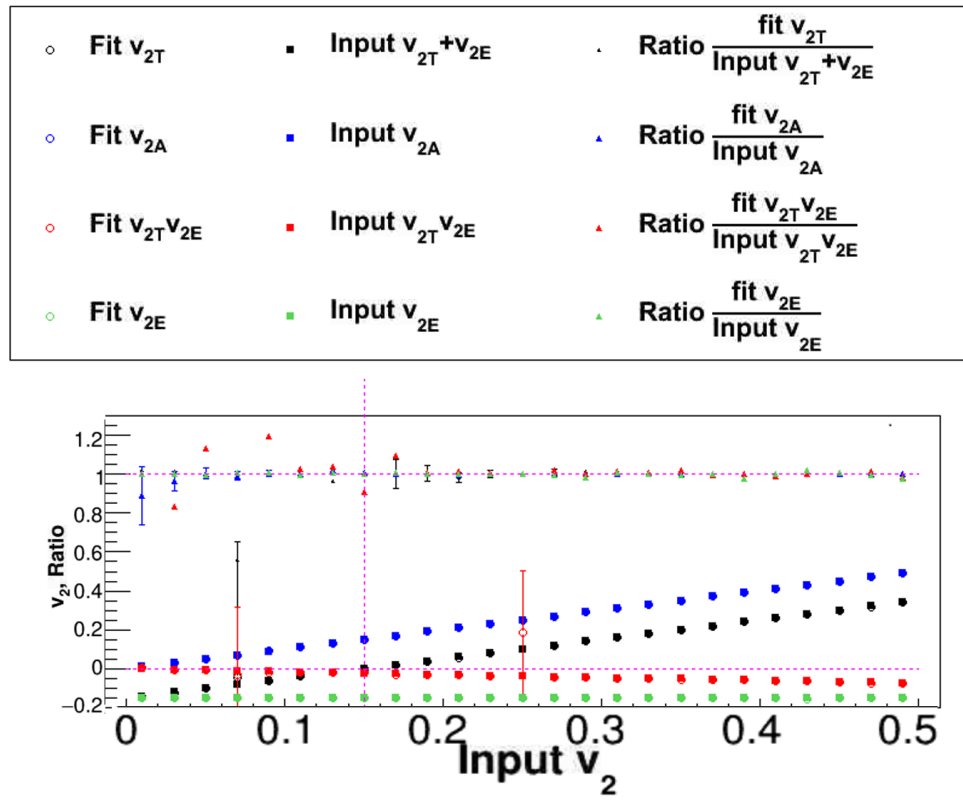


Figure 4.21: Example of agreement of the parameters in Equation 4.3 to the Monte Carlo simulation input parameters. Specifically, fit parameters of Equation 4.3 as a function of input v_{2T} with a fixed $v_{2E} = -0.15$. The vertical magenta line is the absolute value of v_{2E} . The fit values are the open circles, the squares are the true input values, and the triangles near $y = 1$ are the ratio of the fit value to the true value.

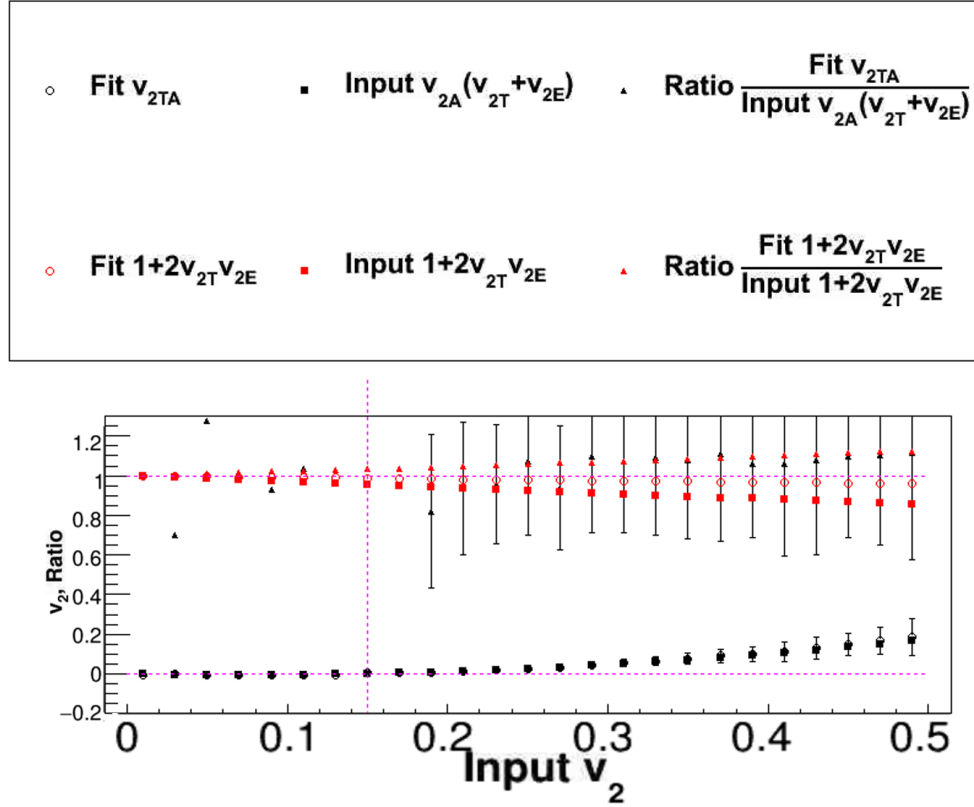


Figure 4.22: Example of agreement of the parameters in Equation 4.5 to the Monte Carlo simulation input parameters. Specifically, fit parameters of Equation 4.5 as a function of input v_{2T} with a fixed $v_{2E} = -0.15$. The vertical magenta line is the absolute value of v_{2E} . The fit values are the open circles, the squares are the true input values, and the triangles near $y = 1$ are the ratio of the fit value to the true value. Note that $v_{2TA} = v_{2A}(v_{2T} + v_{2E})$.

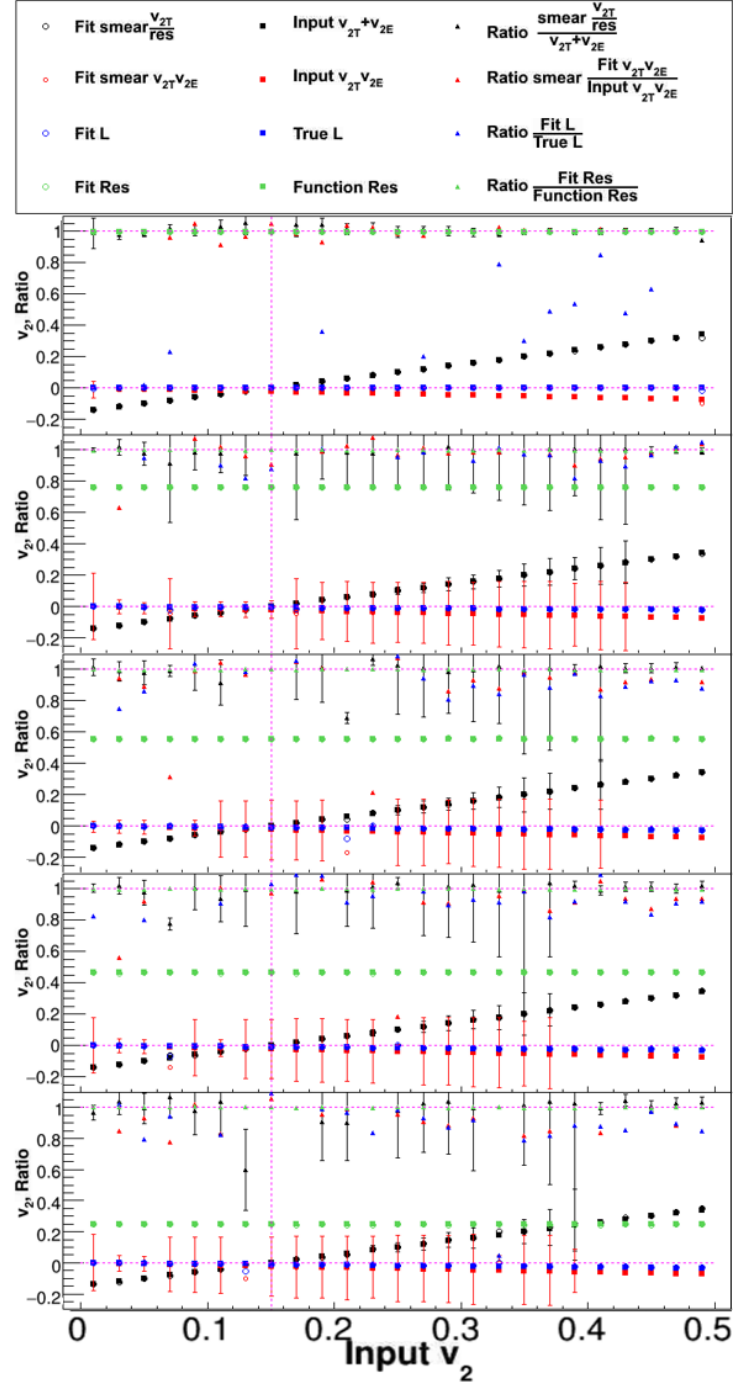


Figure 4.23: Example of agreement of the parameters in Equation 4.29 to the Monte Carlo simulation input parameters. Specifically, fit parameters of Equation 4.29 as a function of input v_{2T} with a fixed $v_{2E} = -0.15$. Each panel is a different value of χ , starting from the top and going down the $\chi = 20, 1.6, 1, 0.8, 0.4$. The vertical magenta line is the absolute value of v_{2E} . The fit values are the open circles, the squares are the true input values, and the triangles near $y = 1$ are the ratio of the fit value to the true value.

All of the ratios in Figure 4.21 are consistent with one. Figure 4.22 has the same general trend as the previous trigger-associated particle fit distributions. The $1 + 2v_{2T}v_{2E}$ fit term is always closer to one than the true value. This makes the ratio above one for most input v_{2T} . All fit parameters agree with the true values in Figure 4.23.

4.6 Conclusion

This chapter has shown that equations 4.3, 4.5, and 4.29 provide for a proper way of extracting v_{2T} of isolated particles. That is, we will measure the isolated particle $\Delta\phi$ distributions and use the functional forms derived above to fit to extract the interesting parameters, as well as extract the v_{2E} in the way described above. These equations work in extreme cases, when $|v_{2T}| = |v_{2E}|$, $|v_{2E}| > |v_{2T}|$, and when $v_{2E} = 0$. They also hold true over a wide range of v_{2T} , v_{2E} , and χ . The next two chapters uses these equations in PHENIX Au+Au data to extract the v_2 .

5 ANALYSIS DETAILS - ISOLATED PARTICLE v_2

5.1 Introduction

This chapter explains the analysis procedure used to extract v_2 in PHENIX data. The acceptance correction is explained first, then the event plane resolution correction. The analysis procedure is outlined for both inclusive and isolated particles. And finally, the systematic errors on the final v_2 values are explained.

5.2 Acceptance Correction

The PHENIX detector has azimuthal coverage for only half the of the full azimuthal angle measured transverse to the beam direction. In this coverage, there can be dead areas in the subdetectors and these dead areas can change over the course of the Run. These areas that have no azimuthal coverage can be corrected for. The correction is nominally a four step process:

- plot ϕ_T versus Ψ_{2EP} (Figure 5.1a),
- also plot ϕ_T versus $\Delta\phi = \phi_T - \Psi_{2EP}$ (Figure 5.1b),
- project this histogram onto the $\Delta\phi$ axis to obtain a one dimensional acceptance function of $\Delta\phi$ ($Acc(\Delta\phi)$) (Figure 5.1c),
- divide the raw distribution by $Acc(\Delta\phi)$ to obtain the corrected two-particle correlation, that is,

$$\frac{dN_{real}}{d\Delta\phi} = \frac{1}{Acc(\Delta\phi)} \frac{dN_{raw}}{d\Delta\phi}, \quad (5.1)$$

where $\frac{dN_{real}}{d\Delta\phi}$ is the corrected distribution and $\frac{dN_{raw}}{d\Delta\phi}$ is the raw distribution.

Event mixing is a better way to obtain the acceptance function. This is carried out by making pairs between triggers and event planes from different events. This ensures there is no physics correlation and the only thing the two angle have in common is the acceptance. Mathematically, this acceptance function is

$$Acc\Delta\phi = \frac{2\pi}{\int \frac{dN_{mix}}{d\Delta\phi} d\Delta\phi} \frac{dN_{mix}}{d\Delta\phi}, \quad (5.2)$$

where the factor of 2π is for normalization and $\frac{dN_{mix}}{d\Delta\phi}$ is the mixed $\Delta\phi$ distribution.

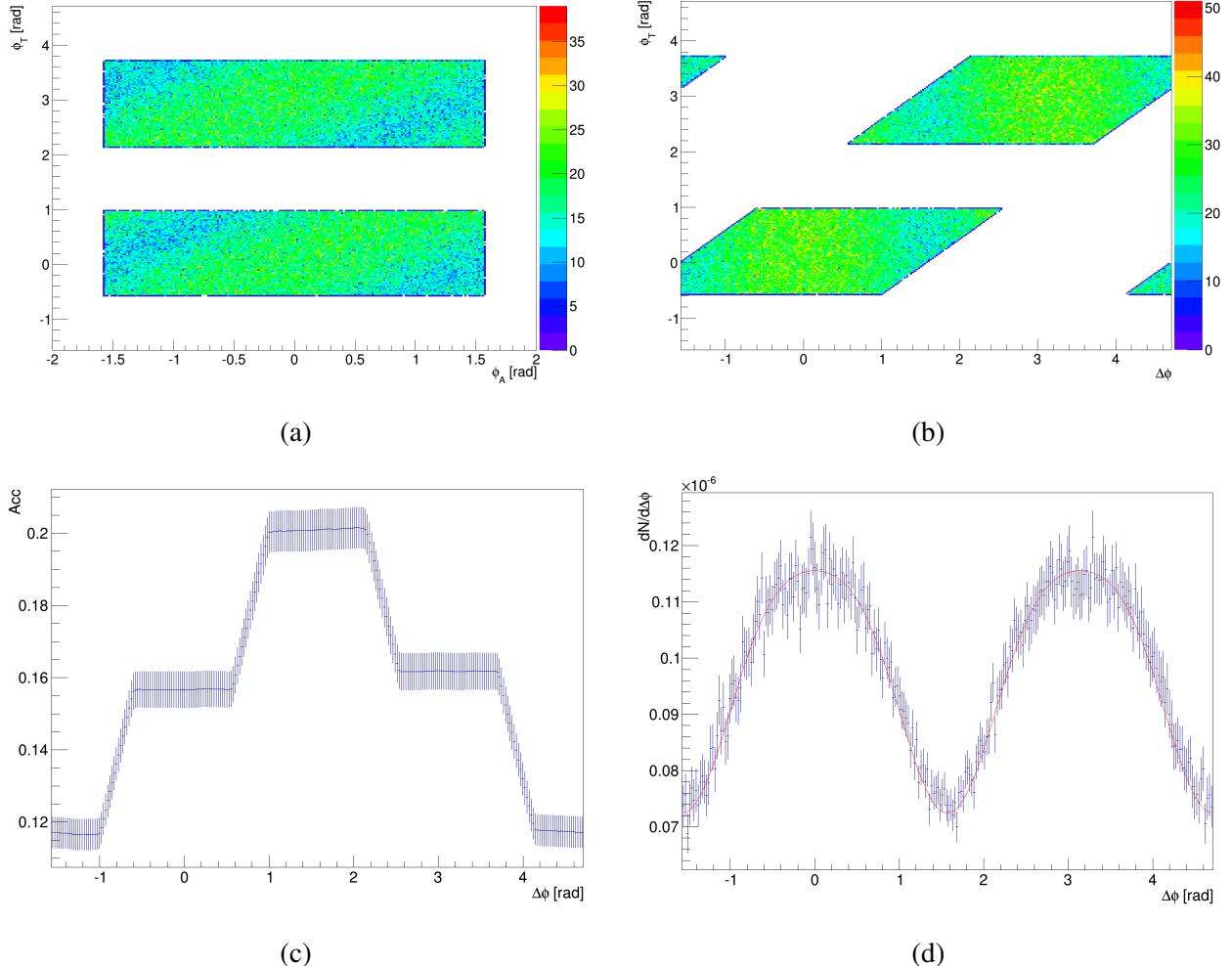


Figure 5.1: (a) Trigger angle versus reaction plane angle. (b) Trigger angle versus $\Delta\phi = \phi_T - \Psi_{2EP}$. (c) Acceptance function for the accepted trigger azimuthal angles and event plane angles. (d) Acceptance corrected trigger-event plane correlation.

5.2.1 Resolution Correction

The event plane resolution is used to correct the experimentally measured event plane to the true reaction plane. The resolution is applied to the raw v_2 values, v_2^{raw} via Equation 1.7, that is,

$$v_2 = \frac{v_2^{raw}}{\langle \cos(2\delta\Psi) \rangle}, \quad (5.3)$$

where $\delta\Psi = \Psi_{RP} - \Psi_{EP}$, Ψ_{EP} is the measured second order event plane, and Ψ_{RP} is the second order reaction plane. The values for the four centrality bins used in this analysis from Run 10 (blue triangles) and Run 11 (magenta triangles) is shown in Figure 5.2. These points were found by calculating the cosine in Equation 1.7 directly. These values are reasonable because they are consistent with the BBC resolution found in Reference [28] (red circles). The blue and magenta points on this figure have no statistical error on them because the systematic error will dominate.

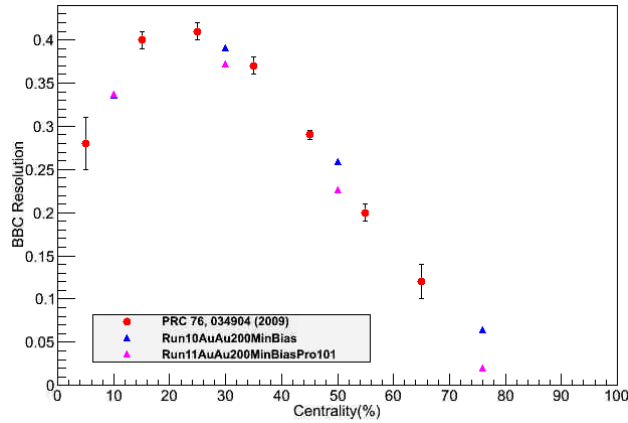


Figure 5.2: BBC event plane resolution as a function of centrality for Run 10 (blue triangles) and Run 11 (magenta triangles) compared to the previously published BBC event plane resolution taken from Reference [28] (red circles).

5.3 Analysis Procedure

5.3.1 Inclusive Photons and π^0

To extract the inclusive particle v_2 , we record trigger p_T , reaction plane, and $\Delta\phi = \phi_T - \Psi_{2EP}$ where ϕ_T is the azimuthal angle of the trigger particle. We also record these for mixed event to get the acceptance correction. We project the trigger p_T range and reaction plane onto the $\Delta\phi$ axis for the raw distribution and the mixed distribution. Then the raw distribution is divided by the mixed distribution to get the real distribution. The real $\Delta\phi$ distribution for inclusive photons is shown in Figure 5.3 for Run 11 Au+Au 0 - 20% central events. The blue line in this figure are fits to

Equation 1.3 truncated at $n = 2$ reprinted here for convenience.

$$\frac{dN}{d(\phi - \Psi_{EP})} = \mathcal{A}(1 + 2v_2 \cos(2(\phi - \Psi_{EP}))), \quad (5.4)$$

where \mathcal{A} is a normalization fit parameter, and v_2 is the desired fit parameter. Once the raw v_2 is extracted from the fit, it is event plane resolution correction using Equation 1.7 and the event plane resolution in Figure 5.2. The corrected v_2 is plotted as a function of p_T in Figure 5.4.

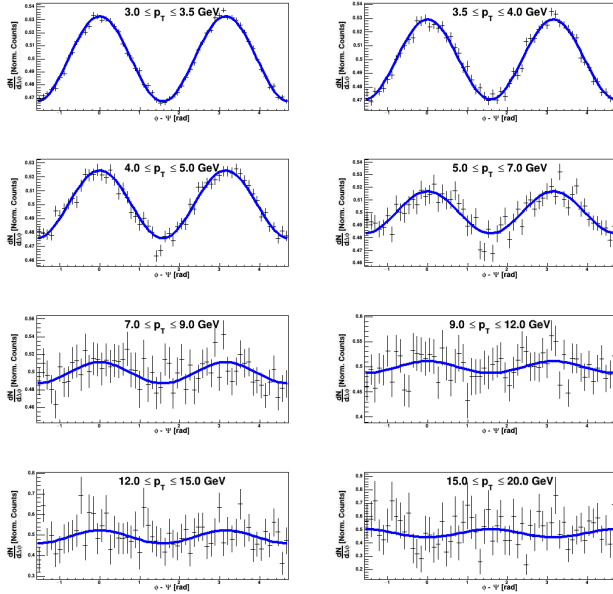


Figure 5.3: Run 11 Au+Au 0 - 20% central event inclusive photon $\Delta\phi = \phi_T - \Psi_{2EP}$ distributions. Each plot is a trigger photon p_T bin. The blue line is a fit to Equation 5.4 and the extracted v_2 are plotted versus p_T in Figure 5.4.

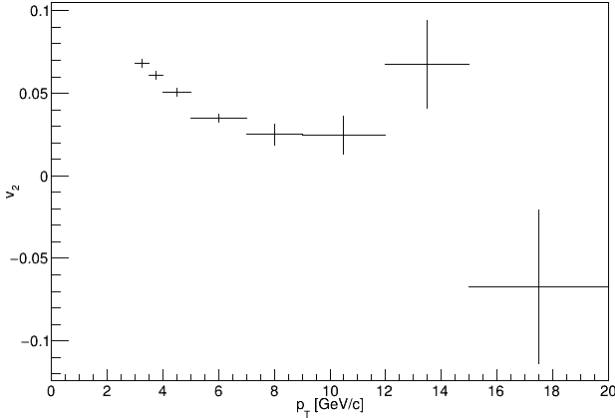


Figure 5.4: Run 11 Au+Au 0 - 20% central event inclusive photon v_2 as a function of p_T . The $\Delta\phi = \phi_T - \Psi_{2EP}$ distributions are shown in Figure 5.3.

5.3.2 Isolated Photons and π^0

The analysis procedure up to the fit function for isolated particles is the same as the inclusive particles, except that the isolated particles are subject to the isolation cut described in Section 3.4.2.

Equation 4.29 was verified in our simulation so now we show how it behaves with the PHENIX Run 11 Au+Au data. We project the isolated photon yield along $\Delta\phi$ for each p_T bin shown in Figure 5.5. We then fit according to Equation 4.29 (green line). The output fit parameters, \mathcal{J} (red points), \mathcal{K} (blue points), and \mathcal{L} (magenta points), are shown as a function of p_T in Figure 5.6.

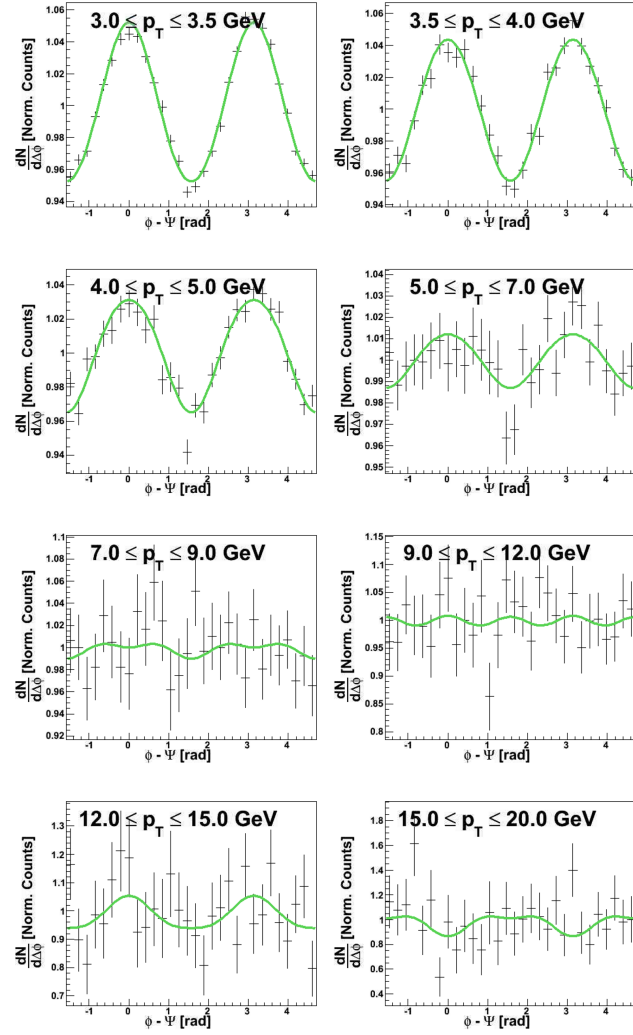


Figure 5.5: Run 11 Au+Au 0 - 20% central events $\Delta\phi$ distributions for photon triggers. The solid green line is a fit to Equation 4.29.

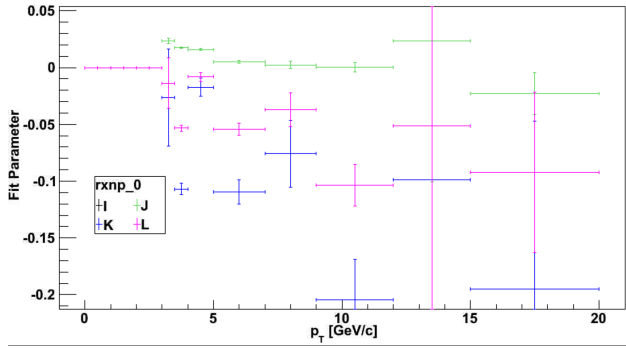


Figure 5.6: Run 11 Au+Au 0 - 20% central events fit parameters, defined by Equation 4.30, extracted from the green lines on Figure 5.5.

For the 2-particle correlations measurements, we need $v_{2T} + v_{2E}$ so we just use parameter \mathcal{J} for the background subtraction. We can go further and extract v_{2T} but first we must extract v_{2E} . We use the an analogous analysis method in the data as the simulation to get v_{2E} (see Figure 4.1 and explanation). This method is outlined in Figure 5.7. We record the $\Delta\phi$ distribution of the thrown random cones. The cones that pass the isolation cut are also recorded. The isolated cone $\Delta\phi$ distribution is then divided by all the cones $\Delta\phi$ distribution and this ratio is fit to

$$\frac{dN_{cone}}{d\Delta\phi} = \mathcal{H}(1 + 2v_{2E} \cos(2\Delta\phi)), \quad (5.5)$$

where \mathcal{H} is a normalization factor and v_{2E} is the isolation cut efficiency v_2 . This is done for each p_T bin for each centrality. Figure 5.8 shows the $\Delta\phi$ distributions for each p_T bin for the Run 11 Au+Au data set. The v_{2E} fit values are shown in Figure 5.9. We expect these values to be negative because the isolation cut preferentially accepts cones near $\Delta\phi = -\pi/2, \pi/2$ and $3\pi/2$ because there is less underlying event in these regions. This causes the normal cosine to become negative.

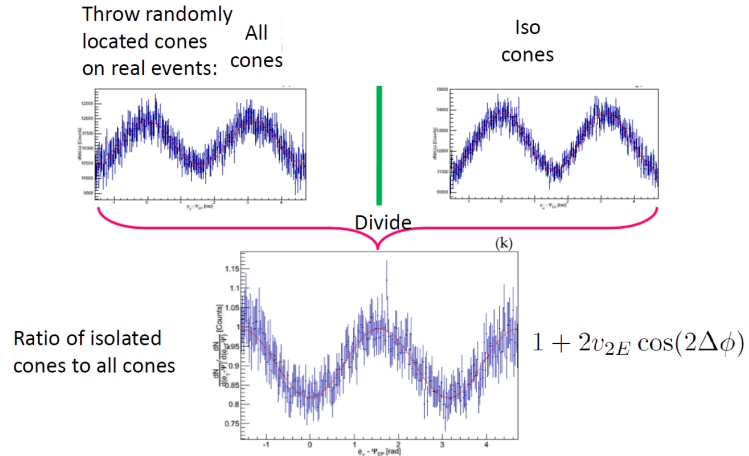


Figure 5.7: Method used to obtain v_{2E} . The $\Delta\phi$ distributions for isolated cones (left) and all cones (right) and the ratio of isolated to all (bottom). The red line on the bottom plot is a fit to Equation 5.5.

This is shown in Figure 5.8 for 0 - 20% central event photons in the Run 11 Au+Au data set. Each plot in this figure is a p_T bin. The red line is a fit to Equation 4.2. The extracted v_{2E} as a function of p_T is shown in Figure 5.9. One can see that all the v_{2E} values are negative, as expected.

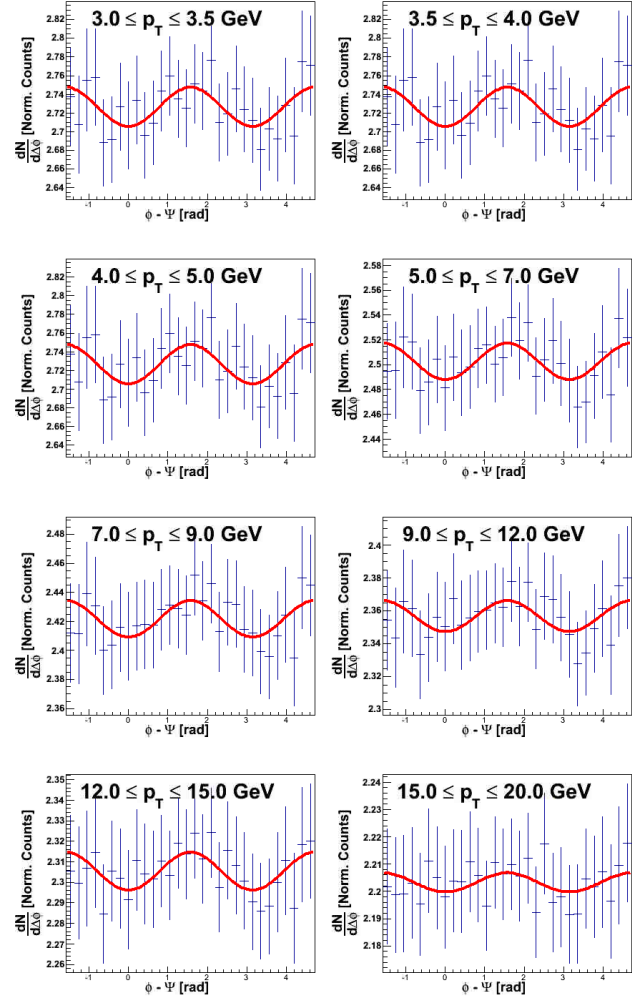


Figure 5.8: Run 11 Au+Au 0 - 20% central events $\Delta\phi$ distributions for isolated cones. The solid red line is a fit to Equation 5.5.

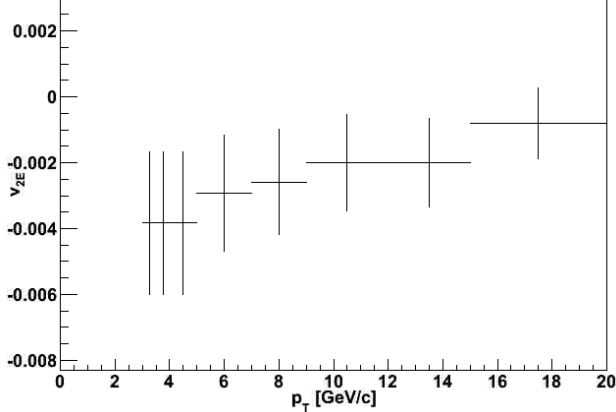


Figure 5.9: Run 11 Au+Au 0 - 20% central events v_{2E} as a function of p_T . These were obtained by fitting 5.5 to each plot in Figure 5.8.

There are potentially three ways to obtain v_{2T} using v_{2E} and the parameters in Equation 4.30, each involving solving for v_{2T} in the three parameter equations. If we multiply \mathcal{J} by the event plane resolution and subtract v_{2E} to get v_{2T} we get something that looks like Figure 5.10a. This figure shows v_{2T} as a function of p_T for the same three reaction planes as the previous ones in this section. The v_{2T} values seem reasonable for photons and this generally descending trend is expected. The error bars get larger for larger p_T because there are few high p_T photons. The second way we have tested to obtain v_{2T} is to divide \mathcal{K} (as defined in Equation 4.30) by the extracted v_{2E} . This is shown as a function of p_T for the three reaction planes in Figure 5.10b. One can see that these values are larger and seem to fluctuate quite a bit. The error bars are large on all the points because the small v_{2E} is in the denominator. The last two p_T bins don't have values because they are out of the range on the figure. For these reasons, it appears that this method is not ideal. A third method could use \mathcal{L} in Equation 4.30, but it has the same problem that the \mathcal{K} method does. Therefore, we will use the \mathcal{J} method to extract the direct photon v_2 . The blue points on Figures 5.10a and 5.10b are 20 - 40% direct photon v_2 measured via the BBC event plane published by PHENIX [29].

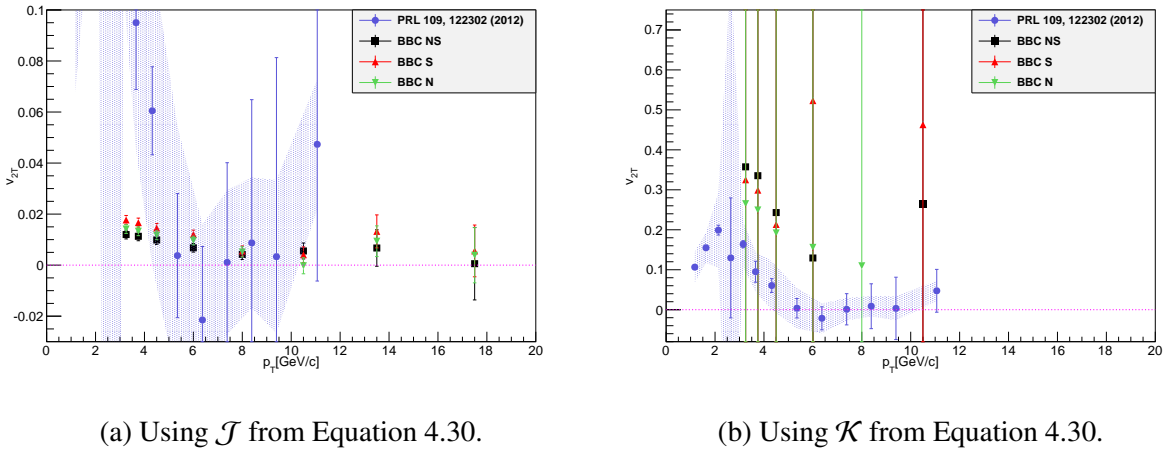


Figure 5.10: Isolated photon v_{2T} as a function of p_T for three event planes, BBNS (red points), BBCN (green points), and BBCNS (black points) measured with 20 - 40% photons in the Run 11 data set. The blue points are direct photon v_2 measured in the Run 7 Au+Au PHENIX data set [29].

5.3.3 Flow Systematic Errors

This section describes the systematic errors on the final v_2 values. The plots shown above were created using one event plane from one event plane detector. We use the BBC north (BBCN) and south (BBCS) modules individually to determine their own event planes as well as an average between them that is labeled BBC north-south (BBCNS).

A substantial part of the systematics is from the event plane resolution and the difference between two different v_2 from different detectors. We use the BBCNS reaction plane for the v_2 value and half the distance between the BBCN v_2 and BBCS v_2 values for the systematic error. We also vary the resolution from its value to the maximum and minimum statistical error to understand how it effects the final v_2 value. There is an additional systematic of 20% on all of the v_2 to account for various contributions. We refer to extensive studies done in Reference [30] to determine the contributions to this 20%. Reference [30] explores many different cuts and reaction plane combinations including ones very similar or the same to this analysis. Below we list the

specific figures therein we used to make these estimates, many of those plots show an increasing trend with p_T , and are for $p_T > 6 \text{ GeV}/c$, so we choose even larger uncertainties to be conservative for the $p_T > 5 \text{ GeV}/c$ region we are interested in. The different contributions are:

- 10% for particle selection (see Figure 5.11),
- 15% for measuring v_2 with different event plane detectors (see Figure 5.11)
- 5% for the v_2 method (see Figure 5.13), and
- 5% for measuring v_2 in 20% centrality bins rather than combining smaller centrality results.

Most other analyses have been in 5% or 10% centrality bins and then averaged to get to a 20% bin. We have re-evaluated the v_2 in 10% bins as a test and got consistent answers within less than 5% as a cross check, so we use 5% as the error here. We choose to still use the 20% binning method results cause the 10% results are not completely finalized for the publication we will switch to 10% bins.

Figure 5.11 shows v_2 for inclusive photons in Au+Au collisions as a function of p_T with different shower shape cuts in the EMCAL on the upper panels. The lower panels of this figure show the ratio of each shower shape cut to the average. Each column is a different centrality range. One can see that the maximum deviation is around 1%. We use 10% for the particle selection error to account for any other errors from our analysis method.

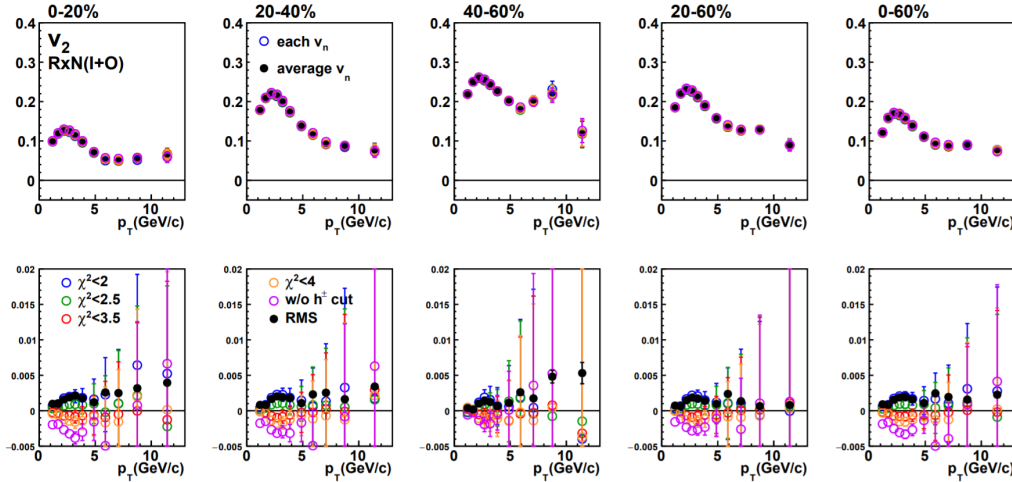


Figure 5.11: Inclusive photon v_2 in Au+Au collisions as a function of p_T for different EmCal shower shape cuts (top row). Ratio of each cut v_2 to the average v_2 . This figure is taken from Reference [30].

The upper panel of Figure 5.12 shows the v_2 for inclusive photons in Au+Au collisions as a function of p_T with different event planes. The lower panels of this figure show the ratio of each event plane to the average. Each column is a different centrality range. One can see that the maximum deviation in the lower panels is less than 10%. We use 15% for the different event plane detectors because Figure 5.12 only shows photons with $p_T < 4$ GeV/c and the analysis in this dissertation is for photons with $p_T < 20$ GeV/c.

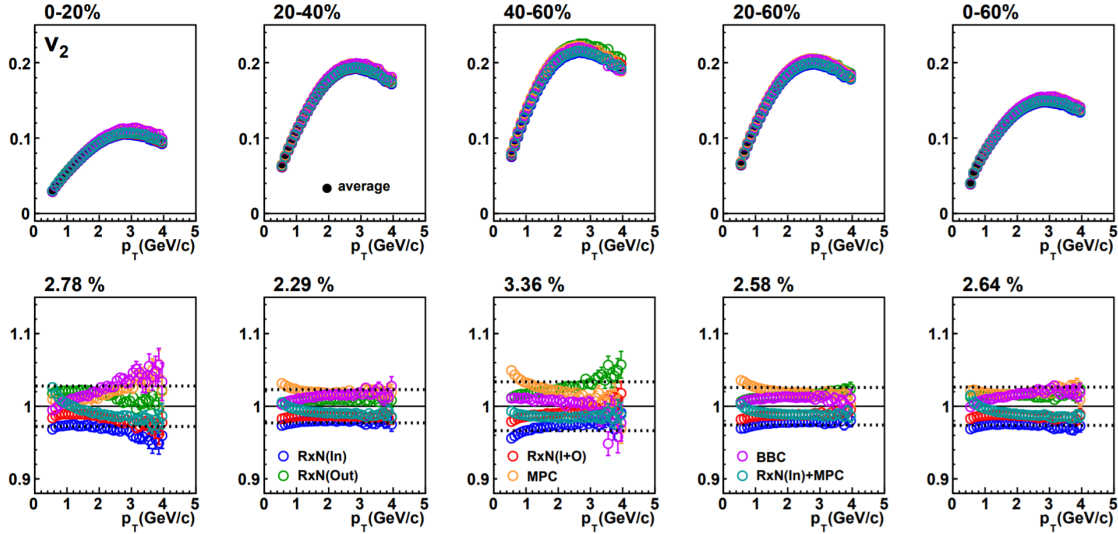


Figure 5.12: Inclusive photon v_2 in Au+Au collisions as a function of p_T using different event planes (top row). Ratio of each event plane v_2 to the average v_2 . This figure is taken from Reference [30].

The upper panel of Figure 5.13 shows the v_2 for inclusive photons in Au+Au collisions as a function of p_T using two different methods for finding the v_2 . The lower panels of this figure show the ratio of each method to the average. Each column is a different centrality range. One can see that the maximum deviation in the lower panels is less than 1%. We use 5% for v_2 extraction procedure.

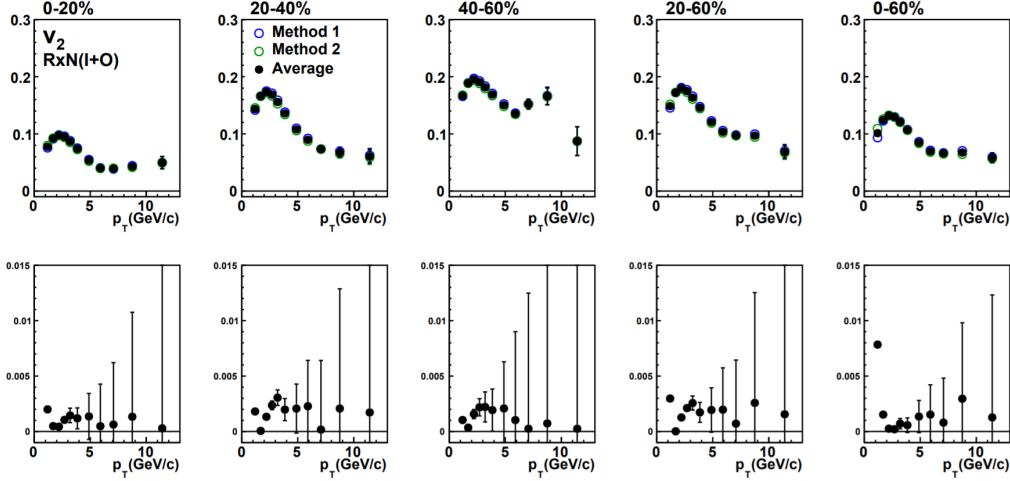


Figure 5.13: Inclusive photon v_2 in Au+Au collisions as a function of p_T using two different methods (top row). Ratio of each method v_2 to the average v_2 . This figure is taken from Reference [30].

To find the total systematic error, each of these error sources are added in quadrature and plotted for each point. The conservative 20% systematic that accounts for various contributions is the dominate error source.

6 RESULTS AND DISCUSSION - ISOLATED PARTICLE v_2

6.1 Introduction

This chapter shows the v_2 as a function of p_T for inclusive photons and π^0 's as well as the $v_{2T} + v_{2E}$ of isolated photons and π^0 's. This is the v_2 used in the background subtraction in the two-particle correlations analysis. The chapter also shows the the final extracted v_{2T} values. All of these v_2 values are compared to published PHENIX data when we are able, mainly from Reference [29]. All of the comparisons to published data are for 0 - 20% and 20 - 40% events because more peripheral events have too small statistics to make comparisons meaningful. We show all four centrality bins used in this analysis in this chapter.

6.1.1 Inclusive Photon and $\pi^0 v_2$

The inclusive photon v_2 , that is the v_2 of the photons that do are not subject to the isolation cut, is shown as a function of p_T for the four centrality bins used in this analysis in Figure 6.1. The brown points are the Run 10 values, the green points are the Run 11 values, and the blue points are the inclusive photon v_2 from Reference [29].

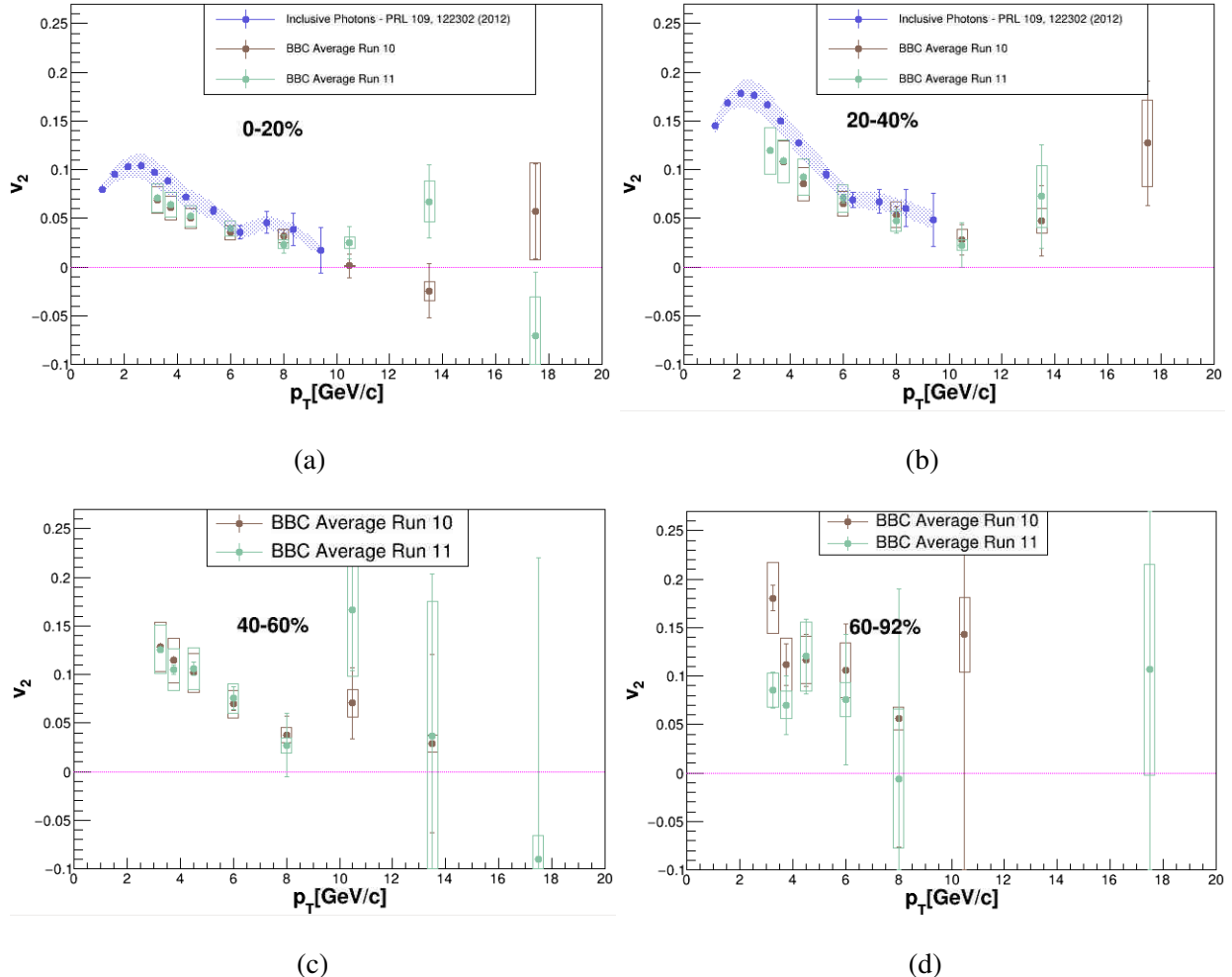


Figure 6.1: Inclusive photon v_2 as a function of p_T for (a) 0 - 20%, (b) 20 - 40%, (c) 40 - 60%, and (d) 60 - 92% events for both Run 10 (brown points) and Run 11 (green points) measured by the BBC. The boxes are systematic error bars. The green points are the inclusive photon v_2 as a function of p_T as measured by the BBC that are taken from Reference [29].

The v_2 of inclusive π^0 are shown as a function of p_T for the four centrality bins used in this analysis in Figure 6.2. The brown points are the Run 10 values, the green points are the Run 11 values, and the blue points are the v_2 of inclusive π^0 from Reference [29].

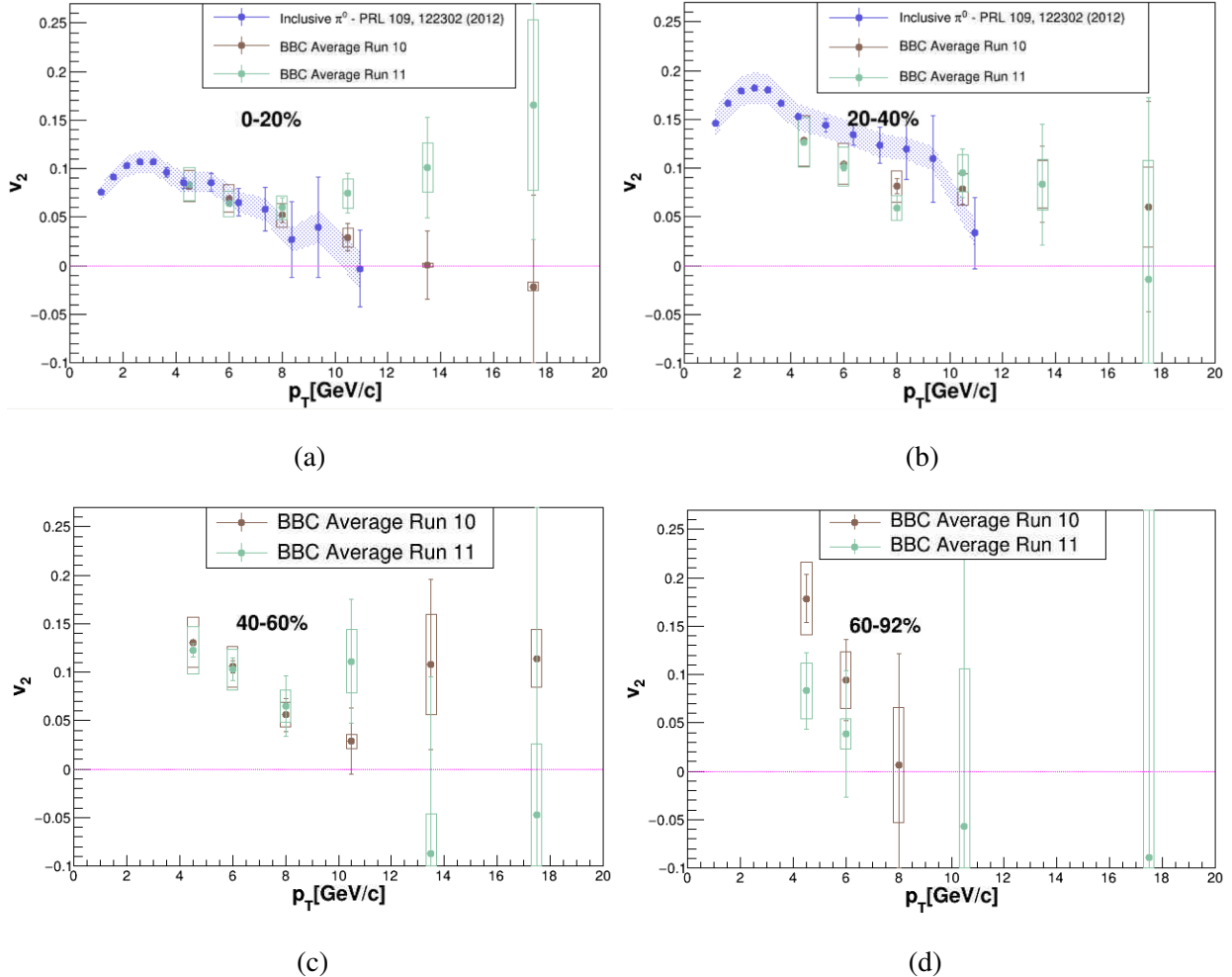


Figure 6.2: Extracted v_2 of inclusive π^0 as a function of p_T for (a) 0 - 20%, (b) 20 - 40%, (c) 40 - 60%, and (d) 60 - 92% events for both Run 10 (brown points) and Run 11 (green points) measured by the BBC. The boxes are systematic error bars. The green points are the v_2 of inclusive π^0 as a function of p_T as measured by the BBC that are taken from Reference [29].

Figures 6.1 and 6.2 show that the Run 10 and Run 11 v_2 values are consistent with one another within the error bars. Generally, for low p_T , the values are almost exactly the same. For high p_T , the error bars are larger because there are less high p_T photons and π^0 's. In peripheral events, (Figures 6.1d and 6.2d) the v_2 values fluctuate due to lack of statistics in this p_T and centrality

range. The large disagreement between the high p_T Run 10 and Run 11 inclusive $\pi^0 v_2$ in 0-20% events has been investigated and the disagreement is attributed to statistical fluctuations.

6.1.1.1 Discussion

The Run 10 and Run 11 v_2 values agree with the PHENIX published v_2 values, this tells us that our basic methods of measuring v_2 and correcting for event plane resolution works. The shape of the v_2 is well known, the low p_T part is due to the hydrodynamics in the QGP but we are primarily interested in high p_T ($> 5\text{GeV}/c$) v_2 for the two-particle correlations analysis presented in the next few chapters. The v_2 at low p_T is highest in 40 - 60% central events because the collision eccentricity is highest in those events. The inclusive photon v_2 is known to be smaller than then the decay photon v_2 to the presence of the direct photons, but is still large due to the many decay photons.

6.1.2 Isolated Photon and $\pi^0 v_2$

6.1.2.1 $v_{2T} + v_{2E}$

Figure 6.3 shows isolated photon $v_{2T} + v_{2E}$ values as a function of p_T for the four centrality bins used in this analysis. The blue points are the Run 10 values, the magenta points are the Run 11 values, the red points are the direct photon v_2 from Reference [29], and the green points are the inclusive photon v_2 from Reference [29]. Figure 6.4 shows $v_{2T} + v_{2E}$ as a function of p_T for isolated π^0 for the four centrality bins used in this analysis. The blue points are the Run 10 values, the magenta points are the Run 11 values, and the green points are the v_2 of inclusive π^0 from Reference [29]. These v_2 values are used in the two-particle analysis background function, Equation 1.13.

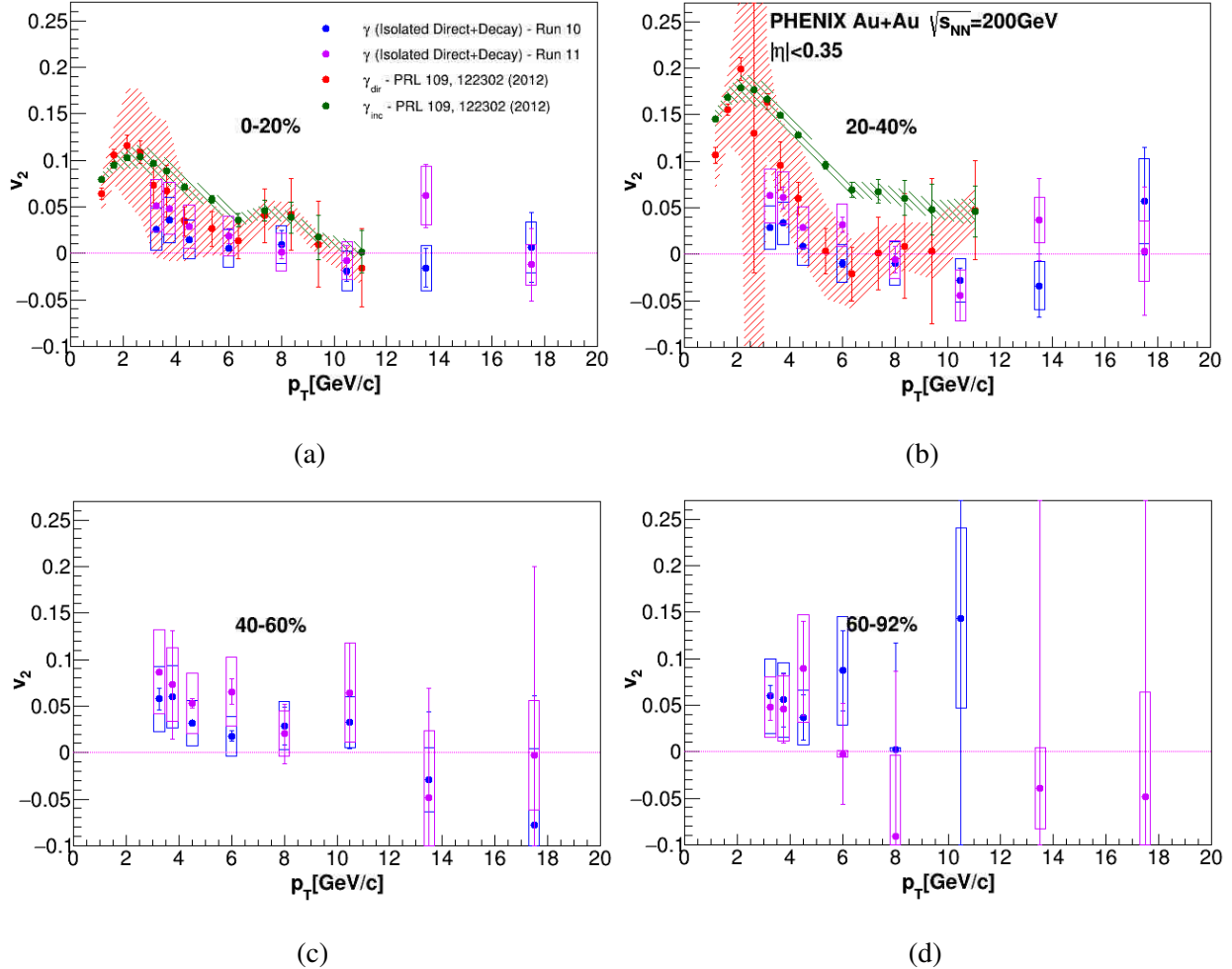


Figure 6.3: Isolated photon $v_{2T} + v_{2E}$ as a function of p_T for (a) 0 - 20%, (b) 20 - 40%, (c) 40 - 60%, and (d) 60 - 92% events for both Run 10 (blue points) and Run 11 (magenta points) measured by the BBC. The boxes are systematic error bars. The red points are the inclusive photon v_2 and the green points direct photon v_2 as a function of p_T as measured by the BBC that are taken from Reference [29].

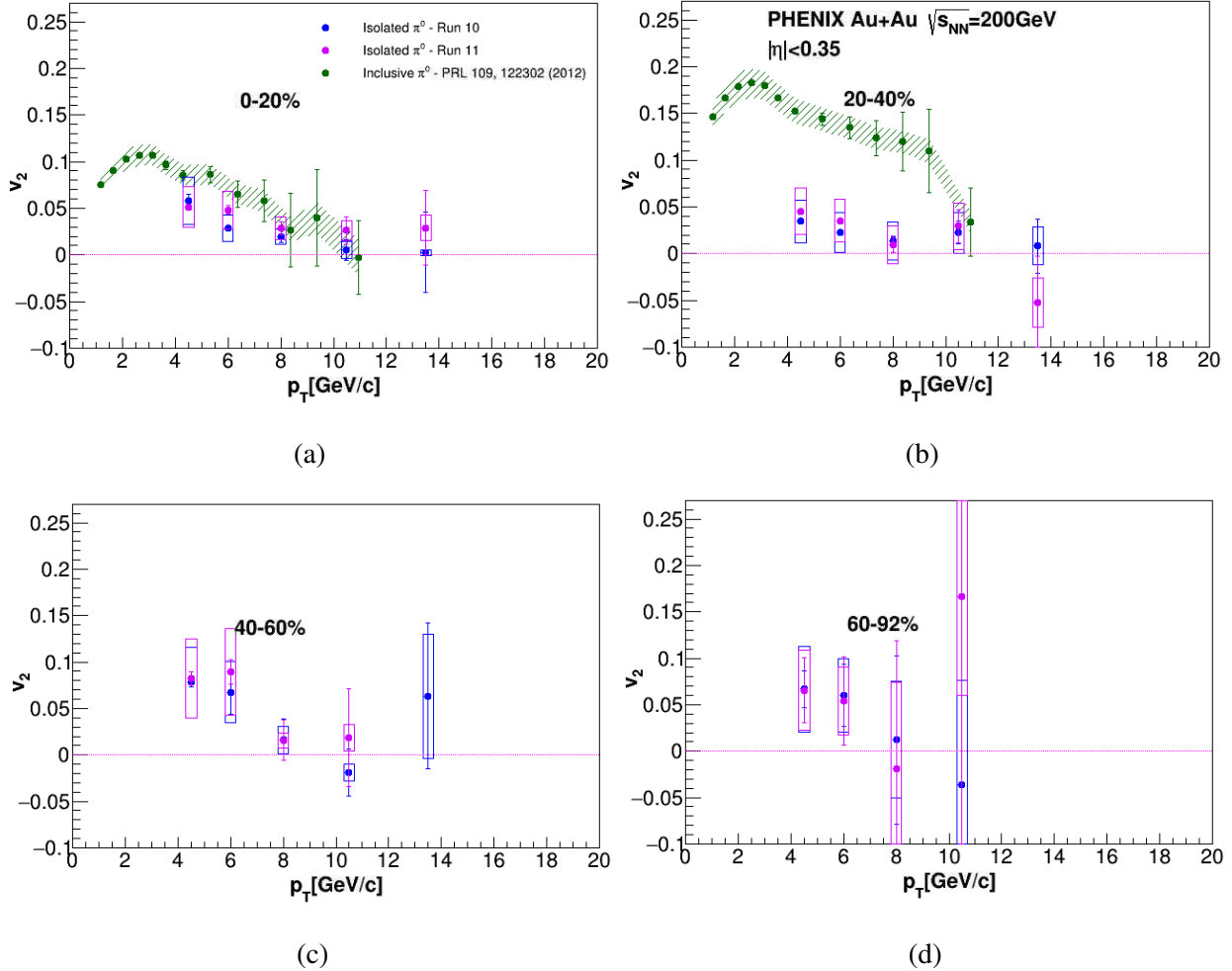


Figure 6.4: Extracted $v_{2T} + v_{2E}$ of isolated π^0 as a function of p_T for (a) 0 - 20%, (b) 20 - 40%, (c) 40 - 60%, and (d) 60 - 92% events for both Run 10 (blue points) and Run 11 (magenta points) measured by the BBC. The boxes are systematic error bars. The green points are the v_2 of inclusive π^0 as a function of p_T as measured by the BBC that are taken from Reference [29].

Figures 6.3 and 6.4 show that the Run 10 and Run 11 v_2 values are consistent with one another within the error bars. For high p_T , the error bars are larger because there are less high p_T photons. In peripheral events, (Figures 6.3d and 6.4d) the v_2 values fluctuate with large error bars due to lack of statistics in this p_T and centrality range. One can see that the isolated photon $v_{2T} + v_{2E}$ is less than the inclusive photon v_2 and consistent with the direct photon v_2 .

6.1.2.2 v_{2T}

Figure 6.5 shows the isolated photon v_{2T} as a function of p_T for the four centrality bins used in this analysis. This is the v_2 without the bias from the isolation cut, the v_{2E} has been corrected for. The blue points are the Run 10 values, the magenta points are the Run 11 values, the red points are the direct photon v_2 from Reference [29], and the green points are the inclusive photon v_2 from Reference [29]. One can see that the isolated photon v_{2T} is less than the inclusive photon v_2 and consistent with the direct photon v_2 . Most importantly, it is larger than the isolated photon $v_{2T} + v_{2E}$ shown in Figure 6.3 but it is still consistent with the points there because of the small v_{2E} is within the larger error bars.

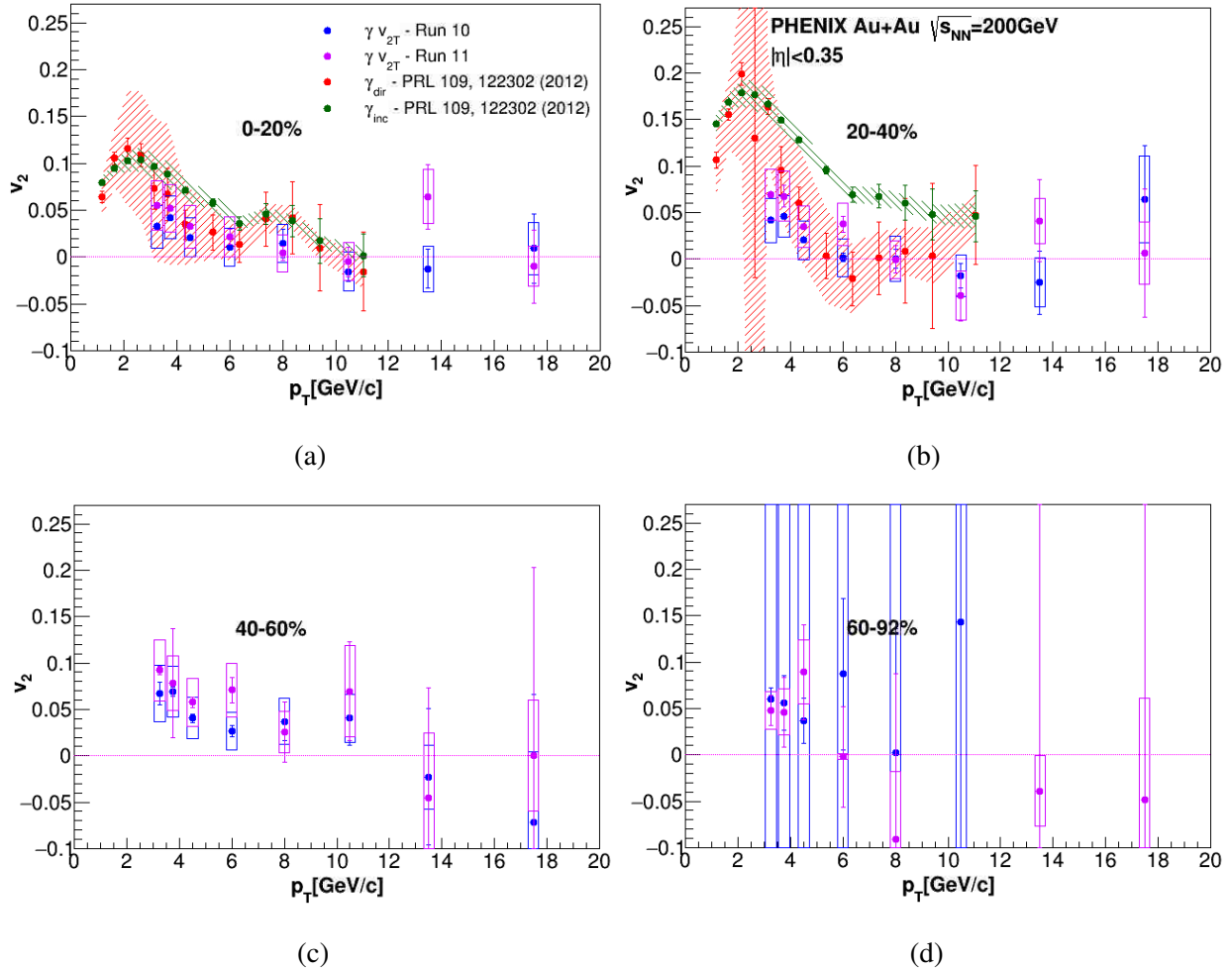


Figure 6.5: Isolated photon v_{2T} as a function of p_T for (a) 0 - 20%, (b) 20 - 40%, (c) 40 - 60%, and (d) 60 - 92% events for both Run 10 (blue points) and Run 11 (magenta points) measured by the BBC. The boxes are systematic error bars. The red points are the inclusive photon v_2 and the green points direct photon v_2 as a function of p_T as measured by the BBC that are taken from Reference [29].

Figure 6.6 shows the v_{2T} of isolated π^0 as a function of p_T for the four centrality bins used in this analysis. The blue points are the Run 10 values, the magenta points are the Run 11 values, the red points are the inclusive $\pi^0 v_2$ from Reference [29]. One can see that the v_{2T} of isolated π^0 is less than the v_2 of inclusive π^0 for most p_T bins in 20 - 40% central events while it appears less

than but consistent with the v_2 of inclusive π^0 for most p_T bins in 0 - 20% central events. Most importantly, it is larger than the $v_{2T} + v_{2E}$ of isolated π^0 shown in Figure 6.3 but it is still consistent.

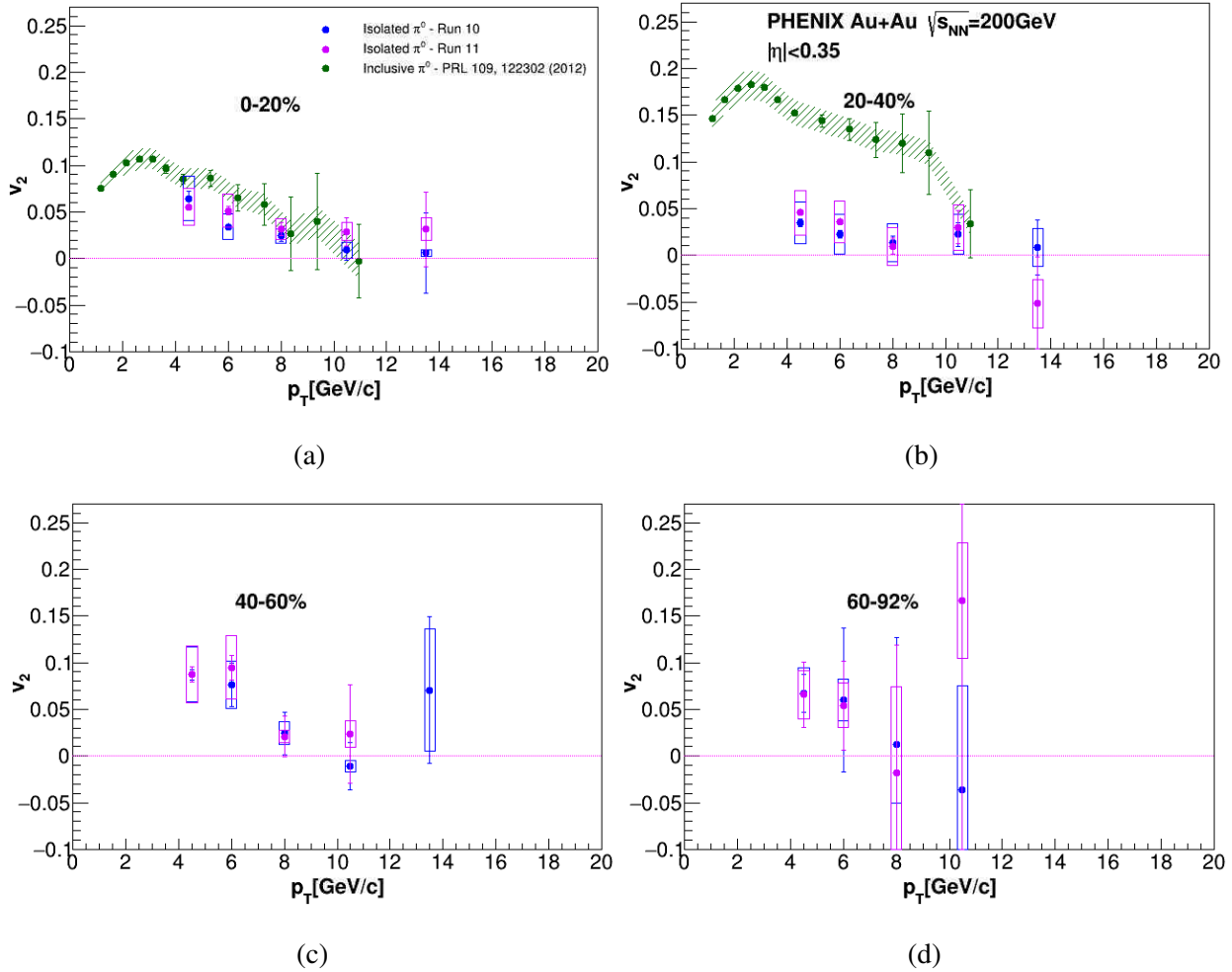


Figure 6.6: Extracted v_{2T} of isolated π^0 as a function of p_T for (a) 0 - 20%, (b) 20 - 40%, (c) 40 - 60%, and (d) 60 - 92% events for both Run 10 (blue points) and Run 11 (magenta points) measured by the BBC. The boxes are systematic error bars. The green points are the v_2 of inclusive π^0 as a function of p_T as measured by the BBC that are taken from Reference [29].

6.1.2.3 Discussion of $v_{2T} + v_{2E}$ and v_{2T}

In the above section, one can see that the isolated photon v_{2T} is less than the inclusive photon v_2 and consistent with the direct photon v_2 . The v_{2T} of isolated photon and π^0 are larger than their $v_{2T} + v_{2E}$ shown in figures 6.3 and 6.4 but are still consistent with those points because of the small v_{2E} is within the larger error bars. The v_{2T} of high p_T ($> 5\text{GeV}/c$) isolated photon and π^0 are consistent with zero for all centrality bins. Like the inclusive photons and π^0 's, the v_{2T} at low p_T is highest in 40 - 60% central events because the collision eccentricity is highest in those events.

Both the $v_{2T} + v_{2E}$ and v_{2T} of isolated π^0 are consistent with zero at very high p_T . At mid-to-high p_T , the v_2 of isolated π^0 is less than the inclusive v_2 but are consistent with the v_2 inclusive π^0 in 0 - 20% central events. The v_2 of isolated π^0 in the 20 - 40% central events are significantly less than the v_2 of inclusive π^0 . This could be a very interesting result. Because we know that requiring the isolation cut for π^0 captures a different type of jet fragmentation than the inclusive π^0 measurement, this could be hint that energy loss might depend on the way a jet fragments, where as in the nominal models, it only depends on the color charge and its kinematics. However, we also know that the isolation cut shifts the jet p_T sampling, and possibly other jet phase space sampling. The isolated π^0 should contain more of the jet momentum than the inclusive π^0 . So the v_2 might be expected to have a different v_2 if the underlying different selection of jets sampled just had a different v_2 for reasons of selection bias. Still it very much warrants further investigation.

To conclude this chapter, we show Figure 6.7 which shows the combined Run 10 and 11 $v_{2T} + v_{2E}$ for isolated photons as a function of p_T for 0 - 20% and 20 - 40% events. The method used to combine the Run 10 and Run 11 data is described in Section 8.7. One can see in this figure that the isolated photon v_2 is closer to the direct photon v_2 than the inclusive photon v_2 . The isolated photon v_2 has some decay photon contribution because some quantity of decay photons survive the isolation cut, but it is clear that it already reduces the decay photon contribution significantly because of the reduction of the v_2 , it is closer to the expected direct photon value of zero. There is no decay photon subtraction on the isolated photons because we want to use the v_2 of what we measure for the two-particle correlations analysis flow subtraction.

One can see that the PHENIX measured 2012 non-isolated direct photon v_2 (red points) at low p_T is rather large— this was initially a surprise at both RHIC and confirmed at the LHC but is thought to be due to the dominance of QGP photons in this p_T range, and a larger than initially expected QGP blue shift, although theoretical models still have difficulty explaining it. It may be interesting that our isolation cut seems to also reduce the v_2 there, although we do not go very low in p_T because we are primarily interested in high p_T ($> 5 \text{ GeV}/c$) v_2 for the two-particle correlations analysis presented in the next few chapters.

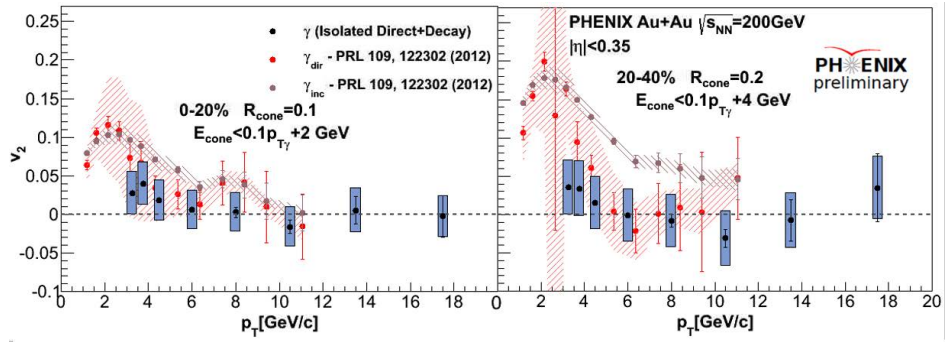


Figure 6.7: Isolated direct + decay photon v_2 ($v_{2T} + v_{2E}$) as a function of p_T for 0 - 20% (left) and 20 - 40% (right) central events in Au+Au collisions. The boxes are systematic error bars. The red points are the direct photon v_2 and the brown points are inclusive photon v_2 for 0 - 20% and 20 - 40% central events that are taken from Reference [29, 31]. This figure has been used with permission. See Appendix C for more details.

7 ANALYSIS DETAILS: GAMMA-HADRON CORRELATIONS

7.1 Introduction

This chapter is devoted to the analysis details of the gamma-hadron correlations. There is a discussion of the how the correlation function background magnitude, using mean seeds mean partners, and shape, from the single particle v_2 measurements are found. The methods used to obtain the decay photons from the π^0 's and direct photons from the isolated and decay photons are also described. Finally, the systematic errors on the yields are explained.

7.2 Analysis Procedure

The ultimate goal of this analysis is to extract I_{AA} . To obtain this, we record trigger particle and associated particle p_T as well as $\Delta\phi = \phi_T - \phi_A$. We also record the same quantities for mixed events to get the acceptance correction. The triggers are subject to the isolation cut and we only record the ones that pass the cut. To make correlation functions, the raw and mixed distributions are projected with the proper p_T bins onto $\Delta\phi$ then the raw distribution is divided by the mixed distribution. To make the jet functions, the background level is determined using mean seeds mean partners and the shape is determined using the trigger and hadron v_2 . These jet functions are then integrated to get the per-trigger yield for each p_T bin combination. The direct photon-hadron correlation yield is found by subtracting the decay photon-hadron correlation yield from the isolated photon-hadron correlation yield. These yields are divided by the yield in $p+p$ collisions to obtain the I_{AA} .

7.3 Hadron v_2

The elliptic flow of the associated hadrons is the v_{2B} factor in Equation 1.14. We are currently using the hadron v^{2B} values used by References [3, 5, 32], these are the values measured in Reference [55]. These are shown as a function of p_T for the four centrality bins in Figure 7.1.

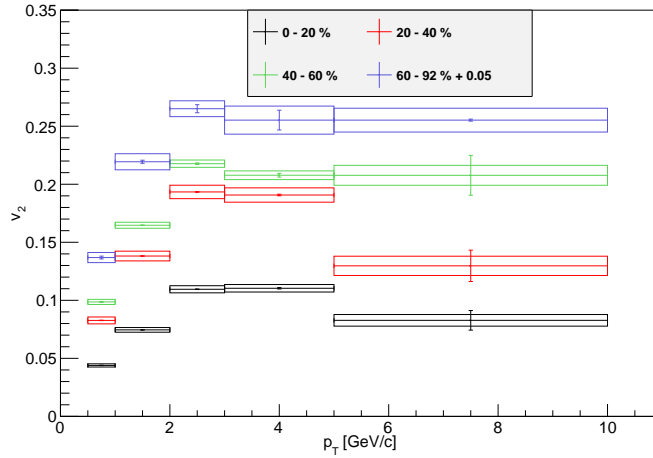


Figure 7.1: Hadron v_2 as function of p_T for the four centrality bins, 0-20% (black points), 20-40% (red points), 40-60% (green points), and 60-92% (blue points). The blue points have a constant offset for clarity. These are the same points used in References [3, 5, 32].

7.4 Background Procedure - Mean Seeds Mean Partners

The background method we use is absolute normalization through the use of mean seeds mean partners (MSMP). This procedure has been used extensively in the past and is only outlined here [3, 5, 16]. The isolation cut modifies this method and this modification is explained below. First, the trigger and partner particle yields are recorded in p_T and centrality bins. Each p_T bin is projected over all centrality and centrality is mapped onto the number of binary collisions, N_{coll} , and the number of participants in the collision, N_{part} . These distributions are shown in Figure 7.2. The top row is the trigger photons, the bottom row is the partner hadron, the left column is the yield as a function of N_{part} and the right column is the yield as a function of N_{coll} . The red and blue solid lines are fits to

$$n^{a,b} = \gamma \arctan(\beta N^\alpha), \quad (7.1)$$

and

$$n^{a,b} = \gamma(1 - e^{-\beta N^\alpha}), \quad (7.2)$$

where α , β , and γ are fit parameters.

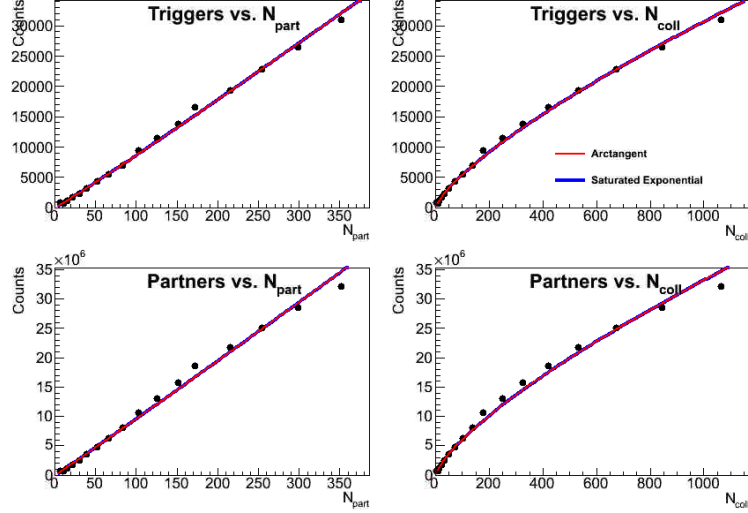


Figure 7.2: Trigger photon yield as a function of N_{part} (top left) and N_{coll} (top right) and Partner hadron yield as a function of N_{part} (bottom left) and N_{coll} (bottom right). These are for triggers with $7 \leq p_T \leq 9$ GeV/c and partners with $3 \leq p_T \leq 5$ GeV/c. The red and blue lines are fits to Equation 7.1 and Equation 7.2.

The MSMP level, ξ , can be obtained mathematically via

$$\xi \equiv \frac{\langle n^A n^B \rangle}{\langle n^A \rangle \langle n^B \rangle}. \quad (7.3)$$

There is a centrality bias for this method though because it doesn't account for the overall increase in yield for more central events, so in practice, ξ is found via

$$\xi = \frac{\sum_i n_i^A n_i^B w_i^{glaub}}{\sum_i n_i^A w_i^{glaub} \sum_i n_i^B w_i^{glaub}}, \quad (7.4)$$

where the sum over i is over each centrality bin and w_i^{glaub} is the Glauber model-calculated distribution for that centrality bin. These are shown for Au+Au collisions in Figure 7.3a for N_{part} and 7.3b for N_{coll} .

The ξ values for inclusive photons in Run 10 Au+Au MinBias collisions are shown as a function of centrality in Figure 7.4. Each trigger p_T bin is a different color and each partner p_T bin is a different row, they have been artificially offset so they are all legible. The open points are points that were used in previous analyses [3, 5]. In those analyses, they were only concerned

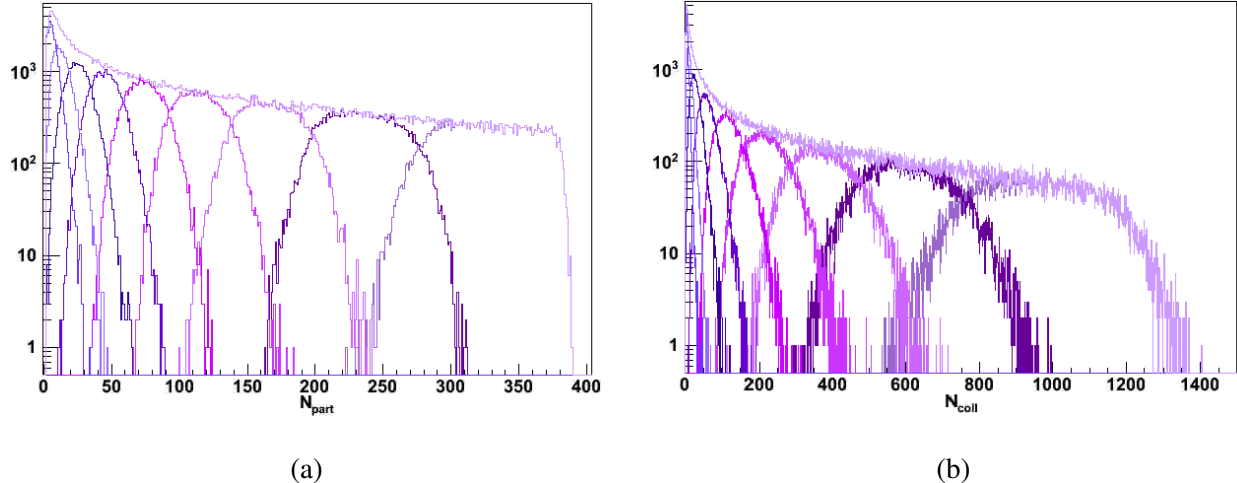


Figure 7.3: Glauber model-calculated probability distributions for 5% centrality bins in Au+Au collisions as a function of N_{part} (a) and N_{coll} (b).

with events with centrality between 0% and 40%. The values they found in those centrality bins are extrapolated from the fit in the 0 - 40% range. We have opened up the fit range to include all centralities, this causes our values to disagree slightly for larger centralities.

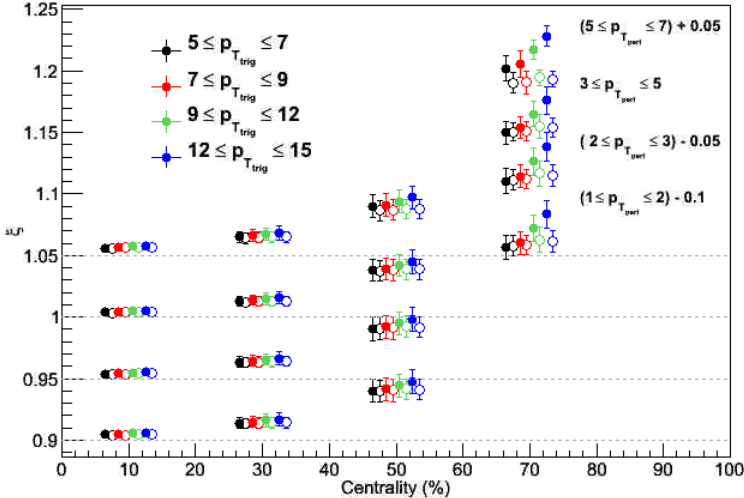


Figure 7.4: MSMP ξ as a function of centrality for inclusive photons in Run 10 Au+Au MinBias collisions. Each color is a trigger p_T bin and each row is a partner p_T bin, both have been artificially offset for clarity. The open points are points used in previous analyses [3, 5].

Once ξ is known for each trigger and partner p_T bin, the background level, b_0 is calculated via

$$b_0 = \xi \frac{N_{mix}^{ab}}{N_{mix}^a} \quad (7.5)$$

where N_{mix}^{ab} is the number of mixed background pairs and N_{mix}^a is the number of mixed background triggers. So now the per-trigger yield, Equation 1.14 is

$$\frac{1}{N_A} \frac{dN^{AB}}{d\Delta\phi_{AB}} = \frac{1}{N_A} \frac{dN_{real}^{AB}}{d\Delta\phi_{AB}} \frac{\epsilon_B}{Acc(\Delta\phi)} - \xi \frac{N_{mix}^{ab}}{N_{mix}^a} (1 + 2v_2^A v_2^B \cos(2\Delta\phi_{AB})). \quad (7.6)$$

7.4.1 Mean Seeds Mean Partners with Isolated Particles

The isolation cut creates a complication in the above MSMP procedure. Since the trigger particles are subject to an isolation cut that depends on the 20% centrality bin. This causes discontinuities in the distribution at the 20% centrality bin edges. Because of these discontinuities, Equation 7.1 and Equation 7.2 do not describe the data well. Instead, the data in the large centrality bins is fit to

$$n^{a,b} = \gamma + \beta x + \alpha x^2, \quad (7.7)$$

where α, β , and γ are fit parameters. The partner fits are unaffected because they don't depend on the isolation cut. These distributions and the fits are shown in Figure 7.5. The ξ values for isolated

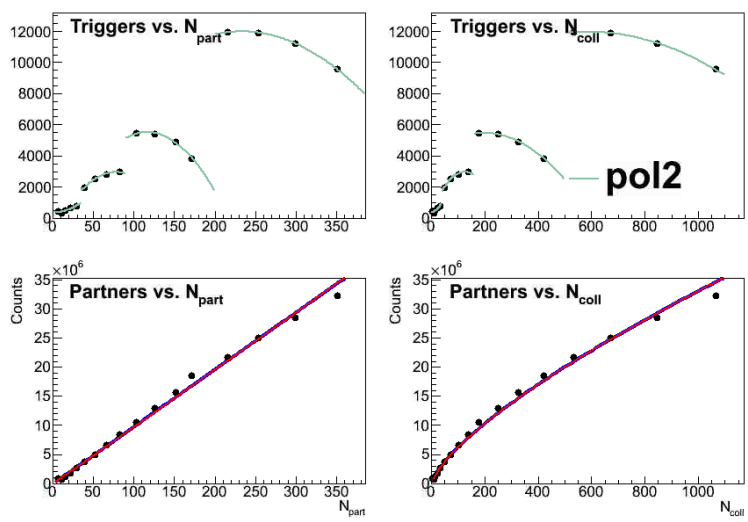


Figure 7.5: Trigger photon yield as a function of N_{part} (top left) and N_{coll} (top right) and partner hadron yield as a function of N_{part} (bottom left) and N_{coll} (bottom right). These are for triggers with $7 \leq p_T \leq 9$ GeV/c and partners with $3 \leq p_T \leq 5$ GeV/c. The red and blue lines are fits to Equation 7.1 and Equation 7.2. The green lines are fits to Equation 7.7.

photons from Run 10 Au+Au MinBias is shown in Figure 7.6. Each color is a trigger p_T bin and each row is a different partner p_T bin. The points have been shifted up and down and left and right for clarity. The open points are the same open points shown in Figure 7.4. We don't expect the isolated photon ξ to be the same as the inclusive particle ξ because the isolation cut changes the centrality distribution of the triggers. According to reference [16], if both the trigger and partner distributions rise we expect ξ to be larger than unity, if one distribution rises while the other falls ξ is less than unity, and if either distribution is independent of centrality, ξ equals unity. Looking at trigger and partner distributions in Figure 7.5 and the ξ values in Figure 7.6 with this intuition in mind can qualitatively verify that the ξ values.

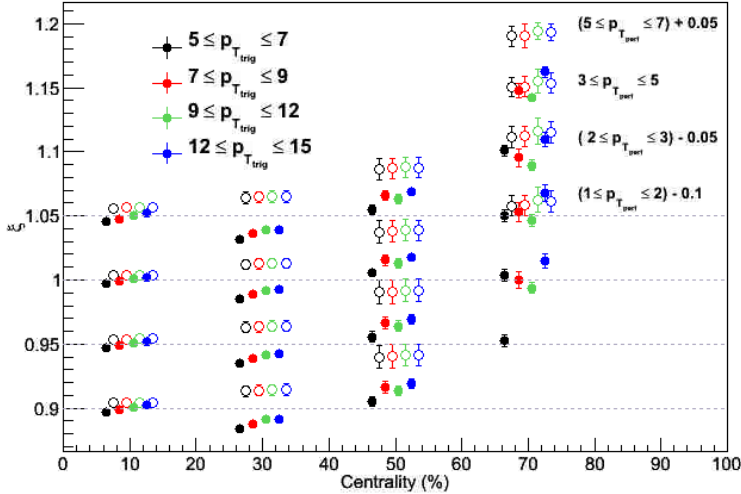


Figure 7.6: MSMP ξ as a function of centrality for isolated photons in Run 10 Au+Au MinBias collisions. Each color is a trigger p_T bin and each row is a partner p_T bin, both have been artificially offset for clarity. The open points are points used in previous analyses [3, 5].

7.5 Decay Photons

Decay photons are found by mapping the π^0 's to their decay photons. This procedure has been developed and used by many previous PHENIX correlations analyses from Au+Au [17, 18] to $p+p$ [56–58]. The $p+p$ analyses used an isolation cut to increase the direct photon signal, then a statistical subtraction method to obtain direct photons. The Au+Au analyses only use a statistical subtraction method to obtain direct photons. The analysis in this dissertation is the first Au+Au analysis using an isolation cut. This section describes the process of obtaining decay photon correlations, the decay photon probability function, or sharkfin, and how the isolation cut modifies that probability function.

We expect there to be a small η decay contribution to the dominate π^0 decay photon sample, this is described in Section 7.5.1.2. For now, we only consider the π^0 decay photons. A Monte Carlo simulation has been developed where the decay $\gamma - h$ pair yield is constructed by integrating

over all $\pi^0 - h$ pairs times a weight factor. That is,

$$N_{decay}^{\gamma-h}(p_T^\gamma) = \int \frac{\epsilon_\gamma(p_T^\gamma, p_T^{\pi^0}) \otimes \mathcal{P}(p_T^\gamma, p_T^{\pi^0})}{\epsilon_{\pi^0}(p_T^{\pi^0})} \otimes N^{\pi^0-h}(p_T^{\pi^0}) \quad (7.8)$$

where $N_{decay}^{\gamma-h}(p_T^\gamma)$ is the decay γ -h pair yield, ϵ_γ is the single decay photon efficiency, ϵ_{π^0} is the π^0 trigger efficiency that is been described in Section 3.5.1, and $\mathcal{P}(p_T^\gamma, p_T^{\pi^0})$ is the probability that a π^0 of $p_T = p_T^{\pi^0}$, to decay into a photon of p_T^γ [17]. This probability function is called a sharkfin because as a function of $p_T^{\pi^0}$, it looks like a sharkfin. This function is analytically calculable and is also found using a Monte Carlo, the Monte Carlo includes Gaussian smearing to account for detector resolution. They are described in more detail in the next section.

7.5.1 Decay Probabilities - Sharkfins

Sharkfins are π^0 decay probability functions that depend on the p_T and EMCAL z coordinate of π^0 for decaying into photons in a given photon p_T range. All the previous PHENIX analyses employ this probability to derive the decay photon-h correlation by adding weighted contributions of all π^0 's encountered in the same centrality. An example sharkfin is shown in Figure 7.7. We use the same sharkfins as References [3, 5, 32, 33] but they are modified by the probability of a π^0 to be isolated, this is described in the next section. Details for calculating sharkfins can be found in References [17, 33, 34].

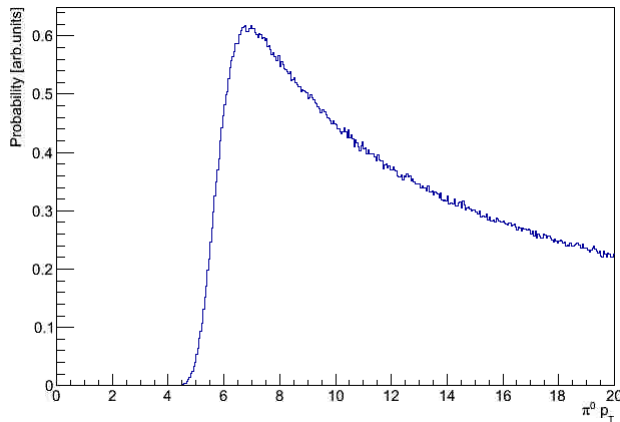


Figure 7.7: An example $\pi^0 - h$ decay probability function, or sharkfin, as a function of p_T of the π^0 .

7.5.1.1 Isolation Modifications to Decay Probabilities

As described in Reference [33], the isolation cut implies the need for alterations to the standard sharkfins. Our method applies a further function which multiplies the same original sharkfins like the one shown in 7.7 to account for these modifications. The shape and efficacy of the new modified sharkfin, along with the efficacy of the entire method to estimate the isolated π^0 decay contribution is studied in Reference [33] but we outline this method briefly here. If a π^0 does not pass the isolation cut, its decay photons will not be isolated. However, if a π^0 is isolated, the π^0 's decay photons may or may not also be isolated. To account for this, we must include the probability that the decay photon is isolated, given that the π^0 is isolated. Equation 7.8 can be rewritten to include this factor as

$$N_{decay}^{\gamma-h}(p_T^\gamma) = \int \frac{\epsilon_\gamma(p_T^\gamma, p_T^{\pi^0}) \otimes \mathcal{P}(p_T^\gamma, p_T^{\pi^0}) \otimes \mathcal{P}_{iso}(p_T^\gamma, p_T^{\pi^0})}{\epsilon_{\pi^0}(p_T^{\pi^0})} \otimes N^{\pi^0-h}(p_T^{\pi^0}), \quad (7.9)$$

where $P_{iso}(p_T^\gamma, p_T^{\pi^0})$ is the isolation probability function is described in more detail in the next paragraph and all the other factors are the same as Equation 7.8.

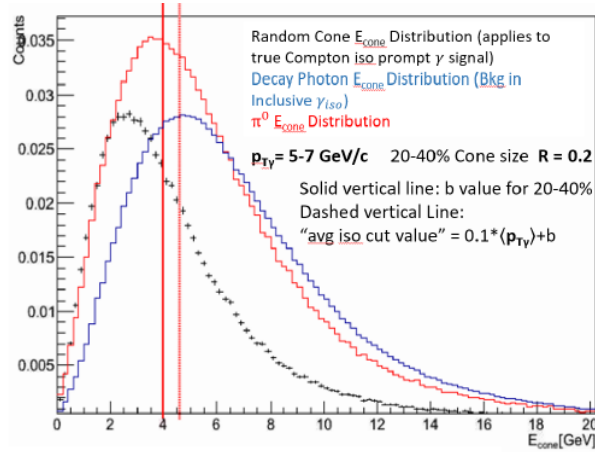


Figure 7.8: Energy distributions within cones of a size used in the analysis around various kinds of particles used in the analysis.

The isolation probability functions are generated by looping over the probability of a π^0 at $p_T^{\pi^0}$ producing decay photons at all possible decay photon p_T 's and for each bin, the π^0 cone

distributions taken from the data (Figure 7.8), are adjusted by first subtracting the p_T of the π^0 , and then averaging over this adjusted cone distribution to find the probability that the partner photon p_T plus the sampled adjusted cone energy would cause a decay photon at given decay photon p_T to fail the isolation cut. The resulting isolation probability function are shown in Figure 7.9 for four different decay photon energy ranges: $5 < E_\gamma < 7$ GeV (top left), $7 < E_\gamma < 9$ GeV (top right), $9 < E_\gamma < 12$ GeV (bottom left), and $5 < E_\gamma < 10$ GeV (bottom right). These functions are multiplied with the standard sharkfin probabilities to obtain the isolated sharkfin.

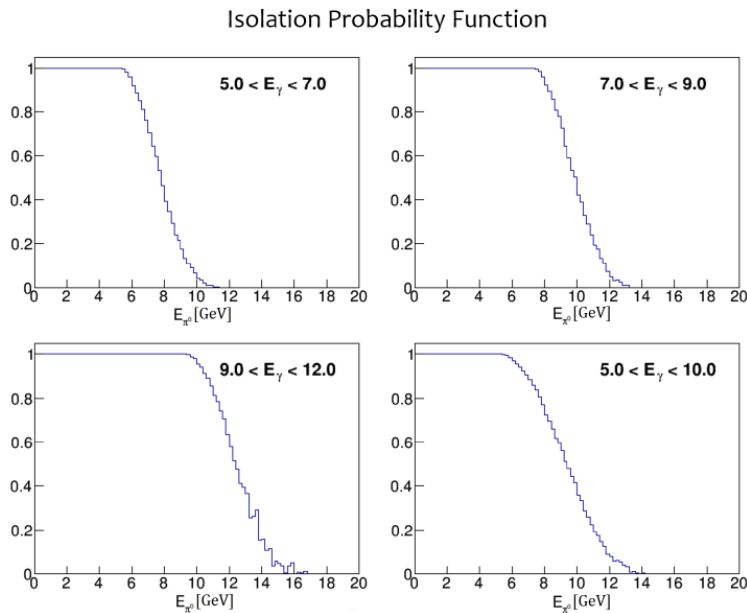


Figure 7.9: Isolation probability function as a function of π^0 energy for four different decay photon energy ranges: $5 < E_\gamma < 7$ GeV (top left), $7 < E_\gamma < 9$ GeV (top right), $9 < E_\gamma < 12$ GeV (bottom left), and $5 < E_\gamma < 10$ GeV (bottom right) [3, 33].

Figure 7.10 shows an example isolation cut sharkfin (red line), with a sharkfin without the isolation cut (green line) and the analytic form of the sharkfin (blue line) as a function of π^0 energy. These sharkfins were made using HIJING in References [3, 33].

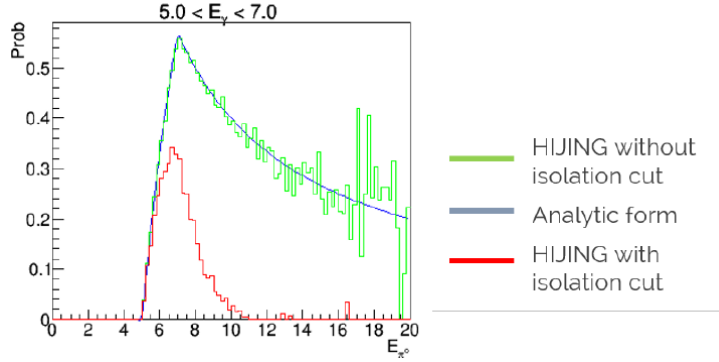


Figure 7.10: An example $\pi^0 - h$ decay probability function (sharkfin) as a function of π^0 energy with an isolation cut (red line) and without an isolation cut (green line) [3, 33].

7.5.1.2 Cutoff Correction to the Sharkfin Procedure

The sharkfins described above were found with a truncation at $p_T^{\pi^0} = 17$ GeV/c. This is because of π^0 's with $p_T > 17$ GeV/c the electromagnetic showers in the EMCAL merge and become indistinguishable. There aren't many π^0 with energy above 17 GeV/c anyway. To quantify this truncation, we make a cutoff deficiency correction, D_{cutoff}

$$D_{cutoff} = 1/C_{cutoff} = \frac{\int_{<17} dp_T^{\pi-h} P(p_T^{\pi-h}) \frac{dN^{\pi-h}}{dp_T^{\pi-h}} / \int_{<\infty} dp_T^{\pi-h} P(p_T^{\pi-h}) \frac{dN^{\pi-h}}{dp_T^{\pi-h}}}{\int_{<17} dp_T^\pi P(p_T^\pi) \frac{dN^\pi}{dp_T^\pi} / \int_{<\infty} dp_T^\pi P(p_T^\pi) \frac{dN^\pi}{dp_T^\pi}}. \quad (7.10)$$

The lower bound of the integrals are the low end of the trigger pt bin we are calculating the correction for and the yields of π^0 and $\pi^0 - h$ pairs, are determined from data and are corrected for the π^0 trigger efficiency. The values for this correction are small ranging mostly around 1% correction or less, with a few values for the highest trigger and associated pt bins (where the statistical error is large) in the 10-20% correction range. The corrections are applied and assigned a conservatively large 50% relative error [5, 59]. We use the previous cutoff corrections used for the statistical methods: inclusion of the isolation cuts to the derivation of these corrections were not included, since the size of the correction is small and the error assigned is already conservative. The HIJING study described later further justifies treating the cutoff correction and its uncertainties in this manner.

7.5.2 π^0 Combinatoric Background Effects in Decay Yield Estimation

Since we use π^0 's to estimate the decay yields, we potentially need to account for fake π^0 's. These come from photon pairs falling in the π^0 peak due to random combinations rather than actually being from the same π^0 . There are two ingredients that contribute to the number of fake π^0 's : the overall level of combinatoric background, the S/B level, and the size of the correlated pair yields, $Y_{fake \pi^0}$.

For the level of S/B , the $m_{\gamma\gamma}$ region near the π^0 mass is fit to a Gaussian plus a line and the yield ratios are extracted. The background is the integral of the line within 2σ of the peak. The signal is the area of the Gaussian minus the integral of the line within 2σ of the peak. This is shown in Figure 7.11 for isolated π^0 's on the left and inclusive π^0 's on the right for the same $\pi^0 p_T$ range, $7 < p_T < 9$ GeV/c. On the left side of this figure, the data are the black points, the red line is the Gaussian plus line fit, the green line is the signal Gaussian and the black line is the background line. On the right side, the data are the the black points, the Gaussian plus line fit is the black line, and the red line is the background line. This figure shows that for isolated π^0 's the level of background is generally greater than about 20% higher (less background) as in the the statistical method. This drives the effect of the fake π^0 's to be generally smaller than the statistical method.

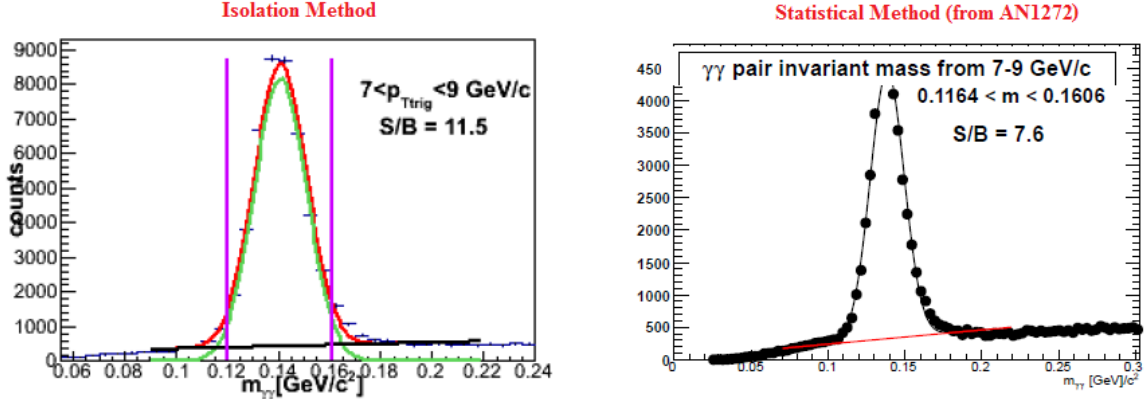


Figure 7.11: Example of increased S/B level for π^0 combinatorics in the isolated sample. The left panel shows the isolated π^0 $m_{\gamma\gamma}$ peak with the ratio if the integral of the red line to the black line (the S/B) shown. The right panel shows the $m_{\gamma\gamma}$ peak of inclusive π^0 with the ratio if the integral of the red line to the black line (the S/B) shown [32].

Once S/B levels of the triggers are collected, the contribution of the fake triggers to the trigger-partner pair yield, Y , follows according to:

$$Y_{tot} = \frac{N_{bkg} Y_{bkg} + N_{signal} Y_{true}}{N_{trigger}}, \quad (7.11)$$

The relative contribution of the background in terms of the factor X by which one needs to correct the Y_{tot} to remove the background contribution (*e.g.* $X = Y_{true}/Y_{tot}$) can be written as

$$X = \frac{(N_{tot} = N_{sig} + N_{bkg}) Y_{tot} - N_{bkg} Y_{bkg}}{N_{sig}} \frac{1.0}{Y_{tot}} = 1 + \frac{1}{s2b} \left(1 - \frac{Y_{bkg}}{Y_{tot}} \right) \quad (7.12)$$

The correction depends on the product of the S/B factor, $1/s2b$, and the ratio of Y_{bkg} to Y_{tot} the latter which is what we measure in the default measurements of Y_{π^0} or correspondingly our measurement of Y_{decay} which is mapped from Y_{π^0} . We measure Y_{bkg} by direct measurement of the pair yields from the upper and lower sidebands around the π^0 peak.

This method follows previous studies for the statistical method where good statistics exist in both the peak and sideband areas. An example is shown in Figure 7.12. This figure shows the inclusive π^0 Y_{bkg} ($\equiv Y_{sideband}/Y_{tot}$) as a function of $\Delta\phi$ for three p_T bin combinations [34]. It was

found, with a few exceptions, that for most bins the yields in the sidebands do not differ much from the peak yields—presumably since they have dominant contributions from asymmetric decays of the same π^0 's as which populate the signal peak region but where one high p_T photon has randomly mixed with the wrong low p_T partner. In Reference [17, 18], since the ratios were mostly close to one, it was decided not to make a correction but to rather assign a very conservative systematic error based on conservative bounds for the $Y_{tot}/Y_{sidebkg}$ ratios, 100% deviations for most bins except the most central events where the S/B is the lowest.

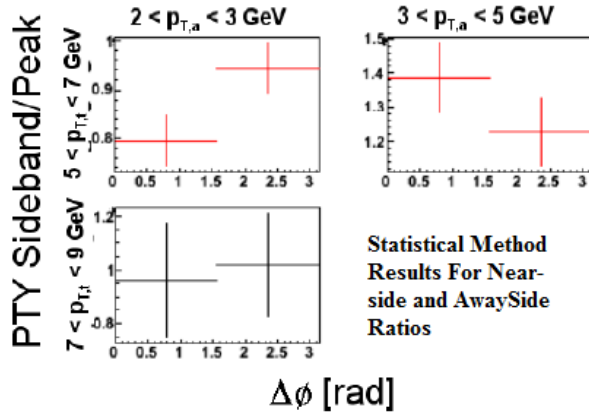


Figure 7.12: Inclusive Y_{bkg} ($\equiv Y_{sideband}/Y_{tot}$) as a function of $\Delta\phi$ for three p_T bin combinations [34].

For the isolation analysis, we performed the entire decay estimation analysis using fake π^0 's instead of real π^0 , with lower and higher invariant mass selections just below and above the sideband selections defining $Y_{sideband}$. Figure 7.13 shows $\Delta\phi - \pi > \pi/2$ away-side Y_{tot} (black points) and Y_{bkg} (red points) in the upper panels and the ratio (Y_{tot}/Y_{bkg}) in the lower panels, both are plotted as a function of trigger p_T . The left side is for $1 < p_T^{hadron} < 2$ in 0-20% central events and the right side is for $3 < p_T^{hadron} < 5$ in 40-60% central events. In a small number of cases, the ratio had statistically significant deviations from one, like in the left-hand panel of Figure 7.13. In these p_T bins, correction of the Y_{decay} with the X factor in Equation 7.12 was performed. In most other p_T bins, the ratio was consistent with one. In more than 50% of the p_T bins, due to the small amount of fake- π^0 's in the sidebands, statistical constraints were not good. So as in the

case of the statistical method, we choose for all bins other than the 0-20% central event p_T bins shown in the figure, to not make corrections and use the conservative bound of 100% deviation in the $Y_{tot}/Y_{sidebkg}$ ratios to assign an systematic error. Due to the even smaller overall S/B level for isolated π^0 's , this conservative error size does not unduly blow up the errors. This systematic error is discussed in Section 7.7.2.

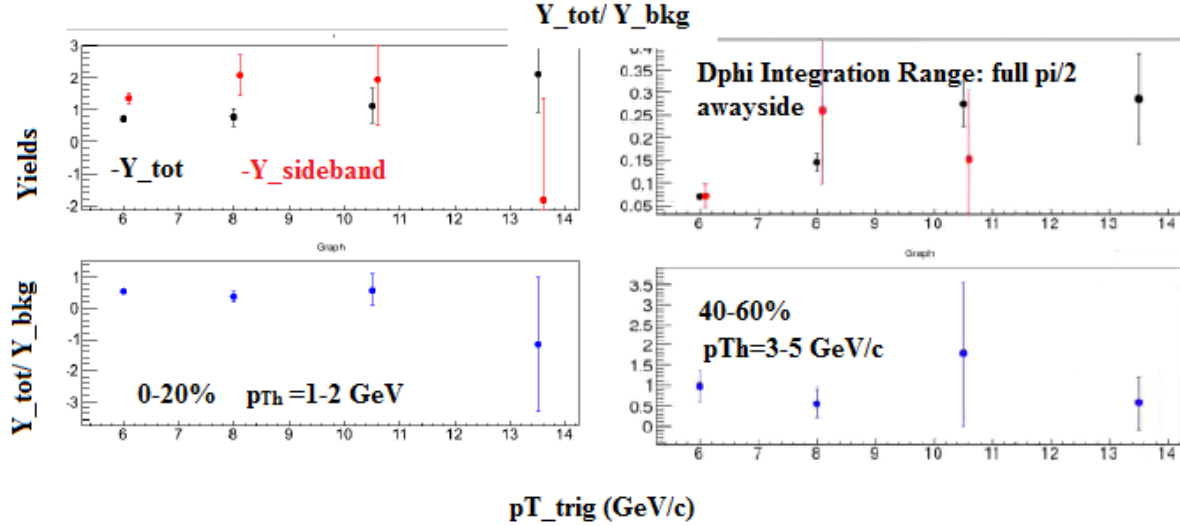


Figure 7.13: $|\Delta\phi - \pi| > \pi/2$ away-side Y_{tot} (black points) and Y_{bkg} (red points) in the upper panels and the ratio (Y_{tot}/Y_{bkg}) in the lower panels, both are plotted as a function of trigger p_T . The left side is for $1 < p_T^{hadron} < 2$ in 0 - 20% central events and the right side is for $3 < p_T^{hadron} < 5$ in 40-60% central events.

7.5.3 Non- π^0 Hadron Decay Effects in Decay Yield Estimation

Other mesons besides π^0 's contribute to the decay photon sample. The second largest contributor is η mesons, which contributes about 20%. For these and the other decay mesons that decay to two photons (about 5% of the total decay photons) contributions we follow what has been done previously in other analyses [5, 18]. It is too difficult to measure η -h correlations in Au+Au, but it has been measured in $p+p$ as shown in Figure 7.14. So far the behavior of η

mesons has been seen to mimic the behavior of π^0 's in other measurements in RHIC collisions, such as the overall suppression [18]. This figure shows the per-trigger yield for $5 < p_T^\gamma < 7 \text{ GeV/c}$ and $2 < p_T^{\text{hadron}} < 3 \text{ GeV/c}$ for $\pi^0 - h$ (red circles), $\gamma_{\text{decay from } \pi^0} - h$ (magenta crosses), $\eta - h$ (green triangles), $\gamma_{\text{decay from } \eta} - h$ (magenta crosses) in $p+p$ collisions [17]. We assume that the Au+Au energy-loss effects do not alter the relative differences/ratios between the number of η and π^0 mesons, in either single particle yields or pair correlation yields. As the plot demonstrates, the difference between $Y_{\eta-h}$ and Y_{π^0-h} is fairly small, within $\sim 10\%$. We use the same correction scheme as in the previous statistical method analyses to correct the Y_{decay} slightly to account for the effects of different $Y_{\eta-h}$ contributions, that is,

$$Y_{\text{decay}} = (1 - \delta_{h/\pi^0}^\gamma) Y_{\text{decay}}^{\pi^0} + \delta_{h/\pi^0}^\gamma Y_{\text{decay}}^\eta, \quad (7.13)$$

where δ is 1.24 calculated from “cocktail” estimations [17]. In this scheme, it is assumed that the other heavier mesons contributing (such as ω) will give similar pair yields as the η meson.

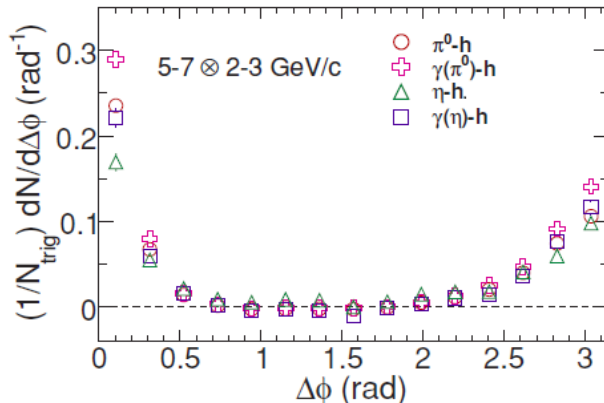


Figure 7.14: Per-trigger yield for $5 < p_T^\gamma < 7 \text{ GeV/c}$ and $2 < p_T^{\text{hadron}} < 3 \text{ GeV/c}$ for $\pi^0 - h$ (red circles), $\gamma_{\text{decay from } \pi^0} - h$ (magenta crosses), $\eta - h$ (green triangles), $\gamma_{\text{decay from } \eta} - h$ (magenta crosses) in $p+p$ collisions [17]. This figure has been used with permission. See Figure C.7 for more details.

All of the above does not include any effects of the isolation cut. Due to the relatively small η vs π^0 mass (0.4 GeV) difference compared to the trigger p_T 's used in the analysis ($> 5 \text{ GeV/c}$)

we do not expect the isolation cut to change the η/π ratio of the per-trigger yields more than a negligible amount. Since the isolation cone cut threshold is at smaller p_T (~ 2 GeV) we expect that the main effect of the isolation cut will be to reduce the contribution of η decay photons to the total slightly, that is, reduce the δ in Equation 7.13. We expect the propagated effect of this change to be smaller than the systematic error currently assigned (which would get smaller if δ gets smaller) which is approximately 100% of the correction size.

7.5.4 HIJING Study of Decay Photon Yield Method with Isolation Cut

In order to test several of the aspects of the methods discussed above for the extraction of the decay photon yield Y_{dec} , a particle level simulation study of the method in HIJING [60] was performed in References [3, 33]. The Au+Au events are simulated using the Monte Carlo software HIJING, we converted the list of HIJING particles output in to the similar type that we have for the real data and applied the nominal PHENIX acceptance and energy resolution.

In the simulation we know exactly the identity of the photons. The deviations from the truth are examined by comparing the $\gamma_{decay} - h$ correlations that are derived from the inclusive photons following the procedures outlined above, Y^{dec} , with the correlations that are obtained directly using the known photon's identity, Y^{true} . The comparison is quantified as the percent error, defined by,

$$\% - error = \frac{Y^{dec} - Y^{true}}{Y^{true}}. \quad (7.14)$$

Figure 7.15 shows the %-error of the derived from the true HIJING $\gamma_{dec} - h$ pair correlation functions, background, and jet functions, as a function of z_T , in all centrality bins with the isolation cut applied. The green points are $7 < p_{Tdec} < 9$ GeV triggers and the red points are the $7 < p_{Tdec} < 9$ GeV triggers. The yellow band indicates 2% ranges and each plot is a centrality bin. For the $5 < p_{Tdec} < 7$ GeV triggers, the agreement was even better so the points in the figures represent only the worse cases. The study did not generate sufficient statistics to study the $12 < p_{Tdec} < 15$ GeV triggers in the study. The points vary from the top of the 2% band to the bottom of it so we choose a 4% systematic error to cover virtually all the deviations. Note that

the lowest z_T point deviations are for the 0.5-1 GeV/c partner hadron bin, which is not used in our analysis. This error is discussed further in Section 7.7.1.

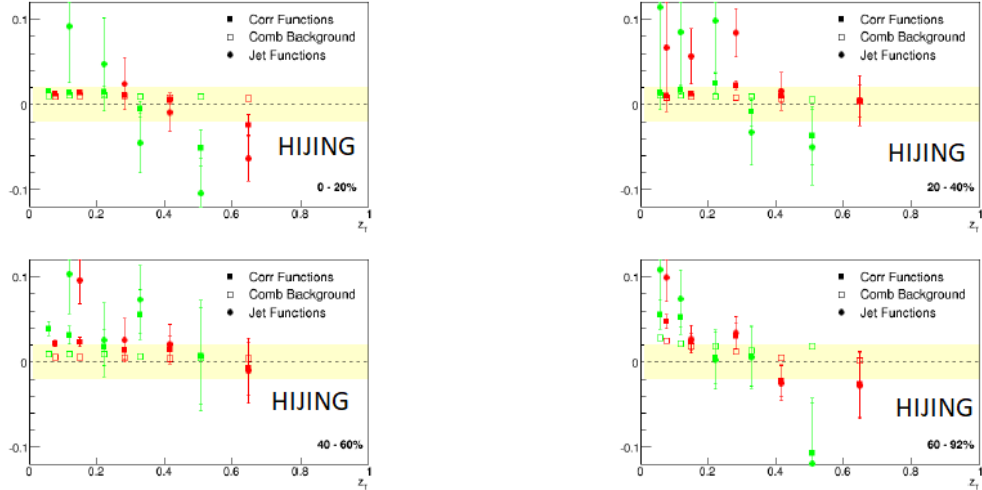


Figure 7.15: The %-error of the derived from the true HIJING $\gamma_{dec} - h$ pair correlation functions, background, and jet functions, as a function of z_T , in all centrality bins with the isolation cut applied. The yellow band indicates 2% ranges. The red points are $7 < p_{Tdec} < 9$ and the green points are $9 < p_{Tdec} < 12$.

7.6 R_γ

The variable R_γ is used to get direct photons from the decay and inclusive photons in the statistical subtraction method. From the definition of direct photons,

$$N_{direct} = N_{inclusive} - N_{decay}, \quad (7.15)$$

where N is the number of direct, inclusive, and decay photons. For the per-trigger yields, this equation can be rewritten as

$$N_{direct} Y_{direct} = N_{inclusive} Y_{inclusive} - N_{decay} Y_{decay}, \quad (7.16)$$

where Y is the per-trigger yield. This equation can be solved for the per-trigger yield of direct photons,

$$Y_{direct} = \frac{R_\gamma Y_{inclusive} - Y_{decay}}{R_\gamma - 1}, \quad (7.17)$$

where

$$R_\gamma = \frac{N_{inclusive}}{N_{decay}}. \quad (7.18)$$

It is sometimes convenient to think about how R_γ in terms of the signal-to-background ratio and rewrite R_γ as

$$R_\gamma = 1 + \frac{N_{direct}}{N_{decay}}. \quad (7.19)$$

We use Equation 7.17 to obtain the direct photon - hadron per-trigger yields when doing the statistical method. The R_γ values we use are taken from previous analyses [3, 5, 32]. The values for the four centrality bins we use are shown in Table 7.1. In Reference [32], a study was done that confirms that the abundance of conversion photons expected in Run 11 from the effects of the VTX has no effect on the final jet function so the R_γ for Run 11 is the same as the R_γ for Run 10.

The isolation cut method also uses the Equation 7.17 to obtain the direct photon - hadron per-trigger yields, but the R_γ is modified. This modified R_γ is called $R_{\gamma effective}$ or R'_γ and is defined by

$$\rho = \frac{R'_\gamma}{R_\gamma} = \frac{N_{inclusive}^{isolated} N_{decay}}{N_{inclusive} N_{decay}^{isolated}}. \quad (7.20)$$

where $N_{inclusive}^{isolated}$ is the total number of isolated photons, $N_{inclusive}$ and N_{decay} are the total number of photons and the number of decay photons, and $N_{decay}^{isolated}$ is the number of decay photons identified in the isolation cone. The values of R_γ , ρ , and R'_γ are listed in Table 7.1 for each centrality and trigger p_T bin.

As with the sharkfin decay probability mapping functions, the R'_γ is defined differently for this analysis compared to the $p + p$ methods also used in PHENIX, notably Reference [18], due to there being only an isolation cut, and no required π^0 anti-tagging cut. It also is only a first order estimate of the enhancement over the base R_γ , possibly not including more complicated effects of detector efficiency. Nonetheless, the estimate is shown to work within a level smaller than the base

Table 7.1: R_γ , ρ , and R'_γ values for each trigger p_T for each centrality.

Centrality (%)	Trigger p_T (GeV/c)	R_γ	ρ	R'_γ
0 - 20	5 - 7	1.66(9)	1.20	1.99(11)
	7 - 9	2.30(16)	1.32	3.06(22)
	9 - 12	3.18(27)	1.36	4.44(37)
	12 - 15	4.65(49)	1.39	7.02(68)
20 - 40	5 - 7	1.42(7)	1.12	1.59(8)
	7 - 9	1.77(12)	1.23	2.18(15)
	9 - 12	2.41(21)	1.38	3.39(29)
	12 - 15	2.85(33)	1.53	4.68(51)
40 - 60	5 - 7	1.24(5)	1.09	1.36(6)
	7 - 9	1.48(9)	1.21	1.80(11)
	9 - 12	1.82(15)	1.37	2.53(21)
	12 - 15	2.60(36)	1.63	4.52(59)
60 - 92	5 - 7	1.19(5)	1.07	1.27(5)
	7 - 9	1.36(9)	1.23	1.67(11)
	9 - 12	1.63(16)	1.47	2.43(24)
	12 - 15	1.77(25)	1.56	2.89(40)

R_γ uncertainties in tests with full HIJING events and realistic detector resolution as described in References [3, 33]. Further in that work, systematics of using this estimate are determined. They are included in our analysis in the total uncertainty of the decay photons contribution described later in the systematic errors Section 7.7.

7.7 Systematic Errors

This analysis is following previous analysis completed by Nowo Rivelis, this section is largely adapted from his Ph.D. dissertation [3]. The systematic errors in the jet functions are derived from

- the v_2 systematic error,
- MSMP ξ error,
- R'_γ error,
- and the procedure used to obtain decay photons.

The R'_γ systematic is from the statistical error on the R'_γ value. This uncertainty includes contributions from the π^0 reconstruction, decay photon extraction, cluster merging, and non-linear energy scaling in the EMCAL. There is an additional 5% systematic for the procedure for getting R_γ to R'_γ .

The isolated particle v_2 systematic error is explained in Section 5.3.3. There is also an additional factor of the hadron v_2 systematic error, this is shown in Figure 7.1.

The MSMP ξ systematic is from the spread in the ξ values from the four fitting combinations described in Section 7.4.1.

There are many sources of error that contribute to the decay photons systematic error. The following subsections describe each of them.

7.7.1 Decay Photon Systematics - Method

The main error source that contributes to the total decay photon systematic is the method of obtaining decay photons. This is a 4% contribution. The method was studied extensively in Reference [33]. See the explanation and figures there for full details. One highlight from Reference [33] is shown in Figure 7.15 and described in Section 7.5.4.

7.7.2 Decay Photon Systematics - S/B

While the above 4% error is the dominate systematic for decay photons in most p_T bins, in other bins, the error from contributions of the combinatoric background of the photon pairs also contributes heavily. This error is defined by

$$\sigma_{comb}^{\pi^0} = \frac{Y_{true} - Y_{measured}}{Y_{measured}}, \quad (7.21)$$

where Y is the per trigger yield, Y_{true} is for the true decay photons, $Y_{measured}$ is for the measured π^0 's that is defined by

$$Y_{measured} = \frac{N_{background}Y_{background} - N_{signal}Y_{true}}{N_{trigger}}, \quad (7.22)$$

where $N_{background}$ is the number of background photons, $Y_{background}$ is the number of photons in the sidebands of the π^0 peak, N_{signal} is the number of photons in the π^0 peak, and $N_{trigger}$ is the number of trigger photons. Combining Equations 7.21 and 7.22, leads to the working equation,

$$\sigma_{comb}^{\pi^0} = \frac{1 - \frac{Y_{background}}{Y_{measured}}}{\frac{N_{signal}}{N_{background}} \frac{Y_{background}}{Y_{measured}}}. \quad (7.23)$$

This form of $\sigma_{comb}^{\pi^0}$ does not depend on knowing Y_{true} . The ratio $N_{signal}/N_{background}$ is the signal-to-background ratio (S/B). It is the ratio of the counts in the π^0 peak to the counts in the sidebands. The signal to background ratios in Run 10 and 11 are similar to previous analyses [3, 32]. We used measured values of the signal to background ratio and differences between sideband yields ($Y_{measured}/Y_{background}$) to estimate the combinatoric pair error. Figure 7.16 shows the isolated π^0 invariant mass peak for 0-20% events for each trigger bin used in this analysis. The red line is a Gaussian plus line fit to the data, the green line is just the Gaussian from the fit, and the black line is just the line from the fit. The signal is found by integrating the Gaussian (green line) in 2σ of the peak, this is the region between the vertical purple lines. The background is found by integrating the line in the same region. The signal-to-background ratio is the ratio of these two integrals and is printed on each panel. There are other smaller sources of error from the decay photons, they are the π^0 cutoff correction and the mapping procedure. We use the same values for Run 10 and Run 11 for these two errors [3].

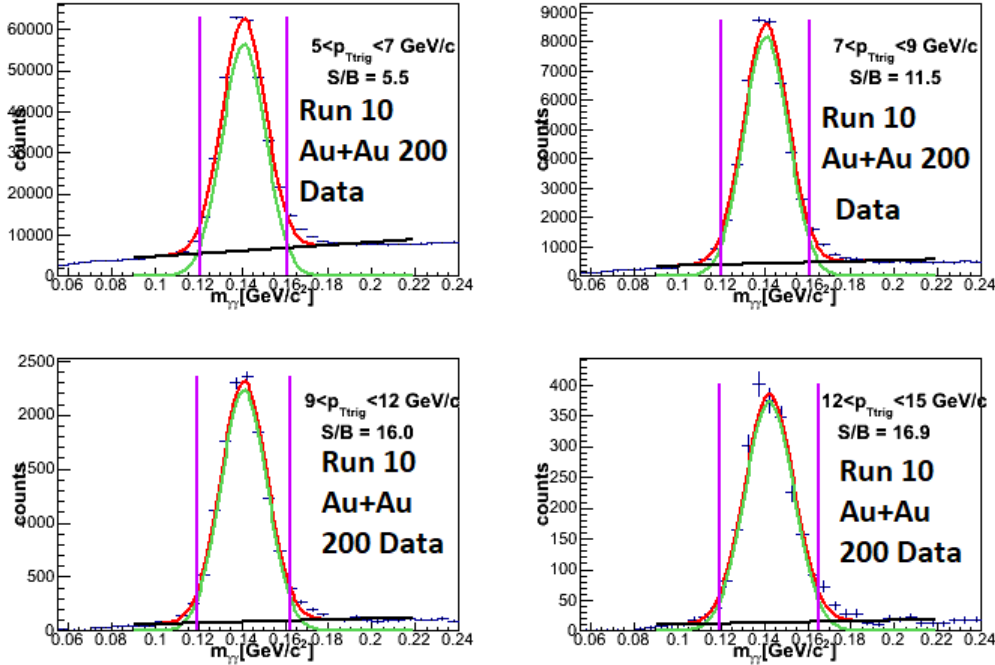


Figure 7.16: Isolated π^0 invariant mass ($m_{\gamma\gamma}$) peak for 0 - 20% events for each trigger bin used in this analysis. The red line is a Gaussian-plus-line fit to the data, the green line is the Gaussian from the fit, and the black line is the line from the fit. The S / B ratios are found by integrating the green line in 2σ of the peak (the region between the vertical magenta lines) and dividing it by the integral of the line in the same region. The signal-to-background ratio (S / B) is shown in each panel.

7.7.3 Decay Photon Systematics - π^0 Cutoff

There is a small systematic for the truncation of the p_T of π^0 's in the sharkfins. This is discussed in more detail in Section 7.5.1.2.

7.7.4 Decay Photon Systematics - η Contribution

There is a constant 2.3% systematic for subtracting the η contribution to the π^0 's. This is discussed in more detail in Section 7.5.3.

7.7.5 Non-Decay Method Systematics

As discussed in Section 7.5.1, a full HIJING study was performed to test the inclusion of the isolation cut on the π^0 -to-decay mapping methods used in the previous statistical method results [3, 33]. Most of the systematic errors from our methods are captured in inclusion of the systematic errors on the decay yield, Y_{dec} , as described in the previous subsections of this section, especially the 4% derived from the HIJING study results.

However, the HIJING study also was able to test other aspects of the method, such as performance of the isolation cut itself on the inclusive sample in the presence of real decays and jets, and in particular, the method of calculating ρ and R'_γ . These other aspects were further tested by comparing the full results of the subtraction method to obtain the actual $Y_{isodirect}$ per trigger yields. These are shown in Figure 7.17. The left side shows the jet functions for the 20 - 40% central events for $7 < p_T^\gamma < 9$ GeV/c and $2 < p_T^{hadron} < 3$ GeV/c (top) and $7 < p_T^\gamma < 9$ GeV/c and $5 < p_T^{hadron} < 7$ GeV/c (bottom) for both the derived direct photons (blue points) and the true direct photons (red). The right side shows the ratio of derived $\pi/2$ away-side direct photon-hadron yield to the true $\pi/2$ away-side direct photon-hadron yield for $7 < p_T^\gamma < 9$ GeV/c (red) and $9 < p_T^\gamma < 12$ GeV/c (green) triggers. The yellow band shows the 20% deviation.

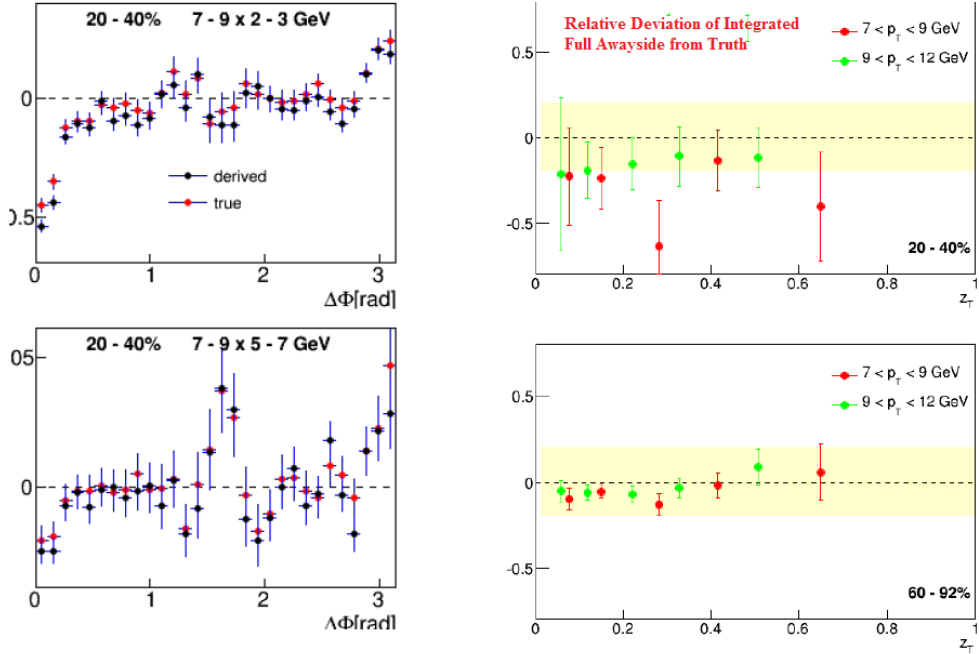


Figure 7.17: Summary of the HIJING study carried out in References [3, 33]. The left side shows the jet functions for the 20-40% central events for $7 < p_T^\gamma < 9 \text{ GeV}/c$ and $2 < p_T^{hadron} < 3 \text{ GeV}/c$ (top) and $7 < p_T^\gamma < 9 \text{ GeV}/c$ and $5 < p_T^{hadron} < 7 \text{ GeV}/c$ (bottom) for both the derived direct photons (blue points) and the true direct photons (red). The right side shows the ratio of derived $\pi/2$ away-side direct photon-hadron yield to the true $\pi/2$ away-side direct photon-hadron yield for $7 < p_T^\gamma < 9 \text{ GeV}/c$ (red) and $9 < p_T^\gamma < 12 \text{ GeV}/c$ (green) triggers. The yellow band shows the 20% deviation.

Figure 7.17 shows the full subtraction procedure demonstrates an agreement with the simulation truth well within 20% relative errors, but does not constrain possible method errors further. For most points, the maximum deviation was found to be in the $\phi \sim 90$ degree region where PHENIX has the worst acceptance and statistics in the simulation were low. The study showed that integrating the away-side peak in the left panel figures results in agreements generally even better than 20% on the deviation from the truth for all points with high statistics. Also, part of these deviations come from the decay method errors (see Section 7.5.4) and should not be double counted. To ensure this doesn't happen, we include a separate non-decay method centrality

independent relative-sized systematic error to account for possible deviations such as those shown in Figure 7.17 as 12% for the 5-7 GeV/c trigger p_T bin and 15% for all other p_T bins. These are relative errors added to the final results. For virtually all bins, the size of the relative errors from this contribution are sub-dominant to either the other systematic or the statistical error.

7.7.6 Systematics Summary

The final systematic error is found by adding all of these contributions in quadrature. The systematic error on the away-side yields is the systematic error on the rebinned jet function. The systematic error on the I_{AA} points is propagated from the away-side yield. The systematic error on the average I_{AA} points is the error on the fit used to average each z_T range.

Figure 7.18 shows the $\pi/2$ away-side error sources for each trigger and partner p_T bin combinations for central events in Run 10 (black lines) and Run 11 (red lines). These error sources are, from left to right, v_2 , normalization (MSMP), decay photons, R_γ , total systematic error and total statistical error. Each plot is a different p_T bin combination. Trigger p_T increases to the right while partner p_T increases going down. Immediately obvious in these plots is that the statistical error is larger than the systematic error in all cases. This is the case for all centralities for all away-side integration regions. Figures 7.19 and 7.20 show the systematic error contribution broken down by source for Run 10 and Run 11 central events for all systematic error sources for the $\pi/2$ and $\pi/5$ away-side. Statistical errors are not included on these figures as they dominate and would mask the individual error contributions. These error sources are, from left to right, v_2 , normalization (MSMP), decay photons, R_γ , and total systematic error. The systematics for the other centralities are shown in Appendix B.

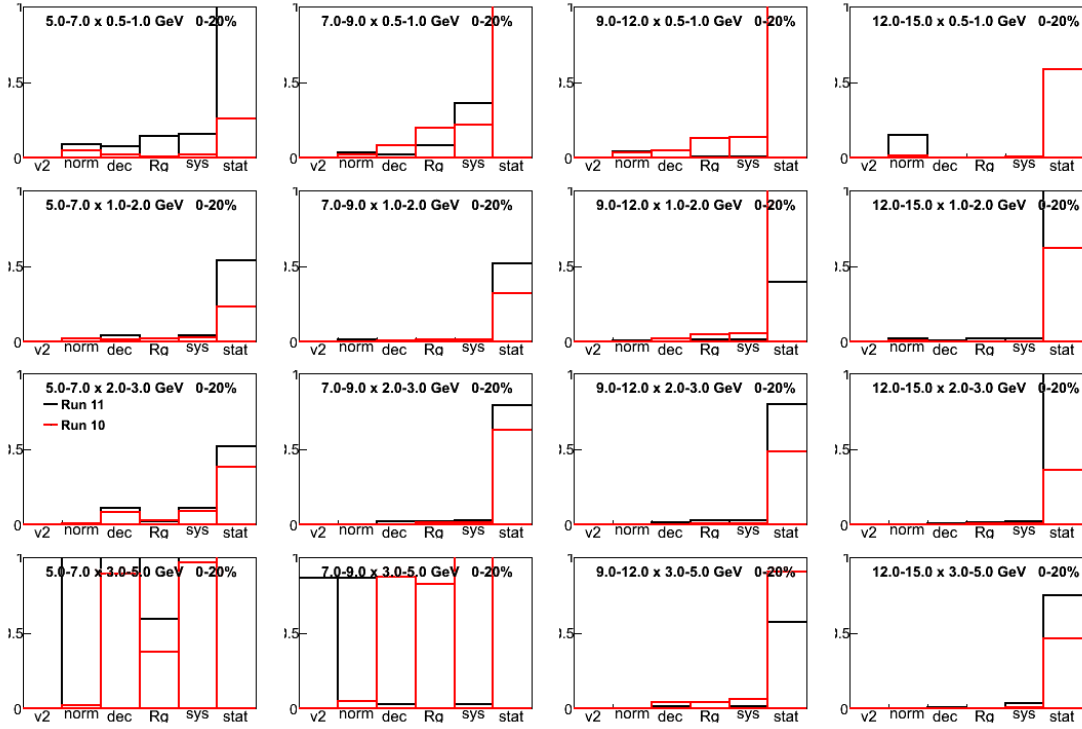


Figure 7.18: Error contributions of the direct photon $\pi/2$ away-side yield broken down by source for Run 10 (red) and Run 11 (black) central events. Each source is a different bin from left to right, v_2 , normalization (MSMP), decay photons, R_γ , total systematic error, and total statistical error. Each plot is a different p_T bin combination. Trigger p_T increases to the right while partner p_T increases going down.

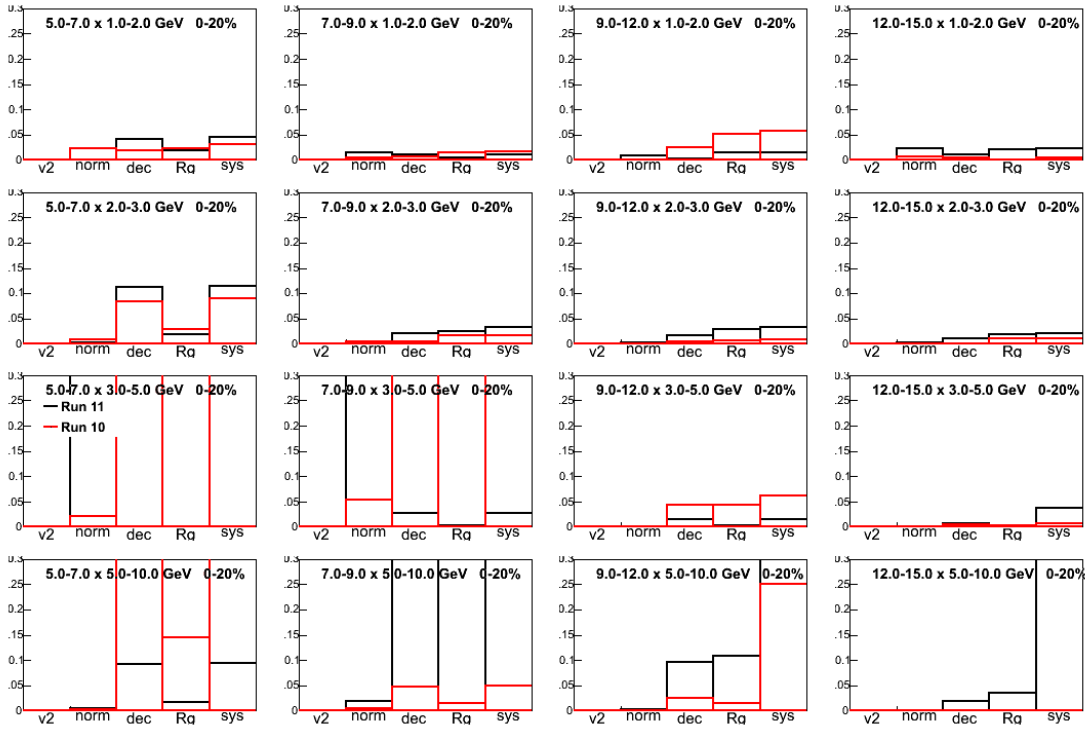


Figure 7.19: Systematic error contributions of the direct photon $\pi/2$ away-side yield broken down by source for Run 10 (red) and Run 11 (black) central events. Each source is a different bin from left to right, v_2 , normalization (MSMP), decay photons, R_γ , and total systematic error. Each plot is a different p_T bin combination. Trigger p_T increases to the right while partner p_T increases going down. This is the same as Figure 7.18 but without the statistical error for each p_T bin combination.

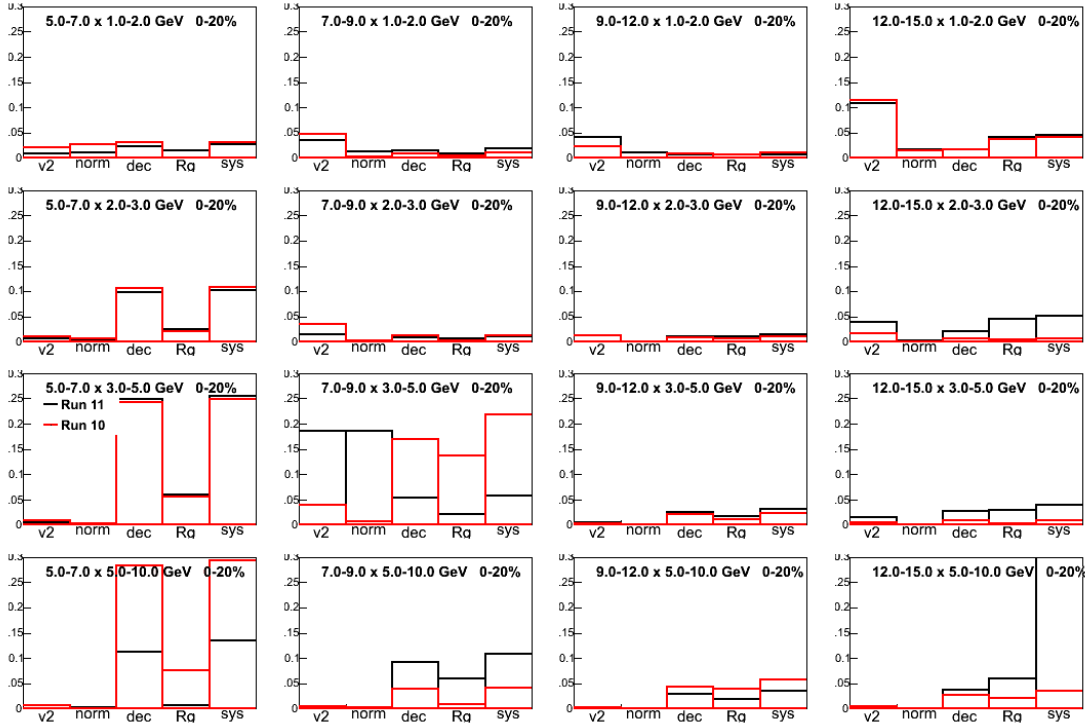


Figure 7.20: Systematic error contributions of the direct photon $\pi/5$ away-side yield broken down by source for Run 10 (red) and Run 11 (black) central events. Each source is a different bin from left to right, v_2 , normalization (MSMP), decay photons, R_γ , and total systematic error. Each plot is a different p_T bin combination. Trigger p_T increases to the right while partner p_T increases going down.

8 RESULTS - ISOLATED GAMMA-HADRON CORRELATIONS

8.1 Introduction

This section is devoted the results of the gamma-hadron correlations. First, the correlation functions and jet functions are shown, then the integrated away-side yields of the jet functions. The scheme for combining Run 10 and Run 11 data is then outlined. Once the per-trigger yields have been combined, the I_{AA} is determined. The chapter ends by comparing the results with the optimized isolation cut to a modified isolation cut to prove that the optimized isolation cut behaves the way we believe it should. And finally, the results determined in this dissertation are compared to other PHENIX results.

8.2 Correlation Functions

An example set of $\gamma_{iso} - h$ correlation functions are shown in Figure 8.1. Each plot is a different p_T bin combination. Trigger p_T increases from left to right while partner p_T increases from top to bottom. The black points are the correlation function. The black line is the background level. The magnitude of the background is found using MSMP and the shape is found using the isolated photon v_2 and hadron v_2 . Notice that for some p_T combinations, $9 < p_{T\text{trig}} < 12 \times 1 < p_{T\text{assoc}} < 2$ and $2 < p_{T\text{assoc}} < 3$, the flow shape is opposite of the positive cosine curve. This is because the trigger isolated photon has a small negative v_2 and the hadron v_2 has increased it so it is obvious in the plot. The background magnitude decreases as both trigger and partner p_T increases. Appendix A shows the $\gamma_{iso} - h$, $\pi^0 - h$, and $\gamma_{dec} - h$ correlation functions for both Run 10 and 11 for all centralities.

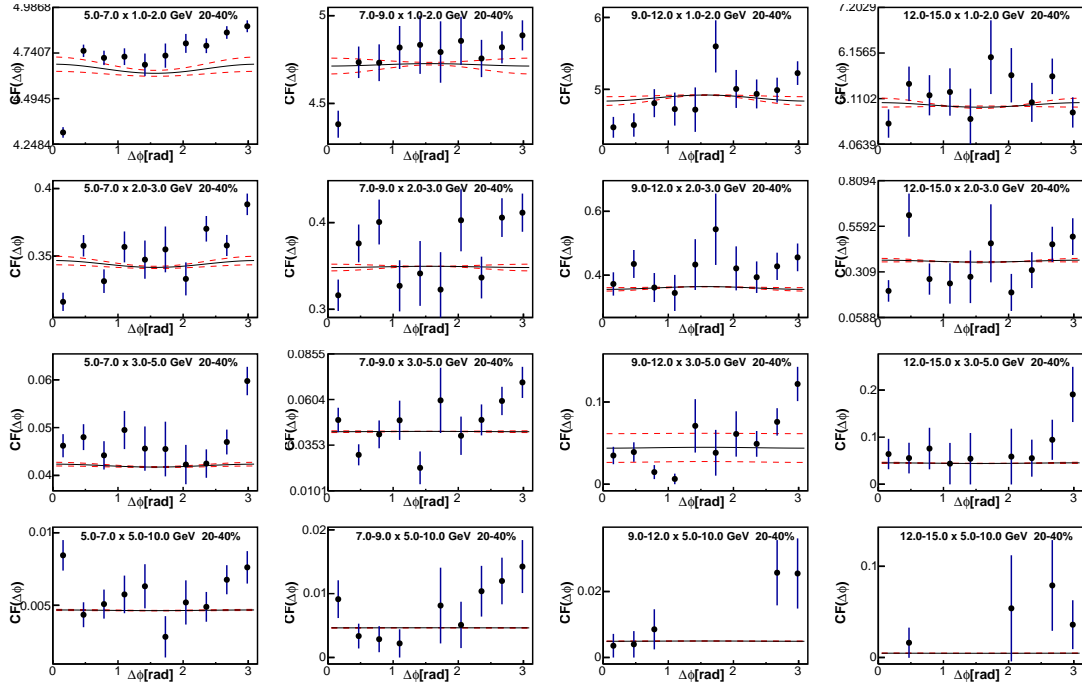


Figure 8.1: Run 11 Au+Au $\gamma_{iso} - h$ correlation functions for the 20-40% central events. Each plot is a different p_T bin combination. Trigger p_T increases from left to right while partner p_T increases from top to bottom. The black line represents the background level, the red lines around it is the error on the black line.

8.3 Jet Functions

Once the background is subtracted from the correlation function, we obtain the jet function. Example jet functions are shown in Figure 8.2. This figure shows the $\gamma_{iso} - h$ (black points), $\gamma_{dec} - h$ (red points), and $\gamma_{dir} - h$ (blue points) for central events in Run 11. Each plot is a p_T bin combination. Trigger p_T increases from left to right while partner p_T increases from top to bottom. The point closest point to $\Delta\phi = 0$ is inside the isolation cone and should be ignored. Even though the y-axes are not the same, it is obvious that the away-sides are largest for the small p_T bin combinatons and decrease as both the trigger and partner p_T increases. The $\gamma_{dir} - h$ (blue points) are obtained via the statistical subtraction method using the modified R'_γ described in the previous chapter. Appendix A shows all the jet functions for Run 10 and 11 for all centralities.

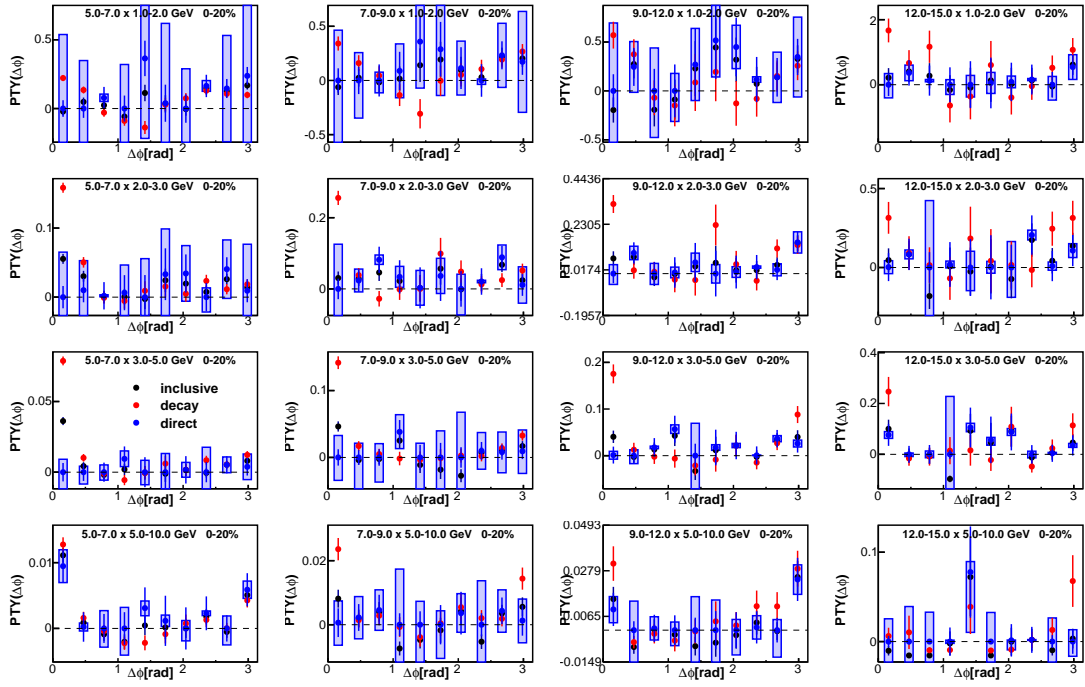


Figure 8.2: Run 11 Au+Au $\gamma_{iso} - h$ (black points), $\gamma_{dec} - h$ (red points), and $\gamma_{dir} - h$ (blue points) jet functions for 0 - 20% central events. Each plot is a different p_T bin combination. Trigger p_T increases from left to right while partner p_T increases from top to bottom.

8.4 Away-side Yields

We now integrate the jet functions to find the away-side yields. We show the integrated per-trigger yields as a function of $z_T = p_T^h/p_T^\gamma$ in the $\pi/3$ away-side region for each centrality bin for Run 10 in Figure 8.3. Each centrality bin is offset by factors of 10 and has different colored points: 0 - 20% (orange points), 20 - 40% (green points), 40 - 60% (blue points), and 60 - 92% (magenta points). The $p+p$ points are shown in red. Each trigger p_T bin has a different marker style. The colored lines are just there to guide the eye. Some of the error bars appear large but that is because the per-trigger yields are consistent with zero and the y-axis is a log scale. We also integrate the $\pi/2$ and $\pi/5$ away-sides for both Run 10 and 11. These yields, with the $p+p$ baseline will be used to make I_{AA} .

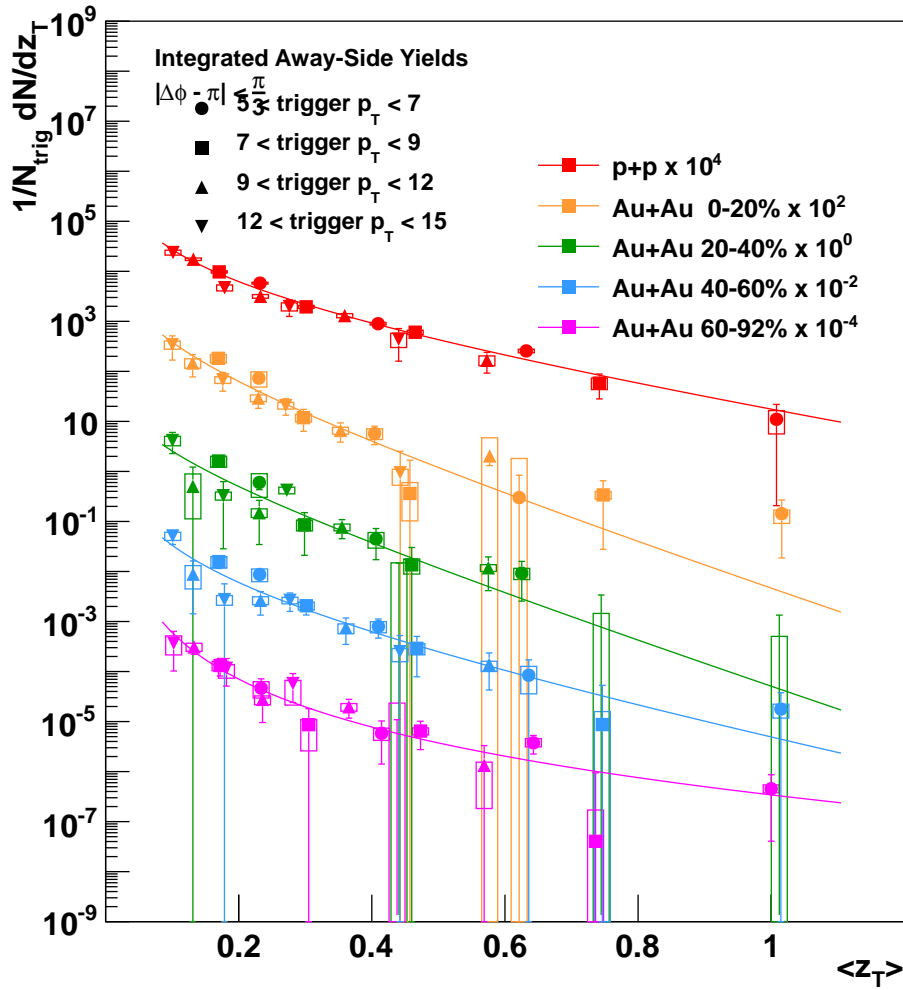


Figure 8.3: Run 10 Au+Au $\gamma_{dir} - h \pi/3$ away-side yield as a function of z_T for the four centrality bins used in this analysis, 0 - 20% (orange points), 20 - 40% (green points), 40 - 60% (blue points), and 60 - 92% (magenta points). The $p+p$ points are shown in red. Each trigger p_T bin has a different marker style. The colored lines are just there to guide the eye.

8.5 I_{AA}

As explained in the introduction, the I_{AA} is the ratio of the away-side yield of Au+Au collisions to $p + p$. The I_{AA} as a function of z_T for the $\pi/3$ integrated away-side is shown in

Figure 8.4 for Run 10 and Figure 8.6 for Run 11. Each trigger p_T bin is a different color and the four $p_{T\text{assoc}}$ bins: 1-2, 2-3, 3-5, and 5-10 GeV/c increase from left to right. The gray horizontal lines with yellow error bars are fits to the two different z_T regions. These are used to average the I_{AA} over these regions. Figure 8.5 shows the I_{AA} as a function of z_T for Run 10 for the other integration regions used in this analysis. Figure 8.7 shows the I_{AA} as a function of z_T for Run 11 for the other integration regions used in this analysis.

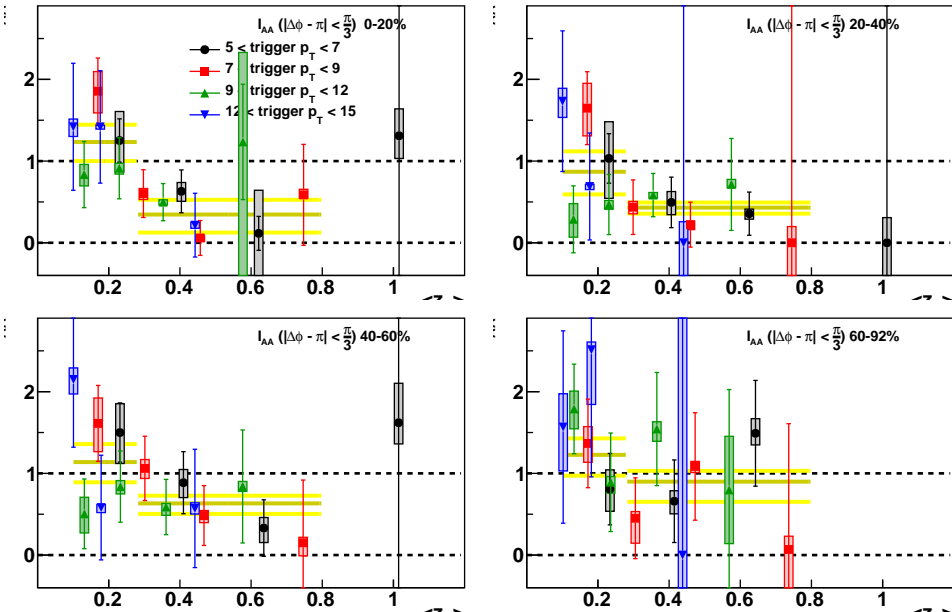
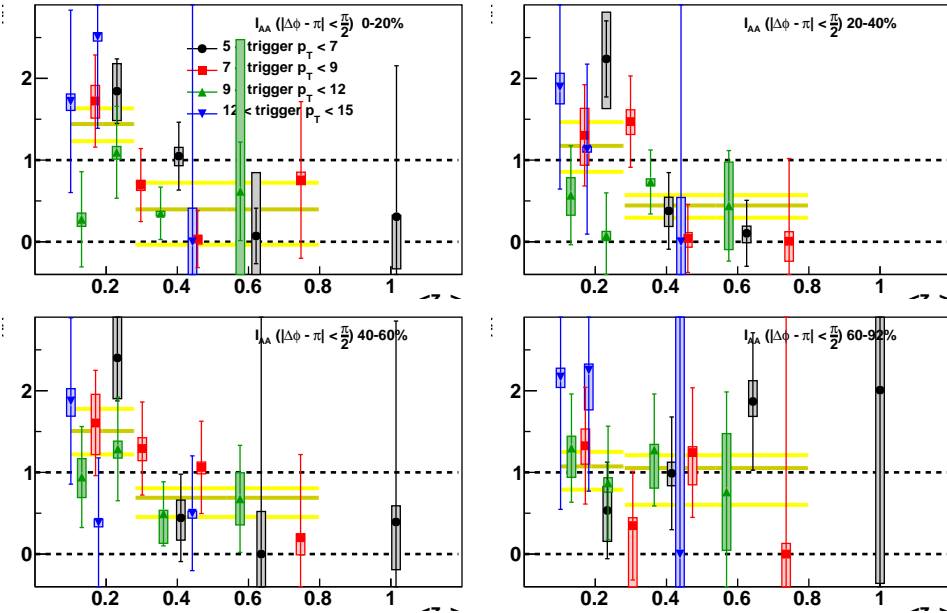
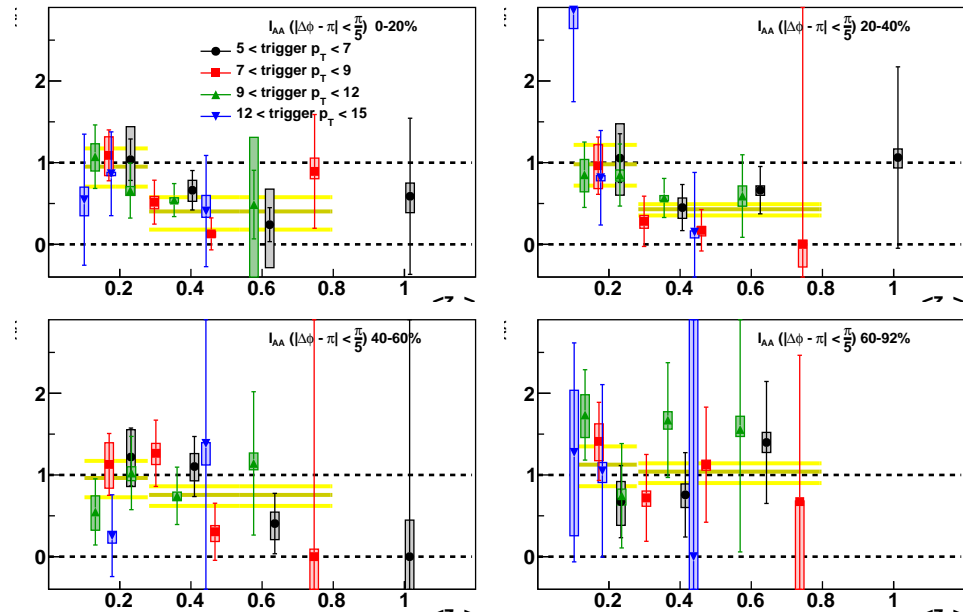


Figure 8.4: Run 10 Au+Au I_{AA} as a function of z_T for the $\pi/3$ integrated away-side for each centrality bin. Each trigger p_T bin is a different color and the four $p_{T\text{assoc}}$ bins: 1-2, 2-3, 3-5, and 5-10 GeV/c increase from left to right. The gray horizontal lines are fits to the data to average it. The yellow bands around them are the error on the fits.



(a)



(b)

Figure 8.5: Run 10 Au+Au I_{AA} as a function of z_T for the $\pi/2$ (a) and the $\pi/5$ (b) integrated away-side for each centrality bin. Each trigger p_T bin is a different color and the four $p_{T\text{assoc}}$ bins: 1-2, 2-3, 3-5, and 5-10 GeV/c that increase from left to right. The gray horizontal lines are fits to the data to average it. The yellow bands around them are the error on the fits.

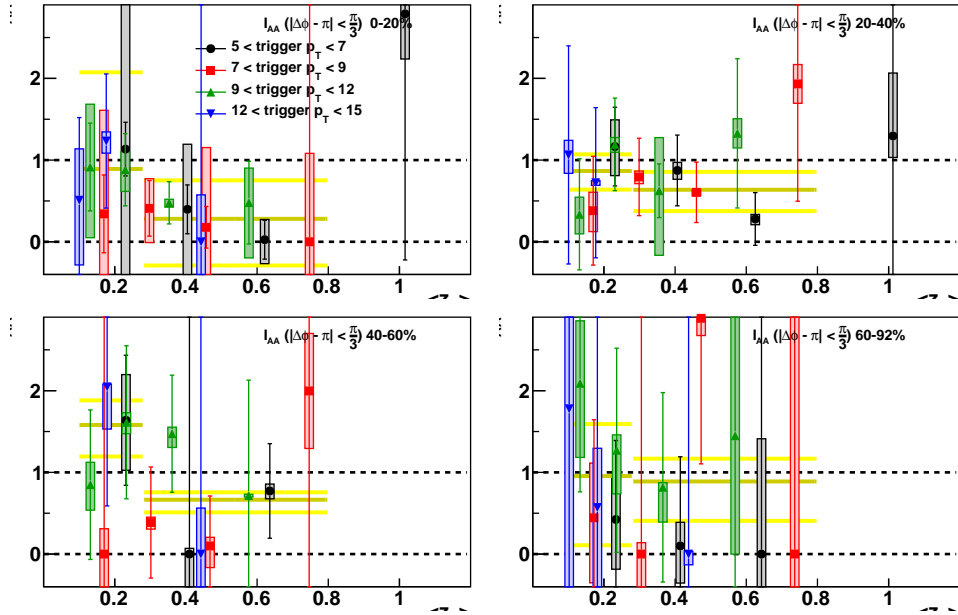


Figure 8.6: Run 11 Au+Au I_{AA} as a function of z_T for the $\pi/3$ integrated away-side for each centrality bin. Each trigger p_T bin is a different color and the four $p_{T\text{assoc}}$ bins: 1-2, 2-3, 3-5, and 5-10 GeV/c that increase from left to right. The gray horizontal lines are fits to the data to average it. The yellow bands around them are the error on the fits.

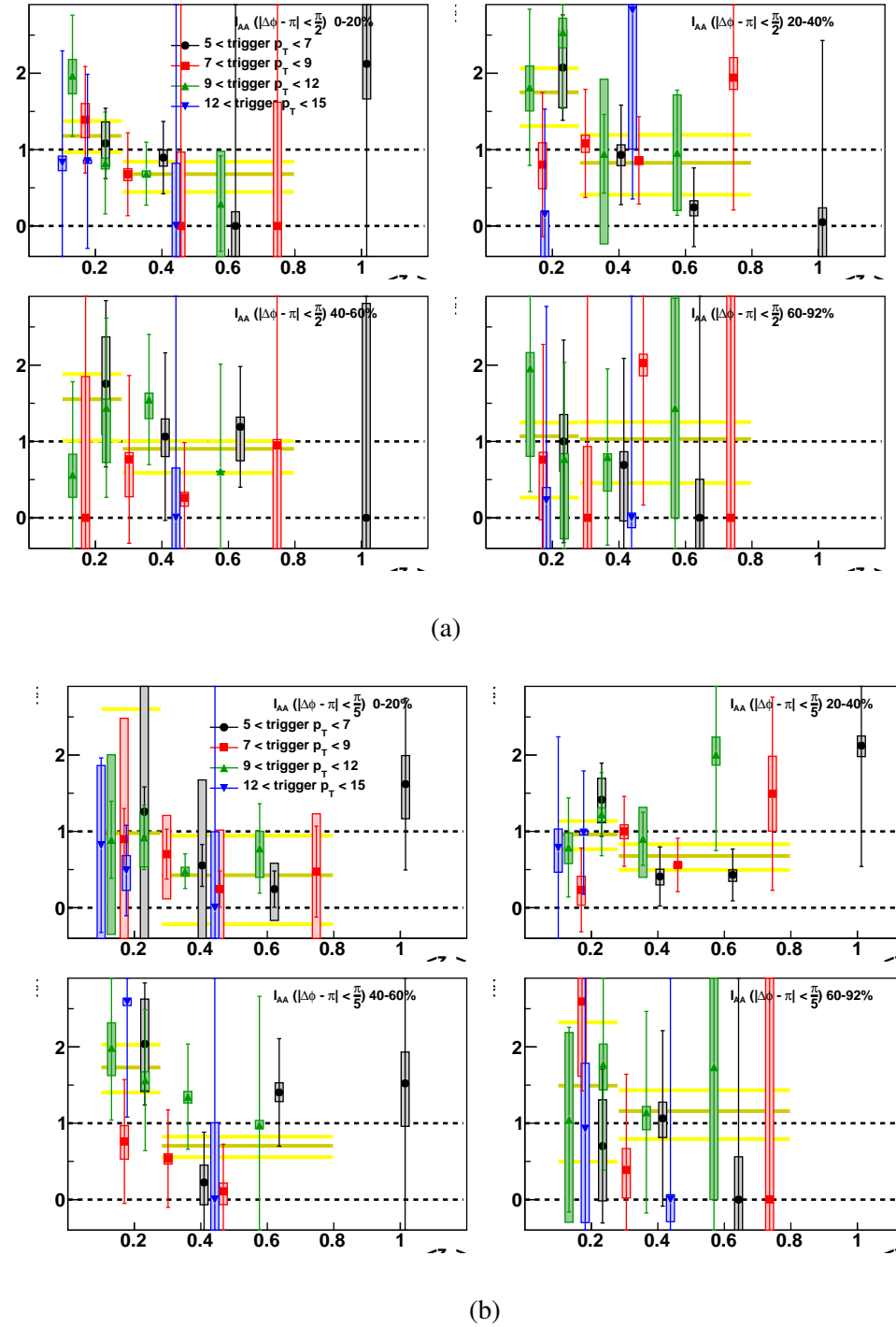


Figure 8.7: Run 11 Au+Au I_{AA} as a function of z_T for the $\pi/2$ (a) and the $\pi/5$ (b) integrated away-side for each centrality bin. Each trigger p_T bin is a different color and the four $p_{T\text{assoc}}$ bins: 1-2, 2-3, 3-5, and 5-10 GeV/c that increase from left to right. The gray horizontal lines are fits to the data to average it. The yellow bands around them are the error on the fits.

The boundary of the two z_T regions was chosen to minimize the z_T overlap of the different p_T bin combinations. Figure 8.8 shows the z_T bin for each associated p_T bin. For each associated p_T bin, the low trigger p_T bin is the right most z_T bin. The vertical lines are the fit regions, the low z_T region is the region between the blue lines while the high z_T region is the region between the red lines. As seen in the plot, there is only one z_T bin that spans the high/low z_T fit boundary. This is the $12 < p_{T\text{trig}} < 15$ and $3 < p_{T\text{assoc}} < 5$ bin combination. To remove any bias from this overlap, we remove this point from the fit and do not plot it on the $I_{AA}(z_T)$ plots. Doing so does no great harm to the average because this point typically has large error bars due to the fact that there are a small number of high p_T triggers.

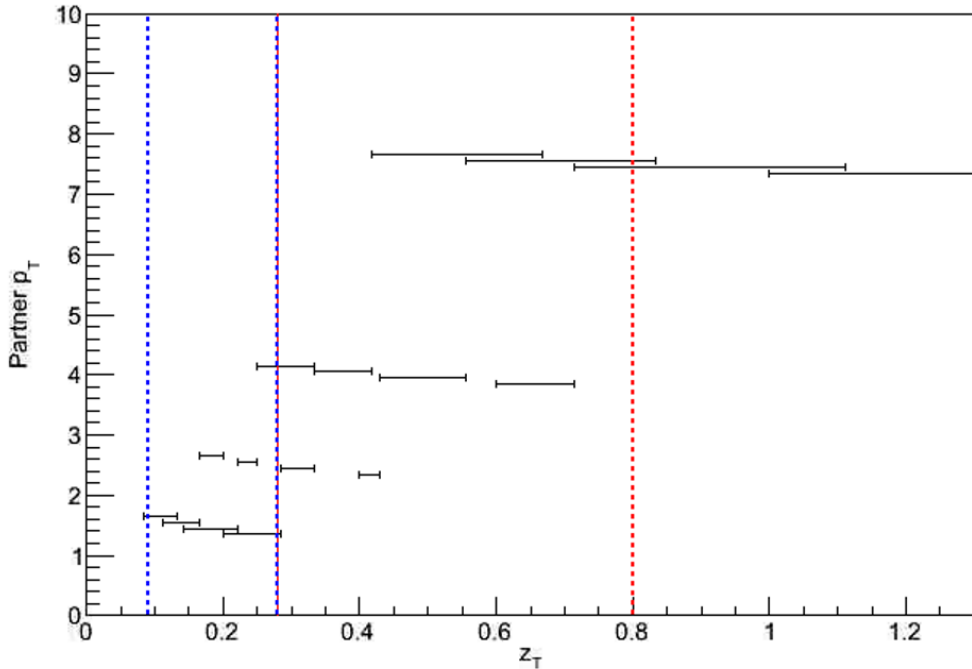


Figure 8.8: Associated particle p_T as a function of z_T . For each associated p_T , the lowest trigger p_T is the right most bin, and increases from left to right. The vertical lines show boundaries of the two averaging ranges.

The average I_{AA} for the two z_T fit regions are plotted as a function of N_{part} for the three integration regions in Run 10 in Figure 8.9 and in Run 11 in Figure 8.10.

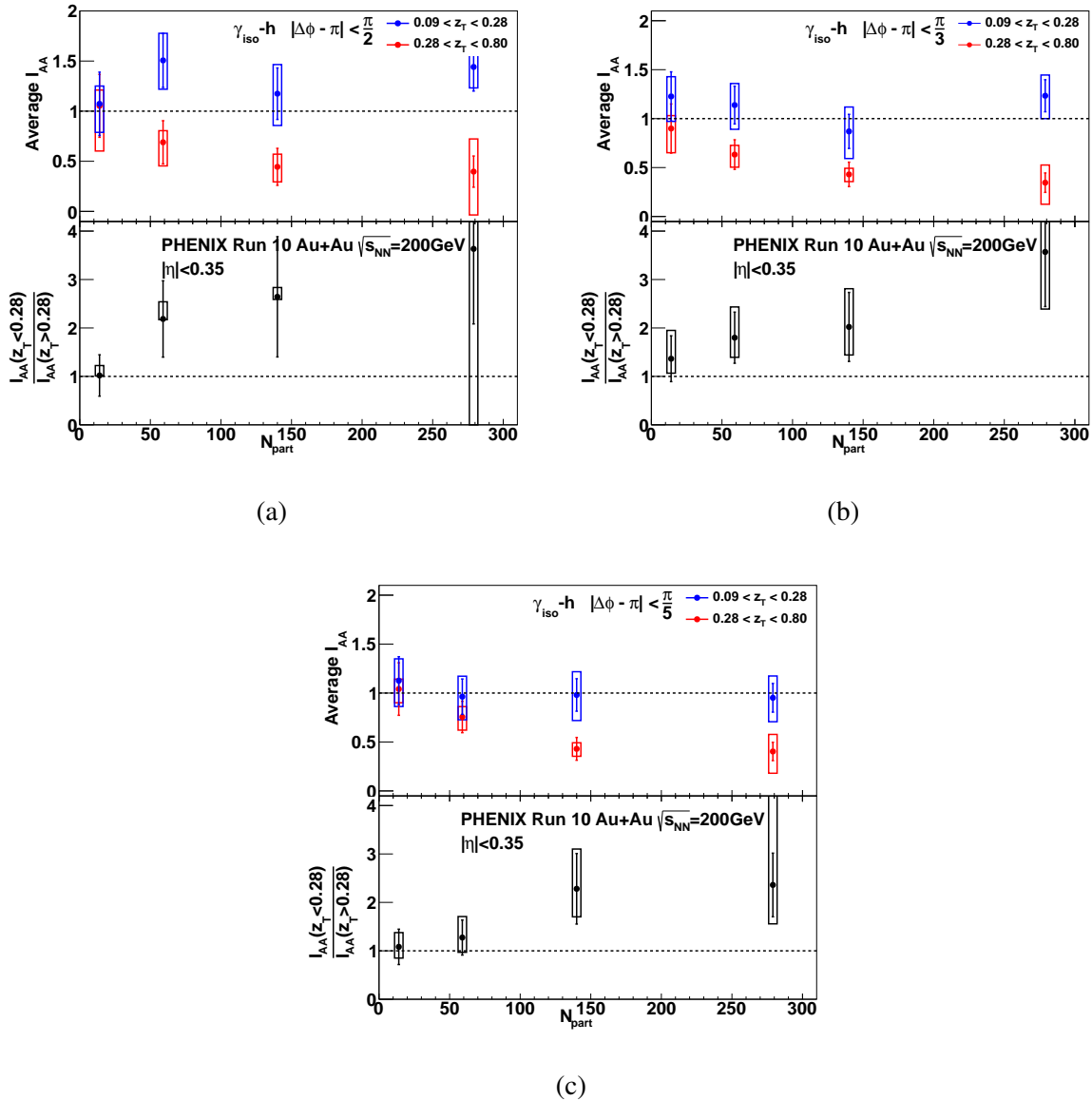


Figure 8.9: Run 10 I_{AA} as a function of N_{part} for each integration region $\pi/2$ (a), $\pi/3$ (b), and $\pi/5$ (c). The red points in the top panels is the high z_T average and the blue points in the low z_T average. The bottom panels shows the centrality dependence of ratio of high to low z_T fit values which more accurately reflects the true centrality dependence of the low z_T enhancement in the per-jet fragmentation function since per-photon I_{AA} always folds in the overall suppression of the away-side jets.

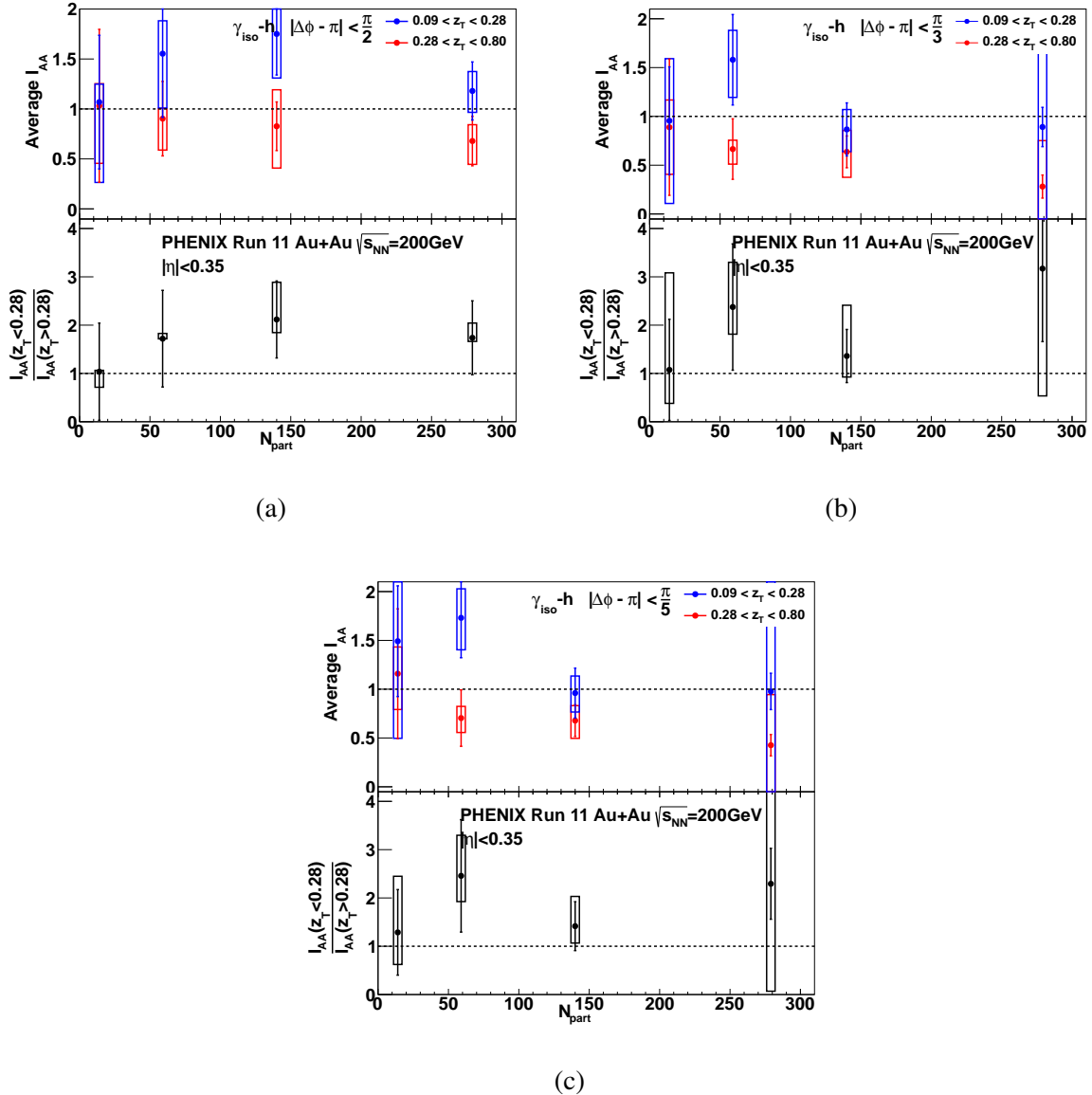


Figure 8.10: Run 11 I_{AA} as a function of N_{part} for each integration region $\pi/2$ (a), $\pi/3$ (b), and $\pi/5$ (c). The red points in the top panels is the high z_T average and the blue points in the low z_T average. The bottom panels shows the centrality dependence of ratio of high to low z_T fit values which more accurately reflects the true centrality dependence of the low z_T enhancement in the per-jet fragmentation function since per-photon I_{AA} always folds in the overall suppression of the away-side jets.

8.6 Isolation Method Cross-checks

This section is devoted to several cross-checks to show the isolation cut method performs as we expect it to. This is done by lowering the energy threshold on the isolation cone by lowering the cone b parameter to show there is no large bias or change because of the chosen parameter set.

The study described in this section just contains data from Run 10 Au+Au . This data set is larger than the Run 11 Au+Au data set and is the main driver behind the results presented in this dissertation. We decreased the cone threshold energy to select photons that are more isolated. To do this, we decreased the b parameter in the cone threshold energy equation, Equation 3.3. The original cone parameters were determined in order to optimize the errors [3]. The cone parameters used in the results in the previous section are summarized in Table 3.1. The parameters used in this cross-check are shown in Table 8.1. Since we decreased the cone threshold, we expect to decrease the number of trigger particles, and therefore increase the statistical errors.

Table 8.1: Isolation cut parameters for all centralities of Au+Au collisions used in the cross-check study described in the text.

Centrality (%)	R_{cone}	a	$b(\text{GeV})$
0 - 20	0.1	0.1	1.5
20 - 40	0.2	0.1	3.5
40 - 60	0.2	0.1	1.5
60 - 92	0.3	0.1	0.5

8.6.1 Modification of the Elliptic Flow and the MSMP ξ

The modification of the cone threshold changes the which photons are selected as isolated trigger photons. It should select less of the underlying even photons, so the $v_{2T} + v_{2E}$ should be

smaller. This section shows the v_2 as a function of p_T for the modified b isolation cut for each centrality bin and compares it to the results in Section 6.1.2. Here we only show the $v_{2T} + v_{2E}$ because that is the v_2 that is subtracted from the correlation function. This is shown in Figure 8.11. The black points are the Run 10 Au+Au collision v_2 for the modified b isolation cut and the blue points are the original b Run 10 v_2 shown in Figure 6.3.

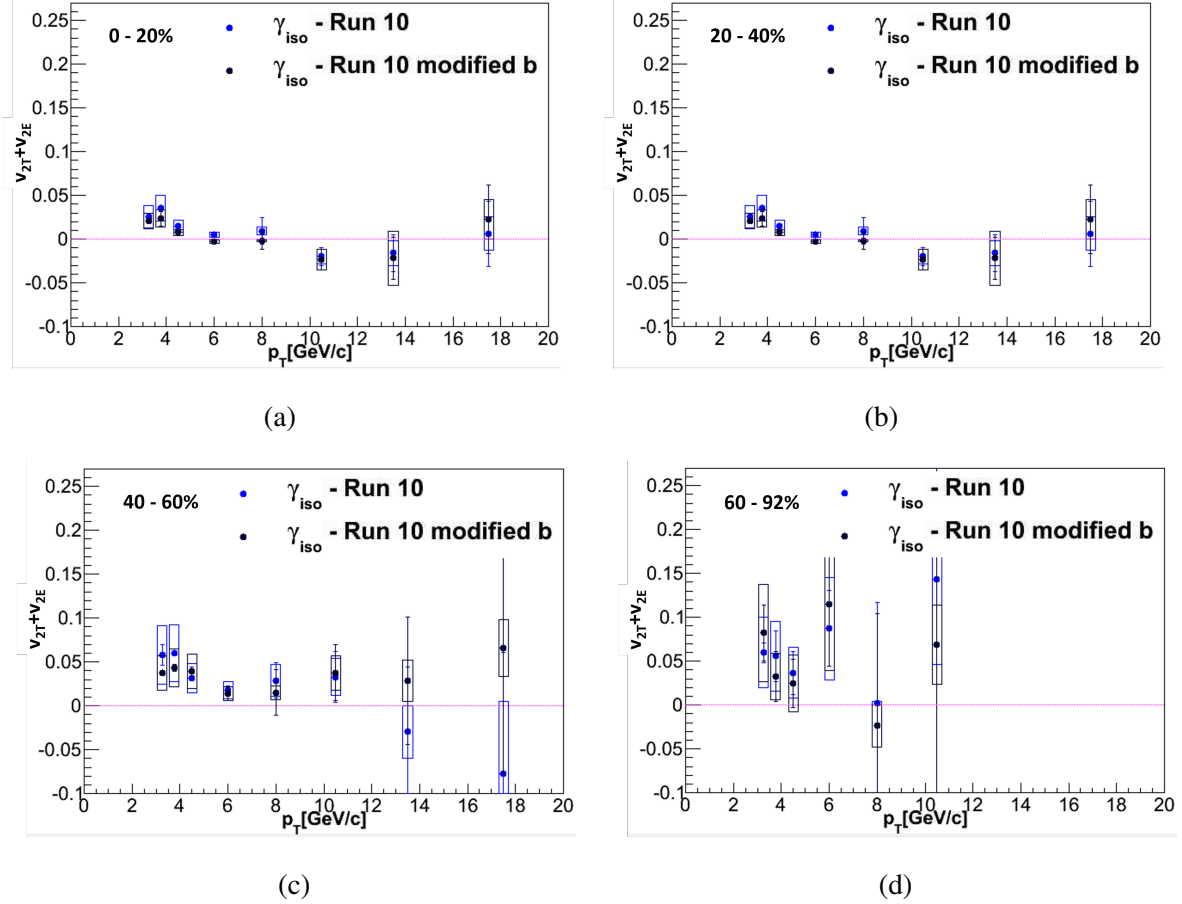


Figure 8.11: Elliptic flow coefficients ($v_{2T} + v_{2E}$) used to subtract background shape from isolated gamma-hadron correlation functions as a function of p_T for the centrality bins used in this analysis. The black points are with the modified b cones and the blue points are the original Run 10 points shown in Figure 6.3.

One can see in Figure 8.11, that the v_2 with the modified b isolation cut appears slightly lower than the v_2 with the original b isolation cut but it is not statistically significant. One doesn't expect the v_2 with the different cut values to necessarily be the same if they are non-zero, since there is potentially a larger isolation cut efficiency v_{2E} , which should be more negative, since more of the larger cone energy fluctuations would be cut away with the lower threshold and thus go in the direction seen. Also potentially more important than that effect is that there is simply a different mix of signal Compton-like direct photons, which are expected to have $v_2=0$, versus background jet decay photons which like the jets are known to have finite v_2 due to energy loss. Further, the latter energy loss v_2 of the jet background could even also depend on details of the fragmentation pattern of the jets which different isolation cut parameters might also be sensitive to.

In addition to the background shape being modified, the size of the background is also modified when using different cone parameters. To see this, we can plot the MSMP ξ and compare it to the ξ using the original b shown in Figure 7.6. The ξ with the modified b are the solid points in Figure 8.12, the open points there are the solid points in Figure 7.6.

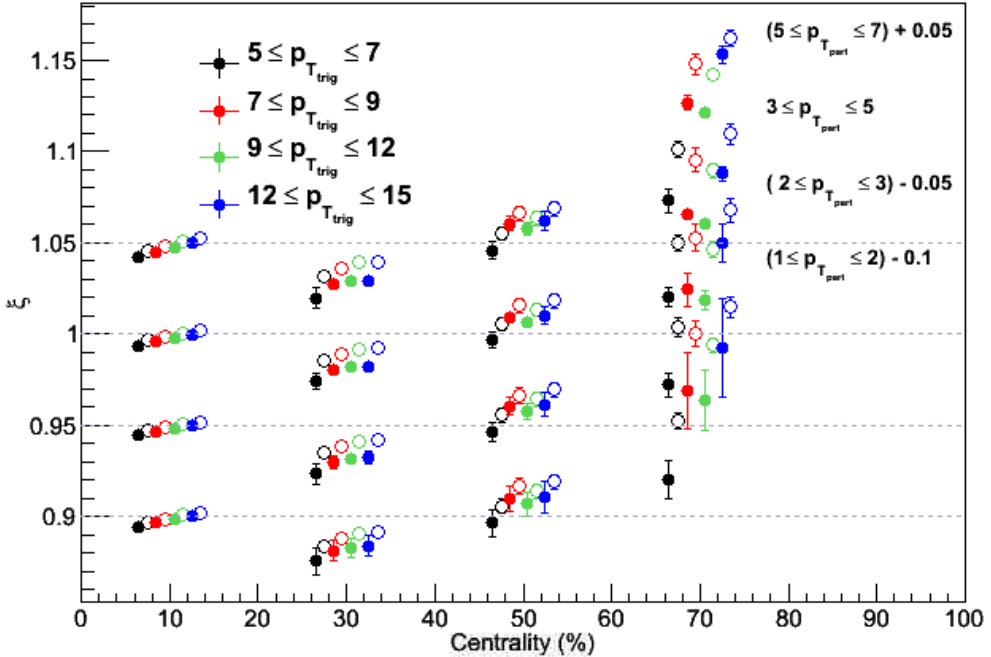


Figure 8.12: MSMP ξ as a function of centrality for isolated photons found with the modified b in Run 10 Au+Au collisions. Each color is a trigger p_T bin and each row is a partner p_T bin, both have been artificially offset for clarity. The open points are the solid points in Figure 7.6.

8.6.2 Modification of the Correlation and Jet Functions

Since we have the elliptic flow coefficients and MSMP ξ values we can now make the correlation jet functions. The 0-20% central events $\gamma_{iso} - h$ correlation functions for Run 10 Au+Au with the modified b are shown in Figure 8.13. Each panel of this figure is a different trigger and hadron p_T bin. The black line on these figures is the MSMP background level that was found using the v_2 and ξ from the modified b described in the previous section. One can see that the background level looks appropriate. The red dashed lines show the systematic error on the black line. When this black line is subtracted from the correlation function, we obtain the jet functions shown in Figure 8.14. Each panel of this figure is a different trigger and hadron p_T bin and the black points are the $\gamma_{iso} - h$ jet function, the red points are the $\gamma_{dec} - h$ jet function, and blue points

are the $\gamma_{dir} - h$ jet function. The first point (near $\Delta\phi = 0$) in both of these figures should be ignored because this point is inside the isolation cone.

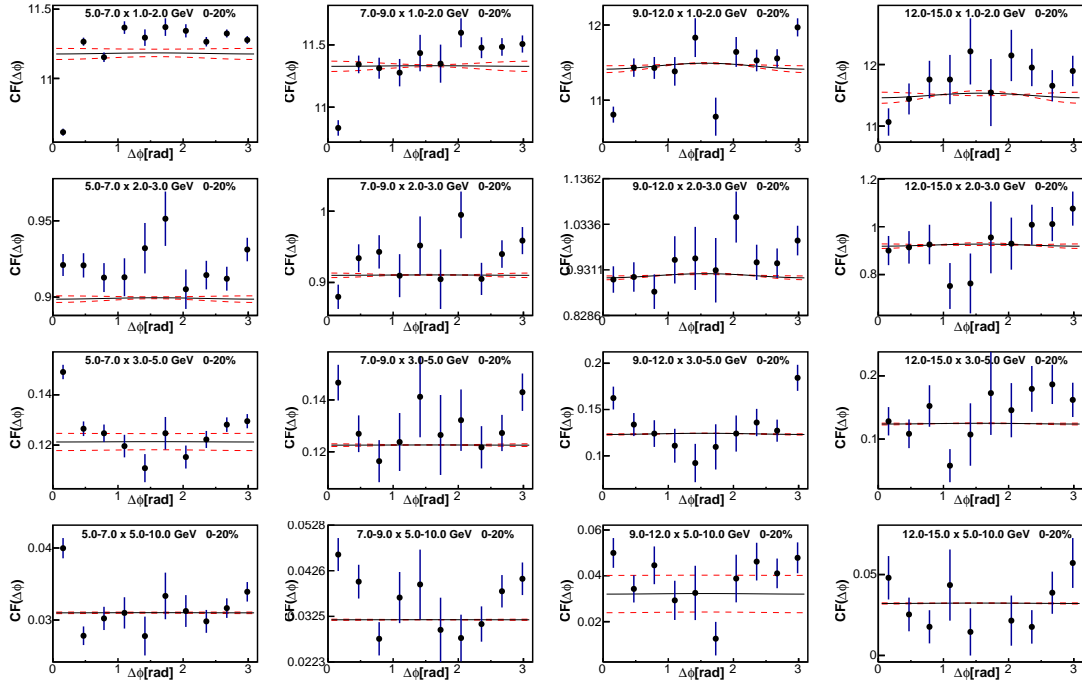


Figure 8.13: Run 10 Au+Au $\gamma_{iso} - h$ correlation functions for 0 - 20% central events with the modified b cone parameter. Each plot is a different p_T bin combination. Trigger p_T increases to the right while partner p_T increases going down. The black line represents the background level, the red lines around it is the error on the black line.

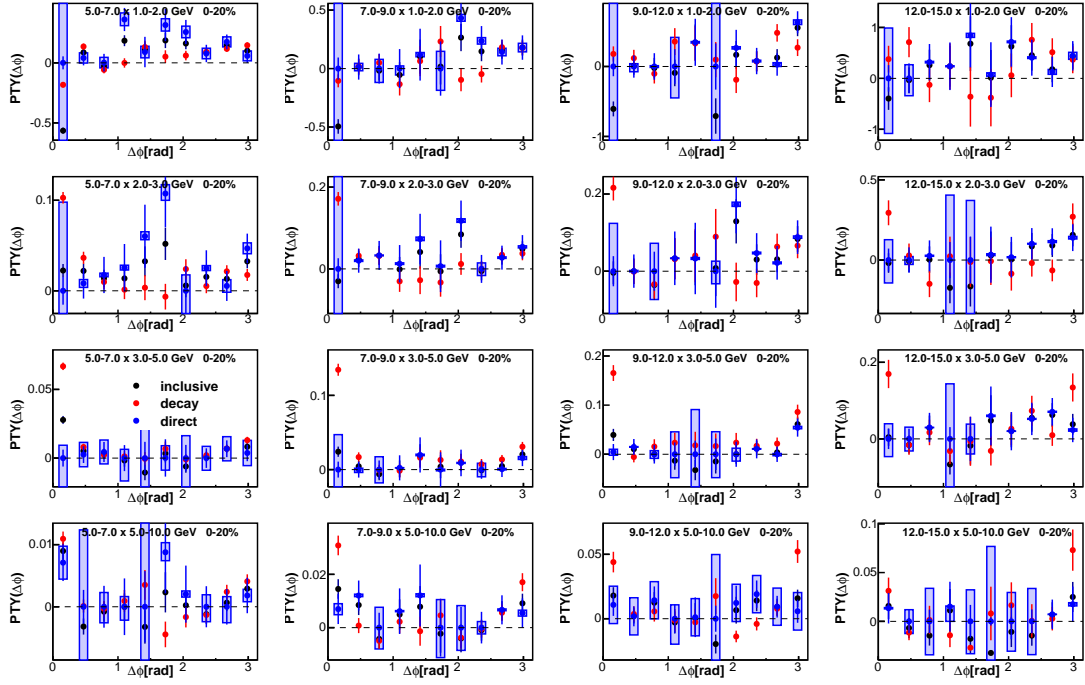


Figure 8.14: Run 10 Au+Au $\gamma_{iso} - h$ (black), $\gamma_{dec} - h$ (red), and $\gamma_{dir} - h$ (blue) jet functions for 0 - 20% central events with the modified b cone parameter. Each plot is a different p_T bin combination. Trigger p_T increases to the right while partner p_T increases going down.

8.6.3 Modification of the I_{AA}

The away-side yields in the three integration regions we are interested in are shown in Figure 8.15. In these figures, each color is a different centrality bin that has been offset by a factors of 10 for clarity. The red points are the $p+p$ baseline. The different marker styles are different trigger p_T bins. The colored lines are just there to guide the eye.

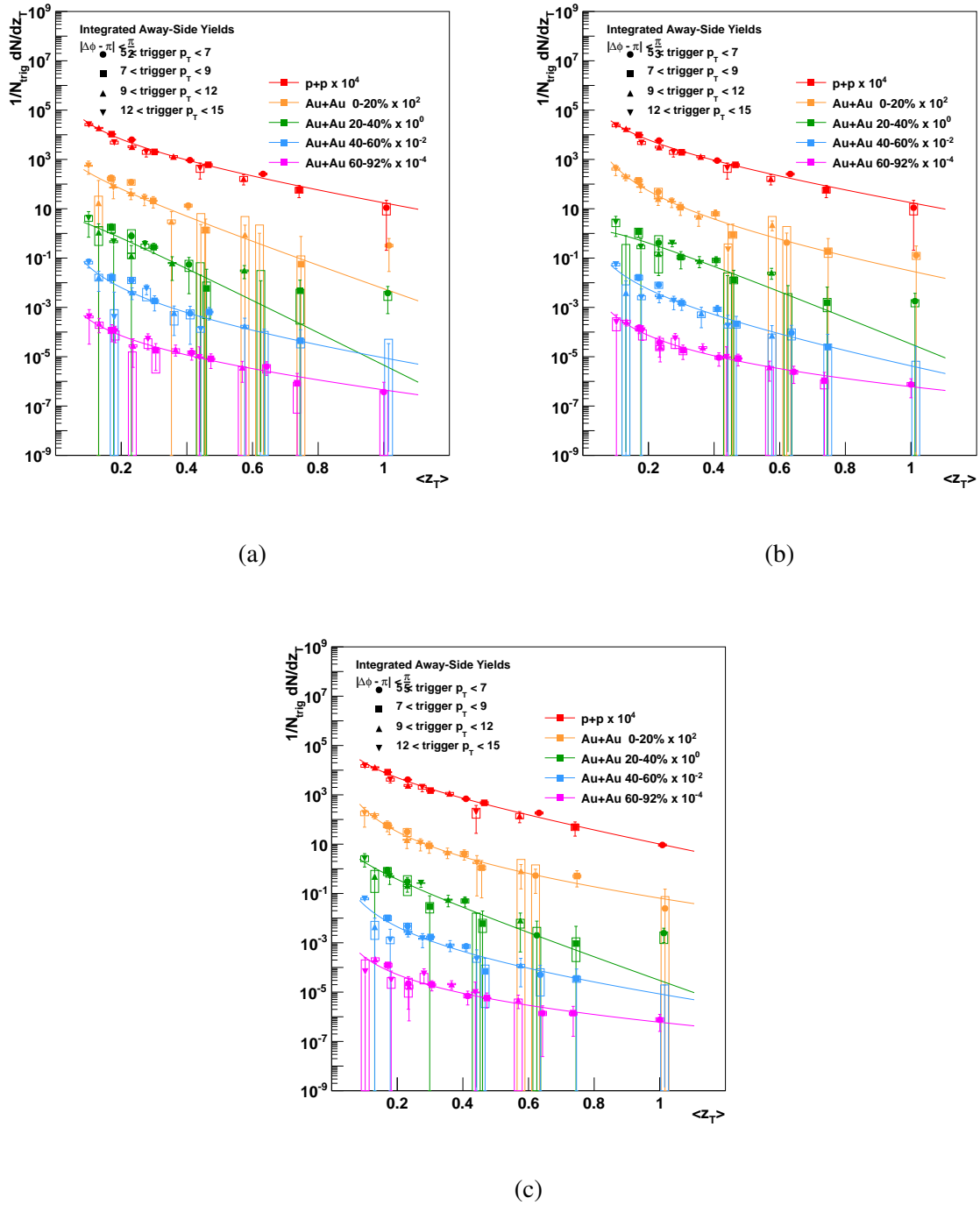


Figure 8.15: Run 10 away-side yields as a function of z_T for modified b cones for each integration region $\pi/2$ (a), $\pi/3$ (b), and $\pi/5$ (c) and each centrality bin: 0 - 20% (orange), 20 - 40% (green), 40 - 60% (blue), and 60 - 92% (magenta). The red points are the $p+p$ baseline. The colored lines are just there to guide the eye.

The modified b cone threshold I_{AA} as a function of z_T for three away-side regions are shown in Figures 8.16. Each panel is a centrality bin and each color is a different trigger p_T bin. The two gray lines in each panel are the average of the low and high z_T points, the yellow lines around the gray lines show the error on the fit.

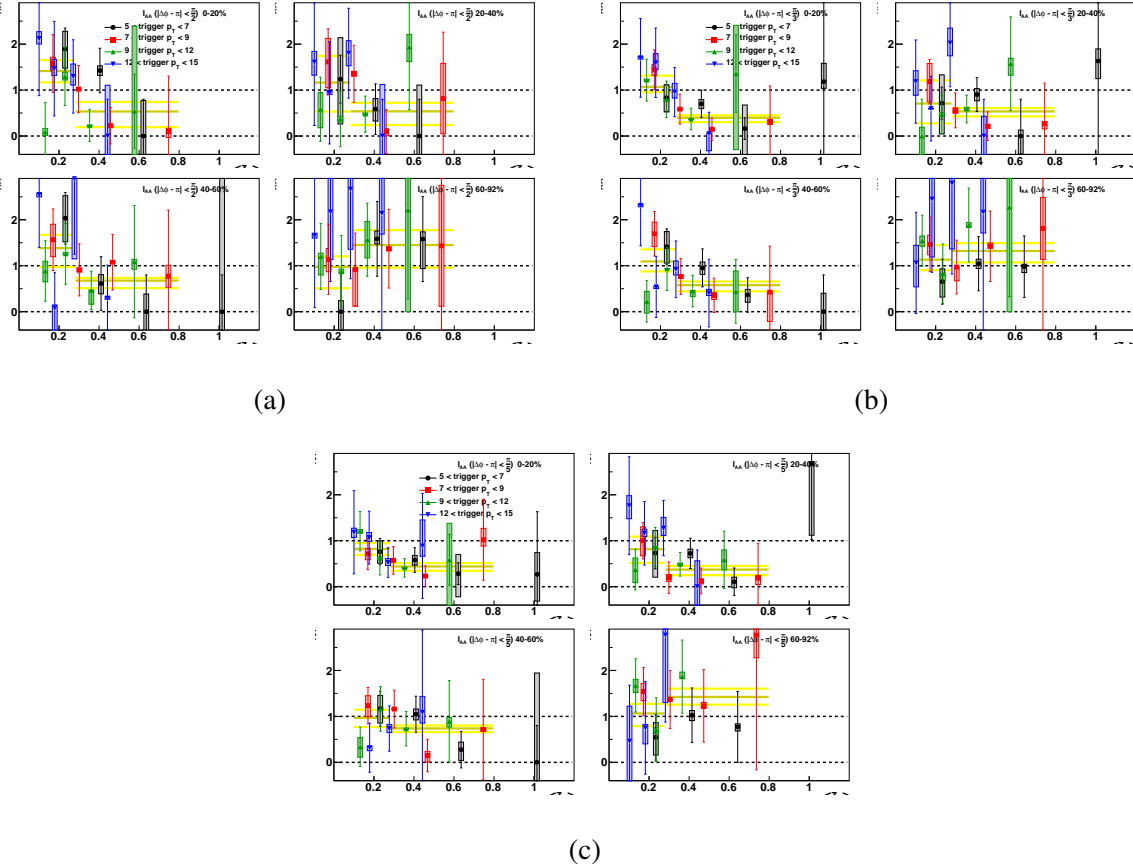


Figure 8.16: Run 10 I_{AA} as a function of z_T for modified b cones for each integration region $\pi/2$ (a), $\pi/3$ (b), and $\pi/5$ (c) for each centrality bin. Each trigger p_T bin is a different color. The gray horizontal lines are fits to the data to average it. The yellow bands around them are the error on the fits.

Figures 8.17 - 8.19 shows the Run 10 I_{AA} as a function of z_T for the original b (solid points), from Figures 8.4 and 8.5, as well as I_{AA} with the modified b from Figure 8.16 (open points). The modified b points have been shifted to a higher z_T for clarity. One can see in these figures that

the original b points are consistent with the modified b points. Some of the modified b systematic errors are smaller than the original errors but others are larger. So no statement can be made about the overall systematic errors.

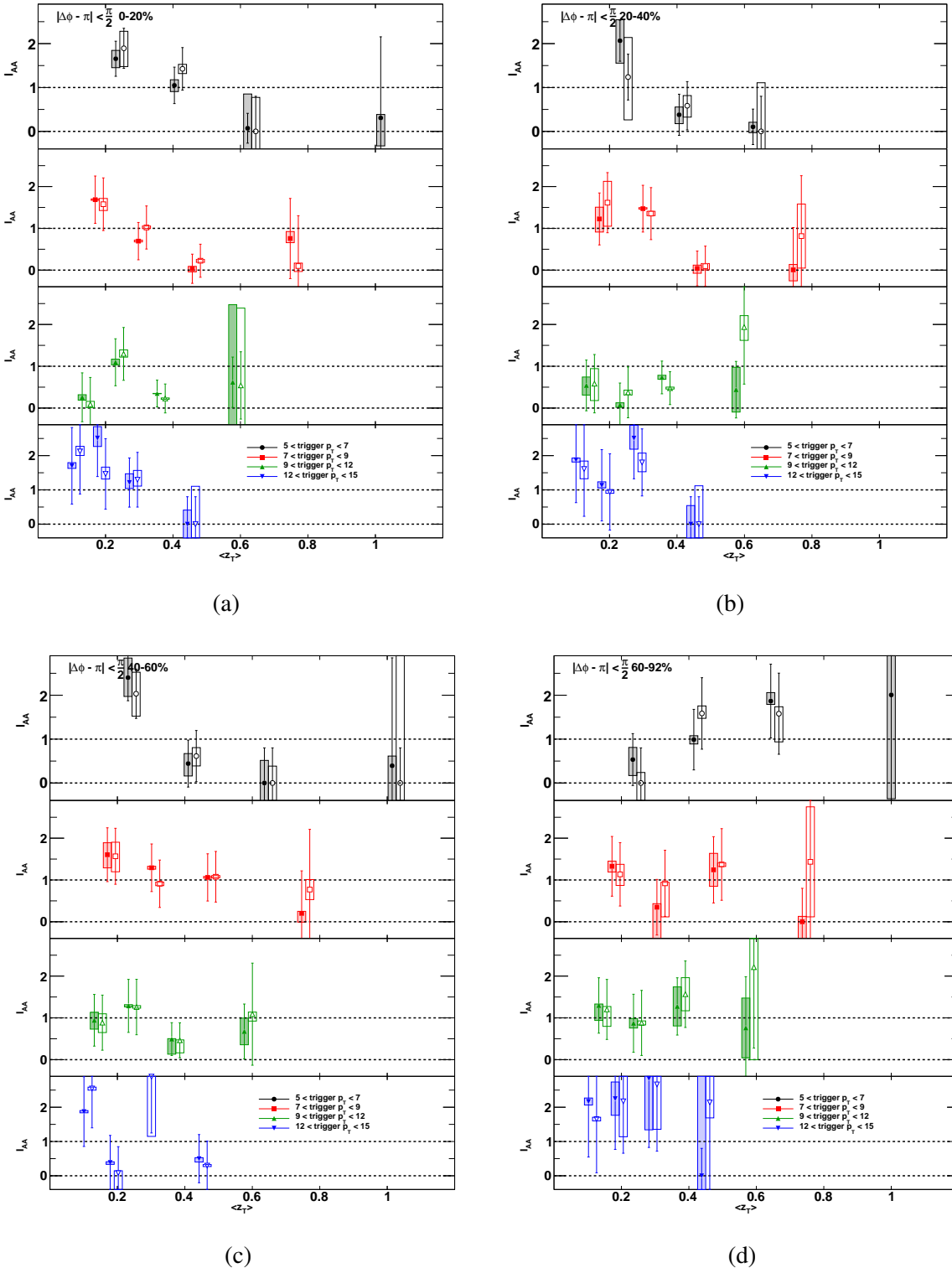


Figure 8.17: Run 10 I_{AA} as a function of z_T with the original b (solid points) and the modified b (open points) for the $\pi/2$ integration region for each centrality bin: 0-20% (a), 20-40% (b), 20-40% (c), 60-92% (d). The solid points are the same as the points in Figure 8.5, the open points are from Figure 8.16.

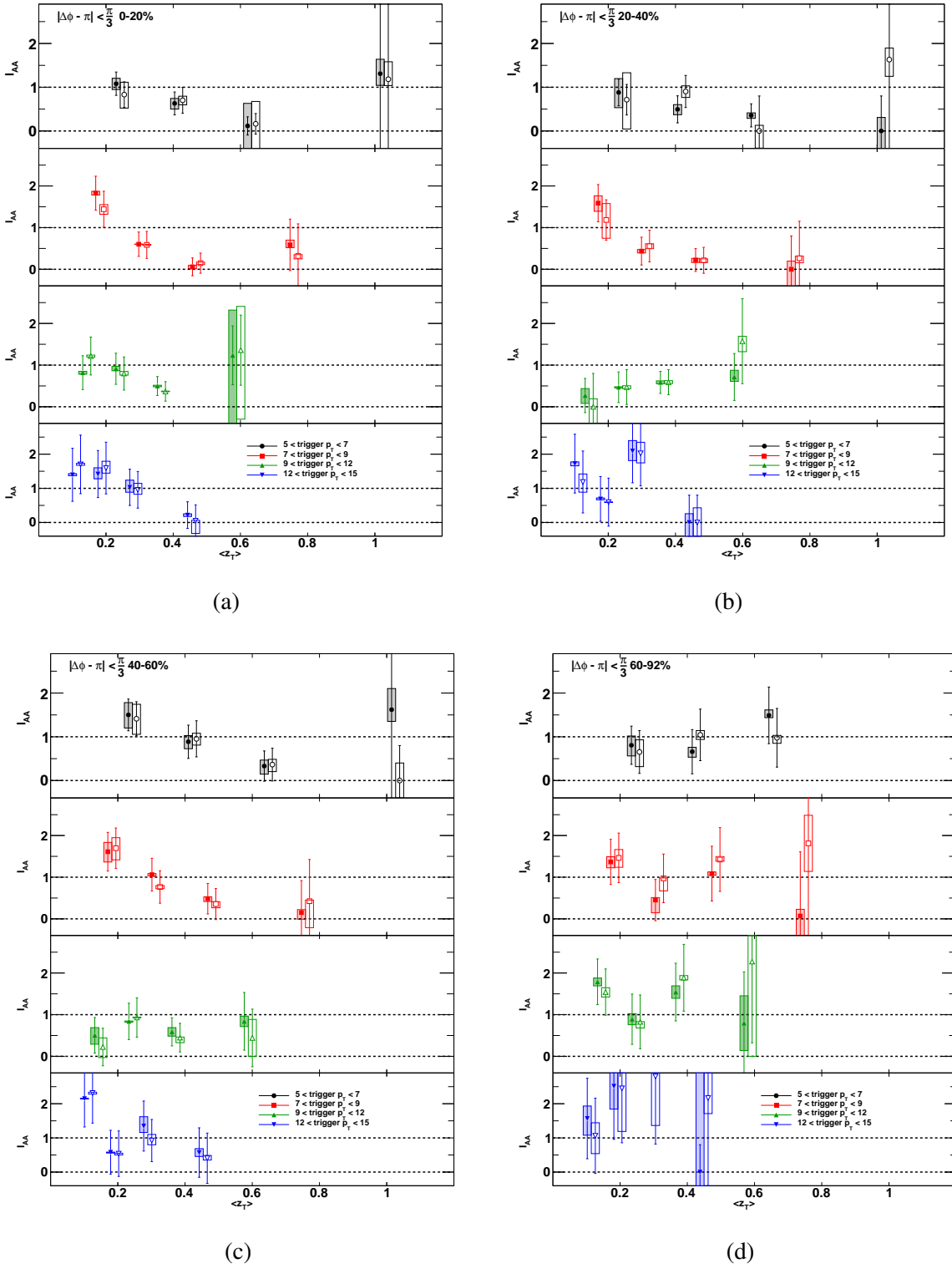


Figure 8.18: Run 10 I_{AA} as a function of z_T with the original b (solid points) and the modified b (open points) for the $\pi/3$ integration region for each centrality bin: 0-20% (a), 20-40% (b), 20-40% (c), 60-92% (d). The solid points are the same as the points in Figure 8.4, the open points are from Figure 8.16.

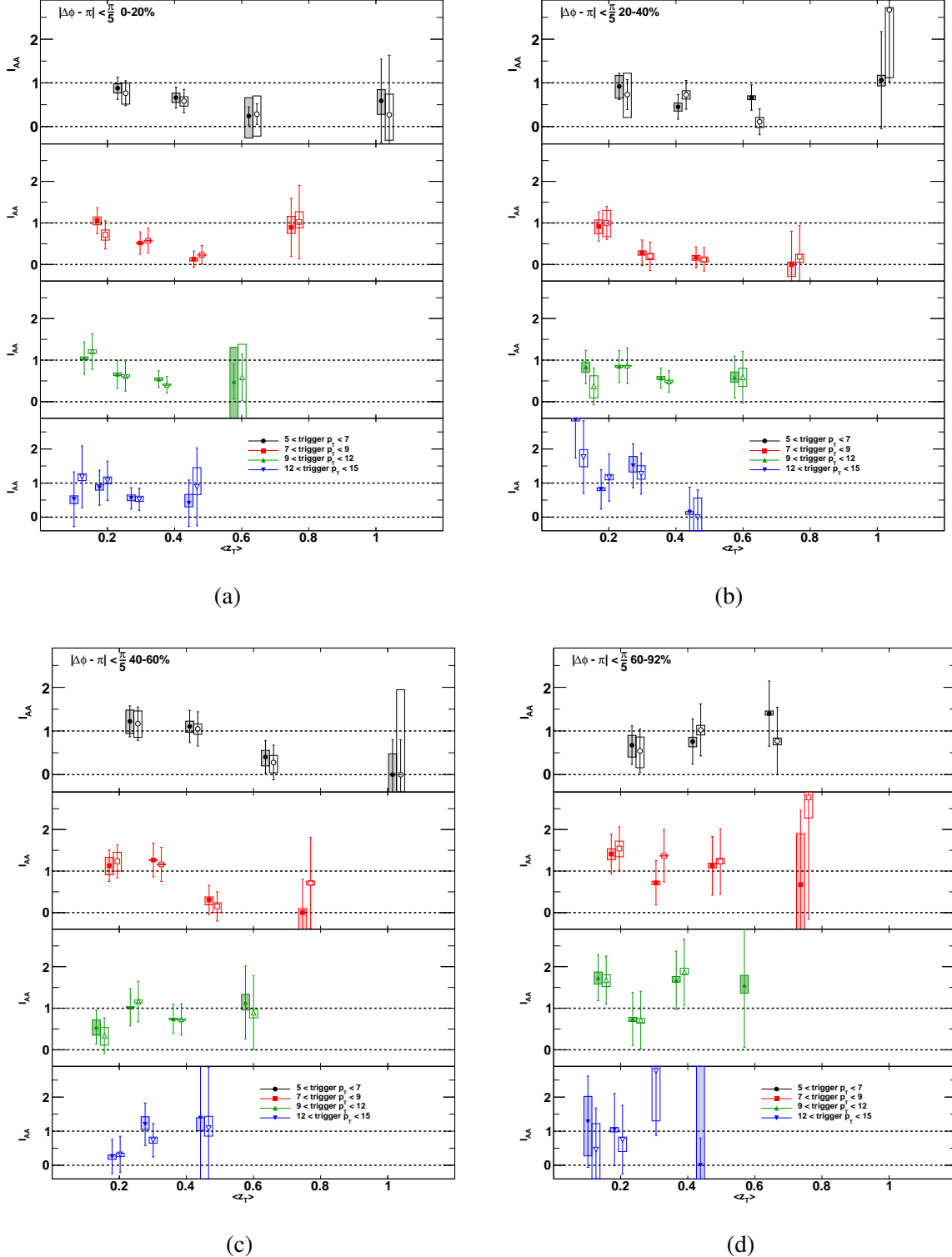


Figure 8.19: Run 10 I_{AA} as a function of z_T with the original b (solid points) and the modified b (open points) for the $\pi/5$ integration region for each centrality bin: 0-20% (a), 20-40% (b), 20-40% (c), 60-92% (d). The solid points are the same as the points in Figure 8.5, the open points are from Figure 8.16.

The high z_T and low z_T fits are plotted as a function N_{part} for the three integration regions, in the top panels of the plots in Figure 8.20. The bottom panels of those plots is the *ERF*. One can see in Figure 8.20 that each point has a larger statistical error than Figure 8.9 but the values remain consistent.

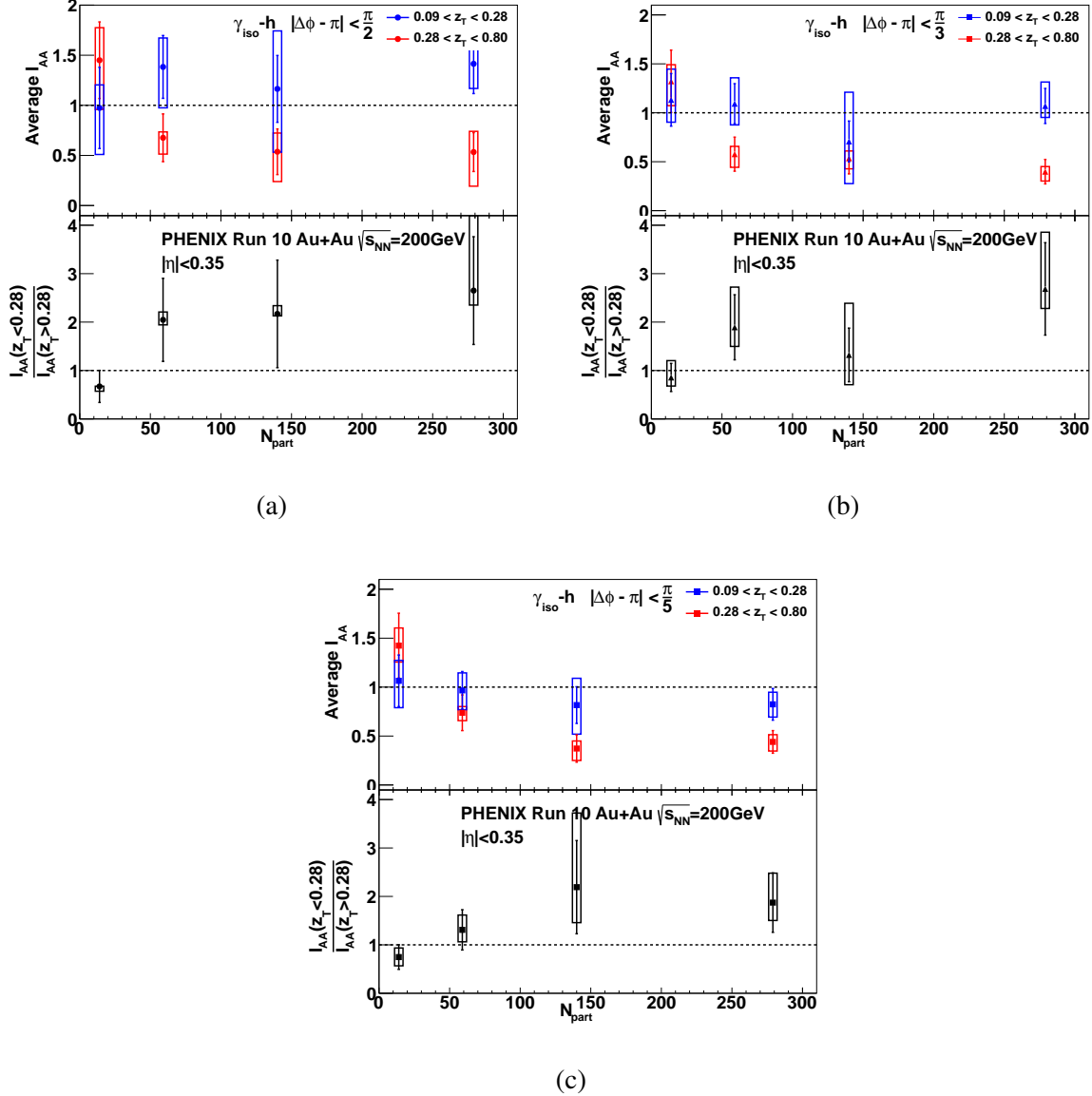


Figure 8.20: Run 10 I_{AA} as a function of N_{part} for modified b cones for each integration region $\pi/2$ (a), $\pi/3$ (b), and $\pi/5$ (c). The red points in the top panels is the high z_T average and the blue points in the low z_T average. The bottom panels shows the centrality dependence of the *ERF*.

8.6.4 Systematic Error with the Modified b

Figure 8.21 shows the systematic error on the full $\pi/2$ away-side yield broken down by source for 0 - 20% central events with the original (red line) and modified b (black line) parameter. The red line in this figure is the same as the red line in Figure 7.19. Figure 8.22 shows the same thing but for the $\pi/5$ away-side yield. The red line in this figure is the same as the red line in Figure 7.20. It is difficult to tell what the dominate systematic difference between the two measurements are because of the fluctuations inherent to this analysis. One can see in the figures above that the systematic errors are of similar size no matter which threshold is used.

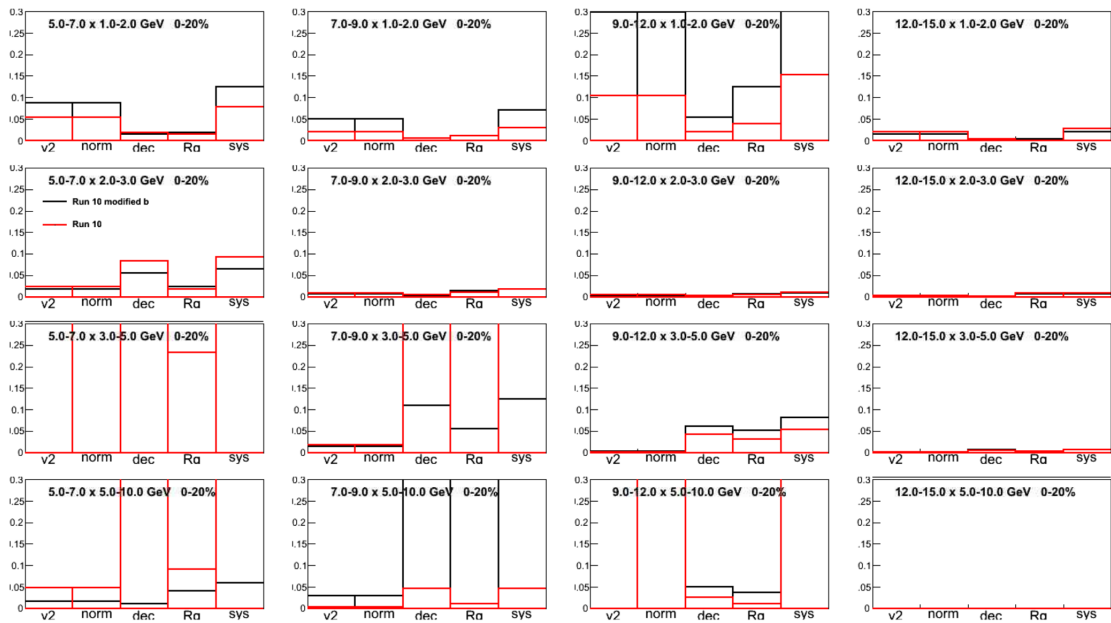


Figure 8.21: Error contributions of the direct photon $\pi/2$ away-side yield broken down by source for Run 10 with the original b (red) and Run 10 with the modified b (black) for 0 - 20% events. Each source is a different bin from left to right, v_2 , normalization (MSMP), decay photons, R_γ , total systematic error, and total statistical error. Each plot is a different p_T bin combination. Trigger p_T increases to the right while partner p_T increases going down.

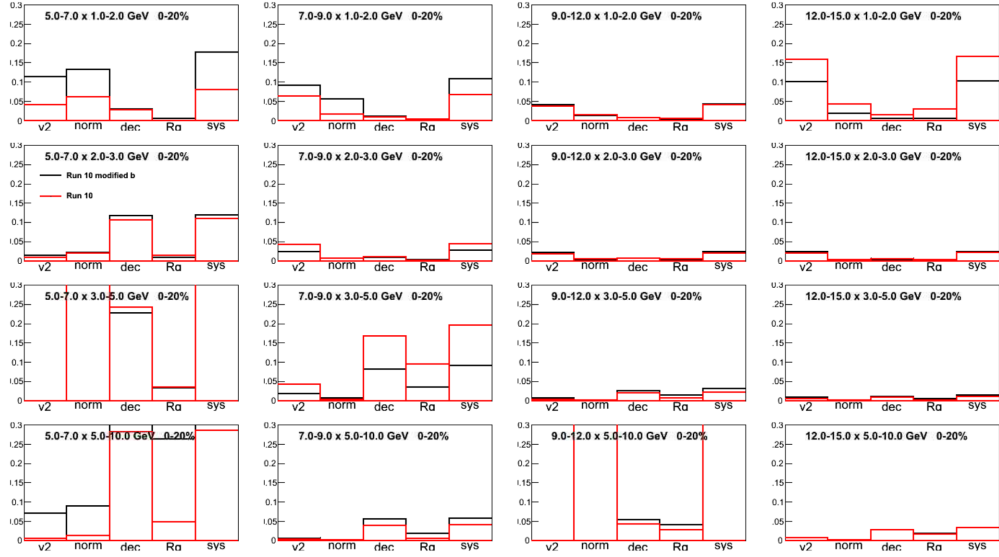


Figure 8.22: Error contributions of the direct photon $\pi/5$ away-side yield broken down by source for Run 10 with the original b (red) and Run 10 with the modified b (black) for 0 - 20% events. Each source is a different bin from left to right, v_2 , normalization (MSMP), decay photons, R_γ , total systematic error, and total statistical error. Each plot is a different p_T bin combination. Trigger p_T increases to the right while partner p_T increases going down.

8.7 Results Summary and Combined Run 10 + Run11 Au+Au Results

In order to combine Run 10 and Run 11 we first verify that the Run 10 and Run 11 yields are consistent within uncertainties. Figure 8.23 shows the ratio between the Run 10 and Run 11 $\pi/5$ away-side integrated per trigger yields for all trigger and partner p_T combinations plotted versus z_T . Each color are the four trigger bins, and for each color the four points left to right are the four $p_{T,assoc}$ bins increasing from 1-2, 2-3, 3-5, and 5-10 GeV/c. Only the most statistically significant points are shown. The comparison shows that the integrated yields of Run 10 and Run 11 are consistent in virtually all cases, the ratio overlaps with one within uncertainties with a small number of points fluctuating outside of this range as expected from statistical fluctuations.

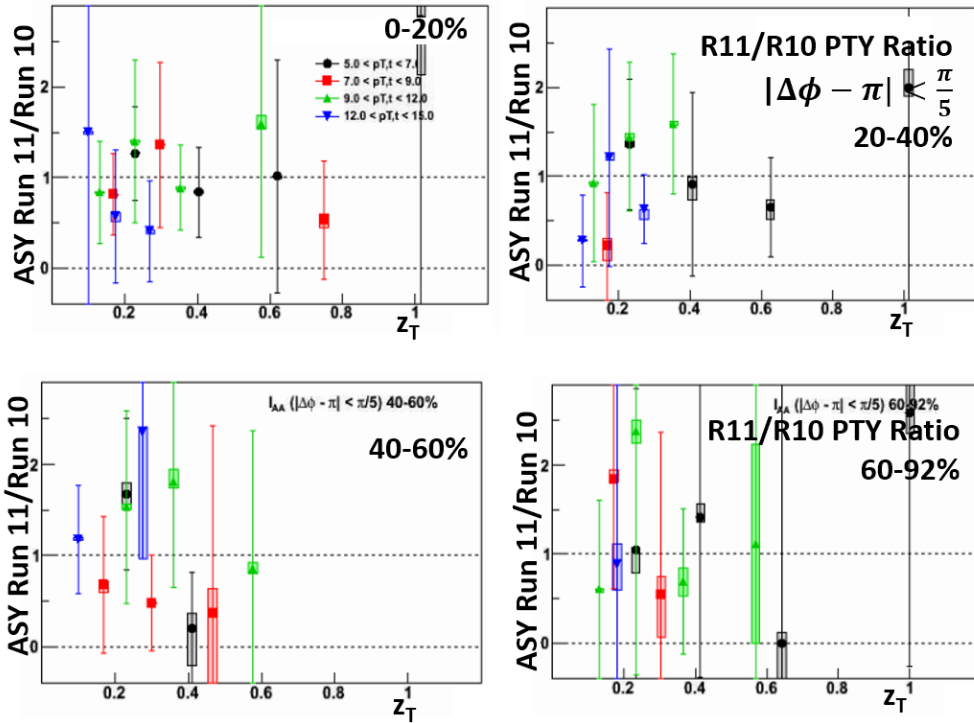


Figure 8.23: Ratios of Run 11 over Run 10 integrated per-trigger yields for the $\pi/5$ away-side. Each trigger p_T bin is a different color and the four $p_{T,assoc}$ bins: 1-2, 2-3, 3-5, and 5-10 GeV/c that increase from left to right.

Having established consistency between the Run 10 and Run 11 away-side yields, we combine the Run 10 and Run 11 at the integrated per-trigger yield level using the PDG method for combining independent results, that is, using $1/\sigma^2$ as weights, w , and $\sigma_{combined} = 1/\sqrt{\sum w}$ [1]. For the systematic errors, we use the statistical error weights to average the values so there is no reduction of the systematic error on any one point. We do this because most of the systematic errors are correlated. This is also how the Run 10 and Run 11 $v_{2T} + v_{2E}$ values in Figure 6.7 were combined.

There is an amount of correlations in the errors between the two Runs. Because of this we make the simplifying assumption, since the statistical errors dominate anyway in any individual integrated yield, that there is no reduction of systematic error, and simply average the systematic error for the two runs using the same statistical error weights used to average the measurement values. This is done because although error sizes at some level are the same or strongly correlated, in some cases their propagation to the final result error is affected by statistical fluctuations.

The combined away-side yields for all three integration regions is shown in Figure 8.24. Each color is a different centrality bin, and the $p+p$ baseline is the red points near the top of the plots. This figure shows that the integrated per-trigger yields scale with z_T , they are high for low z_T and decrease as z_T increases. Some of the error bars appear large but that is because the per-trigger yields are consistent with zero and the y-axis is a log scale.

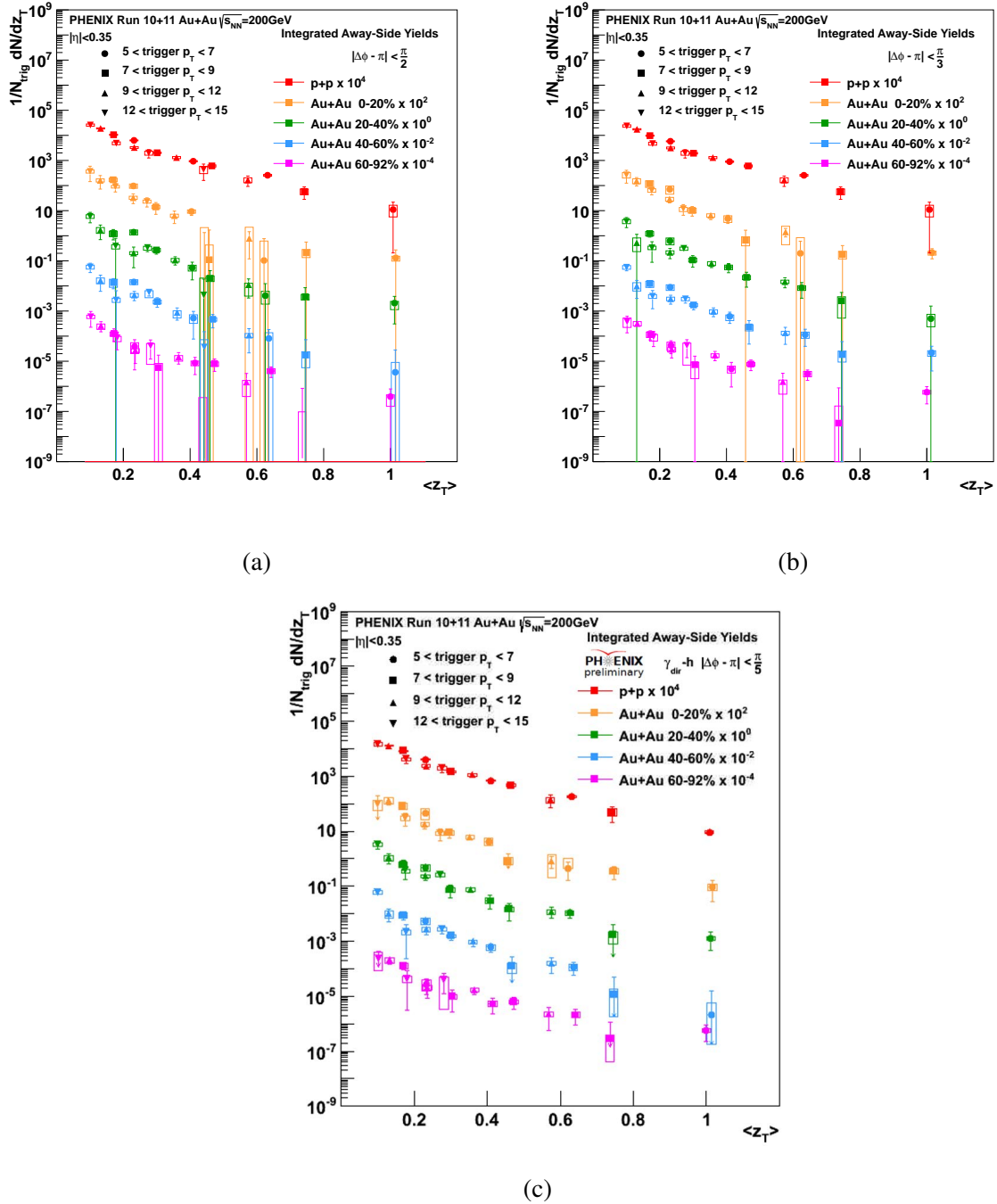


Figure 8.24: Run 10 and Run 11 combined away-side yields as a function of z_T for each integration region $\pi/2$ (a), $\pi/3$ (b), and $\pi/5$ (c) and each centrality bin: 0 - 20% (orange), 20 - 40% (green), 40 - 60% (blue), and 60 - 92% (magenta). The red points are the $p+p$ baseline.

The combined results for I_{AA} as a function of z_T are shown in Figure 8.25, for the $\pi/2$ away-side, Figure 8.26, for the $\pi/3$ away-side, and Figure 8.27, for the $\pi/5$ away-side. Each trigger p_T bin is a different color and the four p_{Tassoc} bins: 1-2, 2-3, 3-5, and 5-10 GeV/c that increase from left to right. Some of the points have large error bars due to a lack of statistics and there are a lot of fluctuations. This is expected in this analysis because there are a lot of fluctuations in the jet functions. Even though there are fluctuations, there is a clear grouping of the high z_T and low z_T points. Generally, the low z_T and high z_T points have similar I_{AA} values. The I_{AA} values of the high z_T points are lower than the I_{AA} value of the low z_T points. Since there is a grouping of the low z_T and high z_T values, we average them so we can plot the average as a function of centrality. The average of each group of points in the purple line in these figures. The lighter purple band is the error on the average, this is found by averaging the upper and lower statistical error of the I_{AA} points. The lower and upper limits on the averaging regions were chosen to limit the overlap of the different p_T bin combinations. See Figure 8.8 and explanation for more details.

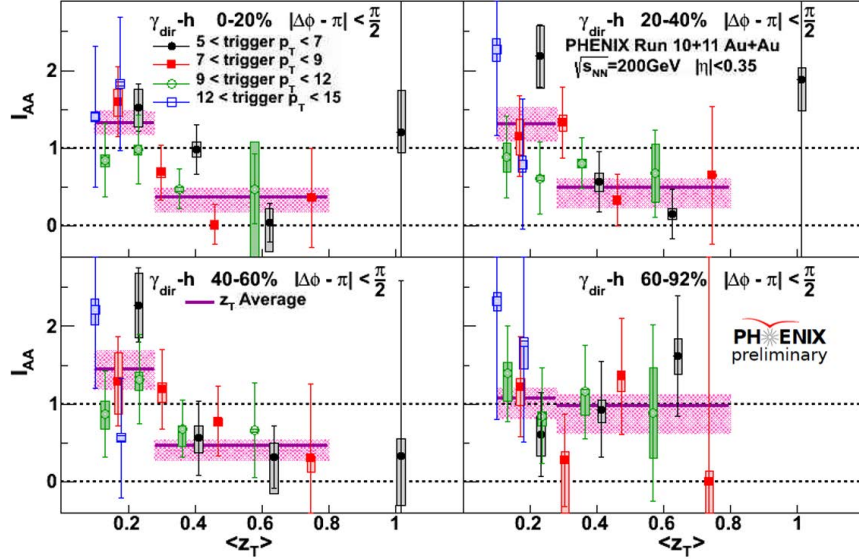


Figure 8.25: Combined Run 10 + Run 11 I_{AA} as a function of z_T for the $\pi/2$ away-side integration region. Each trigger p_T bin is a different color and the four p_{Tassoc} bins: 1-2, 2-3, 3-5, and 5-10 GeV/c that increase from left to right. Constant fits to high and low z_T regions are shown with statistical error in purple [31]. This figure has been used with permission. See Appendix C for more details.

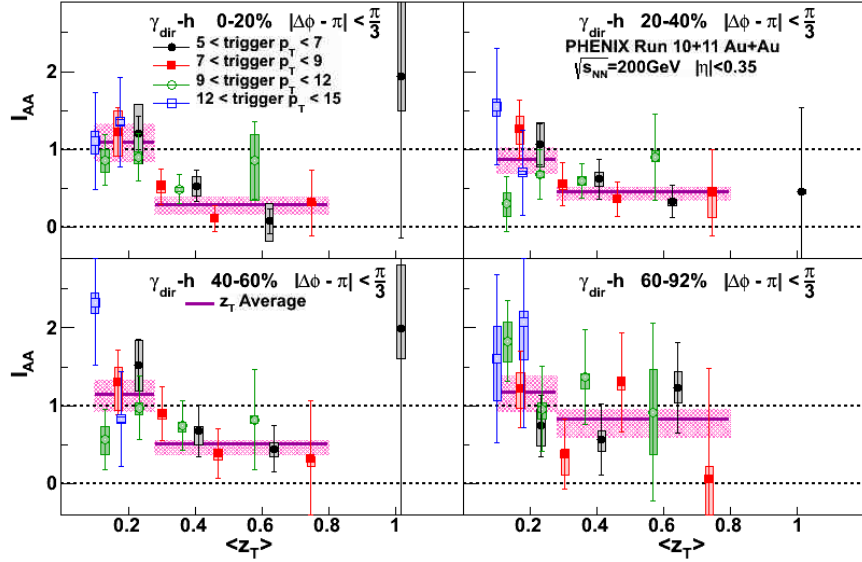


Figure 8.26: Combined Run 10 + Run 11 I_{AA} as a function of z_T for the $\pi/3$ away-side integration region. Each trigger p_T bin is a different color and the four $p_{T\text{assoc}}$ bins: 1-2, 2-3, 3-5, and 5-10 GeV/c that increase from left to right. Constant fits to high and low z regions are shown with statistical error in purple.

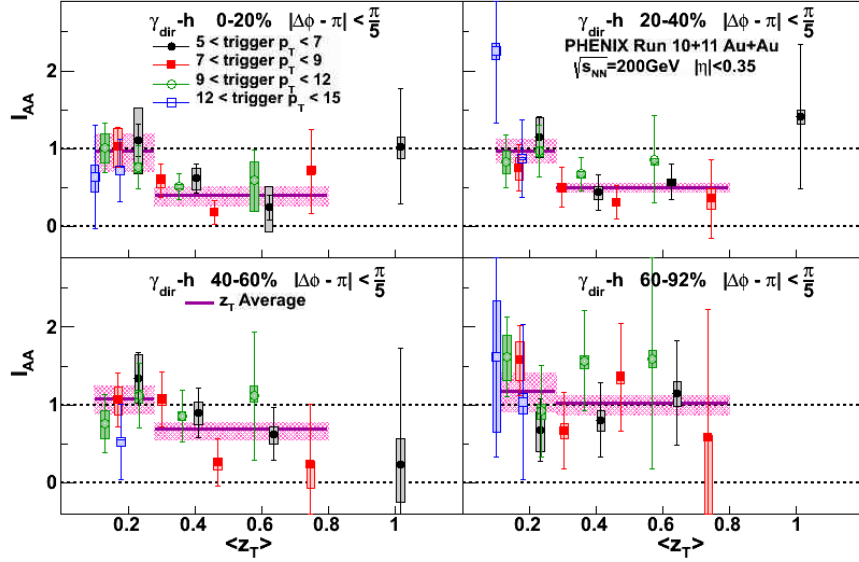


Figure 8.27: Combined Run 10 + Run 11 I_{AA} as a function of z_T for the $\pi/5$ away-side integration region. Each trigger p_T bin is a different color and the four $p_{T\text{assoc}}$ bins: 1-2, 2-3, 3-5, and 5-10 GeV/c that increase from left to right. Constant fits to high and low z regions are shown with statistical error in purple.

Finally, the combined Run 10 + Run 11 I_{AA} values are fit to constant values in the high and low z_T regions for comparison. This is shown as a function of N_{part} in the top panels of Figure 8.28 for the three away-side regions. The red points are the high z_T average I_{AA} , the blue points are the low z_T average I_{AA} . The red points show a strong suppression in central events (high N_{part}) that decreases towards peripheral events. This is due to the high z_T particles losing energy as they traverse the QGP. The blue points are not suppressed, some are consistent with one while some show a hint of enhancement. This is due to the QGP emitting low z_T particles from the energy lost by the high z_T particles. This enhancement is larger for the wider away-side regions as shown by comparing the blue points in Figures 8.28b or 8.28c to those in Figure 8.28a. This means that the low z_T particles are emitted at wide angles compared to the jet.

The high z_T (high $p_{T\text{assoc}}$) suppression evolves with centrality in a similar way to the single particle high p_T suppression. The low z_T level is always enhanced compared to the overall level

of jet suppression, except in the most peripheral bin. This figure shows, for the first time at RHIC, the centrality evolution of this low z_T enhancement, thought to be due to recovered energy loss. The low z_T fit values show a small monotonic centrality (path-length) dependence (increase) to the recovered energy loss energy, mirroring the increase in suppression. The bottom panels in Figure 8.28 shows the centrality dependence of ratio of low to high z_T fit values, called the energy recovery factor (*ERF*), which more accurately reflects the true centrality dependence of the low z_T enhancement in the per-jet fragmentation function. This is because per-trigger direct-photon-normalized I_{AA} always folds in the overall suppression of the away-side jets, since the photons are not suppressed while the away-side is. Thus, the suppressed high I_{AA} of the z_T points divides out to first order the overall suppression level, yielding something closer to the per-suppressed jet fragmentation function enhancement.

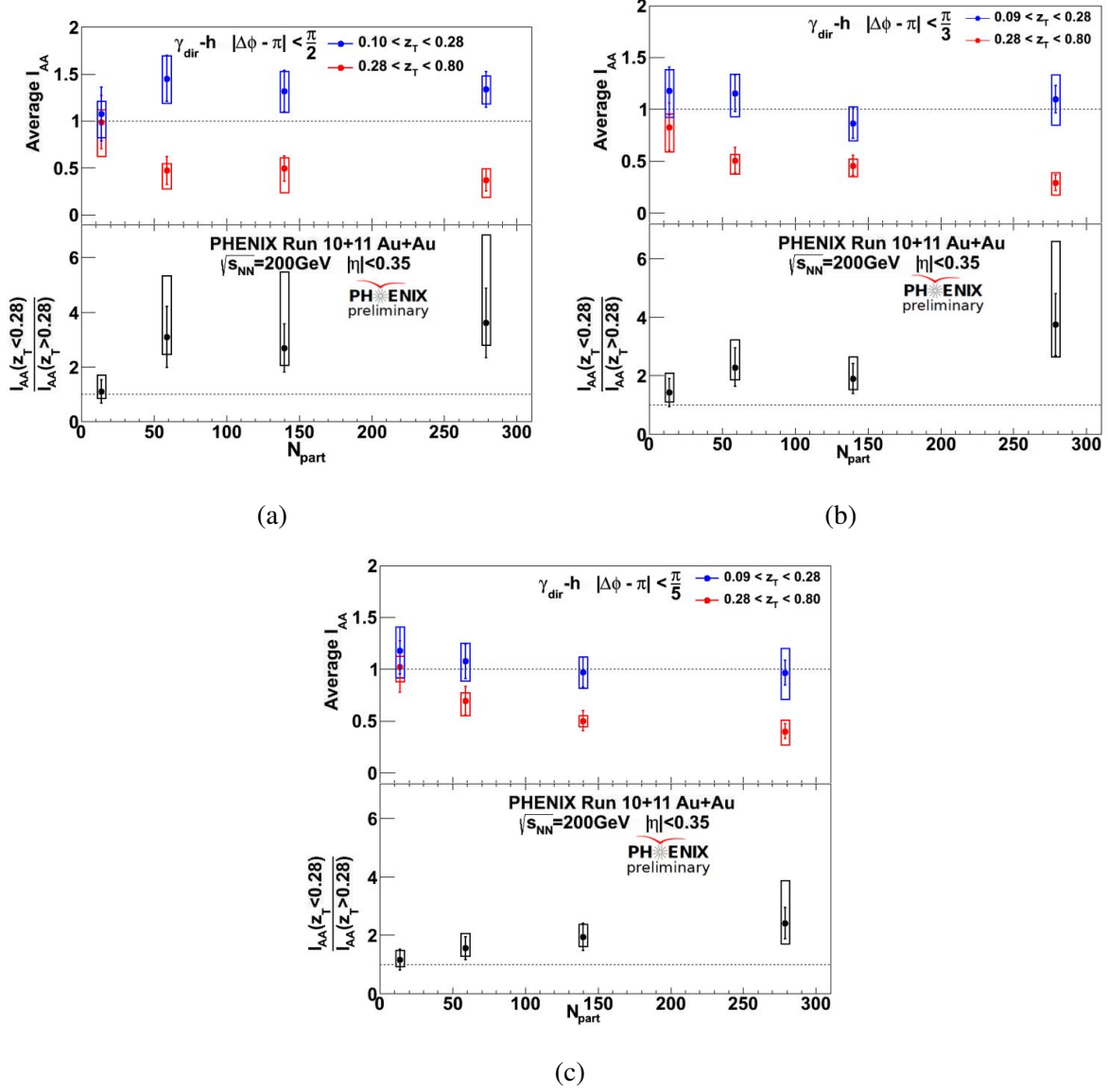


Figure 8.28: Run 10 and Run 11 combined I_{AA} as a function of N_{part} for each integration region $\pi/2$ (a), $\pi/3$ (b), and $\pi/5$ (c). The red points in the top panels is the high z_T average and the blue points in the low z_T average. The bottom panels shows the centrality dependence of ratio of low to high z_T fit values, the energy recovery factor, which more accurately reflects the true centrality dependence of the low z_T enhancement in the per-jet fragmentation function since per-photon I_{AA} always folds in the overall suppression of the away-side jets [31]. These figures has been used with permission. See Appendix C for more details.

8.8 Comparisons to Previous PHENIX Results

The results of this analysis can be compared to previous PHENIX results. The first comparison is shown in Figure 8.29 and is the comparison to the results in References [32, 35]. The black (a) and blue (b) points in Figure 8.29 the Run 7 + 10 + 11 Au+Au 0 - 40 % central events I_{AA} as function of $\xi = \ln(1/z_T)$. The light green points are the centrality averaged 0 - 20% and 20 - 40% I_{AA} from this analysis. The analysis carried out in References [32, 35] used a statistical method to find direct photons. This is the same method that was used in Reference [18, 32, 35]. This comparison proves that even though our methods differ, the results in this analysis are the same as those in Reference [32].

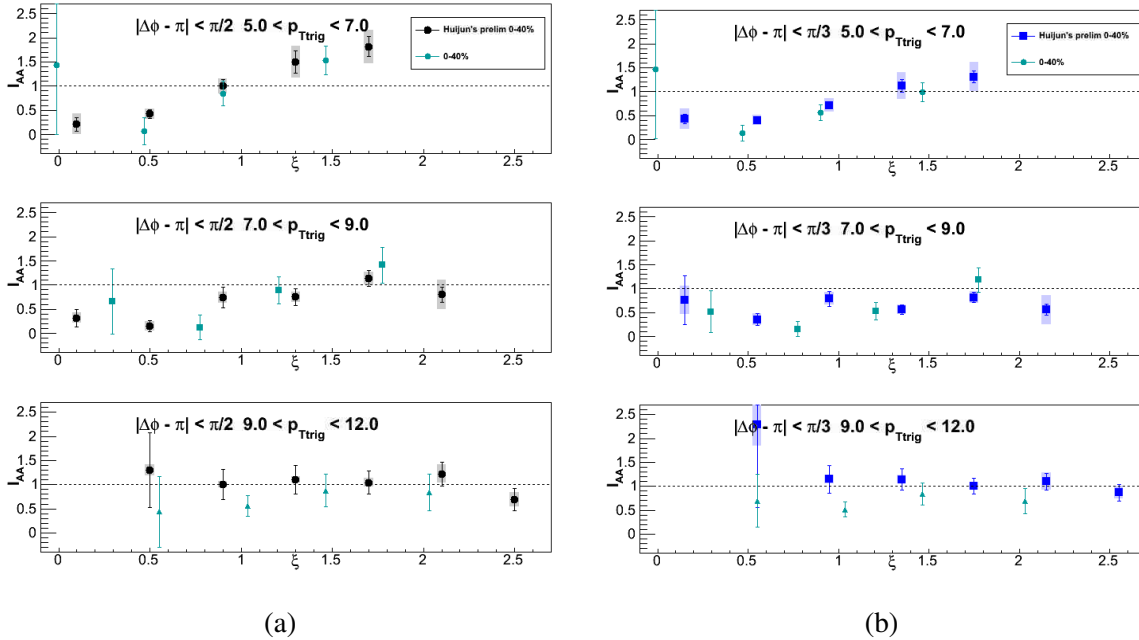


Figure 8.29: Run 10 + 11 Au+Au $\gamma_{dir} - h$ I_{AA} as a function of $\xi = \ln(1/z_T)$ for each integration region $\pi/2$ (a) and $\pi/3$ (b) from this analysis (green points). The black and blue points are Run 7 + 10 + 11 Au+Au 0 - 40 % central events I_{AA} carried out in Reference [32, 35]. Each panel is a trigger p_T bin.

9 DISCUSSION - ISOLATED GAMMA-HADRON CORRELATIONS

Another comparison that can be carried out is on the I_{AA} of the high z_T particles as a function of N_{part} . This is shown in Figure 9.1. The red points are the Run 10 + 11 I_{AA} of high z_T particles and the gray band is the R_{AA} of π^0 for π^0 with $p_T > 5\text{GeV}/c$ from Reference [36]. These quantities are expected to qualitatively agree because the photons from γ -jet are not surface biased, so their jets have the same geometric distribution and path length distribution as inclusive jets.

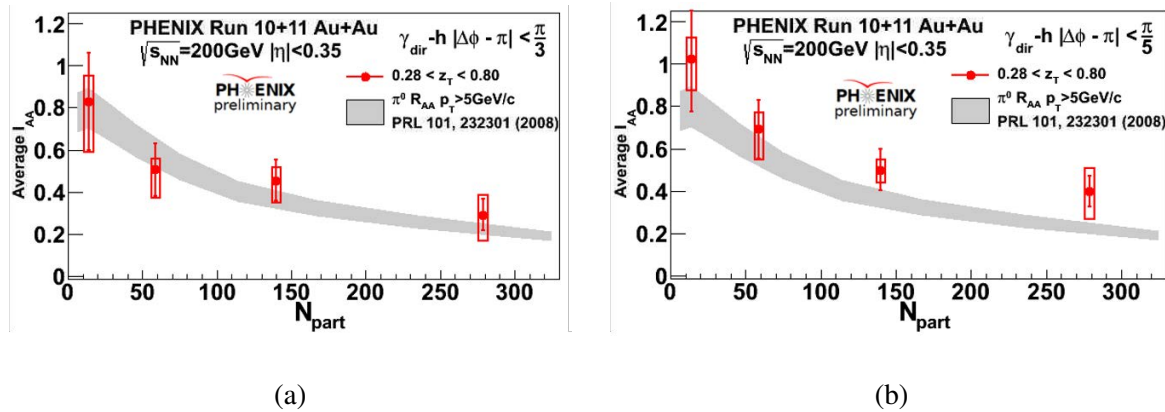


Figure 9.1: Run 10 + 11 Au+Au direct photon I_{AA} as a function of N_{part} for each integration region $\pi/3$ (a) and $\pi/5$ (b) from this analysis [31]. The gray band is the R_{AA} of π^0 for π^0 with $p_T > 5\text{GeV}/c$ from Reference [36]. These figures have been used with permission. See Appendix C for more details.

9.1 Comparisons to Theoretical Calculations

While this work did not carry out theoretical calculations the work carried out in References [32, 35] did. The results in this dissertation were shown to agree with these results in Figure 8.29. The calculations in these references were for I_{AA} as a function of z_T for three trigger p_T bins. They are shown in Figure 9.2. This is the full away-side region; the three trigger p_T bins are: $5 < p_T^\gamma < 7 \text{ GeV}/c$ (top panel), $7 < p_T^\gamma < 9 \text{ GeV}/c$ (middle panel), and $9 < p_T^\gamma < 12 \text{ GeV}/c$ (bottom

panel). These data are compared to two theoretical calculations, CoLBT_Hydro (solid line) and BW-MLLA (dashed line).

The CoLBT_Hydro model is a linearized Boltzman transport model for parton propagation with a hydrodynamic model of the QGP evolution [37]. It tracks the thermal partons and their interactions in the QGP. The model says that the jets excite the medium which causes the high ξ (low z_T) enhancement. It also suggests that the transition from suppression to enhancement takes place at a different ξ value for each trigger p_T bin [35].

The BW-MLLA model is the Borghini and Wiedemann modified leading logarithmic approximation model [38]. This model uses increased parton splitting probability to model the energy loss. The calculation was done for jets with $E=7$ GeV. This model also says that the jets excite the medium which causes the high ξ enhancement.

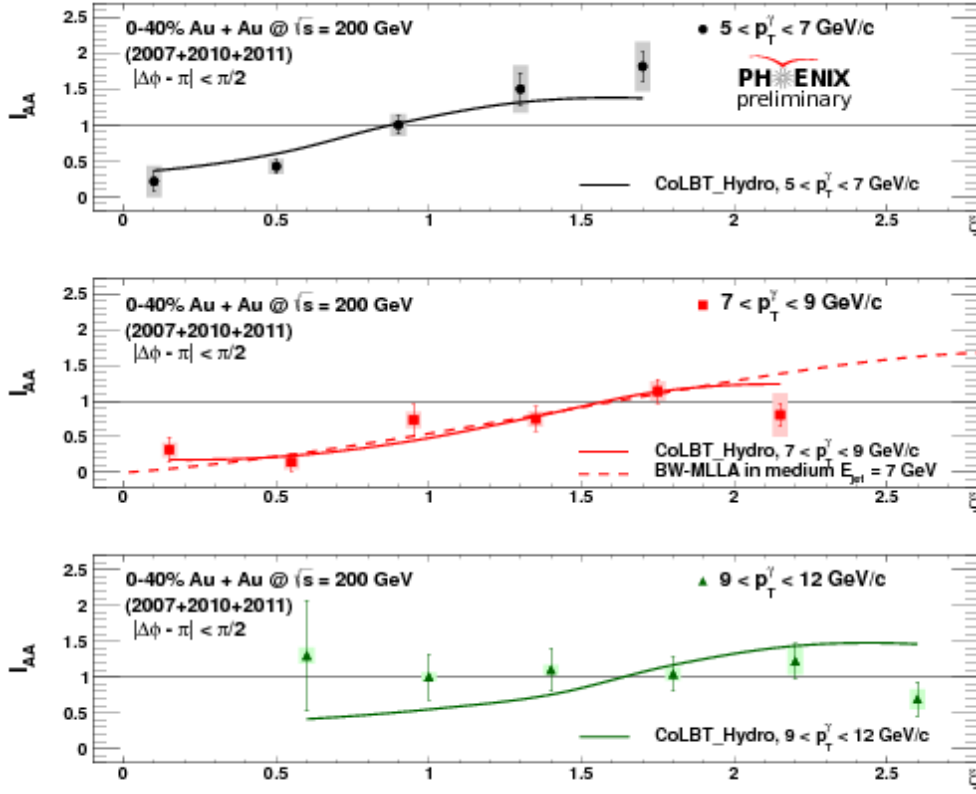


Figure 9.2: Non-Isolated γ -h results from separate analysis—not part of this dissertation—of other PHENIX collaborators Ge H. and Jacak, B et. al. Run 7 + 10 + 11 Au+Au 0 - 40 % central events I_{AA} as function of $\xi = \ln(1/z_T)$ for three trigger p_T bins: $5 < p_T^\gamma < 7 \text{ GeV}/c$ (top panel), $7 < p_T^\gamma < 9 \text{ GeV}/c$ (middle panel), and $9 < p_T^\gamma < 12 \text{ GeV}/c$ (bottom panel). The lines are two theoretical calculations, CoLBT_Hydro (solid line) and BW-MLLA (dashed line) [35, 37, 38]. This figure has been used with permission. See Figures C.17 and C.18 for more details.

9.2 $I_{AA}(p_{Th})$ versus $I_{AA}(z_T)$

Comparisons to the models suggest that the enhancement should scale with hadron p_T because the radiated energy couples to the medium and gains the characteristic energy scale of the medium for soft thermal particles, such as the QGP temperature scale.

If the away-side yields were composed of the unmodified jet fragmentation function, I_{AA} would scale with z_T not p_T . The I_{AA} in Figure 9.2 is plotted as a function of hadron p_T in Figure

9.3 (black points) for the three trigger p_T bins. The magenta points are I_{AA} in d +Au collisions at $\sqrt{s_{NN}} = 200$ GeV. These points show no enhancement or suppression. The black points suggest that the transition from enhancement to suppression takes place near $p_{Th} \approx 3$ GeV/c for all trigger p_T bins. So the medium redistributes the energy of the high p_T particles to particles with $p_T < 3$ GeV/c.

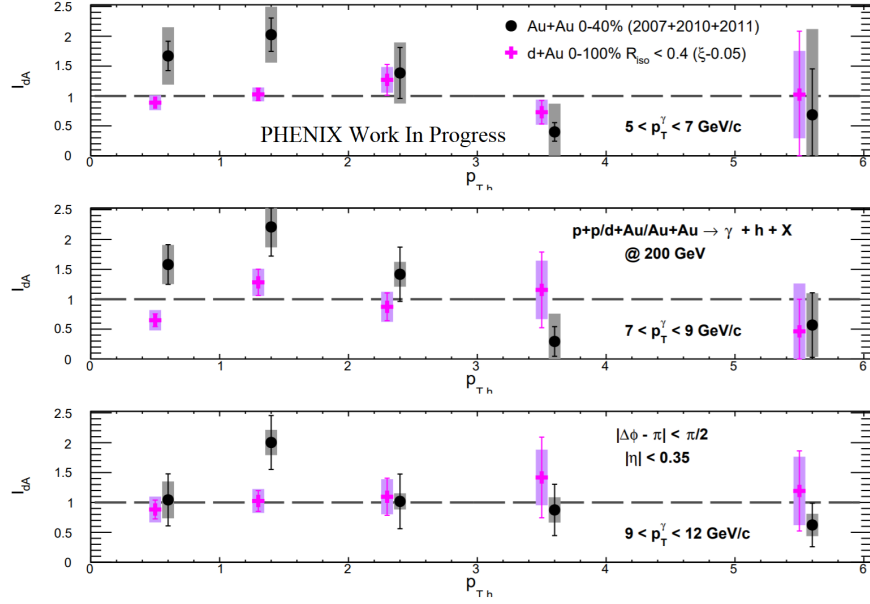


Figure 9.3: Non-Isolated γ -h results from separate analysis—not part of this dissertation—of other PHENIX collaborators Ge H. and Jacak, B et. al. I_{AA} as a function of associated hadron p_T or three trigger p_T bins: $5 < p_T^\gamma < 7$ GeV/c (top panel), $7 < p_T^\gamma < 9$ GeV/c (middle panel), and $9 < p_T^\gamma < 12$ GeV/c (bottom panel). The black points are 0-40% central events in Au+Au collisions, the same points shown in Figure 9.2, and the magenta points are 0-100% central events in d +Au collisions at $\sqrt{s_{NN}} = 200$ GeV [32].

Figure 9.3 shows the enhancement pattern for 0-40% central events for three trigger p_T bins for the full $\pi/2$ away-side region. This figure was taken from the previous PHENIX direct photon-hadron analysis [32]. The large centrality bin allows for small error bars and the three panels makes the p_T transition easy to see. We plot our centrality dependent I_{AA} as a function of hadron

p_T for the three away-side regions used in this analysis in Figures 9.4 - 9.6. It is hard to see the transition from enhancement to suppression in some of these figures because we carry out our analysis for more centrality bins than the results in Figure 9.3. However, some trends are visible, for all away-side integration regions, the 0-20% central events seems to support a similar conclusion as Figure 9.3. To see if these conclusions are also supported by the isolation cut data in this dissertation, we also plot our I_{AA} results as a function of associated p_T in Figures 9.4 - 9.6. Note that we include all trigger p_T bins for completeness but the two higher p_T bins, 9-12 GeV/c (green points) and especially the 12-15 GeV/c (blue points) have very poor statistical significance and should generally be ignored. The two lowest trigger p_T bins mostly have reasonable statistical significance which can confirm the conclusions drawn from Figure 9.3.

For the two smaller away-side integration ranges in Figures 9.5 and 9.4, the two smallest trigger p_T bins (black and red points) agree very well for all hadron p_T and all centrality bins except 60-92% where the statistics are limited. This means that the transition from enhancement to suppression occurs at the same hadron p_T , near 2 GeV/c, for all trigger p_T for both the $\pi/3$ and $\pi/5$ away-sides. This is consistent with the results in Figure 9.3, especially in the most central (0-20%) centrality bin. The rest of the $\pi/2$ I_{AA} (Figure 9.6) centrality bins have too many statistical fluctuations event in the low p_T red and black points to say anything concrete about the transition.

The above discussion of the I_{AA} crossing one as the transition from enhancement to suppression could be more precise. The value crossing one doesn't matter because there is an overall suppression of the away-side jets, this is why we make the *ERF* in Figures 8.28 above. Comparing the I_{AA} to one helps judge the shape of the hadron p_T dependence but really since the central events are the most suppressed, and the more periphial are less so, the crossing one point should shift to higher hadron p_T . Each trigger p_T curve should have the same shape in each centrality bin. A hint of this feature is shown in the $\pi/3$ away-side I_{AA} in Figure 9.5.

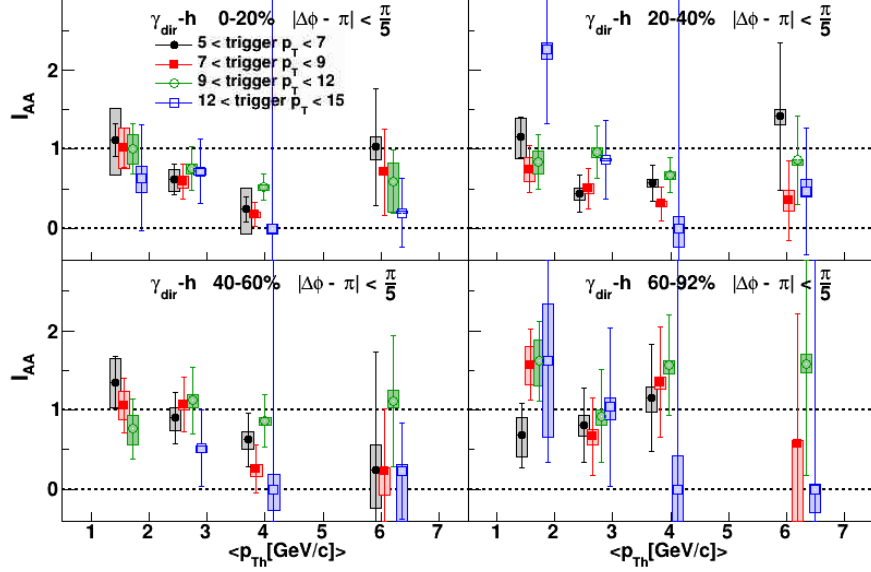


Figure 9.4: Combined Run 10 + Run 11 I_{AA} as a function of associated hadron p_T for the $\pi/5$ away-side integration region. Each trigger p_T bin is a different color that has been offset for clarity.

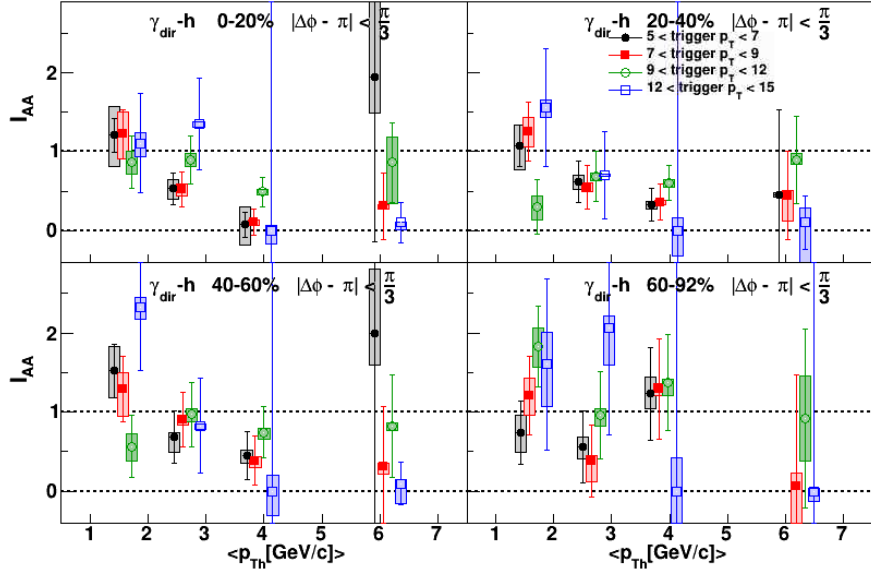


Figure 9.5: Combined Run 10 + Run 11 I_{AA} as a function of associated hadron p_T for the $\pi/3$ away-side integration region. Each trigger p_T bin is a different color that has been offset for clarity.

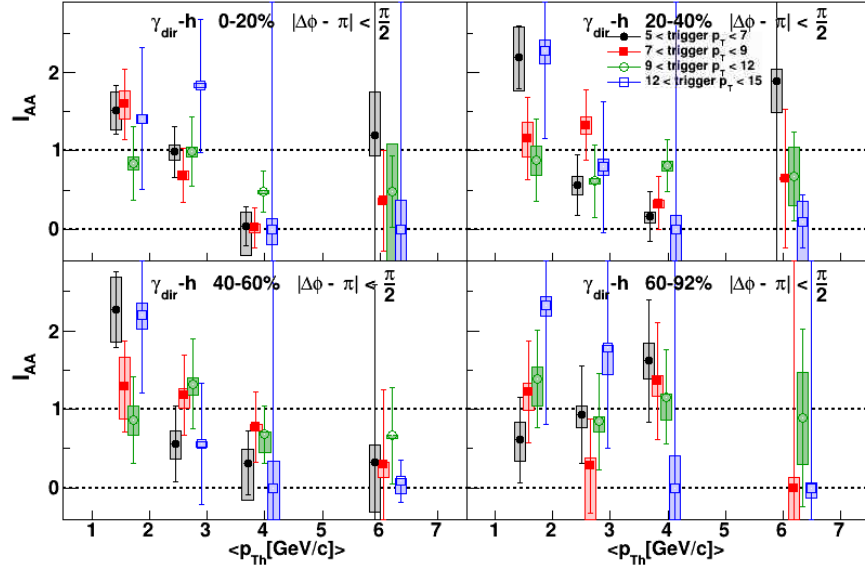


Figure 9.6: Combined Run 10 + Run 11 I_{AA} as a function of associated hadron p_T for the $\pi/2$ away-side integration region. Each trigger p_T bin is a different color that has been offset for clarity.

9.3 Comparisons to Other Experiments

The STAR collaboration at RHIC has also measured I_{AA} as a function of z_T . This is shown in Figure 9.7 for triggers with $12 < p_T^{trig} < 20$ GeV/c in 0-12% central events in Au+Au collisions [39]. The red points are the I_{AA} from $\gamma_{dir} - h$ correlations and the blue points are the I_{AA} from $\pi_0 - h$ correlations. The $\gamma_{dir} - h$ correlations started with an inclusive photon measurement and used the statistical method to obtain direct photons; this measurement does not use an isolation cut. This figure is for the full $\pi/2$ away-side region. The lines in this figure are different energy-loss models: Qin (red dotted line), $\gamma_{dir} - h$ ZOWW (red solid line), $\pi_0 - h$ ZOWW (blue solid line), and the Renk YaJem model (red dot dashed line). The Qin model includes a hydrodynamic evolution with energy loss in the medium and includes fragmentation photons as well as photons from partons in the medium [49]. The ZOWW model is similar to Qin but does not include the fragmentation photons or the photons from the partons in the medium [50]. These two models do not include the redistribution of the energy lost by the high z_T particles to the low z_T particles. The Renk YaJem model uses gluon radiation for the energy loss and includes the energy redistribution to the QGP

[51]. The Renk curve in the figure is for a slightly lower trigger p_T and a the $\pi/5$ away-side region so slight disagreement with the data is expected. The rise at low z_T is from the redistribution of energy to the low z_T particles.

The centrality and trigger p_T selection used in Figure 9.7 makes a direct comparison with the results in this dissertation difficult. The most similar results we have are the blue points in the top left panel of Figure 8.25. This is the trigger p_T bin with the least statistics so the two high z_T points were omitted from that figure because the error bars are large. Nevertheless, one can see that our results are consistent with the red points in Figure 9.7. The lower trigger p_T bins at higher z_T are consistent with the STAR result.

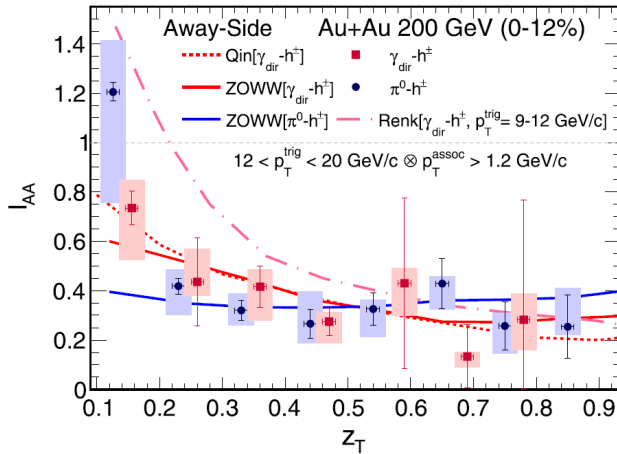


Figure 9.7: I_{AA} as a function of z_T for $\gamma_{dir} - h$ (red points) and $\pi_0 - h$ (blue points) for triggers with $12 < p_T^{trig} < 20$ GeV/c measured with STAR. The lines are theoretical calculations: Qin (red dotted line), $\gamma_{dir} - h$ ZOWW (red solid line), $\pi_0 - h$ ZOWW (blue solid line), and the Renk YaJem model (red dot dashed line) [39]. This figure has been used with permission. See Appendix C for more details.

The ATLAS collaboration at the LHC has published a measurement of $R_{D(p_T)}$, which is the true partonic fragmentation function we are using I_{AA} as a proxy for. The quantity R_D is the ratio of the charged particle jet fragmentation function of one centrality to the charged particle jet

fragmentation function in peripheral centrality. Instead of using photon-hadron correlations to find the jet yield, this measurement uses a jet finding algorithm to find jets. To find the fragmentation function, they measure the charged particles in the jet cone per jet and subtract the charged particles coming from the underlying event. These can be measured as a function of charged particle p_T or $z = \vec{p}_T^{ch} \cdot \vec{p}_T^{jet} / |\vec{p}_T^{jet}|^2$ where \vec{p}_T^{ch} is the p_T of charged particles and \vec{p}_T^{jet} is the jet's p_T . The quantity z is similar to but not exactly the same as z_T . Figure 9.8a shows $R_{D(z)}$ and Figure 9.8b shows $R_{D(p_T)}$ (blue points) for 0-10% central events in Pb+Pb collisions at $\sqrt{s_{NN}} = 2.76$ TeV [40]. The yellow boxes show the systematic error. The higher energy collisions allow for the measurement of higher p_T particles, all the way out to 100 GeV/c. There is enhancement at low and very high z_T and p_T while at mid z_T and p_T there is suppression. This matches the pattern of enhancement to suppression at low hadron p_T presented in this dissertation even though we do not see the high z_T and p_T enhancement which will be described in the next section.

Note also that the suppression level in the LHC results mid p_T is much smaller, only about 10%, than for our I_{AA} results. This is due to the full-jet results' normalization being per-found-jet, and doesn't include a factor of the overall jet suppression like in our I_{AA} . Nonetheless the rate of overall jet suppression is also measured at LHC with the same methods and is consistent with the suppression we see in I_{AA} at high z_T . Therefore the similarity of our results at low z_T and these full jet reconstruction results confirms our interpretations of I_{AA} .

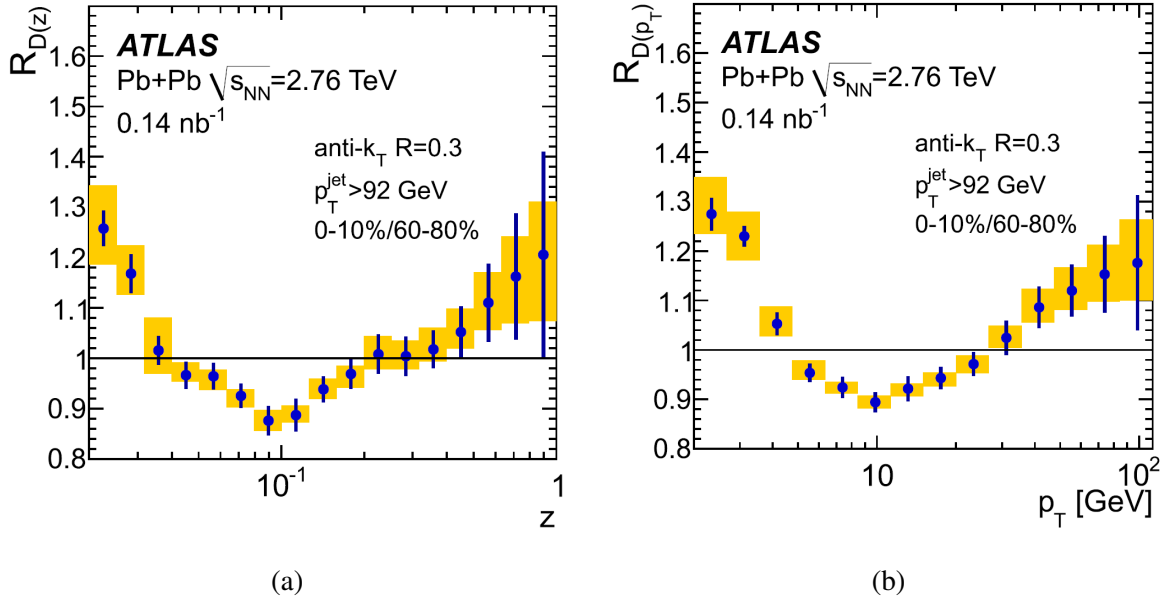


Figure 9.8: $R_{D(z)}$ (left) and $R_{D(p_T)}$ (right) (blue points) in Pb+Pb collisions at $\sqrt{s_{NN}} = 2.76$ TeV with the systematic error in yellow [40]. This figure has been used with permission. See Appendix C for more details.

9.3.1 PYTHIA study of $R_{D(z)}$ shape

To better determine why some experiments see the high z_T enhancement shown in Figure 9.8a, a PYTHIA study was carried out. PYTHIA is a common particle and heavy ion event generator [61]. It was initially thought that the lack of high z_T enhancement in correlation measurements was because the direct photon trigger p_T was not equal to the jet p_T , which will occur for next to leading order production. To study this, we generated $R = 0.3$ jets with $p_T > 8$ GeV/c. We weighted some of the jets with a z factor in order to simulate Au+Au collisions. The yields as a function of z are shown in Figure 9.9. The black points are the normal "p+p" jets and the red points are the simulated Au+Au jets.

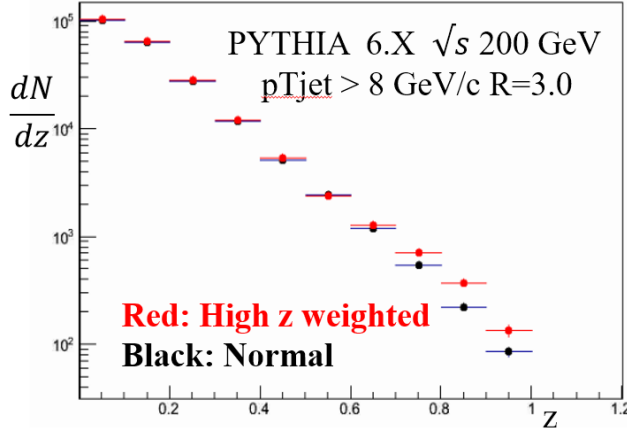


Figure 9.9: PYTHIA jet yield as a function of z_T for $R = 0.3$ jets with $p_T > 8$ GeV/c. The black points are the normal jets and the red points are the high z_T weighted jets.

The ratio of the red points to the black points, $R_{D(z)}$, is shown in Figure 9.10a. This is the true PYTHIA jet $R_{D(z)}$. When a PYTHIA two-particle analysis is carried out, the I_{AA} for trigger particles with $p_T > 10$ GeV/c can be made and plotted as a function of hadron p_T . This is shown in Figure 9.10b. The enhancement begins around $p_T = 7$ GeV/c and the magnitude of the enhancement is not as large as the enhancement in $R_{D(z)}$ (Figure 9.10a). This study shows that when doing a two-particle correlation analysis, like the one presented in this dissertation and the STAR result shown in Figure 9.7, the high z_T enhancement should not be expected because the two-particle correlation smears the high z_T jets to multiple p_T bins. The high z and p_T enhancement is seen in the ATLAS results (Figure 9.8) because that is a full jet reconstruction analysis that captures the full jet z and p_T .

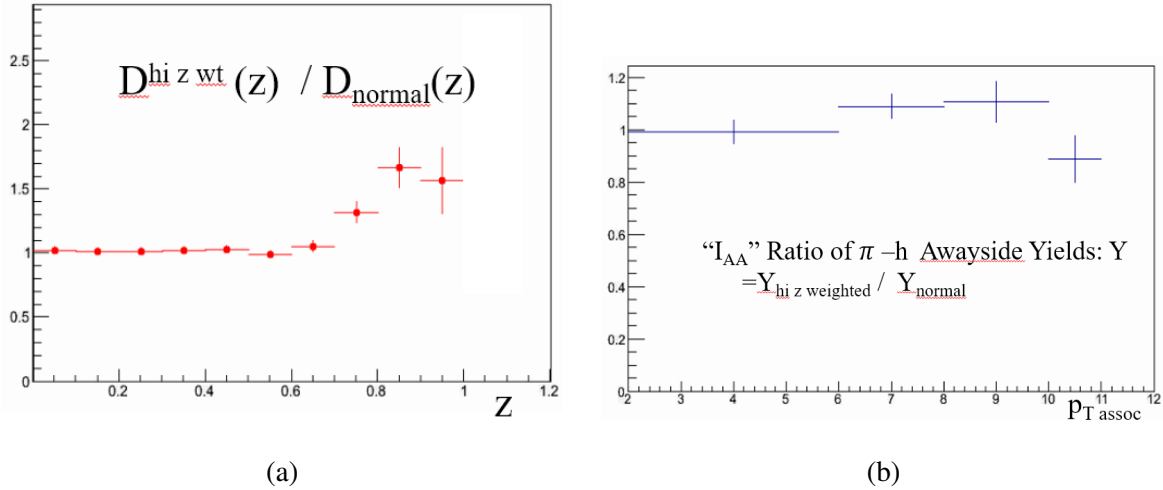


Figure 9.10: True PYTHIA $R_{D(z)}$ (a) and I_{AA} for trigger particles with $p_T > 10$ GeV/c as a function of hadron p_T (b). The I_{AA} shows no high p_T enhancement.

10 SUMMARY AND FUTURE WORK

This work was devoted to measuring the v_2 of isolated photon and π^0 as well as direct photon-hadron correlations using an isolation cut in Au+Au collisions at $\sqrt{s_{NN}} = 200$ GeV collected by the PHENIX detector at RHIC. This is the first time that an isolation cut has been used in the high multiplicity Au+Au collision environment. We use an isolation cut to increase the signal-to-background ratio of direct photons. The two particle correlation procedure requires knowing the flow coefficients of the two particles involved in the correlation. This required us to measure the isolated photon v_2 .

This dissertation has built on the work of others, mainly Nowo Rivelis doctoral dissertation [3]. We used his isolation cut method but we developed a number of things to improve the background estimate of the correlation function which leads to the modification of the final I_{AA} measurement. Most notable of these improvements are the measurements of the isolated particle v_2 and the handling of the background magnitude. The measurement of the isolated particle v_2 required derivation and verification of the particle-reaction plane correlation function which I performed. A good portion of this work was done in my master's thesis, reference [52], and is described at the beginning of Chapter 4. However I made substantial additions for this dissertation, and the rest of that chapter describes the work done since reference [52] was published, this includes derivation and verification the particle-event plane correlation with the event plane resolution. The other important improvement I made was with the estimation of the magnitude of the background in the correlation function. The improvement developed here was recognizing that the isolated trigger distribution has discontinuities at the centrality bin edges because the isolation cut depends on centrality as described in Section 7.4.1. These two improvements allowed for my improvement of the results presented in Nowo Rivelis doctoral dissertation. I ultimately accomplished this by applying the updated complete isolation cut γ - h analysis on a new dataset, Run 11 Au+Au, as well as completely reanalyzing with all improvements the Run 10 Au+Au dataset. The work presented in this dissertation is in the process of being prepared for publication in a peer-reviewed journal.

10.1 Isolated Particle v_2

In this dissertation I derived, studied, and measured how the isolation cut modifies the isolated particle v_2 . I extend the work carried out in Reference [52] by confirming and studying how, even in the presence of the event plane resolution, the v_2 extracted actually has a contribution of v_2 from the underlying event factored into it. This is due to the fact that the isolation cut parameters a and b are constant anywhere in a given event which causes the isolation cut to preferentially accept particles emitted out-of-plane with respect to the event plane as isolated since the underlying event modulates to a lesser extent there. The converse is also true, our isolation cut method finds less isolated particles oriented in-plane relative to the event plane. We also extended the work carried out in Reference [52] to show the mathematical description of this bias when measuring the elliptic flow of the isolated particles, especially with regards to event plane resolution. This bias can be parameterized by $\epsilon \propto 1 + v_{2E} \cos \Delta\phi$ where the efficiency v_2 of the underlying event, v_{2E} , is typically negative. The distribution can be derived by folding into the typical underlying event distribution to obtain

$$\frac{dN_{STSE}}{d\Delta\phi} = \mathcal{I} \left(1 + 2\mathcal{J} \cos(2\Delta\phi) + \mathcal{K} \cos^2(2\Delta\phi) - 4\mathcal{L} \cos(4\Delta\phi) \right), \quad (10.1)$$

where \mathcal{I} is a normalization factor, $\mathcal{J} = v_{2T} + v_{2E} \langle \cos(2\delta\Psi) \rangle$, $\mathcal{K} = v_{2T}v_{2E}$, and $\mathcal{L} \propto v_{2T}v_{2E}$. The $\langle \cos(2\delta\Psi) \rangle$ factor is the typical event plane resolution correction.

We have measured $v_{2T} + v_{2E}$ in Au+Au PHENIX data. This is shown in Figure 6.7 as a function of p_T for 0-20% and 20-40% events. One can see in this figure that the isolated photon v_2 is closer to the direct photon v_2 than the inclusive photon v_2 . The isolated photon v_2 has some decay photon contribution because some quantity of decay photons survive the isolation cut. There is no decay photon subtraction on the isolated photons for the v_2 measurement so their v_2 confirms that the isolation cut has largely removed the decay contribution.

We also measured the v_{2E} to perform the proper subtraction to extract the v_{2T} of isolated photon (Figure 6.3) and π^0 (Figure 6.4). The v_2 of isolated π^0 in the 20-40% central events are significantly less than the v_2 of inclusive π^0 . By definition, the isolation cut captures a different type of jet fragmentation than the inclusive π^0 measurement, so this could be a hint that energy loss

might depend on the way a jet fragments, as where in the nominal models, it only depends on the color charge and its kinematics. However, we also know that the isolation cut shifts the jet p_T sampling, and possibly other jet phase space sampling. The isolated π^0 should contain more of the jet momentum than the inclusive π^0 . So the v_2 might be expected to have a different v_2 if the underlying different selection of jets sampled just had a different v_2 for reasons of selection bias. This warrants further investigation.

Finally, we derived the proper v_2 that must be multiplied by the hadron v_2 to subtract the right background shape from the isolated photon-hadron and π^0 -hadron correlation functions. This is shown in Equation 4.5. All of the derivations concerning v_2 , including those with a realistic event plane resolution, were verified for all ranges of v_{2T} and v_{2E} with a Monte Carlo study.

10.2 Isolated $\gamma - h$ Correlations

In addition to the isolation cut causing the background shape to change, it also changed the magnitude of the background. This required a modification in the standard MSMP method used in previous PHENIX analyses [3, 5, 18, 33]. Once the background modifications were handled we found correlation and jet functions. The $\gamma_{iso} - h$ away-side yields are then mapped to $\gamma_{dir} - h$ away-side yields by using a statistical subtraction method. The resulting Au+Au $\gamma_{dir} - h$ yields are then divided by the $\gamma_{dir} - h$ in $p+p$ collisions to find I_{AA} as a function of $z_T = p_T^h / p_T^\gamma$. The high and low z_T points were averaged and plotted as a function of centrality (N_{part}).

Figure 10.1a shows I_{AA} as a function of N_{part} from Reference [17]. One of the goals of this dissertation was to increase the precision of this measurement. The significant increase in precision allowed us to split the lowest N_{part} bin into two. This allows for a more detailed shape dependence to be observed. The result from this work is shown Figure 10.1b. One can see that the precision is increased and it appears that the suppression follows the $\pi^0 R_{AA}$, this means that the geometry of the suppression in the medium is the same as the geometry of the π^0 's from the suppressed jets which traverse the QGP.

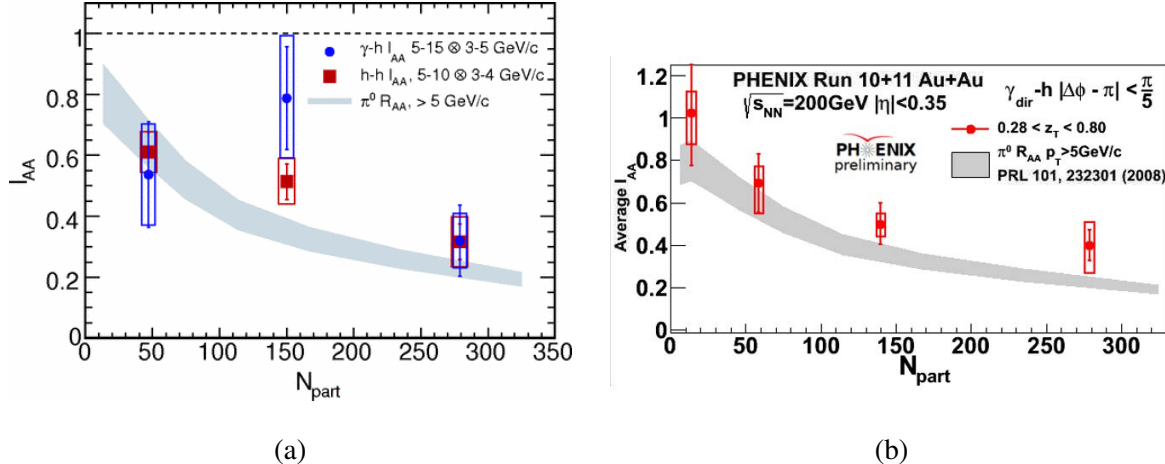


Figure 10.1: (Left) I_{AA} of $\gamma_{dir} - h$ pairs with $5 < p_T^\gamma < 15$ GeV/c and $3 < p_T^h < 5$ GeV/c (blue points), the red points are $h - h$ pairs with $5 < p_T^h < 10$ GeV/c and $3 < p_T^h < 4$ GeV/c (red squares) as a function of N_{part} for the $\pi/5$ away-side region. The shaded gray region is the R_{AA} of π^0 's with $p_T > 5$ GeV/c [17]. (Right) Run 10 + 11 Au+Au $\gamma_{dir} - h$ I_{AA} as a function of N_{part} for the $\pi/5$ away-side region from this analysis. The gray band is the R_{AA} of π^0 for $p_T > 5$ GeV/c from Reference [36].

By contrast there is no suppression of the low z_T particles and in some cases even enhancement. This has been seen in other Au+Au correlation analyses, notably References [17, 18, 35]. To see how both the high z_T suppression and low z_T non-suppression/enhancement vary with centrality, we plot again as a summary in Figure 10.2, the low and high z_T direct photon average I_{AA} as function of N_{part} for three away-side integration regions, $\pi/2$ (Figure 10.2 left), $\pi/3$ (Figure 10.2 middle), and $\pi/5$ (Figure 10.2 right) away-side integration regions. Immediately obvious is that the low and high z_T behaviors are different. There is high z_T suppression for all centrality bins while the low z_T points are not suppressed, so they are relatively flat with centrality. The low z_T behavior has previously been interpreted as being a signal of energy loss recovery by the medium. This is because the high z_T particles' energy loss enhances the production of low z_T particles. There is increasing low z_T enhancement for wider integration regions, as seen in the blue points increasing from the right plot to left. The isolation cut method allows for a more precise

analysis of the semi-peripheral and peripheral centralities. This is the first detailed characterization of the centrality dependence of the low z_T enhancement at RHIC. Although theoretical calculations of this centrality dependence are not yet available, the data should constrain the mechanisms of redistribution of recovered energy in energy loss models.

To judge true centrality dependence of enhancement, we must account for overall reduction of jets due to suppression, because our normalization of the yields is made per trigger photon, and therefore includes the jet suppression factor—which is why the high z_T yields have $I_{AA} < 1$. For this reason, the I_{AA} values at low z_T in this observable, even if they do not exceed $I_{AA} = 1$ can reasonably described as enhancement, as long as they are substantially higher than the overall suppression level measured by the I_{AA} at high z_T . To quantify this, the ratio is made of the low z_T to high z_T average I_{AA} values, the energy recovery factor, is shown in the bottom panel of Figure 10.2. One can see that this ratio monotonically increases towards central events for all away-side integration regions, qualitatively matching expectations of having low z_T energy recovery scaling inversely to the amount of energy loss/suppression.

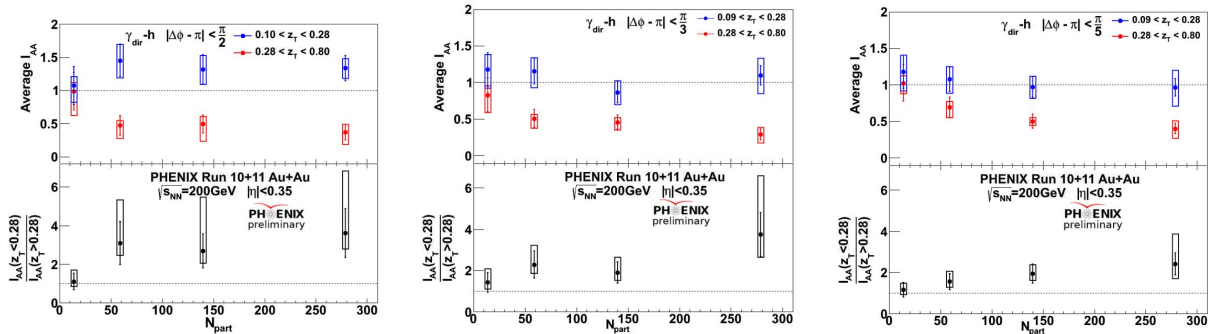


Figure 10.2: Average I_{AA} as a function of N_{part} for each away-side integration region $\pi/2$ (left), $\pi/3$ (middle), and $\pi/5$ (right). The red points in the top panels is the high z_T average and the blue points are the low z_T average. The bottom panels show the centrality dependence of ratio of high to low z_T average I_{AA} , the energy recovery factor.

Results of the centrality integrated I_{AA} as a function of hadron p_T , instead of z_T , (Figure 9.3) suggest that the transition from enhancement to suppression occurs at the same hadron p_T ,

near 3 GeV/c, for all trigger p_T bins. This is confirmed in the I_{AA} as a function of hadron p_T results presented in this dissertation (Figures 9.6 - 9.4). Comparing the shape of $I_{AA}(p_{Th})$ between the centralities hints that all trigger p_T curves have similar values and dependence on p_{Th} in each centrality bin, and showing the well known increasing suppression in more central events.

10.3 Future Work and Outlook

This work measured isolated photon v_2 and isolated photon-hadron correlations in Au+Au collisions at $\sqrt{s_{NN}} = 200$ GeV detected by PHENIX during RHIC-Run 10 and 11. These data sets sampled a total of 12.6 billion MinBias events. PHENIX has taken more Au+Au data since then, for instance, during RHIC-Run 14 a total of 19.9 billion MinBias events were recorded by PHENIX and during RHIC-Run 16 a total of 14 billion MinBias events were recorded by PHENIX. Both of these data sets were also at $\sqrt{s_{NN}} = 200$ GeV. So PHENIX has even more Au+Au data than Run 10 and 11. These datasets could vastly reduce the statistical error bars in Figure 8.28.

This analysis could also be carried out over a different collision species. This could elucidate whether or not the size and shape of the QGP has an effect on the jet suppression. One of the more interesting collision species is Cu+Au at $\sqrt{s_{NN}} = 200$ GeV because the N_{part} value of central Cu+Au collisions corresponds to the N_{part} of mid-central Au+Au collisions. The Cu+Au I_{AA} could be broken up into its centrality bins, all of which would correspond N_{part} of peripheral Au+Au collisions. It would be interesting to see if the I_{AA} suppression pattern of high z_T particles continues toward the lowest N_{part} values. There could even be some small enhancement for the most peripheral events. It would be especially interesting because the I_{AA} suppression in Au+Au seems to be geometry influenced and Cu+Au collisions have a different geometry than Au+Au collisions.

The longer term future prospects for this analysis is the sPHENIX project at RHIC. PHENIX was decommissioned in 2016 to make way for the next generation detector called sPHENIX, shown in Figure 10.3. The sPHENIX detector has full azimuthal coverage and $|\eta| < 1$. It consists of inner and outer hadron calorimeters (HCal), an intermediate silicon tracker (INTT), a Monolithic-

Active-Pixel-Sensor-based VerTeX Detector (MVTX), a solenoid magnet, an electromagnetic calorimeter (EMCal), and the time projection chamber (TPC) [41]. This detector is projected to record over 200 billion MinBias Au+Au events. It has the ability to extend this analysis to a much higher p_T range which will be extremely useful to make comparisons to LHC data and thereby compare two vastly different initial energies in the QGP evolution. This detector is projected to begin data taking in 2023.

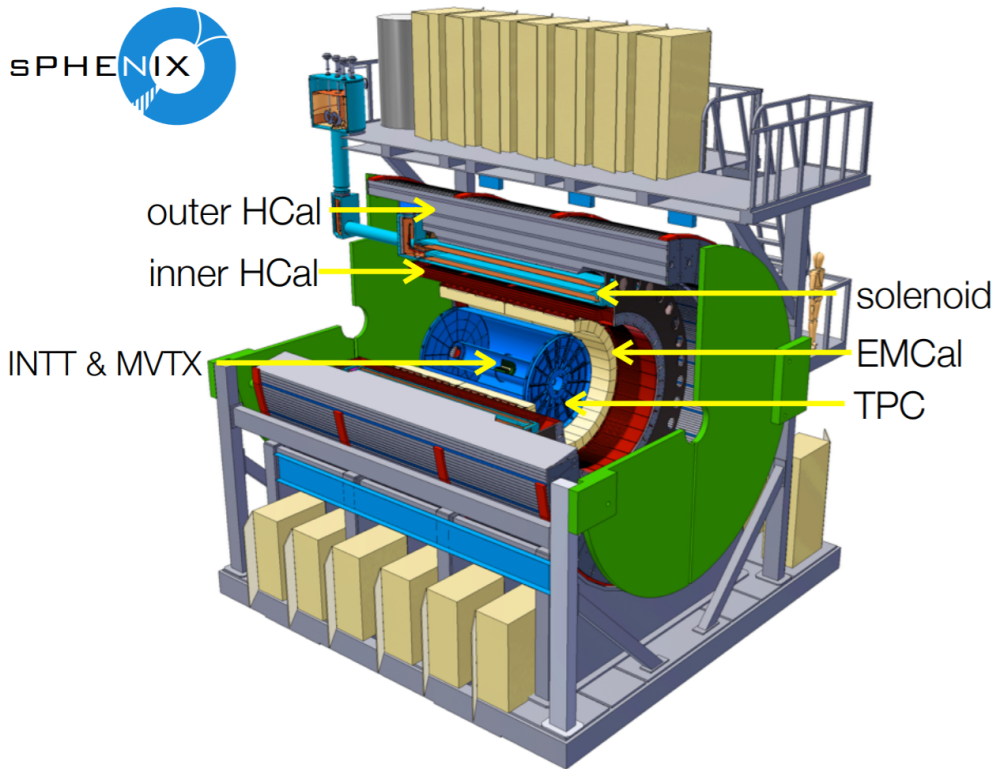


Figure 10.3: Current sPHENIX design with the major subsystems labeled: inner and outer hadron calorimeters (HCal), intermediate silicon tracker (INTT), Monolithic-Active-Pixel-Sensor-based VerTeX Detector (MVTX), the solenoid magnet, electromagnetic calorimeter (EMCal), and the time projection chamber (TPC) [41].

REFERENCES

- [1] J. Beringer *et al.* (Particle Data Group), Phys.Rev. **D86**, 010001 (2012).
- [2] “An Introduction to PHENIX: Detectors,” <https://www.phenix.bnl.gov/phenix/WWW/intro/detectors/index.html>.
- [3] N. Rivelis, *Direct Photon - Hadron Correlations Measurement in Au+Au Collision at Nucleon Center-Of-Mass Energy of 200 GeV With Isolation Cut Methods*, Ph.D. thesis, Ohio University (2014).
- [4] A. Adare, *Transverse momentum evolution of neutral pion triggered dihadron correlations in Au+Au collisions at $\sqrt{s_{NN}} = 200 \text{ GeV}$* , Ph.D. thesis, University of Colorado (2010).
- [5] M. Connors, *Direct Photon Tagged Jets in 200 GeV Au+Au Collisions at PHENIX*, Ph.D. thesis, Stony Brook University (2011).
- [6] H. Ge, “Run-11 Au+Au 200 GeV Direct Photon-Hadron Correlations,” <https://www.phenix.bnl.gov/cdsagenda/askArchive.php?base=agenda&categ=a17119&id=a17119s1t5/moreinfo>, HHJ meeting, April 20, 2017.
- [7] S. Bushwick, “How Low Can RHIC Go?” <http://www.bnl.gov/newsroom/news.php?a=21870> (2010).
- [8] Particle Data Group, LBNL, “History of the Universe,” <http://www.particleadventure.org/images/history-of-the-universe-2015.pdf> (2014).
- [9] RHIC, “The Physics of RHIC,” <http://www.bnl.gov/rhic/physics.asp>.
- [10] C. Shen, “Sketch of relativistic heavy-ion collisions,” <https://u.osu.edu/vishnu/2014/08/06/sketch-of-relativistic-heavy-ion-collisions> (2014).
- [11] W. A. Horowitz, *Probing the Frontiers of QCD*, Ph.D. thesis, Columbia U. (2010), arXiv:1011.4316 [nucl-th].

- [12] T. Takahito and S. Esumi, “Measurement of Hadron-Hadron Correlations with Higher Harmonic Reaction Plane in Run 7 Au+Au 200GeV Collisions,” (2014), PHENIX internal Analysis Note 991.
- [13] A. Adare *et al.* (PHENIX Collaboration), Phys. Rev. Lett. **98**, 162301 (2007).
- [14] C. Nattress, Private Communication.
- [15] J. Adams *et al.* (STAR Collaboration), Nucl.Phys. **A757**, 102 (2005), nucl-ex/0501009 .
- [16] A. Sickles, M. P. McCumber, and A. Adare, Phys. Rev. C **81**, 014908 (2010).
- [17] A. Adare *et al.* (PHENIX Collaboration), Phys. Rev. C **80**, 024908 (2009).
- [18] A. Adare *et al.* (PHENIX), Phys. Rev. Lett. **111**, 032301 (2013).
- [19] “RHIC Complex,” <https://www.flickr.com/photos/brookhavenlab/7979381212> (2011), Brookhaven National Laboratory.
- [20] A. Adare *et al.* (PHENIX Collaboration), Phys. Rev. C **91**, 044907 (2015).
- [21] S. Aronson *et al.*, Nuclear Instruments and Methods in Physics Research Section A: Accelerators, Spectrometers, Detectors and Associated Equipment **499**, 480 (2003), the Relativistic Heavy Ion Collider Project: RHIC and its Detectors.
- [22] T. Nakamura, “Introduction to PHENIX Beam Beam Counter (BBC),” https://www.phenix.bnl.gov/phenix/WWW/intro/detectors/focus/focus_bbc.pdf (2002).
- [23] L. Aphecetche *et al.*, Nuclear Instruments and Methods in Physics Research Section A: Accelerators, Spectrometers, Detectors and Associated Equipment **499**, 521 (2003), the Relativistic Heavy Ion Collider Project: RHIC and its Detectors.
- [24] K. Adcox *et al.*, Nuclear Instruments and Methods in Physics Research Section A: Accelerators, Spectrometers, Detectors and Associated Equipment **499**, 489 (2003), the Relativistic Heavy Ion Collider Project: RHIC and its Detectors.

- [25] A. Oskarsson, “The Pad Chambers (PC),” http://www.phenix.bnl.gov/phenix/WWW/intro/detectors/focus/focus_pc.pdf (2003).
- [26] M. L. Miller, K. Reygers, S. J. Sanders, and P. Steinberg, Annual Review of Nuclear and Particle Science **57**, 205 (2007), <https://doi.org/10.1146/annurev.nucl.57.090506.123020>.
- [27] M. S. M. Dai, J. Mitchell, “Centrality Calibration for the Run-11 200 GeV Au+Au Dataset,” (2015), PHENIX internal Analysis Note 1076.
- [28] S. S. Adler *et al.* (PHENIX Collaboration), Phys. Rev. C **76**, 034904 (2007).
- [29] A. Adare *et al.* (PHENIX Collaboration), Phys. Rev. Lett. **109**, 122302 (2012).
- [30] S. Mizuno, “The Higher Order Azimuthal Anisotropy Of Inclusive Photon and π^0 In Run7 Au+Au $\sqrt{s_{NN}} = 200$ GeV For Final Results,” (2015), PHENIX internal Analysis Note 1211.
- [31] T. Danley, Journal of Physics: Conference Series **1070**, 012023 (2018).
- [32] H. Ge *et al.*, “Direct photon-hadron correlations in Run-11 Au+Au 200 GeV and combined results with Run7 + Run10 + Run11 for preliminary,” (2016), PHENIX internal Analysis Note 1272.
- [33] N. Riveli and J. Frantz, “Analysis of Run 7 + Run 10 Au+Au Photon-Hadron Correlations With Isolation Cut,” (2014), PHENIX internal Analysis Note 1183.
- [34] C. Chen *et al.*, “Final Analysis of the Run 4 Au+Au and Run 5+6 $p+p$ Direct Photon-Hadron Correlations (PPG090),” (2009), PHENIX internal Analysis Note 718.
- [35] H. Ge (PHENIX), *Proceedings, 8th International Conference on Hard and Electromagnetic Probes of High-energy Nuclear Collisions: Hard Probes 2016 (HP2016): Wuhan, Hubei, China, September 23-27, 2016*, Nucl. Part. Phys. Proc. **289-290**, 313 (2017), arXiv:1703.09374 [nucl-ex].
- [36] A. Adare *et al.* (PHENIX Collaboration), Phys. Rev. Lett. **101**, 232301 (2008).

- [37] Y. He, T. Luo, X.-N. Wang, and Y. Zhu, Phys. Rev. **C91**, 054908 (2015), arXiv:1503.03313 [nucl-th] .
- [38] N. Borghini and U. A. Wiedemann, (2005), arXiv:hep-ph/0506218 [hep-ph] .
- [39] L. Adamczyk *et al.* (STAR), Phys. Lett. **B760**, 689 (2016), arXiv:1604.01117 [nucl-ex] .
- [40] G. Aad *et al.* (ATLAS), Phys. Lett. **B739**, 320 (2014), arXiv:1406.2979 [hep-ex] .
- [41] A. Frawley, “The sPHENIX Experiment,” https://indico.bnl.gov/event/4611/contributions/22168/attachments/18782/24182/sPHENIX_Users_Meeting_2018_frawley.pdf, RHIC/AGS User’s Meeting, June 2018.
- [42] D. Griffiths, *Introduction to Particle Physics* (Wiley-VCH, 2008).
- [43] S. Chatrchyan *et al.* (CMS), Phys. Lett. **B716**, 30 (2012), arXiv:1207.7235 [hep-ex] .
- [44] G. Aad *et al.* (ATLAS), Phys. Lett. **B716**, 1 (2012), arXiv:1207.7214 [hep-ex] .
- [45] CERN, “Heavy Ions and Quark-Gluon Plasma,” <http://home.web.cern.ch/about/physics/heavy-ions-and-quark-gluon-plasma>.
- [46] J. D. Bjorken, Phys. Rev. D **27**, 140 (1983).
- [47] A. M. Poskanzer and S. A. Voloshin, Phys. Rev. **C58**, 1671 (1998), arXiv:nucl-ex/9805001 .
- [48] J.-Y. Ollitrault, (1997), arXiv:nucl-ex/9711003 [nucl-ex] .
- [49] G.-Y. Qin, J. Ruppert, C. Gale, S. Jeon, and G. D. Moore, Phys. Rev. **C80**, 054909 (2009), arXiv:0906.3280 [hep-ph] .
- [50] H. Zhang, J. F. Owens, E. Wang, and X.-N. Wang, Phys. Rev. Lett. **103**, 032302 (2009), arXiv:0902.4000 [nucl-th] .
- [51] T. Renk, Phys. Rev. **C80**, 014901 (2009), arXiv:0904.3806 [hep-ph] .

- [52] T. Danley, *Measurement of Elliptic Flow Coefficients and Derivation of Reaction Plane Dependent Efficiency of Isolated Photons and π^0 Mesons in $\sqrt{s_{NN}} = 200$ GeV Au+Au Collisions at RHIC-PHENIX*, Master's thesis, Ohio University (2014).
- [53] M. Harrison, T. Ludlam, and S. Ozaki, Nuclear Instruments and Methods in Physics Research Section A: Accelerators, Spectrometers, Detectors and Associated Equipment **499**, 235 (2003), the Relativistic Heavy Ion Collider Project: RHIC and its Detectors.
- [54] K. Adcox *et al.*, Nuclear Instruments and Methods in Physics Research Section A: Accelerators, Spectrometers, Detectors and Associated Equipment **499**, 469 (2003), the Relativistic Heavy Ion Collider Project: RHIC and its Detectors.
- [55] S. Esumi *et al.*, “High p_T Charged Hadron v_2 in Au + Au Collisions at $\sqrt{s_{NN}} = 200$ GeV,” (2005), PHENIX internal Analysis Note 473.
- [56] A. Adare *et al.* (PHENIX), Phys. Rev. **D82**, 072001 (2010), arXiv:1006.1347 [hep-ex].
- [57] A. Adare *et al.* (PHENIX), Phys. Rev. **D95**, 072002 (2017), arXiv:1609.04769 [hep-ex].
- [58] C. Aidala *et al.* (PHENIX), Submitted to: Phys. Rev. D (2018), arXiv:1805.02450 [hep-ex].
- [59] C. Chen *et al.*, “Preliminary Analysis of the Run7 Au+Au -(Also Including Run 4,5,6) Direct Photon- Hadron Correlations for Hard Probes 2008,” (2008), PHENIX internal Analysis Note 708.
- [60] X.-N. Wang and M. Gyulassy, Phys. Rev. D **44**, 3501 (1991).
- [61] T. Sjostrand, P. Eden, C. Friberg, L. Lonnblad, G. Miu, S. Mrenna, and E. Norrbin, Comput. Phys. Commun. **135**, 238 (2001), arXiv:hep-ph/0010017 [hep-ph].

APPENDIX A: CORRELATION AND JET FUNCTIONS

A.1 Correlation Functions for All Centralities

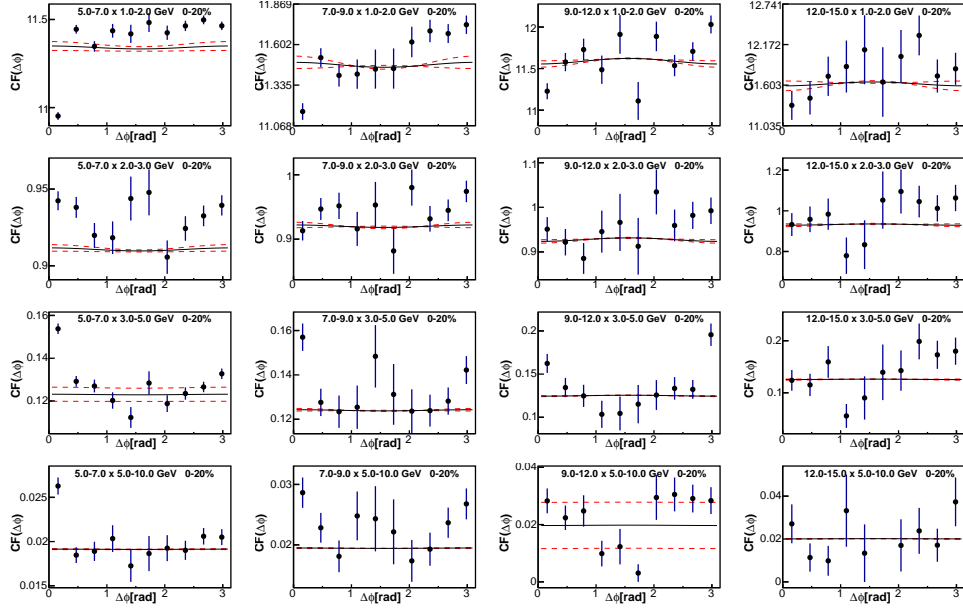


Figure A.1: Run 10 Au+Au $\gamma_{iso} - h$ correlation functions for 0-20% events. Each plot is a different p_T bin combination. Trigger p_T increases to the right while partner p_T increases going down. The black line represents the background level, the red lines around it is the error on the black line.

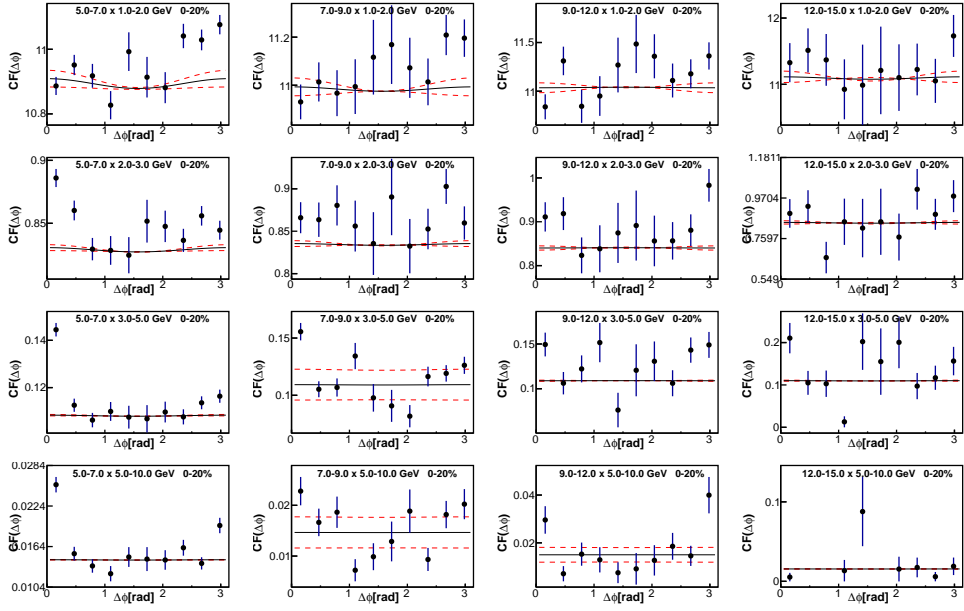


Figure A.2: Run 11 Au+Au $\gamma_{iso} - h$ correlation functions for the centrality labeled in the figure. Each plot is a different p_T bin combination. Trigger p_T increases to the right while partner p_T increases going down. The black line represents the background level, the red lines around it is the error on the black line.

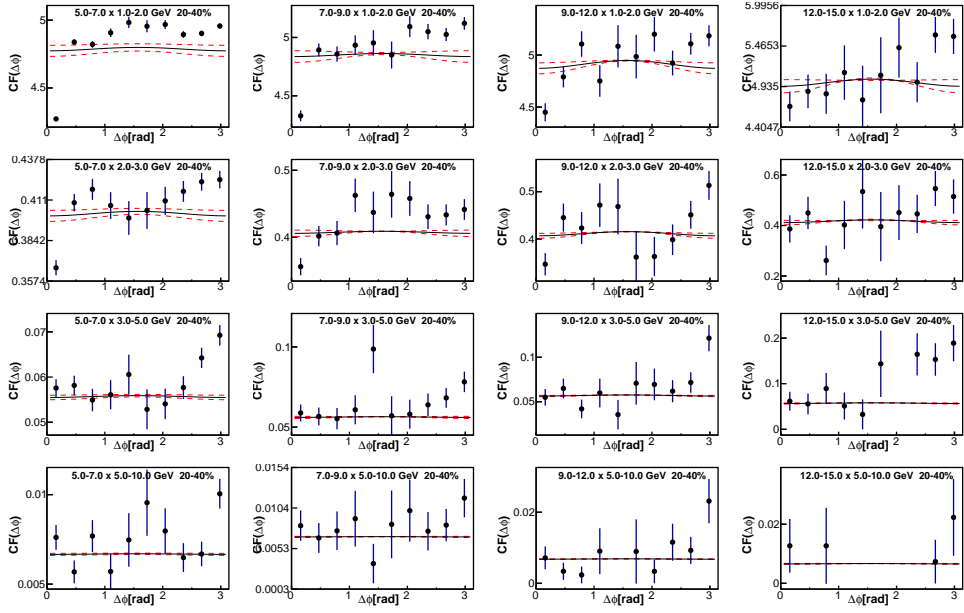


Figure A.3: Run 10 Au+Au $\gamma_{iso} - h$ correlation functions for the centrality labeled in the figure. Each plot is a different p_T bin combination. Trigger p_T increases to the right while partner p_T increases going down. The black line represents the background level, the red lines around it is the error on the black line.

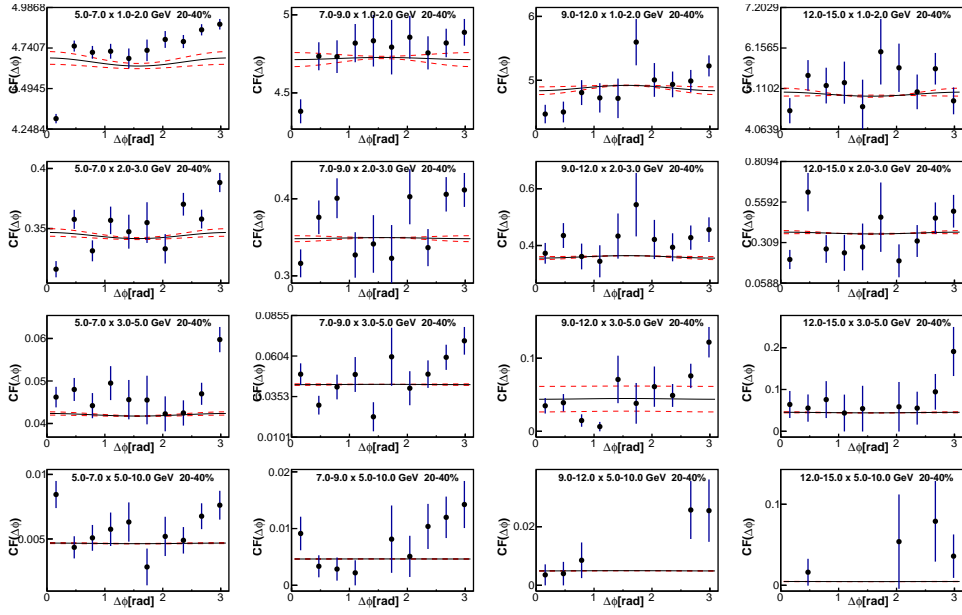


Figure A.4: Run 11 Au+Au $\gamma_{iso} - h$ correlation functions for the centrality labeled in the figure. Each plot is a different p_T bin combination. Trigger p_T increases to the right while partner p_T increases going down. The black line represents the background level, the red lines around it is the error on the black line.

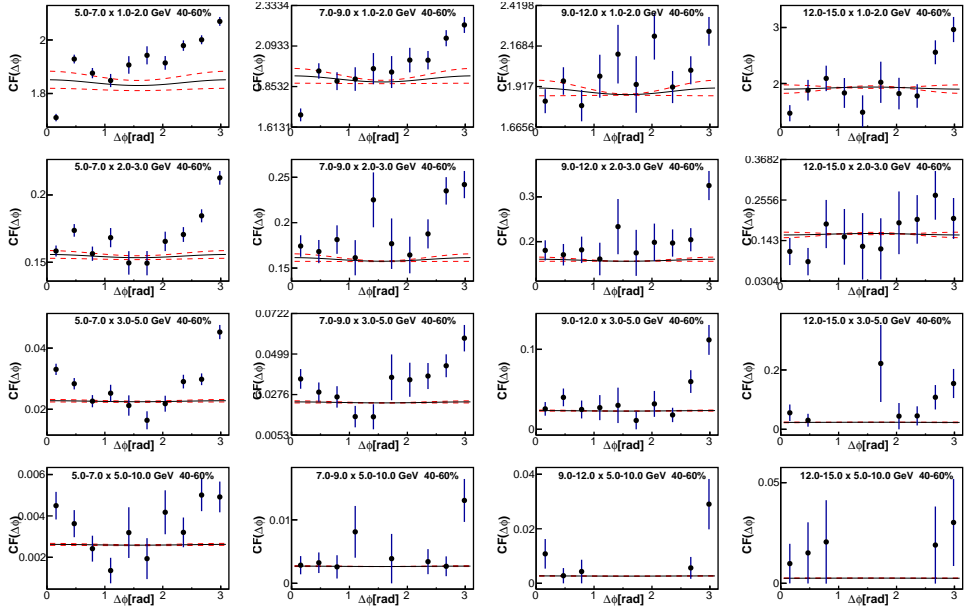


Figure A.5: Run 10 Au+Au $\gamma_{iso} - h$ correlation functions for 0-20% events. Each plot is a different p_T bin combination. Trigger p_T increases to the right while partner p_T increases going down. The black line represents the background level, the red lines around it is the error on the black line.

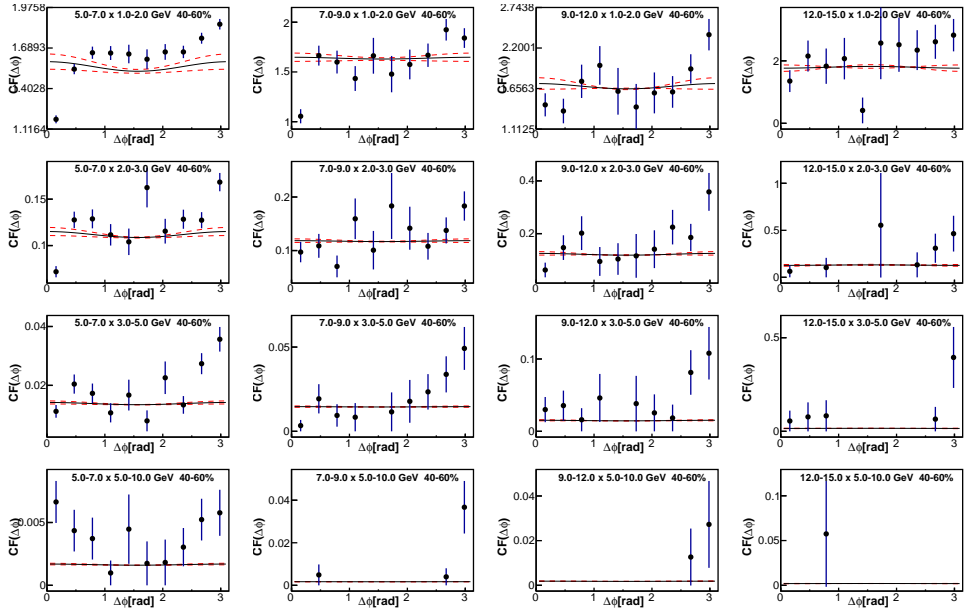


Figure A.6: Run 11 Au+Au $\gamma_{iso} - h$ correlation functions for the centrality labeled in the figure. Each plot is a different p_T bin combination. Trigger p_T increases to the right while partner p_T increases going down. The black line represents the background level, the red lines around it is the error on the black line.

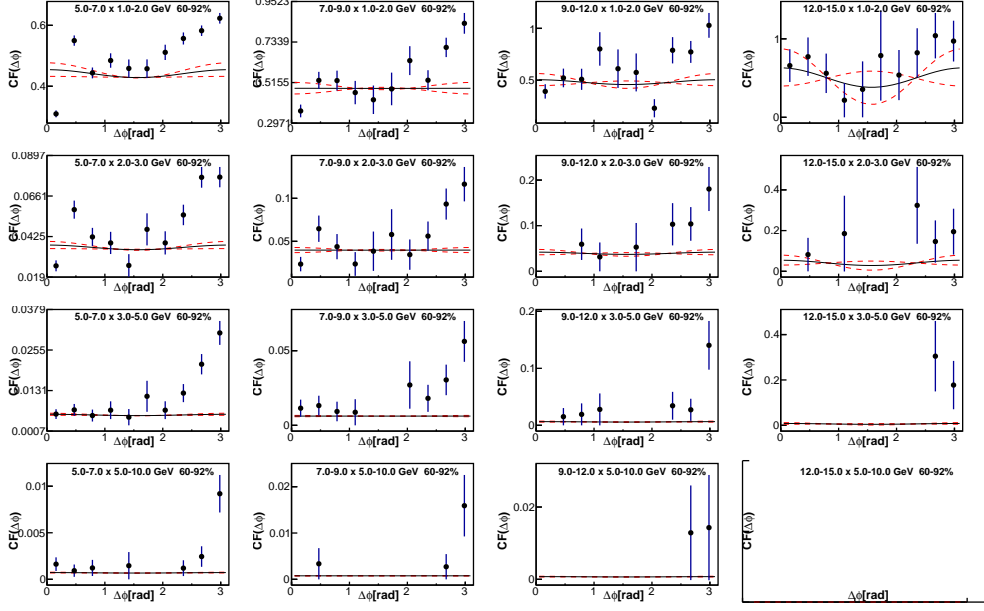


Figure A.7: Run 10 Au+Au $\gamma_{iso} - h$ correlation functions for the centrality labeled in the figure. Each plot is a different p_T bin combination. Trigger p_T increases to the right while partner p_T increases going down. The black line represents the background level, the red lines around it is the error on the black line.

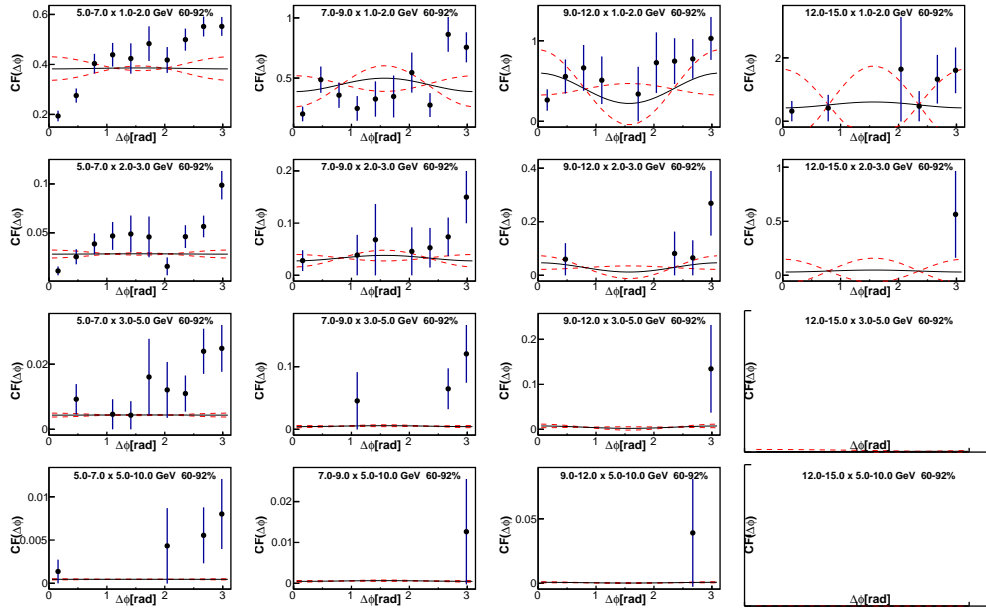


Figure A.8: Run 11 Au+Au $\gamma_{iso} - h$ correlation functions for the centrality labeled in the figure. Each plot is a different p_T bin combination. Trigger p_T increases to the right while partner p_T increases going down. The black line represents the background level, the red lines around it is the error on the black line.

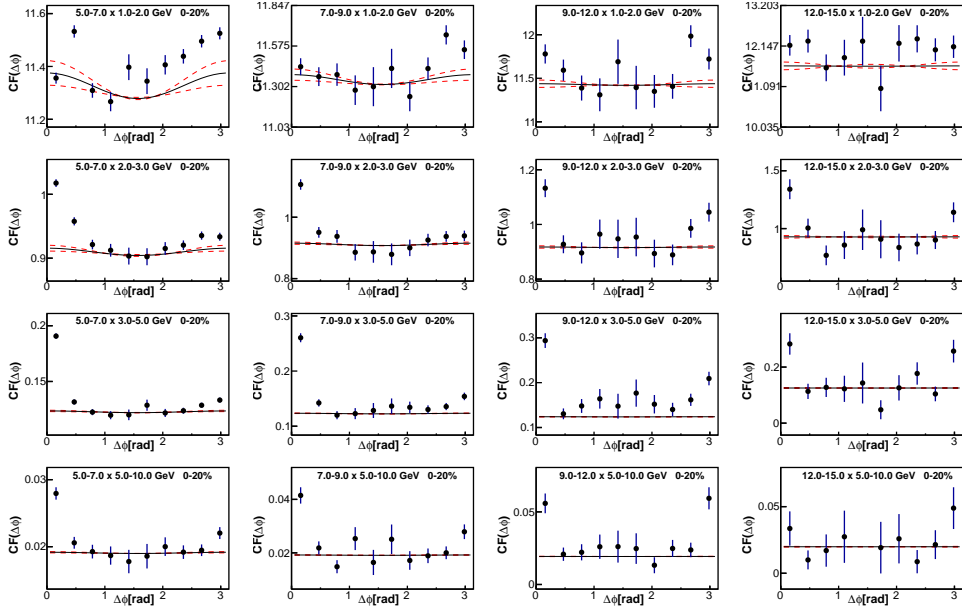


Figure A.9: Run 10 Au+Au $\pi^0 - h$ correlation functions for 0-20% events. Each plot is a different p_T bin combination. Trigger p_T increases to the right while partner p_T increases going down. The black line represents the background level, the red lines around it is the error on the black line.

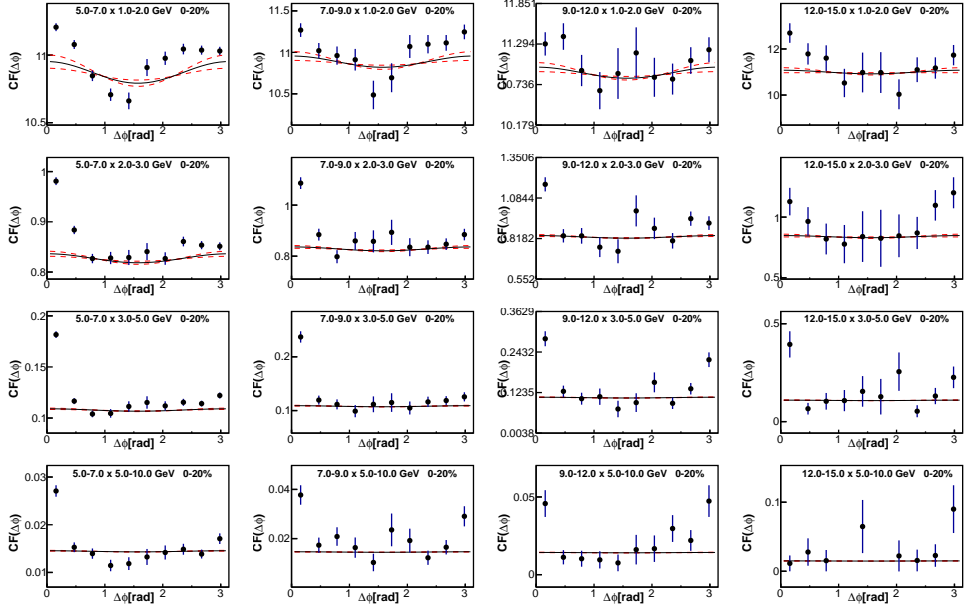


Figure A.10: Run 11 Au+Au $\pi^0 - h$ correlation functions for the centrality labeled in the figure. Each plot is a different p_T bin combination. Trigger p_T increases to the right while partner p_T increases going down. The black line represents the background level, the red lines around it is the error on the black line.

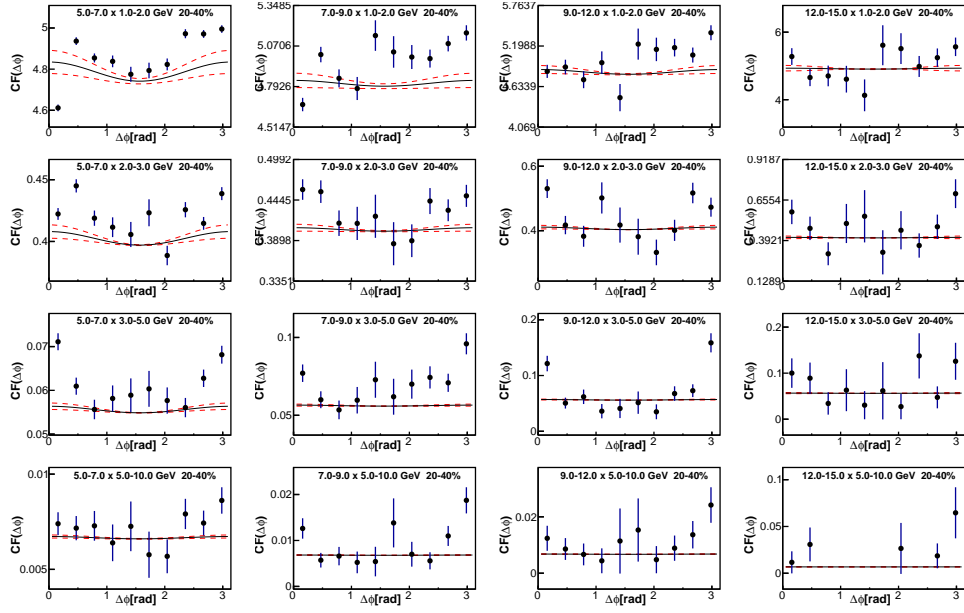


Figure A.11: Run 10 Au+Au $\pi^0 - h$ correlation functions for the centrality labeled in the figure. Each plot is a different p_T bin combination. Trigger p_T increases to the right while partner p_T increases going down. The black line represents the background level, the red lines around it is the error on the black line.

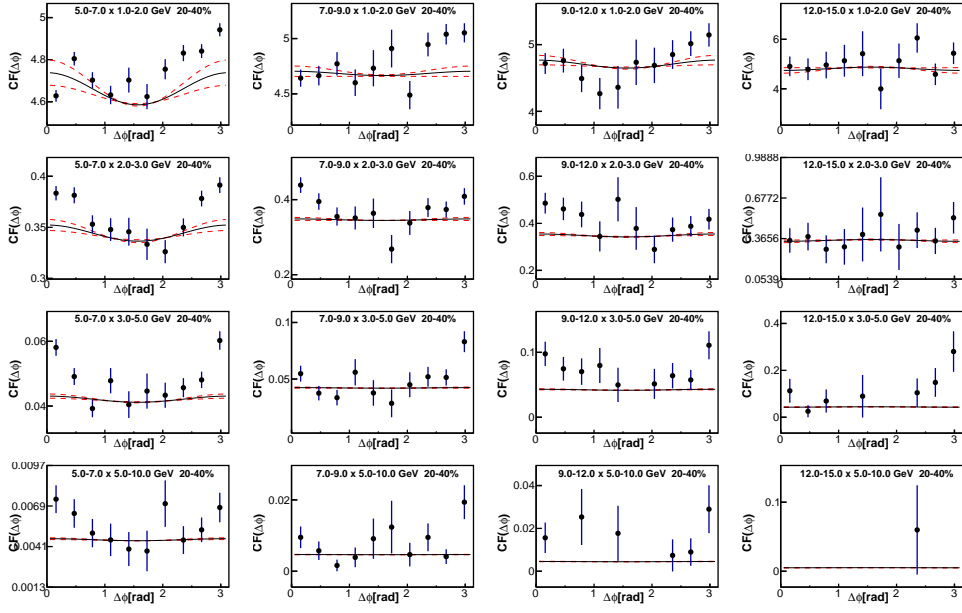


Figure A.12: Run 11 Au+Au $\pi^0 - h$ correlation functions for the centrality labeled in the figure. Each plot is a different p_T bin combination. Trigger p_T increases to the right while partner p_T increases going down. The black line represents the background level, the red lines around it is the error on the black line.

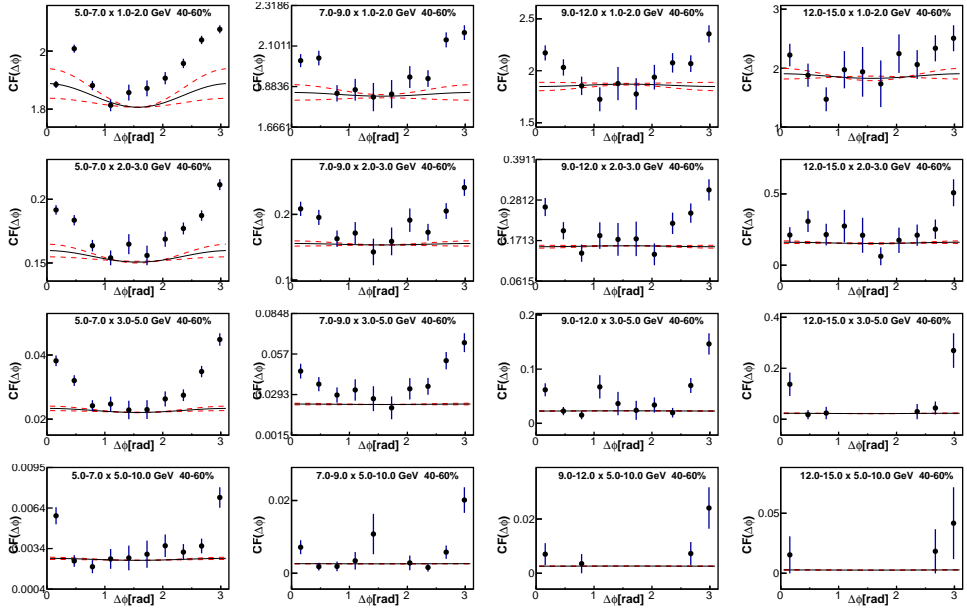


Figure A.13: Run 10 Au+Au $\pi^0 - h$ correlation functions for 0-20% events. Each plot is a different p_T bin combination. Trigger p_T increases to the right while partner p_T increases going down. The black line represents the background level, the red lines around it is the error on the black line.

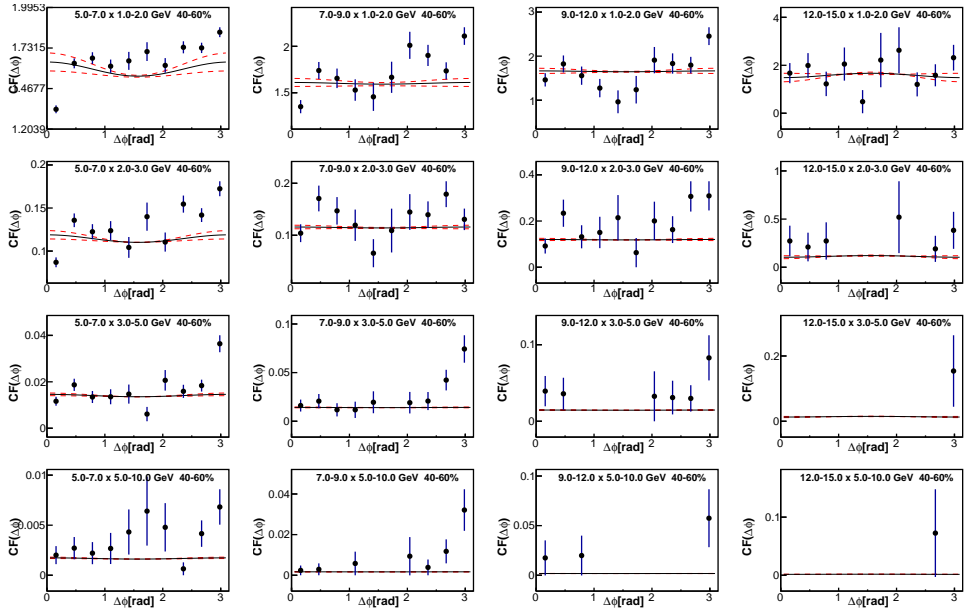


Figure A.14: Run 11 Au+Au $\pi^0 - h$ correlation functions for the centrality labeled in the figure. Each plot is a different p_T bin combination. Trigger p_T increases to the right while partner p_T increases going down. The black line represents the background level, the red lines around it is the error on the black line.

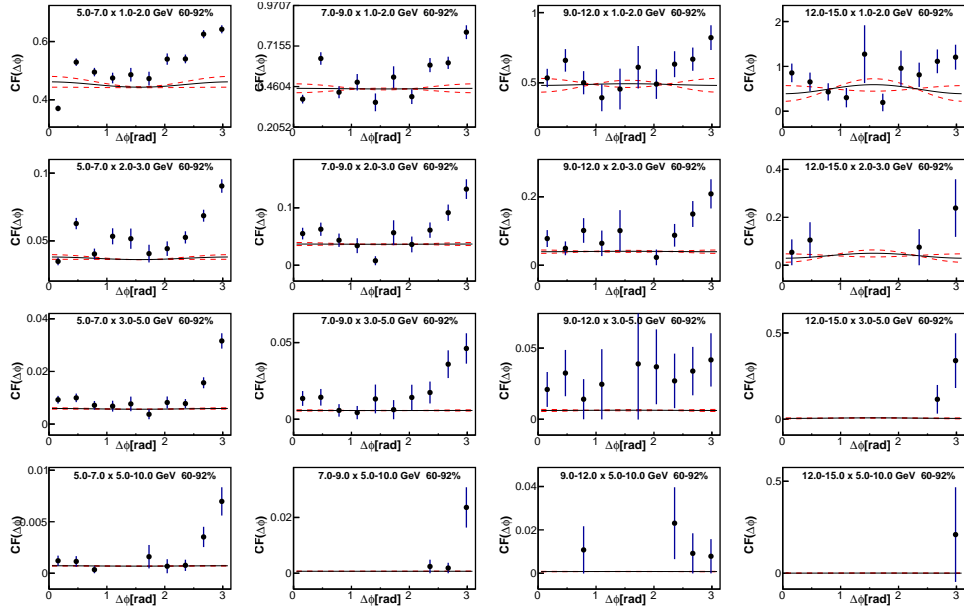


Figure A.15: Run 10 Au+Au $\pi^0 - h$ correlation functions for the centrality labeled in the figure. Each plot is a different p_T bin combination. Trigger p_T increases to the right while partner p_T increases going down. The black line represents the background level, the red lines around it is the error on the black line.

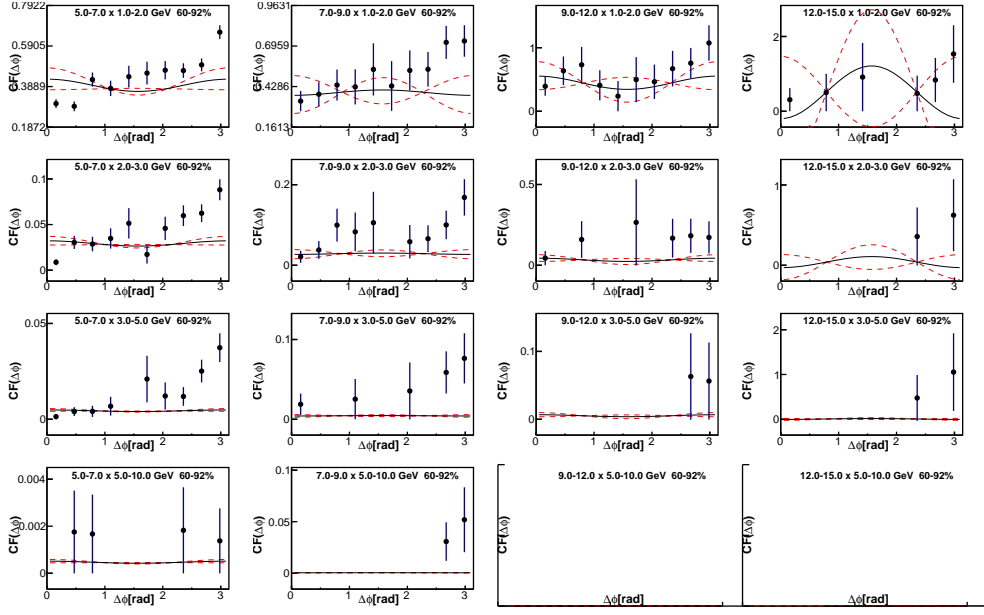


Figure A.16: Run 11 Au+Au $\pi^0 - h$ correlation functions for the centrality labeled in the figure. Each plot is a different p_T bin combination. Trigger p_T increases to the right while partner p_T increases going down. The black line represents the background level, the red lines around it is the error on the black line.

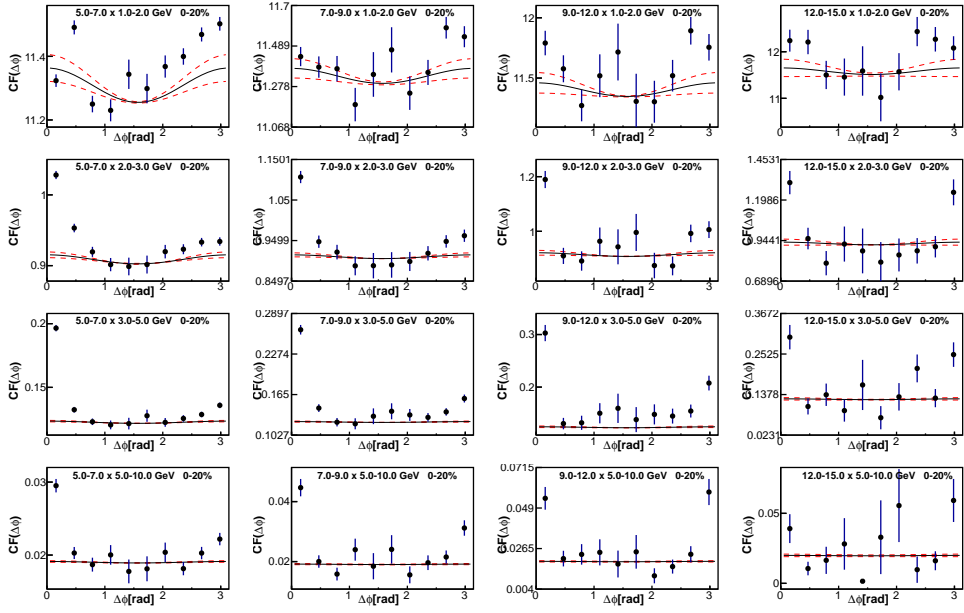


Figure A.17: Run 10 Au+Au $\gamma_{dec}-h$ correlation functions for 0-20% events. Each plot is a different p_T bin combination. Trigger p_T increases to the right while partner p_T increases going down. The black line represents the background level, the red lines around it is the error on the black line.

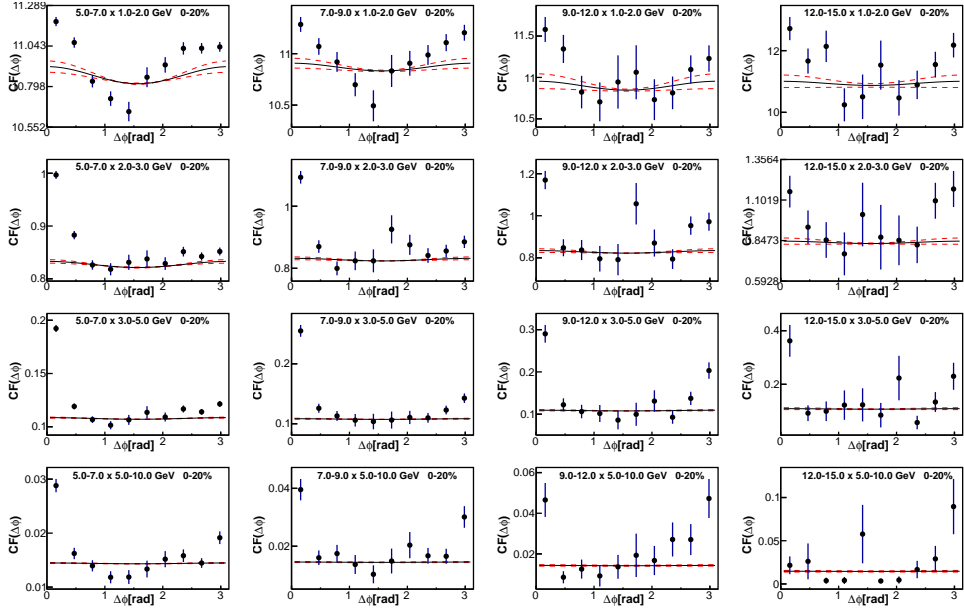


Figure A.18: Run 11 Au+Au $\gamma_{dec} - h$ correlation functions for the centrality labeled in the figure. Each plot is a different p_T bin combination. Trigger p_T increases to the right while partner p_T increases going down. The black line represents the background level, the red lines around it is the error on the black line.

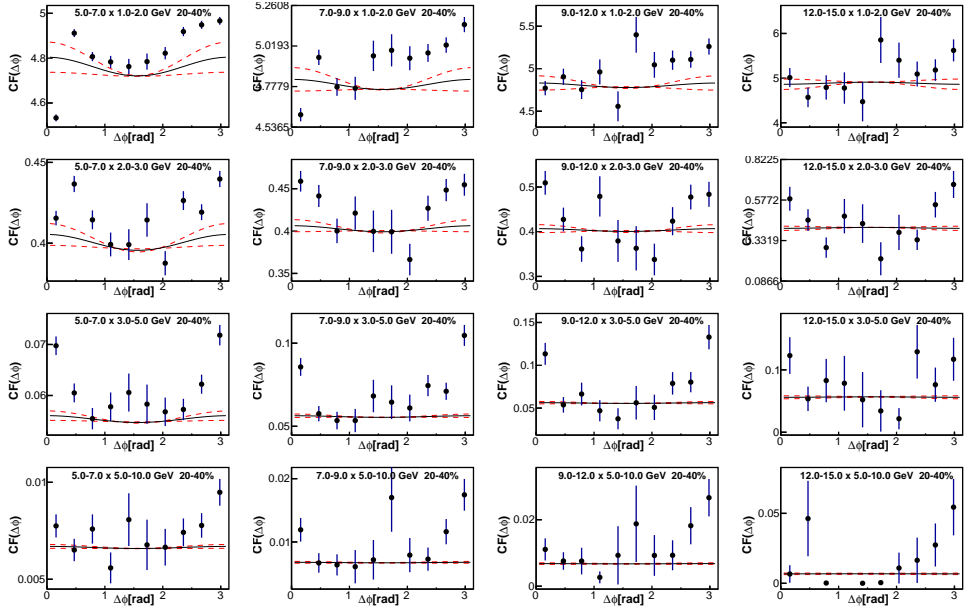


Figure A.19: Run 10 Au+Au $\gamma_{dec} - h$ correlation functions for the centrality labeled in the figure. Each plot is a different p_T bin combination. Trigger p_T increases to the right while partner p_T increases going down. The black line represents the background level, the red lines around it is the error on the black line.

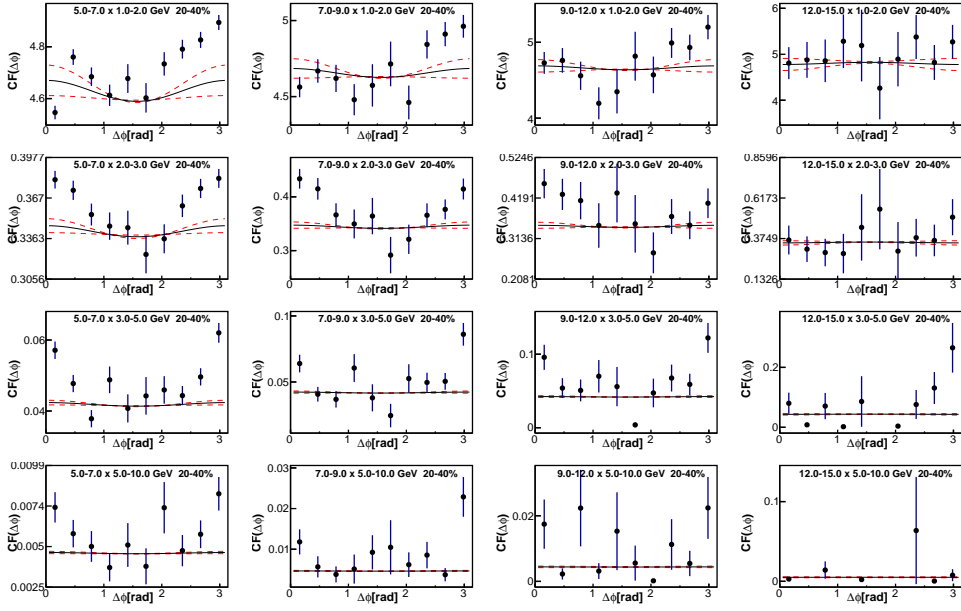


Figure A.20: Run 11 Au+Au $\gamma_{\text{dec}} - h$ correlation functions for the centrality labeled in the figure. Each plot is a different p_T bin combination. Trigger p_T increases to the right while partner p_T increases going down. The black line represents the background level, the red lines around it is the error on the black line.

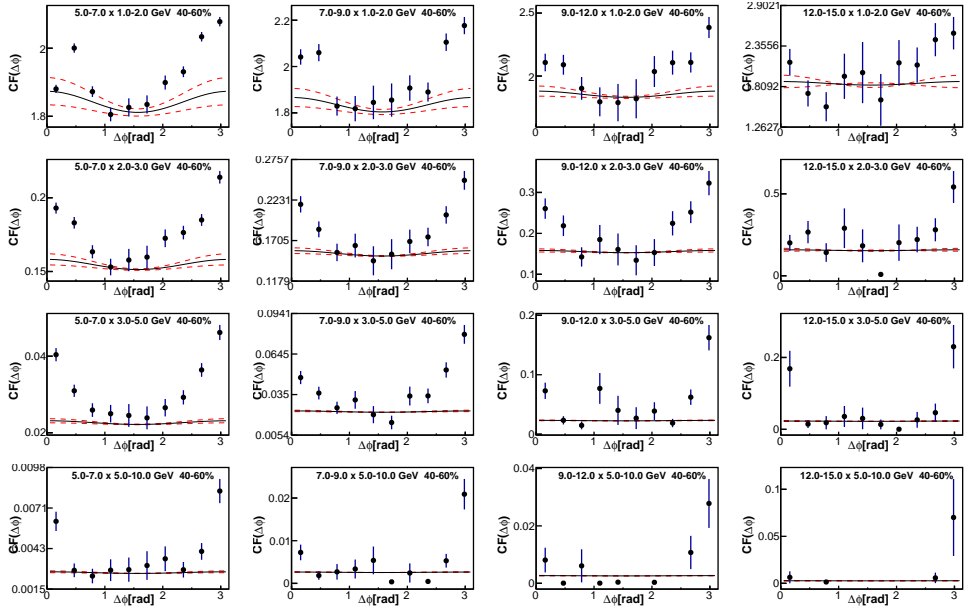


Figure A.21: Run 10 Au+Au $\gamma_{dec}-h$ correlation functions for 0-20% events. Each plot is a different p_T bin combination. Trigger p_T increases to the right while partner p_T increases going down. The black line represents the background level, the red lines around it is the error on the black line.

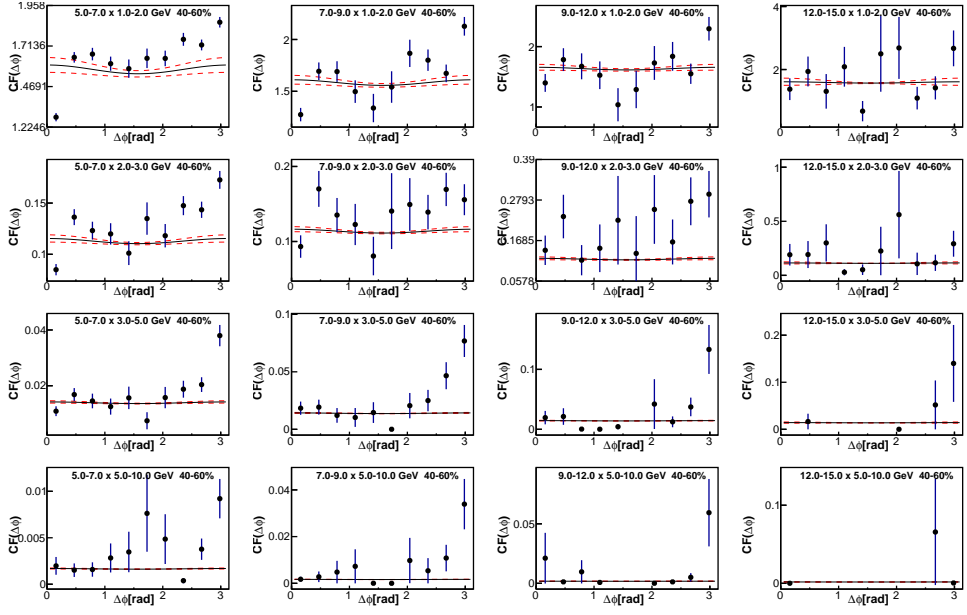


Figure A.22: Run 11 Au+Au $\gamma_{dec} - h$ correlation functions for the centrality labeled in the figure. Each plot is a different p_T bin combination. Trigger p_T increases to the right while partner p_T increases going down. The black line represents the background level, the red lines around it is the error on the black line.

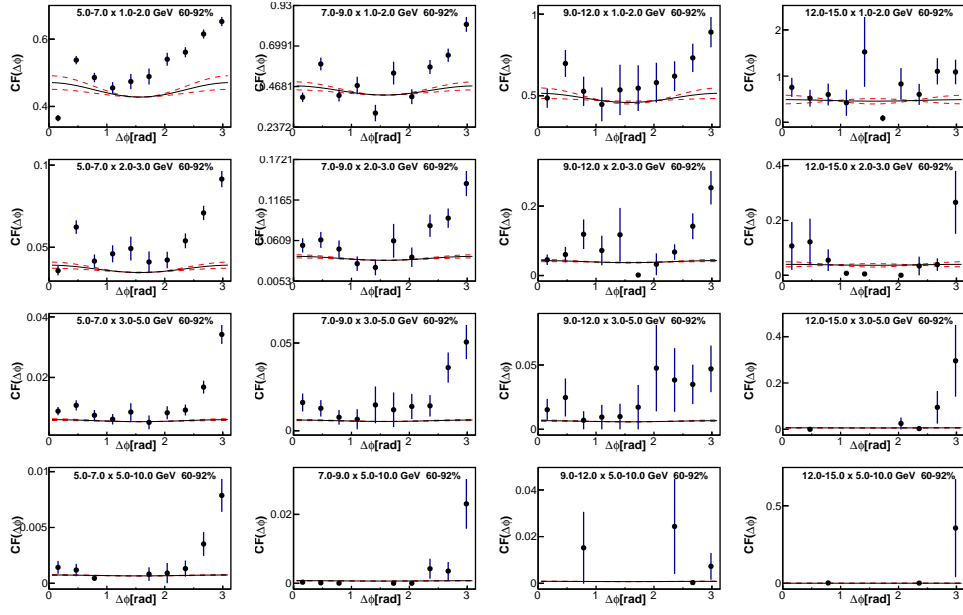


Figure A.23: Run 10 Au+Au $\gamma_{dec} - h$ correlation functions for the centrality labeled in the figure. Each plot is a different p_T bin combination. Trigger p_T increases to the right while partner p_T increases going down. The black line represents the background level, the red lines around it is the error on the black line.

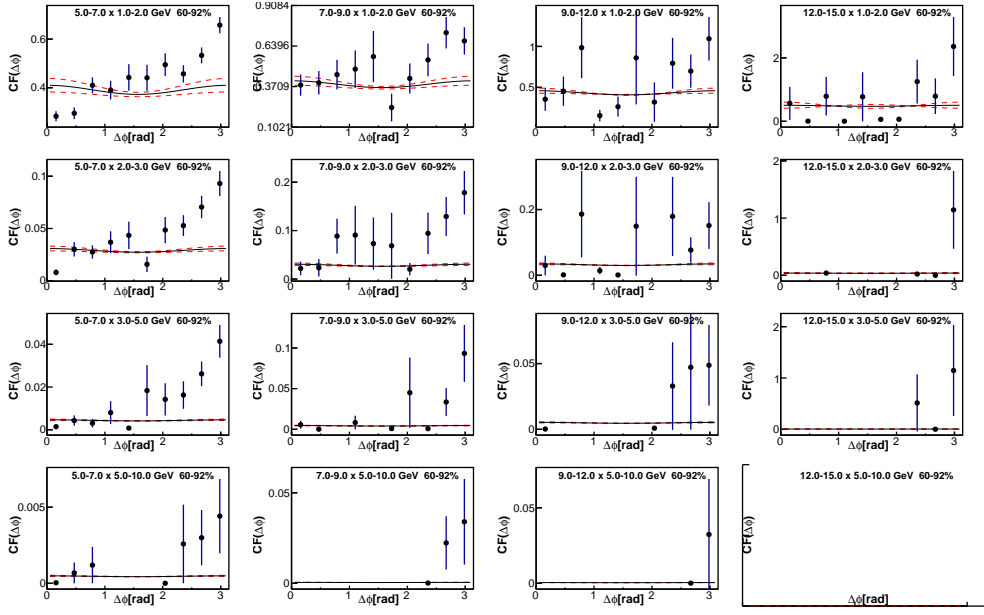


Figure A.24: Run 11 Au+Au $\gamma_{dec} - h$ correlation functions for the centrality labeled in the figure. Each plot is a different p_T bin combination. Trigger p_T increases to the right while partner p_T increases going down. The black line represents the background level, the red lines around it is the error on the black line.

A.2 Jet Functions for Other Centralities

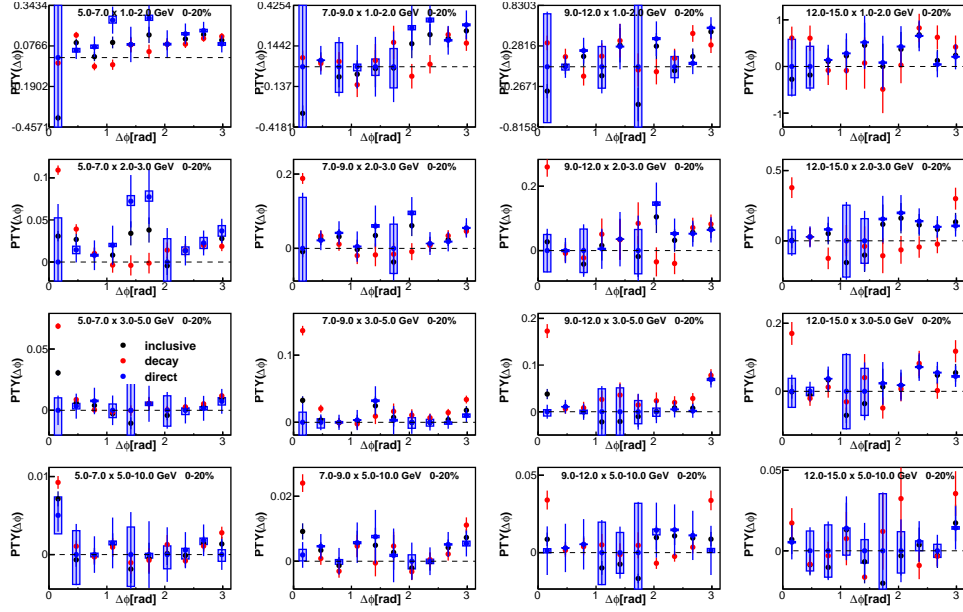


Figure A.25: Run 10 Au+Au $\gamma_{iso} - h$ (black points), $\gamma_{dec} - h$ (red points), and $\gamma_{dir} - h$ (blue points) jet functions for 0-20% events. Each plot is a different p_T bin combination. Trigger p_T increases to the right while partner p_T increases going down.

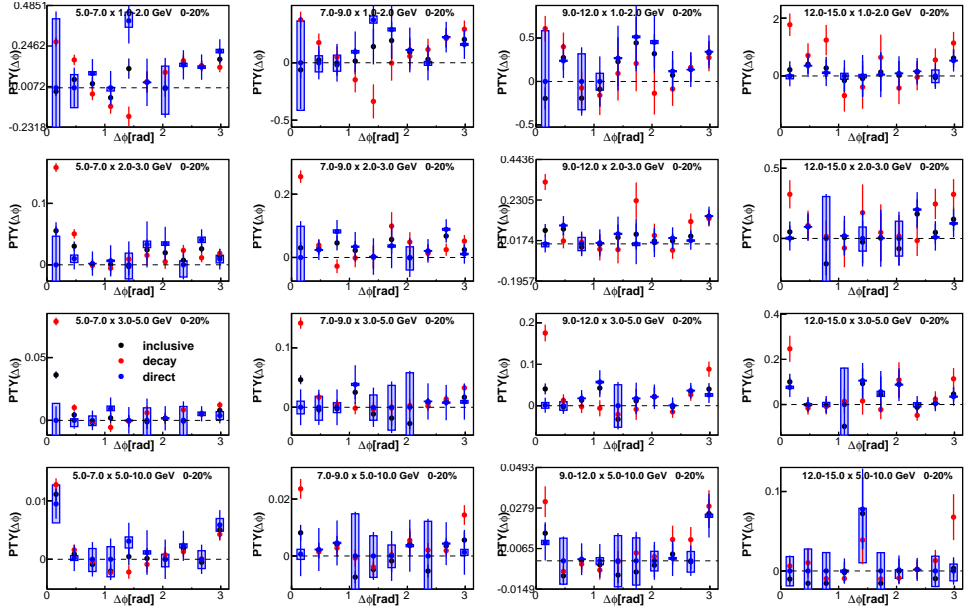


Figure A.26: Run 11 Au+Au $\gamma_{iso} - h$ (black points), $\gamma_{dec} - h$ (red points), and $\gamma_{dir} - h$ (blue points) jet functions for 0-20% events. Each plot is a different p_T bin combination. Trigger p_T increases to the right while partner p_T increases going down.

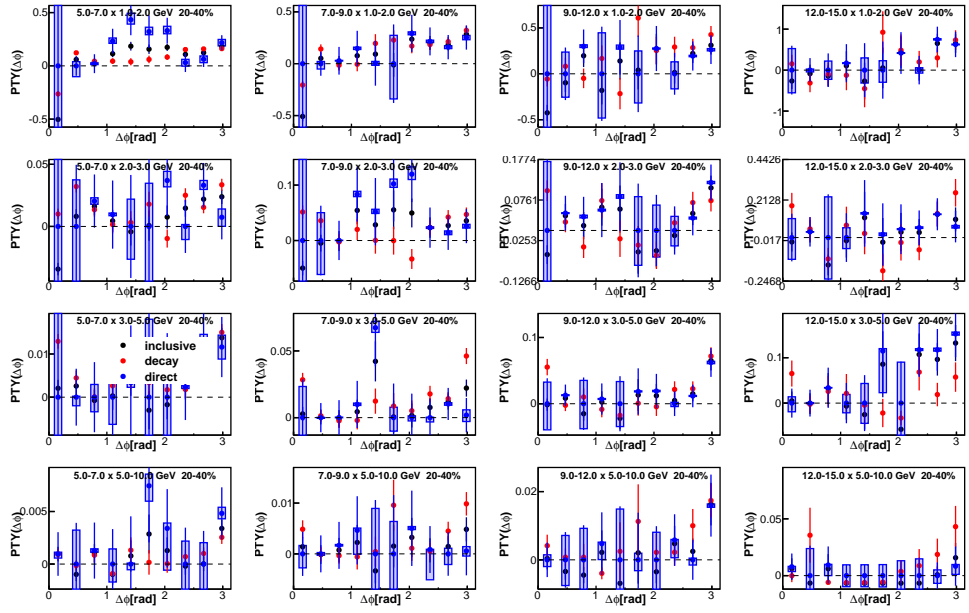


Figure A.27: Run 10 Au+Au $\gamma_{iso} - h$ (black points), $\gamma_{dec} - h$ (red points), and $\gamma_{dir} - h$ (blue points) jet functions for 20-40% events. Each plot is a different p_T bin combination. Trigger p_T increases to the right while partner p_T increases going down.

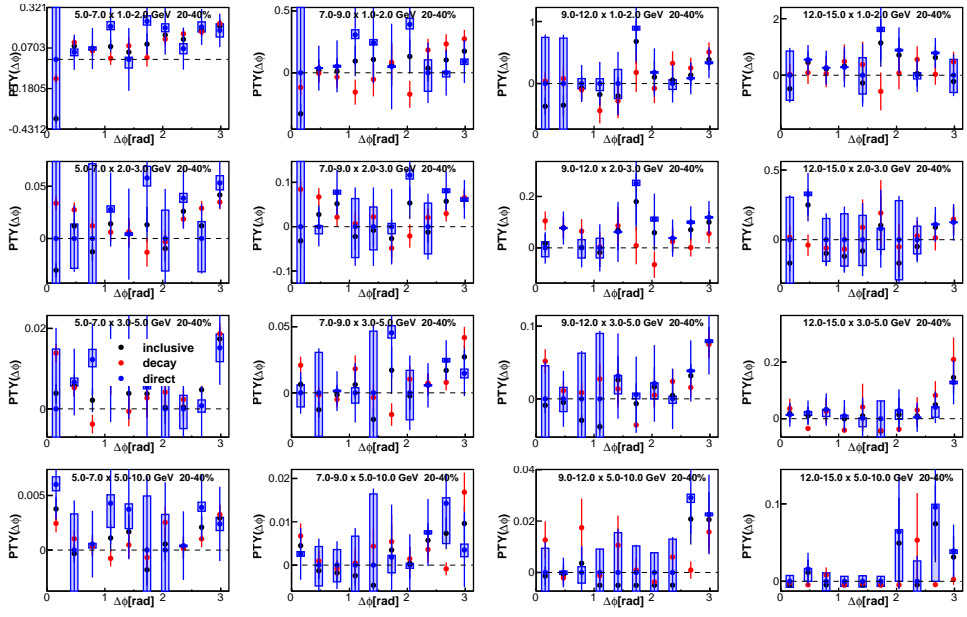


Figure A.28: Run 11 Au+Au $\gamma_{iso} - h$ (black points), $\gamma_{dec} - h$ (red points), and $\gamma_{dir} - h$ (blue points) jet functions for 20-40% events. Each plot is a different p_T bin combination. Trigger p_T increases to the right while partner p_T increases going down.

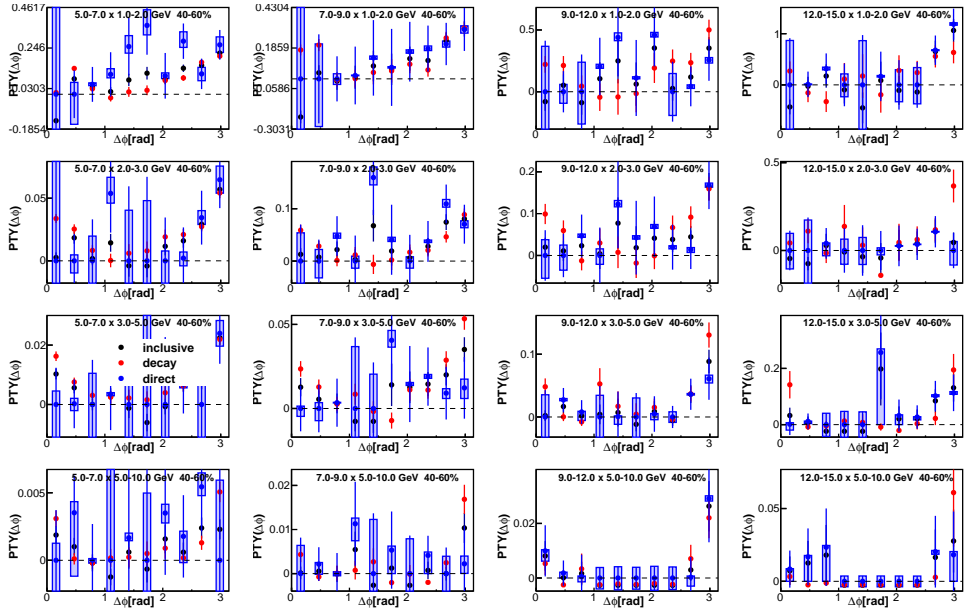


Figure A.29: Run 10 Au+Au $\gamma_{iso} - h$ (black points), $\gamma_{dec} - h$ (red points), and $\gamma_{dir} - h$ (blue points) jet functions for 40-60% events. Each plot is a different p_T bin combination. Trigger p_T increases to the right while partner p_T increases going down.

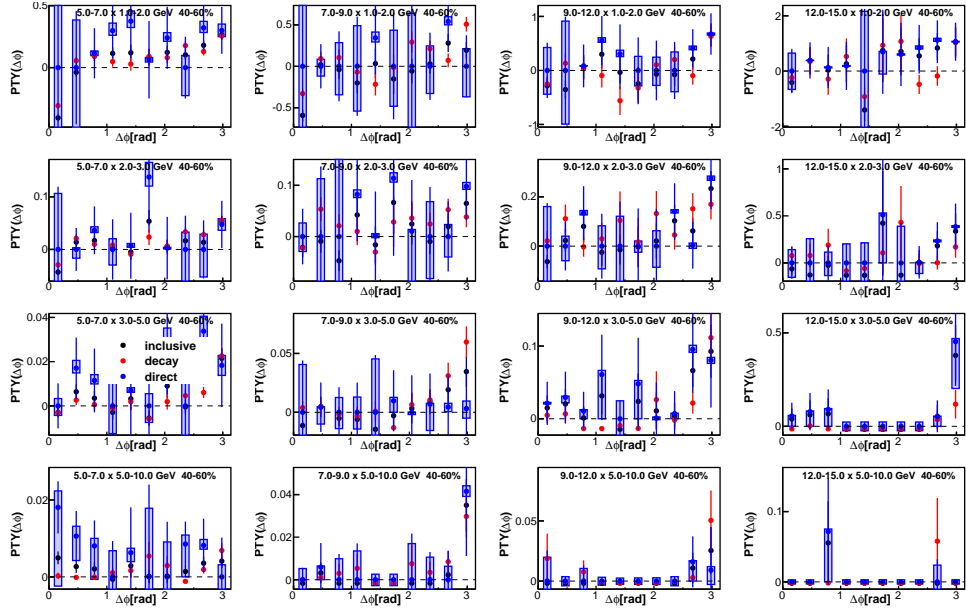


Figure A.30: Run 11 Au+Au $\gamma_{iso} - h$ (black points), $\gamma_{dec} - h$ (red points), and $\gamma_{dir} - h$ (blue points) jet functions for 40-60% events. Each plot is a different p_T bin combination. Trigger p_T increases to the right while partner p_T increases going down.

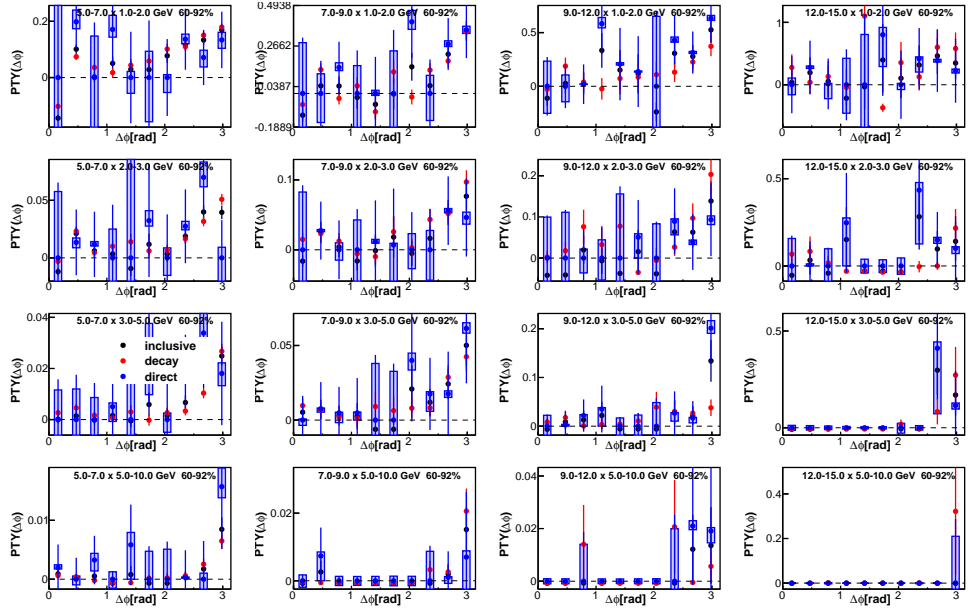


Figure A.31: Run 10 Au+Au $\gamma_{iso} - h$ (black points), $\gamma_{dec} - h$ (red points), and $\gamma_{dir} - h$ (blue points) jet functions for 60-92% events. Each plot is a different p_T bin combination. Trigger p_T increases to the right while partner p_T increases going down.

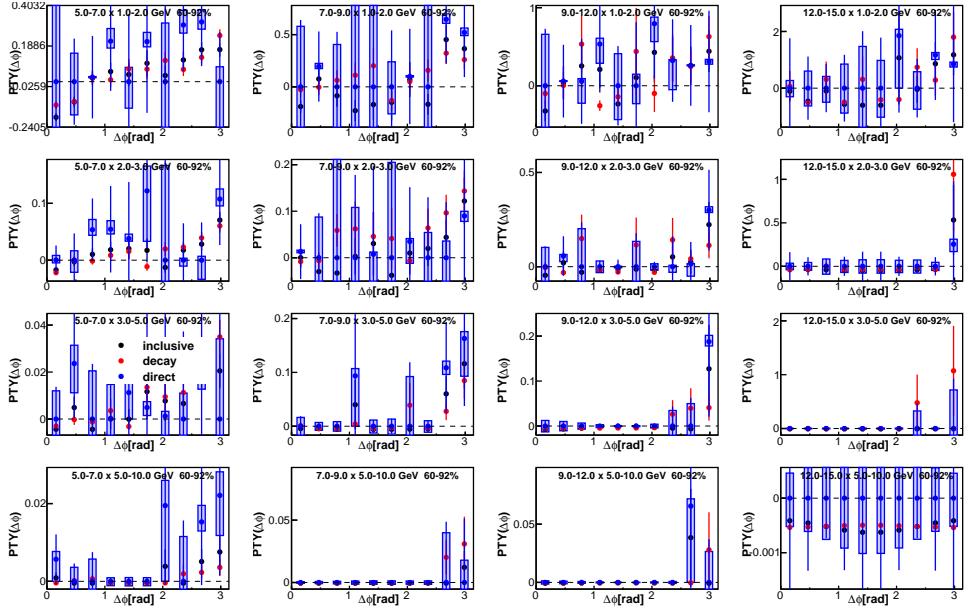


Figure A.32: Run 11Au+Au $\gamma_{iso} - h$ (black points), $\gamma_{dec} - h$ (red points), and $\gamma_{dir} - h$ (blue points) jet functions for 60-92% events. Each plot is a different p_T bin combination. Trigger p_T increases to the right while partner p_T increases going down.

APPENDIX B: SYSTEMATIC ERRORS ON THE AWAY-SIDE YIELDS

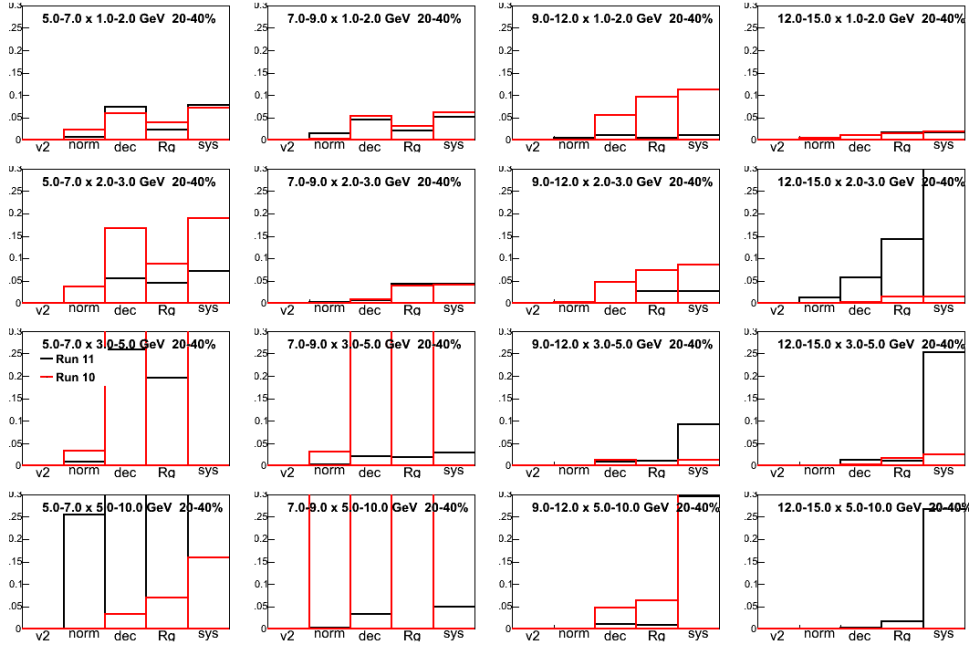


Figure B.1: Systematic error contributions of the direct photon $\pi/2$ away-side yield broken down by source for Run 10 (red) and Run 11 (black) 20-40% events. Each source is a different bin from left to right, v_2 , normalization (MSMP), decay photons, R_γ , and total systematic error. Each plot is a different p_T bin combination. Trigger p_T increases to the right while partner p_T increases going down.

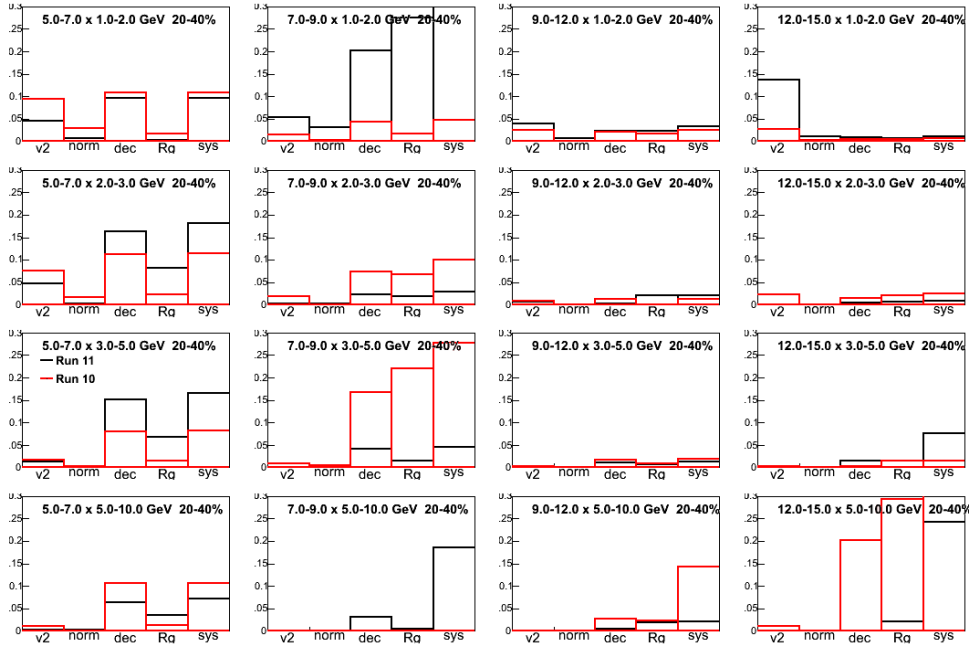


Figure B.2: Systematic error contributions of the direct photon $\pi/5$ away-side yield broken down by source for Run 10 (red) and Run 11 (black) 20-40% events. Each source is a different bin from left to right, v_2 , normalization (MSMP), decay photons, R_γ , and total systematic error. Each plot is a different p_T bin combination. Trigger p_T increases to the right while partner p_T increases going down.

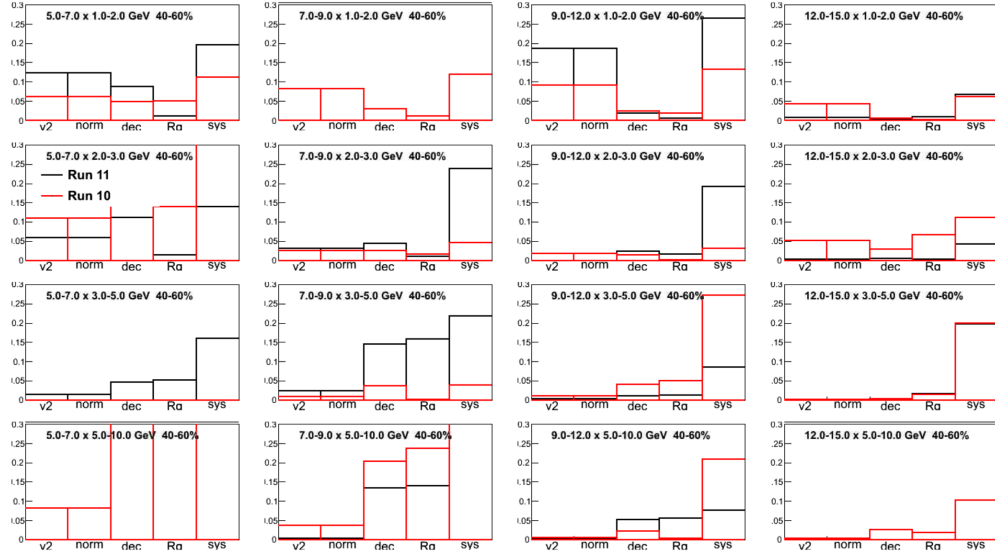


Figure B.3: Systematic error contributions of the direct photon $\pi/2$ away-side yield broken down by source for Run 10 (red) and Run 11 (black) 40-60% events. Each source is a different bin from left to right, v_2 , normalization (MSMP), decay photons, R_γ , and total systematic error. Each plot is a different p_T bin combination. Trigger p_T increases to the right while partner p_T increases going down.

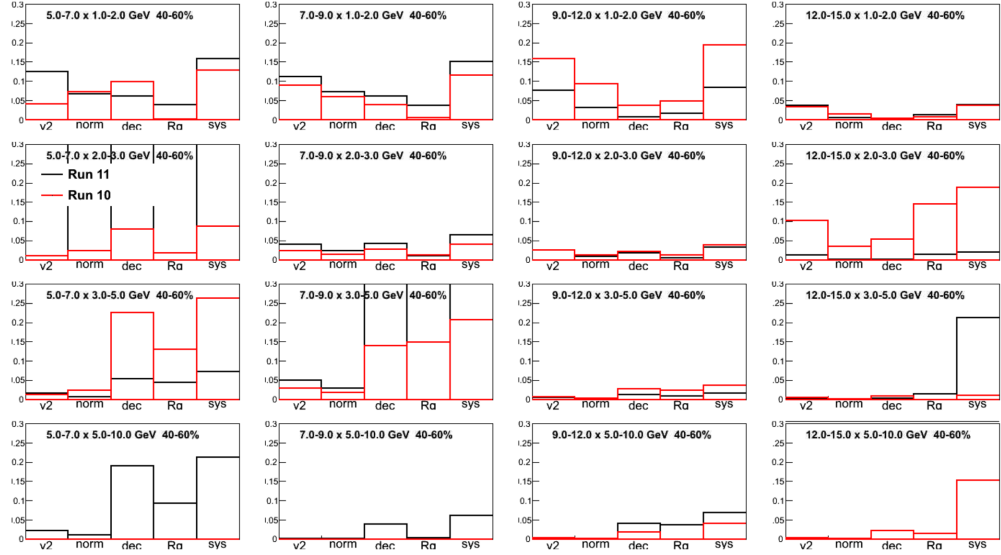


Figure B.4: Systematic error contributions of the direct photon $\pi/5$ away-side yield broken down by source for Run 10 (red) and Run 11 (black) 40-60% events. Each source is a different bin from left to right, v_2 , normalization (MSMP), decay photons, R_γ , and total systematic error. Each plot is a different p_T bin combination. Trigger p_T increases to the right while partner p_T increases going down.

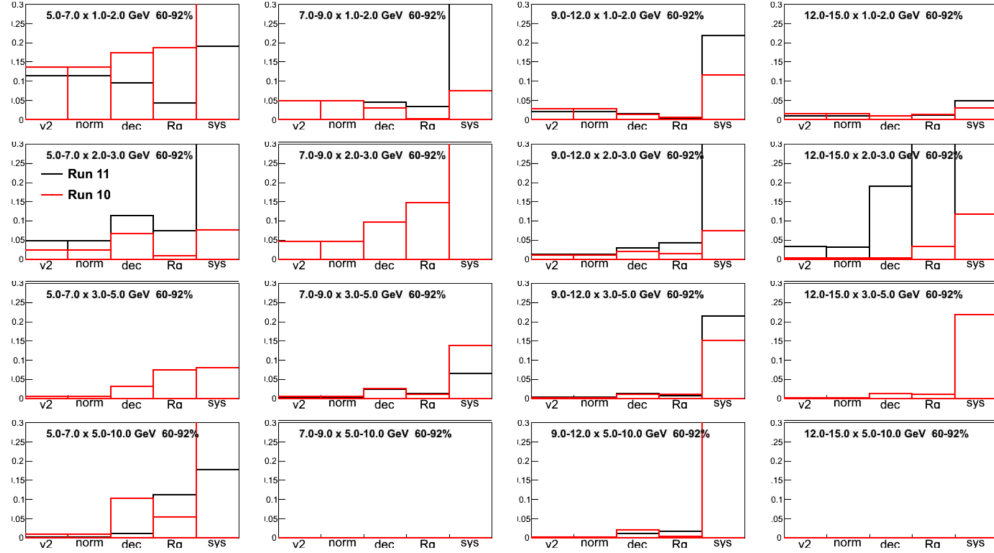


Figure B.5: Systematic error contributions of the direct photon $\pi/2$ away-side yield broken down by source for Run 10 (red) and Run 11 (black) 60-92% events. Each source is a different bin from left to right, v_2 , normalization (MSMP), decay photons, R_γ , and total systematic error. Each plot is a different p_T bin combination. Trigger p_T increases to the right while partner p_T increases going down.

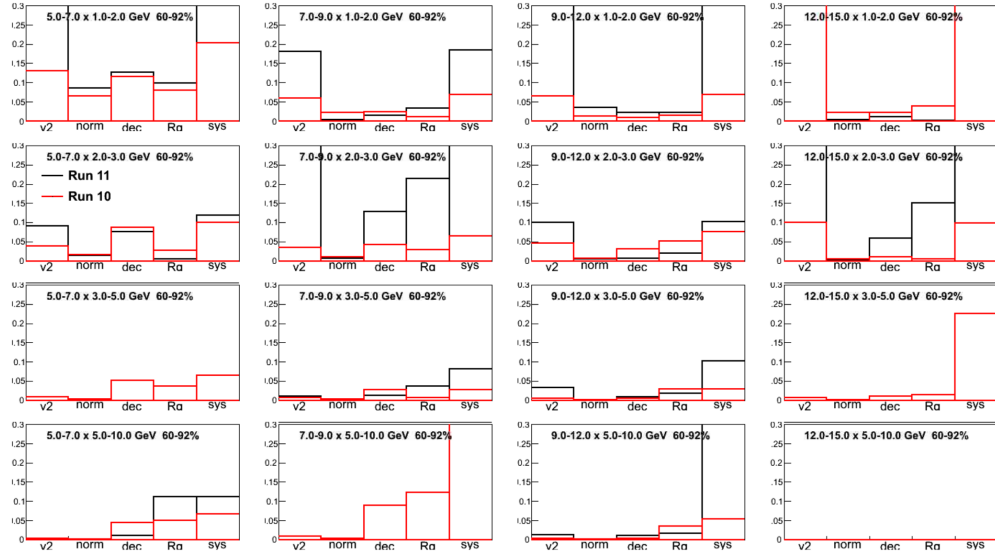


Figure B.6: Systematic error contributions of the direct photon $\pi/5$ away-side yield broken down by source for Run 10 (red) and Run 11 (black) 60-92% events. Each source is a different bin from left to right, v_2 , normalization (MSMP), decay photons, R_γ , and total systematic error. Each plot is a different p_T bin combination. Trigger p_T increases to the right while partner p_T increases going down.

APPENDIX C: LICENSES FOR FIGURES

This appendix shows the permissions for the figures that have been taken from other sources, mainly peer-reviewed journals. The licenses appear in the order their figures in this dissertation. Figures 6.7, 8.25, 8.28, 9.1, 9.7, 9.8a, and 9.8b are under a Creative Commons license (Attribution 3.0 Unported (CC BY 3.0)) -

<https://creativecommons.org/licenses/by/3.0/legalcode>.

Mail - td533712@ohio.edu

<https://outlook.office.com/owa/?realm=ohio.edu&path=/mail/inbox>

Re: permission to use images in my dissertation

Danley, Tyler

Mon 9/24/2018 10:44 AM

Sent Items

To:Koropsak, Jane <jane@bnl.gov>;

Thanks for the quick response and the luck.

Tyler

Tyler Danley

Graduate Student
Ohio University
Physics & Astronomy Department

From: Koropsak, Jane <jane@bnl.gov>
Sent: Sunday, September 23, 2018 8:55:42 PM
To: Danley, Tyler
Subject: Re: permission to use images in my dissertation

Tyler,

Permission is granted to use the images you cite here for your dissertation. Note that images may not be altered except for size. Please include the acknowledgement, "Courtesy Brookhaven National Laboratory."

Thanks, and good luck!

Jane

Get [Outlook for iOS](#)

From: Danley, Tyler <td533712@ohio.edu>
Sent: Sunday, September 23, 2018 8:50:39 PM
To: Koropsak, Jane
Cc: Danley, Tyler
Subject: permission to use images in my dissertation

Hello Jane,

I am working on my dissertation analyzing PHENIX data and I would like permission to use a few images that have been published on the BNL website.

The three figures I would like permission to use are:

The top figure, "The Phases of QCD" in the article "How Low Can RHIC Go?":

Figure C.1: Page 1 of 2 of the permissions license is for Figures 1.1, 1.3, and 2.1.

Mail - td533712@ohio.edu

<https://outlook.office.com/owa/?realm=ohio.edu&path=/mail/inbox>

<https://www.bnl.gov/newsroom/news.php?a=21870>

The four panel figure showing two ions colliding:

<https://www.bnl.gov/rhic/physics.asp>

And finally, I would like to use this aerial photo of RHIC:

<https://www.flickr.com/photos/brookhavenlab/7979381212/in/album-72157627989559182/>

Thanks,
Tyler Danley

Tyler Danley

Graduate Student
Ohio University
Physics & Astronomy Department

Figure C.2: Page 2 of 2 of the permissions license is for Figures 1.1, 1.3, and 2.1.



12-Sep-2018

This license agreement between the American Physical Society ("APS") and Tyler Danley ("You") consists of your license details and the terms and conditions provided by the American Physical Society and SciPris.

Licensed Content Information

License Number:	RNP/18/SEP/007754
License date:	12-Sep-2018
DOI:	10.1103/PhysRevLett.98.162301
Title:	Scaling Properties of Azimuthal Anisotropy in $\text{Au} + \text{Au}$ and $\text{Cu} + \text{Cu}$ Collisions at $\sqrt{s_{\text{NN}}} = 200 \text{ GeV}$
Author:	A. Adare et al. (PHENIX Collaboration)
Publication:	Physical Review Letters
Publisher:	American Physical Society
Cost:	USD \$ 0.00

Request Details

Does your reuse require significant modifications:	No
Specify intended distribution locations:	Worldwide
Reuse Category:	Reuse in a thesis/dissertation
Requestor Type:	Student
Items for Reuse:	Figures/Tables
Number of Figure/Tables:	2
Figure/Tables Details:	Figures 2 and 3
Format for Reuse:	Electronic and Print
Total number of print copies:	Up to 1000

Information about New Publication:

University/Publisher:	Ohio University
Title of dissertation/thesis:	Photon-Related Elliptic Azimuthal Asymmetry and Photon-Hadron Correlations with an Isolation Cut in Au+Au Collisions at $\sqrt{s_{\text{NN}}} = 200 \text{ GeV}$ at RHIC-PHENIX
Author(s):	Tyler Danley
Expected completion date:	Dec. 2018

License Requestor Information

Name:	Tyler Danley
Affiliation:	Individual
Email Id:	td533712@ohio.edu
Country:	United States

Page 1 of 3

Figure C.3: Page 1 of 1 of the permissions license is for Figures 1.8 and 1.9.



Title: Experimental and theoretical challenges in the search for the quark-gluon plasma: The STAR Collaboration's critical assessment of the evidence from RHIC collisions

Logged in as:
Tyler Danley
Account #:
3001334847

[LOGOUT](#)

Author: J. Adams,M.M. Aggarwal,Z. Ahammed,J. Amonett,B.D. Anderson,D. Arkhipkin,G.S. Averichev,S.K. Badyal,Y. Bai,J. Balewski,O. Barannikova,L.S. Barnby,J. Baudot,S. Bekele,V.V. Belaga,A. Bellingeri-Laurikainen,R. Bellwied,J. Berger,B.I. Bezverkhny et al.

Publication: Nuclear Physics A

Publisher: Elsevier

Date: 8 August 2005

Copyright © 2005 Published by Elsevier B.V.

Order Completed

Thank you for your order.

This Agreement between Tyler Danley ("You") and Elsevier ("Elsevier") consists of your license details and the terms and conditions provided by Elsevier and Copyright Clearance Center.

Your confirmation email will contain your order number for future reference.

printable details

License Number	4426840429495
License date	Sep 12, 2018
Licensed Content Publisher	Elsevier
Licensed Content Publication	Nuclear Physics A
Licensed Content Title	Experimental and theoretical challenges in the search for the quark-gluon plasma: The STAR Collaboration's critical assessment of the evidence from RHIC collisions
Licensed Content Author	J. Adams,M.M. Aggarwal,Z. Ahammed,J. Amonett,B.D. Anderson,D. Arkhipkin,G.S. Averichev,S.K. Badyal,Y. Bai,J. Balewski,O. Barannikova,L.S. Barnby,J. Baudot,S. Bekele,V.V. Belaga,A. Bellingeri-Laurikainen,R. Bellwied,J. Berger,B.I. Bezverkhny et al.
Licensed Content Date	Aug 8, 2005
Licensed Content Volume	757
Licensed Content Issue	1-2
Licensed Content Pages	82
Type of Use	reuse in a thesis/dissertation
Portion	figures/tables/illustrations
Number of figures/tables /illustrations	1
Format	both print and electronic

Figure C.4: Page 1 of 2 of the permissions license is for Figure 1.11.

Are you the author of No
this Elsevier article?

Will you be translating? No

Original figure numbers figure 29 left

Title of your Photon-Related Elliptic Azimuthal Asymmetry and Photon-Hadron Correlations with an Isolation Cut
thesis/dissertation in Au Au Collisions at $\sqrt{s_{NN}} = 200$ GeV at RHIC-PHENIX

Expected completion Dec 2018
date

Estimated size (number 250
of pages)

Requestor Location Tyler Danley
Edwards Accelerator Lab
123 University Terrace

ATHENS, OH 45701
United States
Attn: Tyler Danley

Publisher Tax ID 98-0397604

Total 0.00 USD

ORDER MORE **CLOSE WINDOW**

Copyright © 2018 [Copyright Clearance Center, Inc.](#). All Rights Reserved. [Privacy statement](#). [Terms and Conditions](#).
Comments? We would like to hear from you. E-mail us at customercare@copyright.com

Figure C.5: Page 2 of 2 of the permissions license is for Figure 1.11.



12-Sep-2018

This license agreement between the American Physical Society ("APS") and Tyler Danley ("You") consists of your license details and the terms and conditions provided by the American Physical Society and SciPris.

Licensed Content Information

License Number:	RNP/18/SEP/007755
License date:	12-Sep-2018
DOI:	10.1103/PhysRevC.81.014908
Title:	Extraction of correlated jet pair signals in relativistic heavy ion collisions
Author:	Anne Sickles, Michael P. McCumber, and Andrew Adare
Publication:	Physical Review C
Publisher:	American Physical Society
Cost:	USD \$ 0.00

Request Details

Does your reuse require significant modifications:	No
Specify intended distribution locations:	Worldwide
Reuse Category:	Reuse in a thesis/dissertation
Requestor Type:	Student
Items for Reuse:	Figures/Tables
Number of Figure/Tables:	1
Figure/Tables Details:	Figure 1
Format for Reuse:	Print and Electronic
Total number of print copies:	Up to 1000

Information about New Publication:

University/Publisher:	Ohio University
Title of dissertation/thesis:	Photon-Related Elliptic Azimuthal Asymmetry and Photon-Hadron Correlations with an Isolation Cut in Au+Au Collisions at $\sqrt{s_{NN}} = 200$ GeV at RHIC-PHENIX
Author(s):	Tyler Danley
Expected completion date:	Dec. 2018

License Requestor Information

Name:	Tyler Danley
Affiliation:	Individual
Email Id:	td533712@ohio.edu
Country:	United States

Figure C.6: Page 1 of 1 of the permissions license is for Figure 1.13.



12-Sep-2018

This license agreement between the American Physical Society ("APS") and Tyler Danley ("You") consists of your license details and the terms and conditions provided by the American Physical Society and SciPris.

Licensed Content Information

License Number:	RNP/18/SEP/007757
License date:	12-Sep-2018
DOI:	10.1103/PhysRevC.80.024908
Title:	Photon-hadron jet correlations in $\text{Sp}+\text{p}$ and $\text{Au}+\text{Au}$ collisions at $\sqrt{s_{\text{NN}}} = 200 \text{ GeV}$
Author:	A. Adare et al. (PHENIX Collaboration)
Publication:	Physical Review C
Publisher:	American Physical Society
Cost:	USD \$ 0.00

Request Details

Does your reuse require significant modifications: No

Specify intended distribution Worldwide
locations:

Reuse Category:	Reuse in a thesis/dissertation
Requestor Type:	Student
Items for Reuse:	Figures/Tables
Number of Figure/Tables:	4
Figure/Tables Details:	Figures 2, 3, 4, 6
Format for Reuse:	Print and Electronic
Total number of print copies:	Up to 1000

Information about New Publication:

University/Publisher:	Ohio University
Title of dissertation/thesis:	Photon-Related Elliptic Azimuthal Asymmetry and Photon-Hadron Correlations with an Isolation Cut in Au+Au Collisions at $\sqrt{s_{\text{NN}}} = 200 \text{ GeV}$ at RHIC-PHENIX
Author(s):	Tyler Danley
Expected completion date:	Dec. 2018

License Requestor Information

Name:	Tyler Danley
Affiliation:	Individual
Email Id:	td533712@ohio.edu
Country:	United States

Page 1 of 3

Figure C.7: Page 1 of 1 of the permissions license is for Figures 1.14a, 1.15a, 1.17 and 7.14.



12-Sep-2018

This license agreement between the American Physical Society ("APS") and Tyler Danley ("You") consists of your license details and the terms and conditions provided by the American Physical Society and SciPris.

Licensed Content Information

License Number:	RNP/18/SEP/007758
License date:	12-Sep-2018
DOI:	10.1103/PhysRevLett.111.032301
Title:	Medium Modification of Jet Fragmentation in $\mathrm{Au}+\mathrm{Au}$ Collisions at $\sqrt{s_{\mathrm{NN}}} = 200 \text{ GeV}$ Measured in Direct Photon-Hadron Correlations
Author:	A. Adare et al. (PHENIX Collaboration)
Publication:	Physical Review Letters
Publisher:	American Physical Society
Cost:	USD \$ 0.00

Request Details

Does your reuse require significant modifications:	No
Specify intended distribution locations:	Worldwide
Reuse Category:	Reuse in a thesis/dissertation
Requestor Type:	Student
Items for Reuse:	Figures/Tables
Number of Figure/Tables:	3
Figure/Tables Details:	Figures 1, 2, 3
Format for Reuse:	Print and Electronic
Total number of print copies:	Up to 1000

Information about New Publication:

University/Publisher:	Ohio University
Title of dissertation/thesis:	Photon-Related Elliptic Azimuthal Asymmetry and Photon-Hadron Correlations with an Isolation Cut in Au+Au Collisions at $\sqrt{s_{\mathrm{NN}}} = 200 \text{ GeV}$ at RHIC-PHENIX
Author(s):	Tyler Danley
Expected completion date:	Dec. 2018

License Requestor Information

Name:	Tyler Danley
Affiliation:	Individual
Email Id:	td533712@ohio.edu
Country:	United States

Page 1 of 3

Figure C.8: Page 1 of 1 of the permissions license is for Figures 1.14b, 1.15b, and 1.16.



13-Sep-2018

This license agreement between the American Physical Society ("APS") and Tyler Danley ("You") consists of your license details and the terms and conditions provided by the American Physical Society and SciPris.

Licensed Content Information

License Number:	RNP/18/SEP/007789
License date:	13-Sep-2018
DOI:	10.1103/PhysRevC.91.044907
Title:	Heavy-quark production and elliptic flow in Au + Au collisions at $\sqrt{s_{NN}} = 62.4 \text{ GeV}$
Author:	A. Adare et al. (PHENIX Collaboration)
Publication:	Physical Review C
Publisher:	American Physical Society
Cost:	USD \$ 0.00

Request Details

Does your reuse require significant modifications:	No
Specify intended distribution locations:	Worldwide
Reuse Category:	Reuse in a thesis/dissertation
Requestor Type:	Student
Items for Reuse:	Figures/Tables
Number of Figure/Tables:	1
Figure/Tables Details:	figure 1
Format for Reuse:	Print and Electronic
Total number of print copies:	Up to 1000

Information about New Publication:

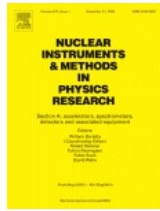
University/Publisher:	Ohio University
Title of dissertation/thesis:	Photon-Related Elliptic Azimuthal Asymmetry and Photon-Hadron Correlations with an Isolation Cut in Au+Au Collisions at $\sqrt{s_{NN}} = 200 \text{ GeV}$ at RHIC-PHENIX
Author(s):	Tyler Danley
Expected completion date:	Dec. 2018

License Requestor Information

Name:	Tyler Danley
Affiliation:	Individual
Email Id:	td533712@ohio.edu
Country:	United States

Page 1 of 3

Figure C.9: Page 1 of 1 of the permissions license is for Figure 2.2.



Title: PHENIX magnet system
Author: S.H. Aronson, J. Bowers, J. Chiba, G. Danby, A. Drees, O. Fackler, A. Franz, J.P. Freidberg, W. Guryan, A. Harvey, T. Ichihara, J. Jackson, R. Jayakumar, S. Kahn, V. Kashikhin, P.J. Kroon, M. Libkind, M.D. Marx, W.Z. Meng, F. Messer, S. Migluolio, I.D. Ojha, R. Prigl et al.
Publication: Nuclear Instruments and Methods in Physics Research Section A: Accelerators, Spectrometers, Detectors and Associated Equipment
Publisher: Elsevier
Date: 1 March 2003
 Copyright © 2002 Elsevier Science B.V. All rights reserved.

Logged in as:

Tyler Danley

Account #:

3001334847

[LOGOUT](#)

Order Completed

Thank you for your order.

This Agreement between Tyler Danley ("You") and Elsevier ("Elsevier") consists of your license details and the terms and conditions provided by Elsevier and Copyright Clearance Center.

Your confirmation email will contain your order number for future reference.

[printable details](#)

License Number	4426831475147
License date	Sep 12, 2018
Licensed Content Publisher	Elsevier
Licensed Content Publication	Nuclear Instruments and Methods in Physics Research Section A: Accelerators, Spectrometers, Detectors and Associated Equipment
Licensed Content Title	PHENIX magnet system
Licensed Content Author	S.H. Aronson, J. Bowers, J. Chiba, G. Danby, A. Drees, O. Fackler, A. Franz, J.P. Freidberg, W. Guryan, A. Harvey, T. Ichihara, J. Jackson, R. Jayakumar, S. Kahn, V. Kashikhin, P.J. Kroon, M. Libkind, M.D. Marx, W.Z. Meng, F. Messer, S. Migluolio, I.D. Ojha, R. Prigl et al.
Licensed Content Date	Mar 1, 2003
Licensed Content Volume	499
Licensed Content Issue	2-3
Licensed Content Pages	9
Type of Use	reuse in a thesis/dissertation
Portion	figures/tables/illustrations
Number of figures/tables /illustrations	1
Format	both print and electronic

Figure C.10: Page 1 of 2 of the permissions license is for Figure 2.3.

Are you the author of No
this Elsevier article?

Will you be translating? No

Original figure numbers figure 3

Title of your Photon-Related Elliptic Azimuthal Asymmetry and Photon-Hadron Correlations with an Isolation Cut
thesis/dissertation in Au Au Collisions at $\sqrt{s_{NN}} = 200$ GeV at RHIC-PHENIX

Expected completion Dec 2018
date

Estimated size (number 250
of pages)

Requestor Location Tyler Danley
Edwards Accelerator Lab
123 University Terrace

ATHENS, OH 45701
United States
Attn: Tyler Danley

Publisher Tax ID 98-0397604

Total 0.00 USD

ORDER MORE **CLOSE WINDOW**

Copyright © 2018 [Copyright Clearance Center, Inc.](#). All Rights Reserved. [Privacy statement](#). [Terms and Conditions](#).
Comments? We would like to hear from you. E-mail us at customercare@copyright.com

Figure C.11: Page 2 of 2 of the permissions license is for Figure 2.3.



Title: PHENIX calorimeter
Author: L Aphectche,T.C Awes,J Banning,S Bathe,A Bazilevsky,S Belikov,S.T Belyaev,C Blume,M Bobrek,D Bucher,V Bumazhnov,H Büsching,S Chernichenkov,V Cianciolo,M Cutshaw,D,G D'Enterria,S Daniels,G David,H Delagrange,A Denisov,A Durum,Y.V Efremenko et al.
Publication: Nuclear Instruments and Methods in Physics Research Section A: Accelerators, Spectrometers, Detectors and Associated Equipment
Publisher: Elsevier
Date: 1 March 2003
 Copyright © 2002 Elsevier Science B.V. All rights reserved.

Logged in as:

Tyler Danley

Account #: 3001334847

[LOGOUT](#)

Order Completed

Thank you for your order.

This Agreement between Tyler Danley ("You") and Elsevier ("Elsevier") consists of your license details and the terms and conditions provided by Elsevier and Copyright Clearance Center.

Your confirmation email will contain your order number for future reference.

[printable details](#)

License Number	4426840615808
License date	Sep 12, 2018
Licensed Content Publisher	Elsevier
Licensed Content Publication	Nuclear Instruments and Methods in Physics Research Section A: Accelerators, Spectrometers, Detectors and Associated Equipment
Licensed Content Title	PHENIX calorimeter
Licensed Content Author	L Aphectche,T.C Awes,J Banning,S Bathe,A Bazilevsky,S Belikov,S.T Belyaev,C Blume,M Bobrek,D Bucher,V Bumazhnov,H Büsching,S Chernichenkov,V Cianciolo,M Cutshaw,D,G D'Enterria,S Daniels,G David,H Delagrange,A Denisov,A Durum,Y.V Efremenko et al.
Licensed Content Date	Mar 1, 2003
Licensed Content Volume	499
Licensed Content Issue	2-3
Licensed Content Pages	16
Type of Use	reuse in a thesis/dissertation
Portion	figures/tables/illustrations
Number of figures/tables /illustrations	2
Format	both print and electronic

Figure C.12: Page 1 of 2 of the permissions license is for Figure 2.5.

Are you the author of No
this Elsevier article?

Will you be translating? No

Original figure numbers Figures 1, 10

Title of your Photon-Related Elliptic Azimuthal Asymmetry and Photon-Hadron Correlations with an Isolation Cut
thesis/dissertation in Au Au Collisions at $\sqrt{s_{NN}} = 200$ GeV at RHIC-PHENIX

Expected completion Dec 2018
date

Estimated size (number 250
of pages)

Requestor Location Tyler Danley
Edwards Accelerator Lab
123 University Terrace

ATHENS, OH 45701
United States
Attn: Tyler Danley

Publisher Tax ID 98-0397604

Total 0.00 USD

ORDER MORE **CLOSE WINDOW**

Copyright © 2018 [Copyright Clearance Center, Inc.](#). All Rights Reserved. [Privacy statement](#). [Terms and Conditions](#).
Comments? We would like to hear from you. E-mail us at customercare@copyright.com

Figure C.13: Page 2 of 2 of the permissions license is for Figure 2.5.



RightsLink®

[Home](#) [Account Info](#) [Help](#) [Email](#)



Title: PHENIX central arm tracking detectors

Author: K. Adcox,N.N. Ajitanand,J. Alexander,D. Autrey,R. Averbeck,B. Azmoun,K.N. Barish,V.V. Baublis,R. Belkin,S. Bhaganatula,J.C. Biggs,D. Borland,S. Botelho,W.L. Bryan,J. Burward-Hoy,S.A. Butsyk,W.C. Chang,T. Christ,O. Dietzsch,A. Drees,R. du Rietz et al.

Publication: Nuclear Instruments and Methods in Physics Research Section A: Accelerators, Spectrometers, Detectors and Associated Equipment

Publisher: Elsevier

Date: 1 March 2003

Copyright © 2002 Published by Elsevier B.V.

Logged in as:
Tyler Danley
Account #:
3001334847

[LOGOUT](#)

Order Completed

Thank you for your order.

This Agreement between Tyler Danley ("You") and Elsevier ("Elsevier") consists of your license details and the terms and conditions provided by Elsevier and Copyright Clearance Center.

Your confirmation email will contain your order number for future reference.

[printable details](#)

License Number	4426831225833
License date	Sep 12, 2018
Licensed Content Publisher	Elsevier
Licensed Content Publication	Nuclear Instruments and Methods in Physics Research Section A: Accelerators, Spectrometers, Detectors and Associated Equipment
Licensed Content Title	PHENIX central arm tracking detectors
Licensed Content Author	K. Adcox,N.N. Ajitanand,J. Alexander,D. Autrey,R. Averbeck,B. Azmoun,K.N. Barish,V.V. Baublis,R. Belkin,S. Bhaganatula,J.C. Biggs,D. Borland,S. Botelho,W.L. Bryan,J. Burward-Hoy,S.A. Butsyk,W.C. Chang,T. Christ,O. Dietzsch,A. Drees,R. du Rietz et al.
Licensed Content Date	Mar 1, 2003
Licensed Content Volume	499
Licensed Content Issue	2-3
Licensed Content Pages	19
Type of Use	reuse in a thesis/dissertation
Portion	figures/tables/illustrations
Number of figures/tables /illustrations	1
Format	both print and electronic

Figure C.14: Page 1 of 2 of the permissions license is for Figure 2.6.

Are you the author of No
this Elsevier article?

Will you be translating? No

Original figure numbers figure 3

Title of your Photon-Related Elliptic Azimuthal Asymmetry and Photon-Hadron Correlations with an Isolation Cut
thesis/dissertation in Au Au Collisions at $\sqrt{s_{NN}} = 200$ GeV at RHIC-PHENIX

Expected completion Dec 2018
date

Estimated size (number 250
of pages)

Requestor Location Tyler Danley
Edwards Accelerator Lab
123 University Terrace

ATHENS, OH 45701
United States
Attn: Tyler Danley

Publisher Tax ID 98-0397604

Total 0.00 USD

ORDER MORE **CLOSE WINDOW**

Copyright © 2018 [Copyright Clearance Center, Inc.](#). All Rights Reserved. [Privacy statement](#). [Terms and Conditions](#).
Comments? We would like to hear from you. E-mail us at customercare@copyright.com

Figure C.15: Page 2 of 2 of the permissions license is for Figure 2.6.

 Copyright Clearance Center

Note: Copyright.com supplies permissions but not the copyrighted content itself.

1 PAYMENT 2 REVIEW 3 CONFIRMATION

Step 3: Order Confirmation

Thank you for your order! A confirmation for your order will be sent to your account email address. If you have questions about your order, you can call us 24 hrs/day, M-F at +1.855.239.3415 Toll Free, or write to us at info@copyright.com. This is not an invoice.

<p>Confirmation Number: 11748395 Order Date: 09/13/2018</p> <p>Payment Information</p> <p>Tyler Danley td533712@ohio.edu +1 (478) 951-8919 Payment Method: n/a</p>	<p>If you paid by credit card, your order will be finalized and your card will be charged within 24 hours. If you choose to be invoiced, you can change or cancel your order until the invoice is generated.</p>
---	--

Order Details

Annual review of nuclear and particle science

<p>Order detail ID: 71552424 Order License Id: 4427280500205 ISSN: 1545-4134 Publication Type: e-Journal Volume: Issue: Start page: Publisher: ANNUAL REVIEWS</p>	<p>Permission Status:  Granted Permission type: Republish or display content Type of use: Thesis/Dissertation</p> <p>Requestor type Academic institution Format Print, Electronic Portion chart/graph/table/figure</p> <p>Number of charts/graphs/tables /figures 1</p> <p>The requesting person/organization Tyler Danley</p> <p>Title or numeric reference of the portion(s) Figure 8</p> <p>Title of the article or chapter the portion is from Glauber Modeling in High-Energy Nuclear Collisions</p>
--	--

Note: This item will be invoiced or charged separately through CCC's **RightsLink** service. [More info](#) **\$ 0.00**

Figure C.16: Page 1 of 1 of the permissions license is for Figure 3.1.



RightsLink®

 ELSEVIER

Title: PHENIX results on direct photon-hadron correlations Author: Huijun Ge Publication: Nuclear and Particle Physics Proceedings Publisher: Elsevier Date: August–September 2017 <small>© 2017 Published by Elsevier B.V.</small>	Logged in as: Tyler Danley Account #: 3001334847 LOGOUT
---	--

Order Completed

Thank you for your order.

This Agreement between Tyler Danley ("You") and Elsevier ("Elsevier") consists of your license details and the terms and conditions provided by Elsevier and Copyright Clearance Center.

Your confirmation email will contain your order number for future reference.

[printable details](#)

License Number	4427300514412
License date	Sep 13, 2018
Licensed Content Publisher	Elsevier
Licensed Content Publication	Nuclear and Particle Physics Proceedings
Licensed Content Title	PHENIX results on direct photon-hadron correlations
Licensed Content Author	Huijun Ge
Licensed Content Date	August–September 2017
Licensed Content Volume	289
Licensed Content Issue	n/a
Licensed Content Pages	4
Type of Use	reuse in a thesis/dissertation
Portion	figures/tables/illustrations
Number of figures/tables /illustrations	1
Format	both print and electronic
Are you the author of this Elsevier article?	No
Will you be translating?	No
Original figure numbers	figure 5
Title of your thesis/dissertation	Photon-Related Elliptic Azimuthal Asymmetry and Photon-Hadron Correlations with an Isolation Cut in Au Au Collisions at $\sqrt{s_{NN}} = 200$ GeV at RHIC-PHENIX
Expected completion date	Dec 2018
Estimated size (number of pages)	250

Figure C.17: Page 1 of 2 of the permissions license is for Figure 9.2.

Rightslink® by Copyright Clearance Center

<https://s100.copyright.com/AppDispatchServlet>

Requestor Location Tyler Danley
Edwards Accelerator Lab
123 University Terrace

ATHENS, OH 45701
United States
Attn: Tyler Danley

Publisher Tax ID 98-0397604
Total 0.00 USD

ORDER MORE **CLOSE WINDOW**

Copyright © 2018 [Copyright Clearance Center, Inc.](#). All Rights Reserved. [Privacy statement](#). [Terms and Conditions](#).
Comments? We would like to hear from you. E-mail us at customercare@copyright.com

Figure C.18: Page 2 of 2 of the permissions license is for Figure 9.2.



Thesis and Dissertation Services